DEVELOPMENT AND SIMULATION OF 3D DIAMOND DETECTORS

A thesis submitted to The University of Manchester for the degree of Doctor of Philosophy in the Faculty of Science and Engineering

2018

By
Giulio T. Forcolin
School of Physics and Astronomy

Contents

Abstract

Ever increasing demand for more radiation resistant detectors from experiments such as those at the Large Hadron Collider has pushed the development of novel radiation resistant technologies. Recent developments in the laser processing of diamond have led to the construction of the first 3D diamond detectors: diamond detectors with graphitic electrodes embedded in the sensor material bulk rather than on the surface. This technology also presents interesting properties for the medical field, where 3D diamond detectors are also of interest.

This thesis details some of the steps that were carried out between the fabrication of some of the first 3D diamond devices to the present day production and testing of the first 3D pixel devices and the first use of 3D diamond devices in Particle Physics experiments. This progress has in part been pushed by improvements in the laser processing techniques allowing the production of columns with lower resistances and more consistent properties.

This thesis describes the fabrication of a number of these devices and details the experiments that these devices have undergone in a number of different conditions at the Diamond Light Source (Oxford), the Ruđer Bošković Institute (Zagreb), the Paul Scherrer Institute (Zürich), and the test beam facilities at CERN.

This thesis also describes the simulations that were carried out to replicate the data obtained from some of the earlier devices, and hence understand how charge is collected in 3D diamond detectors and to explain some of the observed behavior of these devices.

Declaration

No portion of the work referred to in the thesis has been submitted in support of an application for another degree or qualification of this or any other university or other institute of learning

Copyright

Acknowledgements

First of all I would like to thank my supervisor, Alex Oh, for the guidance and opportunities he has given me over the course of the PhD, allowing me to participate in such a large array of projects, as well as all the travel, with the US being a particular highlight.

Over the course of the PhD I have worked closely with Steve Murphy, Iain Haughton, and Francisca Munoz Sanchez, with whom I have had many fruitful conversations over the years and who have helped me on all the different aspects of the project.

I would like to thank the whole diamond community for being so welcoming over these last few years, in particular the RD42 and ADAMAS Collaborations. I would especially like to thank Harris Kagan, Dmitry Hits, Felix Bachmair, Diego Sanz Becerra and Michael Reichmann for the many constructive discussions, particularly during the many, long, sleep-deprived days spent at testbeams.

I would also like to thank Arianna Morozzi for working closely with me on the simulations and Keida Kanxheri for all the work on the dosimetry part of the project. Thanks also to Florian Kassel for the many constructive discussions on simulations, Marcin Bartosik for irradiating our samples and Moritz Guthoff for volunteering to put our samples in CMS.

I would like to thank the Christie Hospital for letting us use their machines, and in particular Adam Aitkenhead, for staying with us late into the evening running the machines for us.

I would also like to thank Jiri Masik for all his help during my ATLAS service task.

I would like to thank Mal McGowan for letting me use the D16 lab, and all the other users, especially Umberto Monteverde and Rakesh Kumar for always fielding my many questions.

Many thanks to all the members of Manchester HEP group making my time in the group such a delight and keeping me well fed on chocolate, cake, pizza and beer. Special thanks to Chris Parkes for letting me do a Masters project which led

me into detector development, Fred Loebinger for letting me study in Manchester and Sabah for all the computational support.

Thanks to everyone at CERN for making my LTA such a fantastic experience, with a special mention to Ben and Iwan for organizing the ski trips.

I would like to thank the Manchester Gilbert and Sullivan Society, the renowned Manchester drinking society for constantly reminding me that there is more to life than Physics and that there is always some room for 19th and 20th century operettas.

Thanks to my parents for getting me interested in science as a child and being unconditionally supportive of all my scientific pursuits and endeavors.

Finally thank you Monica, your unconditional love and support has helped me immensely, especially during these last few months of stress, anxiety and sleepless nights, you have always been there to help me make it through the difficult times and to make sure I have always been looking after myself.

"*Cherish wisdom as a means of traveling from youth to old age, for it is more lasting than any other possession.*" Bias of Priene

List Of Acronyms

ALICE A Large Ion Collider Experiment

ATLAS A Toroidal LHC ApparatuS

B-Layer Barrel Layer

BCM Beam Condition Monitor

CAD Computer Aided Design

CCE Charge Collection Efficiency

CERN Conseil Européen pour la Recherche Nucléaire

CMOS Complementary Metal Oxide Semiconductor

CMS Compact Muon Solenoid

CP Charge Parity

CVD Chemical Vapour Deposition

DBM Diamond Beam Monitor

DLS Diamond Light Source

DRIE Deep Reactive Ion Etching

E6 Element 6

FE-I4 Front End I4

FTK Fast Tracker

HEP High Energy Physics

HL-LHC High Luminosity Large Hadron Collider

HPHT High Pressure High Temperature

IBIC Ion Beam Induced Current

IBL Insertable B-Layer

II-VI II-VI Incorporated

IIa IIa Technologies

LHC Large Hadron Collider

LHCb Large Hadron Collider beauty

LINAC Linear Accelerator

LS Long Shutdown

MIP Minimum Ionizing Particle

PCB Printed Circuit Board

pCVD Polycrystalline Chemical Vapour Deposition

PD Pixel Detector

PKA Primary Knock On Atom

PS Proton Synchrotron

PSI Paul Scherrer Institute

RBI Ruđer Bošković Institute

ROC Read-out Chip

scCVD Single Cyrstal Chemical Vapour Deposition

SCT Semiconductor Tracker

SLM Spatial Light Modulator

SPS Super Proton Synchrotron

TCAD Technology Computer Assisted Design

TCT Transient Current Technique

TRIBIC Time Resolved Ion Beam Induced Current

TRT Transition Radiation Tracker

UBM Under Bump Metal/Metalization

UV Ultraviolet

VELO Vertex Locator

1. Motivation

1.1 The LHC accelerator complex

CERN, the Organization Européenne pour la Recherche Nucléaire, (formerly known as the Conseil Européen pour la Recherche Nucléaire) has, since its foundation in 1954 [1], been pushing the frontiers of scientific understanding in the fields of Nuclear Physics and High Energy Physics. This has resulted in the construction of a range of particle accelerators and colliders. Currently there are several accelerators in operation at CERN [2], the largest of these being the Large Hadron Collider (LHC), which has been providing proton and heavy ion collisions for the detectors located around its 27 km circumference: A Toroidal LHC ApparatuS (ATLAS), the Compact Muon Solenoid experiment (CMS), the LHC beauty experiment (LHCb) and A Large Ion Collider Experiment (ALICE). Due to the extremely high energy of the protons in the LHC, a series of smaller accelerators is used to raise the energy of protons before injection into the LHC ring.

The protons used for LHC Physics begin their journey at LINAC2, from which they are injected into the booster ring, the Proton Synchrotron (PS), followed by the Super Proton Synchrotron (SPS), and finally the LHC. The protons enter the LHC as two beams traveling in opposite directions with an energy of 450 GeV, after which they are accelerated to an energy of 7 TeV before they are made to collide at four points around the circumference of the LHC. Alternatively protons from the SPS can be sent to the beam lines such as H6 in the experimental hall of the north area [3], where they can be used in experiments to test detector devices, such as those described later in this thesis. The full complex is shown in Fig. 1.1.

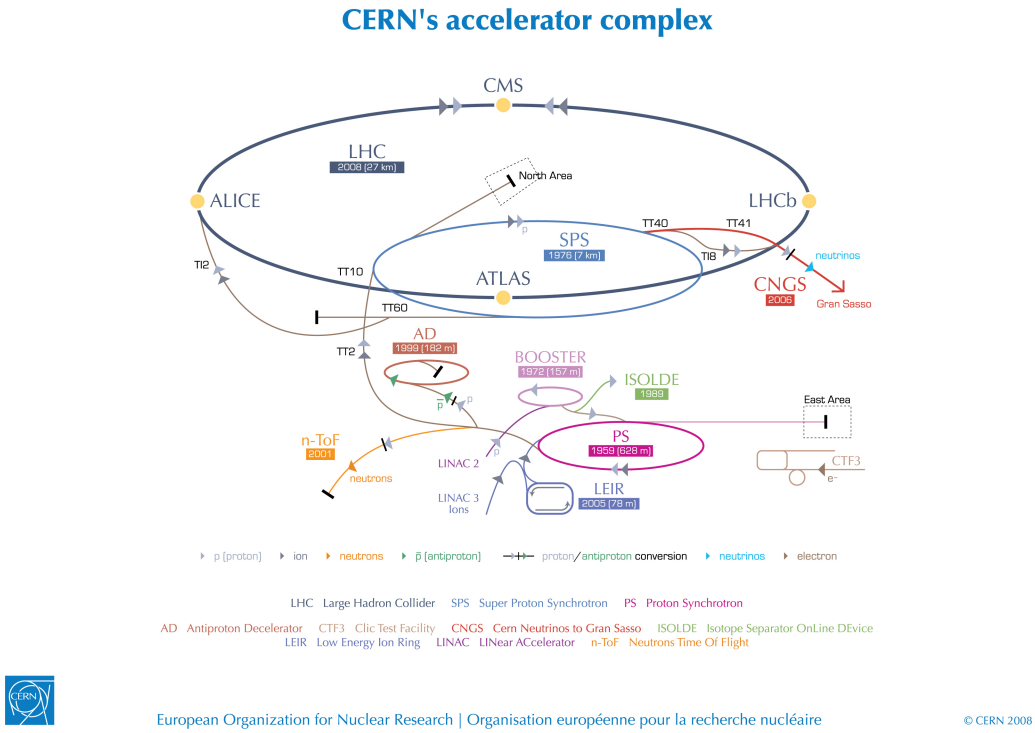

Figure 1.1: The accelerator complex at CERN [4]

1.2 Particle detection with the ATLAS experiment

Radiation is detected by its interaction with matter. When radiation passes through a detector it generates a signal that can be read out. The phenomena involved in generating this signal generally involve soft electrons and photons, as well as other nuclear, atomic or molecular excitations.

Many different methods are used in order to detect particles. The ATLAS experiment (Fig. 1.2) employs a selection of these techniques to reach an improved understanding of a large number of important topics in High Energy Physics (HEP), the most important of which has been to gain an understanding of electroweak symmetry breaking [5]. This eventually lead to the discovery of the Higgs boson [6] achieved simultaneously with the CMS experiment [7].

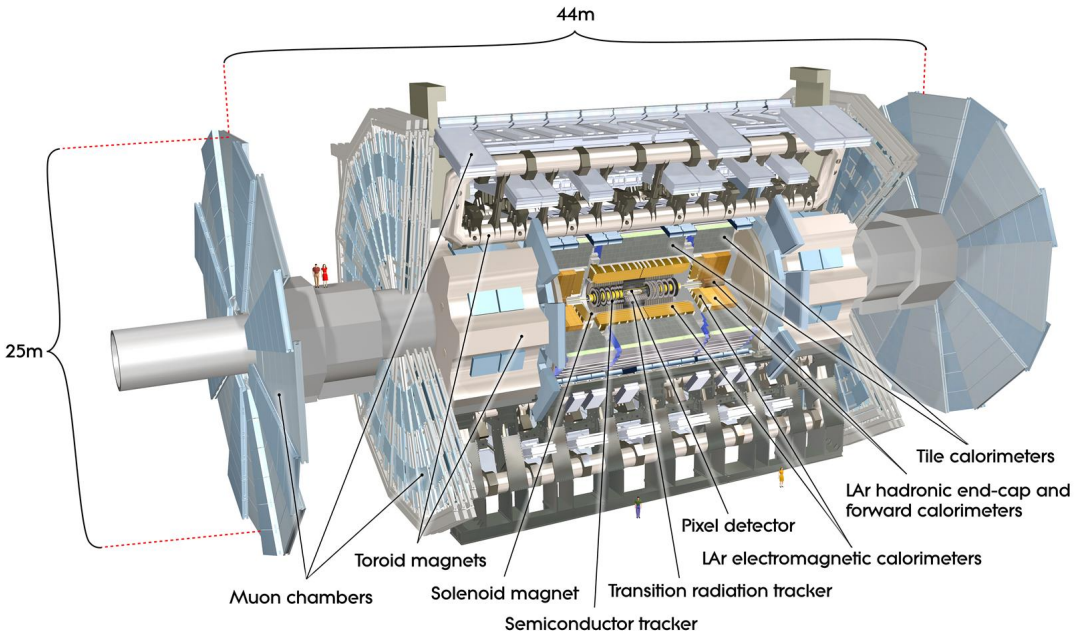

Figure 1.2: The ATLAS detector [8]

Due to the high energy and luminosity of the LHC, it is also envisioned that the ATLAS detector will be able to probe more exotic theories such as Super-Symmetry and Technicolor theories [5], either demonstrating their existence or excluding some versions of these theories by setting limits on some of their parameters (e.g. coupling strengths to standard model particles, or new particle masses).

ATLAS also provides high precision measurements of model parameters such as the masses of the W boson and the top quark as well as triple gauge couplings and also be able to investigate phenomena such as CP Violation and rare decays of the B system [5].

The ATLAS detector consists of several sub-detectors that employ different detection techniques and technologies to determine an array of information about particles produced in the collision events. The ATLAS experiment can broadly be divided into three sections. The outermost section is the muon system, designed to track the muons produced in the LHC interactions as muons are the only detectable particles that can travel through the inner detector layers. Inside the muon system are the hadronic and electromagnetic calorimeters. These are used to measure the energies of hadrons and electrons produced in the LHC interactions. Inside the calorimeters is the ATLAS inner detector. The work described in this thesis concerns the development of tracking detectors to be used in the inner layers of the inner detector.

1.2.1 Inner detector

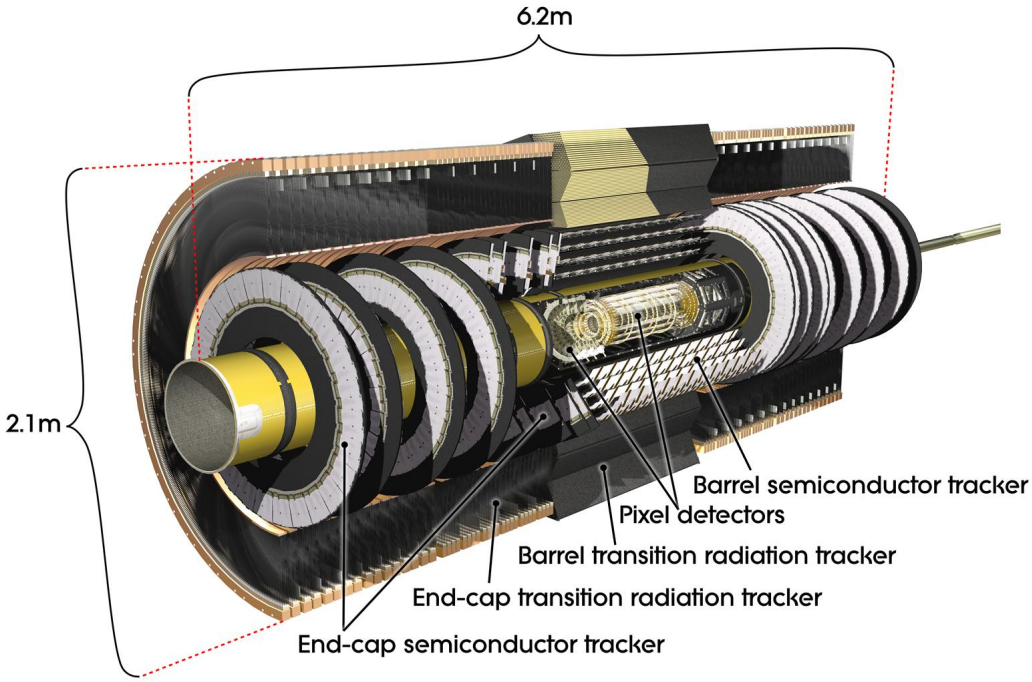

Figure 1.3: The full structure of the ATLAS inner detector at the start of the LHC operation [9]

The ATLAS inner detector (shown in Fig. 1.3) consists of 3 parts: the pixel detector, the semiconductor tracker and the transition radiation tracker. All these sections are composed of end-caps to detect particles with high pseudorapidities (pseudorapidity is a measure of the angle collision products travel relative to the beam pipe, with $\eta = 0$ perpendicular to the beam axis and $\eta = \infty$ parallel to the beam axis) as well as barrel layers (the layout of which is shown in Fig. 1.4) to detect particles at low pseudorapidity. The main purpose of the inner detector is to track particles to determine the position of the vertex from which they originate, and to measure their momentum by measuring how much their tracks are bent by the magnetic field due to the solenoid magnet seen in Fig. 1.2.

The pixel detector (PD) consists of a number of Silicon sensors with a thickness of 250 µm n doped bulk material with n^+ implants on the readout side and p-n junctions on the back side (a more detailed description of these concepts is given in Section 2.1), arranged in 3 barrel layers and 6 end cap discs (3 on each side of the interaction point). Each sensor consists of 2880 pixels, each of size 400×50 µm^2 and are based on the FE-I3 chip [10]. The sensors overlap slightly in order to provide

complete coverage. The innermost layer of this detector (and hence the one most prone to radiation damage) is called the B-Layer.

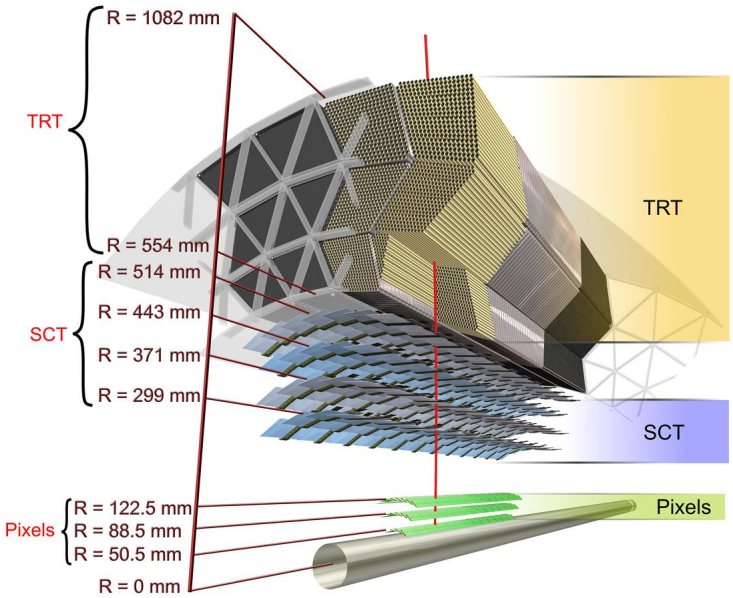

Figure 1.4: Schematic diagram of the inner detector showing the position of the barrel components with respect to the beam pipe at the start of the LHC running [9]

To study events among the debris caused by having ~ 60 collisions per bunch crossing it is necessary to have an accurate tracking system. This is particularly important for long lived particles ($\tau > 10^{-13}$ s), such as B mesons. As these particles typically travel a distance of the order of a few millimeters from a primary vertex (the location of the proton-proton collision that produced them) before decaying at a secondary vertex. Consequently, it is necessary to determine with very high accuracy whether these particles are produced at a primary vertex (during a proton-proton collision) or at a secondary vertex (due to the decay of a long lived particle produced in a proton-proton collision).

The material the particles have to travel through should be minimized to reduce the likelihood of the particles being absorbed or deflected by the detector material. To achieve the required precision and to reconstruct the curvature of the tracks due to the magnetic field, it is also necessary to have at least 3 measurements for each particle track.

However due to the extreme conditions at such a small distance from the interaction point, radiation damage to the innermost layer of the pixel detector is

expected to greatly reduce its performance and even cause some of the modules to fail. To counteract this problem, a new layer of pixel modules was designed: the Insertable B-Layer (IBL), to be placed between the B-Layer and a reduced diameter beam pipe during the LHC long shutdown 1 (2013-2014) [11]. The IBL contains Silicon detectors which use both planar and 3D geometries.

Outside of the pixel detector is the Semiconductor Tracker (SCT) which consists of 4 barrel layers and 18 end-cap discs, providing a minimum of 4 tracking points per particle. The modules of this detector are made up of 1 layer of single sided micro-strip Silicon p-on-n sensors. Both the PD and the SCT detectors are based on the same detection principles, described in Section 2.1.

The outermost element of the inner detector is the Transition Radiation Tracker (TRT).It consists of a barrel and two endcaps containing straw tubes each with 4 mm diameter which are used for tracking [12]. This subdetector is also capable of particle identification by detecting the transition radiation generated when the particles pass through the filling material between the straws [13].

1.2.2 The ATLAS upgrade program

It is expected for the LHC to remain in operation until ~ 2035, however as technology improves and the aging hardware of the experiment starts to degrade due to radiation damage and damage cause by the interaction of atoms and dust particles in the atmosphere, it is expected to undergo a series of long shutdowns to allow the detectors to be upgraded in order to replace malfunctioning and radiation damaged parts of the detector to allow for better performance.

The first of these long shutdowns (LS1) has finished, allowing operations to resume in 2015. During this shutdown the main goals were to replace the beam pipe to reduce its diameter, thus allowing the Insertable B-Layer (IBL) to be inserted between the new beam pipe and the current B-Layer.

This upgrade was necessary as the B-Layer was designed for a peak luminosity of 10^{34} cm^{-2}s^{-1}, however it was realized that the peak luminosity could reach at least 2×10^{34} cm^{-2}s^{-1}. It is therefore expected for the LHC to achieve an integrated luminosity of of $50 - 100$ fb^{-1} before LS2 [14]. This means that the hardware will be subjected to a much greater integrated luminosity before the detectors can be replaced, hence making this measure necessary [11]. During this period the Fast TracKer (FTK) was also implemented to use a system of electronics to perform global track reconstruction in order to make this information available for the level-2 trigger [15].

The second long shutdown is expected to start in late 2018, with data taking to

resume in 2021, at which point the peak luminosity is expected to reach $2-3\times10^{34}$ $\text{cm}^{-2}\text{s}^{-1}$ allowing the ATLAS experiment to achieve a total integrated luminosity of $300-400$ fb^{-1} before the next long shutdown [14]. This would increase the number of interactions per bunch crossing from the current value of ~ 20 up to ~ 55 and ~ 80 [16]. During this shutdown it is planned to upgrade the muon system by replacing the innermost end cap layer with a new small muon wheel [17]. The calorimeter system will need to be upgraded to provide better triggering due to the increased interaction rate.

LS3 is expected to commence in 2023, with data taking to resume in ≈ 2026 [16]; this will be the era of the High Luminosity LHC (HL-LHC). This upgrade is expected to take the peak luminosity up to 5×10^{34} $\text{cm}^{-2}\text{s}^{-1}$ with the aim of bringing the total integrated luminosity of the LHC up to 3000 fb^{-1} over the following decade. However this upgrade will bring with it unprecedented challenges as it is expected that the interaction rate will reach 200 interactions per bunch crossing, and will require the ATLAS components to withstand extreme amounts of radiation.

To overcome these challenges several upgrades are to be carried out during this shutdown, replacing most of the detector electronics. An important part of this upgrade will involve the inner detector. It will need to be completely replaced with new technology that will allow it to withstand the increased radiation dose at the HL-LHC as well as increased granularity in order to provide good performance with the expected increase in pileup. It is also desired for the detector to be more modular, in order to allow sections of it, particularly the innermost layers, to be replaced with minimal disruption to the rest of the experiment [18].

Various options are being considered for the inner pixel layers, including planar Silicon, 3D Silicon, CMOS [19] and diamond if it can be proven as a viable technology, with the aim of reducing thickness of material, effects of radiation damage and cost [20]. Several different layouts are also being considered in order to take advantage of the physics that will be available at the HL-LHC. Some of these options, such as an LHCb style vertex locator for b and τ tagging [21] will require detectors that are extremely radiation resistance that current technology would struggle to achieve. Work will also need to be carried out to upgrade the trigger system to allow it to cope with the vast volume of data that will be generated.

3D diamond detectors present an interesting prospect for future upgrades of the ATLAS tracker as it would be a technology that combines the radiation hardness of diamond as a material, with the radiation hardness of the 3D detector geometry. It is hoped that this combination of approaches will provide detectors that are radiation hard enough to survive in this hostile environment, particularly those encountered

close to the interaction point in the future HL-LHC. Diamond detectors are already in use as beam monitors in a number of the LHC experiments, and Silicon devices taking advantage of a 3D geometry are already present in the ATLAS IBL.

1.3 Medical applications

Significant progress has been made in cancer treatment in recent years due to the development of new radiotherapy techniques. One such technique is stereotactic radiotherapy, where radiation beams are aimed at tumors from different directions in order to maximize the dose received by the tumors while minimizing the dose received by the surrounding tissue, hence reducing the damage to this tissue. Normally this is achieved by having a rotating radiation source, such that a small volume of tissue (the target of the therapy) is always being irradiated while the surrounding tissue is only irradiated for a short period of time, reducing the risk of collateral damage. However for this technique to be used successfully it is important to have highly accurate patient positioning to maximize the radiation dose to the affected area and minimize the dose received by nearby healthy tissue. Due to the small size of these beams (5-40 mm) a small deviation can result in the affected area receiving only a small amount of radiation with the bulk of it going to nearby healthy tissue [22]. A radiotherapy machine used at the Christie hospital in Manchester is shown in Fig. 1.5. A particle accelerator is located behind the wall which produces high energy photons which then travel down from the overhanging section shown in the picture towards the surface where a diamond detector is placed and where a patient would normally be. A section of the back wall can rotate allowing the beam to enter the patient from different directions.

Using diamond detectors as dosimeters for these treatments presents an interesting prospect of future improvement of these techniques. Using semiconductor detectors for dosimetry would allow for the real time measurement of delivered dose and the position of the beam, allowing for quick correction if any problems are discovered. Among these options diamond especially is an interesting material as it is tissue equivalent ($Z = 6$, compare to $Z_{eff} = 7.42$ for human tissue) allowing to easily convert the dose received by the detector to the dose received by the patient, as well as being non toxic. These detectors can also be very small (1-2 mm) in size and thus could be placed very close to the affected area. In this case a 3D geometry also allows for a reduction in the applied voltage, which is safer to operate.

Figure 1.5: A stereotactic radiotherapy machine used at the Christie hospital in Manchester, with a diamond sample ready for testing.

1.4 Principles of radiation detection

Particles are detected as they deposit energy into the detector material by interacting with it through either the strong, electromagnetic or weak forces (gravity is many orders of magnitude weaker on the scale of elementary particle interactions, and hence can safely be ignored). They can do this in a variety of ways depending on the particle properties.

1. Photons, electrons and muons generally interact only via the electromagnetic force; they are not hadrons and hence cannot interact via the strong force, and the electromagnetic force is orders of magnitude stronger than the weak force, allowing it to dominate. Electrons and photons have a short radiation length, meaning that in general they do not travel far within the detector and produce electromagnetic showers. Muons have a long radiation length and therefore typically travel all the way through the detector mostly unimpeded, losing only a small amount of energy producing an ionization track.

2. While hadrons can interact via the strong force, the nuclear strong force is a short range force. Therefore hadrons can travel further into the detector before they are stopped. Charged hadrons can also interact by the electromagnetic

force, creating an ionization track in the material similarly to electrons, however they typically travel much further in the material before they initiate a hadronic shower by undergoing a nuclear interaction with a nucleus in the detector.

3. Neutrinos are a class of particles that can only interact via the weak force. This means that they are extremely unlikely to interact with any detector they pass through, however if a large enough number of these particles is present, a small proportion can be detected as they interact with matter via the weak force. This allows some experiments to broadly determine their properties, however it is not possible in practice for experiments such as those at the LHC to measure individual neutrinos, production of these particles has to be deduced by observing events where not all the energy can otherwise be accounted for.

4. Finally there are many hypothesized particles that interact through none of these forces. It is therefore impossible to directly measure their properties in experiments. However, like neutrinos their existence can be deduced by the observation of events where not all the energy can be accounted for. These can be differentiated from neutrinos by using the detectable products of the interaction to determine the properties of the particle(s) required to account for the missing energy.

There are a number of different ways to take advantage of particle properties and how they interact with matter in order to be able to measure the momentum, energy, position and charge of the particles as they pass through a detector medium. Thus many different categories of detectors have been invented to take advantage of different interaction to measure these particle properties [23].

1.4.1 Photons

The energy loss of photons is dominated by three different phenomena, depending on the energy of the photon and the material through which it is passing through:

Pair production

For photon energies higher than two times the rest mass of an electron, a photon can produce an electron-positron pair. This can only happen as the electrons travels close to a massive charged object, in order to conserve momentum [23]. This process becomes dominant for photon energies $E \sim 10 m_e c^2$.

For very high energy photons, where the produced electrons have an energy

high enough to undergo radiative energy losses, this step initiates an electromagnetic shower where the electrons undergo bremsstrahlung and the resulting photons can also undergo pair production. The positrons that are produced can annihilate with an electron in the surrounding matter. A diagram of the pair production process is shown in Fig. 1.6.

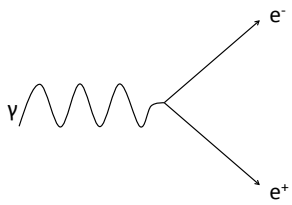

Figure 1.6: A high energy photon producing an electron-positron pair.

Compton scattering

For intermediate photon energies, energy loss is dominated by the Compton effect; an incoming photon can interact with a quasi free atomic electron, the electron recoils from the interaction at an angle ϕ while the photon is scattered by and angle θ as shown in Fig. 1.7 [23].

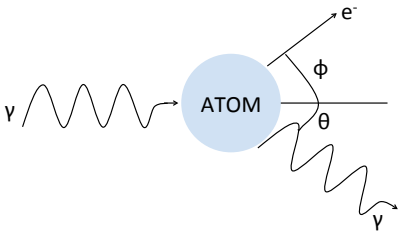

Figure 1.7: The Compton effect, a photon is scattered at an angle as it transfers some of its energy to an atomic electron

Photoelectric effect

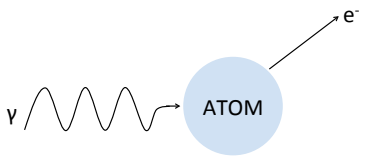

Figure 1.8: The emission of an atomic electron due to a photon with an energy higher than the work function of the material

Finally, when the photon energy is very low ($\sim$ few eV), but still higher than the binding energy of atomic electrons, photons can be absorbed as they interact with an atom, resulting in the emission of an atomic electron; a diagram of this phenomenon is shown in Fig. 1.8.

1.4.2 Charged particles

As shown in Fig. 1.9, the energy loss of charged particles in matter follows the Bethe-Bloch equation for energies in the range $0.1 < \beta\gamma < 10^4$:

$$-\left\langle \frac{dE}{dx} \right\rangle = Kz^2 \frac{Z}{A} \frac{1}{\beta^2} \left[\frac{1}{2} \ln \frac{2m_e c^2 \beta^2 \gamma^2 T_{max}}{I^2} - \beta^2 - \frac{\delta(\beta\gamma)}{2} \right] \tag{1.1}$$

At higher energy, the energy loss is dominated by the emission of photons (bremsstrahlung) as shown in Fig. 1.9, and therefore it can initiate an electromagnetic shower as described previously.

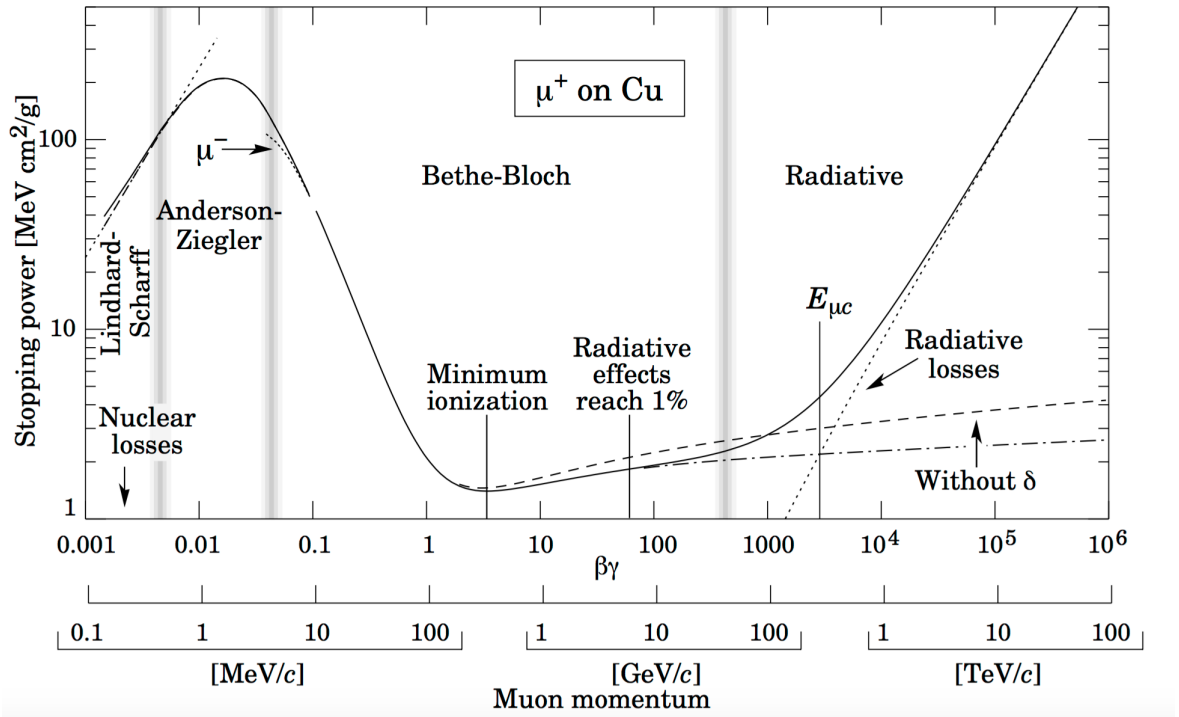

Figure 1.9: Stopping power for positive muons in copper, showing that the bulk of the radiation loss at high energy is due to radiative losses, at low energy it is due to nuclear effects, while at intermediate energies it is described by the Bethe-Bloch function [24]

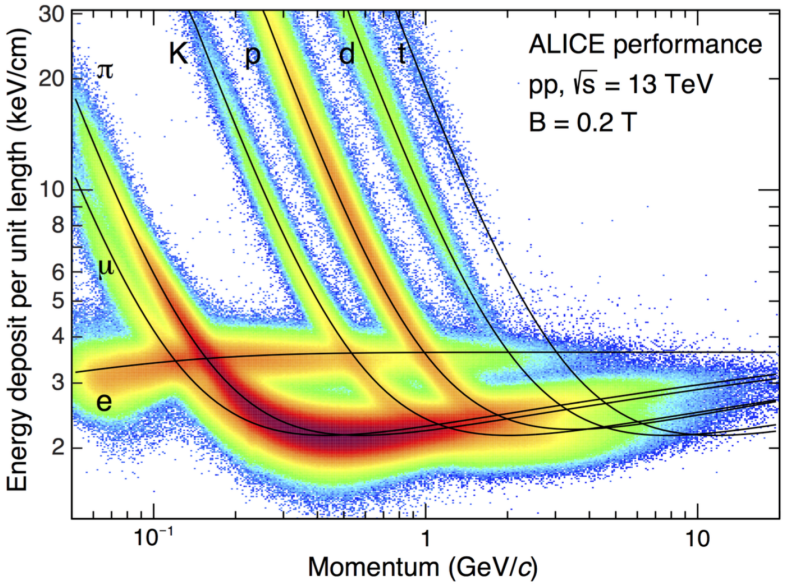

Figure 1.10: Energy loss versus particle momentum in the ALICE TPC at 13 TeV. The lines show the expected mean energy loss according to Bethe-Bloch [25].

2. Semiconductor particle detectors

2.1 Semiconductor theory

While individual atoms can have electrons in discrete energy levels, if a large number of atoms is brought together to form a crystal the degenerate levels of the constituent atoms will split into a large number of closely spaced energy levels, essentially forming a continuum. These bands are separated by a set of energy levels from which electrons are forbidden (the energy gap E_g). The upper band is called the conduction band, and the lower band is called the valence band [26].

Materials can be broadly separated into 3 different categories based on their band structure and how the bands are filled:

1. Conductors are a class of material where either the bands overlap, or one of the bands is partially filled in the lowest energy state allowing charge to flow. Metals fall into this category.
2. Insulators are materials in which the conduction band is completely empty while the valence band is completely filled, not allowing charge to flow freely. In insulators, the bandgap is large ($>$10 eV), meaning that electrons are not easily excited from the valence band to the conduction band.
3. Semiconductors are a similar class of material to insulators, but the bandgap is small ($\sim$ few eV) enough to allow electrons to be easily excited to the conduction band. The distinction between semiconductors and insulators is usually made based on their resistance at room temperature [27].

2.1.1 Defects, doping and charge trapping in semiconductors

For a perfect semiconductor crystal with no impurities or defects (known as an intrinsic semiconductor), charge does not flow through the material unless an electron is excited from the valence band directly to the conduction band either due to thermal excitations or radiation incident on the semiconductor, creating a pair of mobile charge carriers; a negative electron and a positive hole.

In practice however, it is impossible to have a perfectly pure material and thus defects and impurities are introduced in the material which affect the properties of the material.

Defects in a semiconductor crystal can be classed in three broad categories [28]:

1. Substitutional impurities; where an atom in the lattice has been replaced by an atom of a different element
2. Native defects; these are defects in the crystal lattice, such as vacancies or interstitial atoms
3. Complexes; these are defects formed when two or more defects are combined

Polycrystalline materials are also used for semiconductor devices, and the grain boundaries in this type of material also affect the device performance.

Some defects are generated during crystal growth, for example contaminants during the growth process will result in substitutional impurities, whereas some defects will be introduced afterwards. For example, when the material is irradiated, an atom can be displaced from its lattice site by a high energy particle, producing a vacancy-interstitial pair (known as a Frenkel pair [29]). A more detailed explanation of radiation damage is presented in Section 2.1.1.3.

2.1.1.1 Doping

In some cases, impurities are purposefully added to the material to change its conducting properties. This is known as doping. Impurities can be added either during growth to create a crystal with a uniform concentration of dopants, or through an implantation or diffusion process after the crystal growth if dopants are required only in certain areas of the device. These processes are central to the current silicon centered semiconductor industry as they are used to produce p/n junctions [30].

Dopant atoms can be either donors or acceptors.

- Donors have a state close to the conduction band from which an electron can be excited and become mobile, creating an excess of electrons in the material. Materials with an excess of donors are known as n-doped semiconductors.
- Acceptors have a state close to the valence band which can easily accept an electron from the valence band, creating a mobile hole, resulting in an excess of holes in the material. Materials with an excess of acceptors are known as p-doped semiconductors.

Both of these allow current to flow through the material by greatly reducing the energy required to create one type of charge carrier. The type of doping that is used

depends on the desired properties of the material for specific applications.

A key application of this is the creation of p/n junctions, regions of p-type and n-type material connected together, allowing current to flow easily in only one direction [26].

On one side of the junction there is a large number of holes, while the other side contains a large number of electrons. The charge carriers on each side of the junction diffuse into the other material, while nearby donor and acceptor atoms remain uncompensated, creating an electric field due to the resulting space charge in the material.

Devices containing a p/n junction can be operated with both a positive (forward) bias, in which case the current increases rapidly as the applied voltage is increased, and negative (reverse) bias, where the current is very small until a critical bias is reached, at which point the junction breaks down.

Silicon particle detectors are generally operated as a reverse bias p/n junction. When a reverse bias is applied it greatly reduces the carrier concentration in a region close to the junction, called the depletion region. This region increases in size as the reverse bias is increased. This means that when a particle hits the device it creates electron-hole pairs, resulting in a current pulse as they drift towards the electrodes which is measurable due to the low leakage current.

2.1.1.2 Charge trapping

Defects and impurities can also introduce various states within the bandgap of the material, that can trap one type of charge carrier. The presence of this sort of defect can have important effects on the electrical properties of the device.

Diamond particle detectors in HEP experiments are generally operated as intrinsic devices. The presence of defects is undesirable, as they act as charge traps: if the trap is shallow (usually refers to trap states that are ionized at room temperature [29]) then the charge carrier can be excited back into the conduction band by the thermal energy in the material, thus arriving at the electrodes at a delayed time (~ 1 µs). This causes a reduction of the original signal, as well as some noise after the pulse.

If the trap is deep, a lot of energy is required to excite the charge carrier back into the conduction band (such as a UV photon). In this case, if no UV light is present, the charge carrier can remain in the trap indefinitely [31], thus passivating the traps and improving the signal collected from the detector. The process of irradiating the detector to passivate the traps is known as pumping or priming [32].

In diamond, due in part to the large bandgap, a large number of the traps are

deep traps. This allows the device to operate at room temperature with a low intrinsic concentration of charge carriers even after heavy radiation damage [33].

For silicon however, the lower bandgap means that more of the radiation induced traps are shallow, causing them to have a greater effect on the performance of the device. However it has been shown that lowering the operating temperature of the devices reduces the thermal excitations in the material meaning that trapped charges are less likely to be de-trapped [34]. This allows devices to work after larger radiation doses.

2.1.1.3 Radiation damage

As previously described the performance of semiconductor devices can deteriorate due to radiation. The damage is primarily caused when a hadron or high energy lepton displaces a primary knock on atom (PKA), creating a Frenkel pair (an interstitial atom and a vacancy) [29], as well as potentially displacing other atoms from their lattice site if there is enough energy.

In diamond this process normally takes ~ 0.05 ps and only forms point defects, with almost all the energy dissipated after 60 fs. Some of the resulting vacancies and interstitials can then undergo thermal diffusion and eventually recombine, or form complexes with other defects [35]. For other semiconductor materials like Silicon however amorphous pockets can be created, leading to more extended defects [36].

Depending on the material used and the incident particle type, nuclei in the detector can also undergo nuclear reactions.

Radiation damage causes increases in leakage current. This is due to the defect states produced by the radiation which have energies that are close to the middle of the band gap. This causes problems, as in a small band gap material, the energy required to excite these centers into producing electrons or holes is low and hence they can be thermally excited, resulting in a leakage current. Defects caused by radiation damage can also affect the doping of the material which then requires significantly higher voltages to achieve full depletion by creating defects that can then combine with dopant atoms, changing their properties. This can eventually lead to type inversion, where p-type material becomes n-type material or vice versa.

In diamond, however, since it is a large band gap material, these states require a high energy to be excited. This is not achievable by thermal excitation alone under normal operating conditions, and therefore results in a lower leakage current [37].

Above a certain temperature, defects can start to migrate through the lattice until they reach sinks (such as dislocations), they combine with their counterparts and annihilate, thus becoming inactive (e.g. the recombination of a Frenkel pair),

or they can combine with other defects forming complexes. Alternatively, existing complexes may be dissociated into their components, and these components will start migrating separately [29]. The process of heating a material, allowing the constituent atoms atoms to migrate, improving the material properties is known as annealing.

It has been shown that after heavy irradiation of diamond samples, their performance can be significantly improved by annealing the sample [38]. This resulted in a recovery of up to 70% of the charge lifetime.

2.1.2 TCAD simulation of semiconductor devices

Sentaurus TCAD (Technology Computer Assisted Design) was used for the simulations described in this thesis. This is a software package that can simulate the behavior of semiconductor devices in a large range of circumstances. The package contains a large amount of data about common semiconductor materials, and given a set of initial conditions can compute properties of a device, such as the carrier concentration and the electric field, using the governing equations of semiconductors.

The equations used by TCAD to simulate the behavior of semiconductor devices are the Poisson equation:

$$\epsilon_s \nabla \cdot E = q(p - n + N) \tag{2.1}$$

The Electron Continuity equation:

$$\frac{\partial n}{\partial t} = \frac{1}{q}\nabla \cdot J_n + (G - R) \tag{2.2}$$

and the Hole Continuity equation:

$$\frac{\partial p}{\partial t} = -\frac{1}{q}\nabla \cdot J_p + (G - R) \tag{2.3}$$

where

$$J_p = q\mu_n E - qD_p \nabla p \tag{2.4}$$

and

$$J_n = q\mu_n E - qD_n \nabla n \tag{2.5}$$

are the current densities of holes and electrons respectively, ϵ_s is the permittivity of the material, E is the electric field, q is the the electron charge, n is the electron density, p is the hole density, G is the charge carrier generation rate, R is the charge

carrier recombination rate, μ_n is the electron mobility and D_p and D_n are the diffusion constants for hole and electrons respectively [26]. These equations can be reduced to a summation, making them solvable by a computer. The TCAD package uses the Newton method to solve them [39].

2.1.3 Ramo's theorem

Ramo's theorem is a method for calculating the current induced in a conductor by a nearby moving charge if the motion of the charge is known, first derived by Shockley [40] and Ramo [41]. According to Ramo's theorem, the current induced by a moving charge is given by

$$i = E_{v_e} e v_e \tag{2.6}$$

where i is the instantaneous current at an electrode due the motion of a single charge; e is the charge of the moving carrier; v_e is the instantaneous velocity of the charge and E_{v_e} is the component in the direction of v of the weighting field at the position of the charge. The weighting field is defined as the electric field due to the electrode if the charge is removed, the electrode being analyzed is raised to unit potential and all other conductors are grounded.

Due to the linearity of Maxwell's equations, the theorem is also valid if other charges are present in the volume of the material. If numerous moving charges are present, it is possible to obtain the induced current by summing the contributions from all the individual charges [42].

2.1.4 Field dependent mobility

Drift velocity is linearly proportional to the applied field at low electric fields [26]. This means that assuming that the drift velocity is small compared to the thermal velocity ($\sim 10^7$ cms^{-1} for silicon at room temperature [26]), it can be assumed that the time interval between collisions is independent of the electric field, thus the mobility can be defined as follows:

$$\frac{v_{drift}}{E} = \mu_n \equiv \frac{q\tau_c}{m_n} \tag{2.7}$$

for electrons, and a similar equation for holes, where v_{drif} is the drift velocity, E is the electric field q is the charge of the carrier, τ_c is the time between collisions, and m_n is the effective mass of the electrons.

The relationship between the drift velocity and the applied electric field was empirically found to fit the equation:

$$v_{drift} = \frac{v_s}{[1 + (\epsilon_0/\epsilon)^\gamma]^{1/\gamma}} \tag{2.8}$$

where ϵ is the electric field, γ is equal to 2 for electrons and 1 for holes, v_s is the saturation velocity, and ϵ_0 is a constant [43].

2.1.5 Charge collection distance

The charge collection distance is the average distance that a charge carrier travels in the device, it is a quantity used to quantify what proportion of the charge deposited in a material is collected by electrodes.

The charge collection distance d_{cc} is given by

$$d_{cc} = q\frac{L}{Q} \tag{2.9}$$

Where q is the charge collected, Q is the charge generated and L is the sample thickness [37]. This quantity should not be confused with the average distance traveled before carriers get trapped d_{trap} given by the equation:

$$d_{trap} = \mu E \tau \tag{2.10}$$

Where μ is the average carrier mobility, E is the applied electric field, τ is the mobility weighted average carrier lifetime,

The charge collection distance varies with electrode separation. In planar devices if the electrode separation $D >> d_{trap}$ then $d_{cc} \approx d_{trap}$, however if the charges are unlikely to be trapped such that $D << d_{trap}$, then $d_{cc} \approx D$ and this means that all the deposited charge has been collected by the electrodes.

2.2 Planar detectors and detector geometries

3D detectors are a recent development, before the advent of the IBL, semiconductor tracking detectors have always been planar devices. The general operating principle of these devices is to have contacts on opposite surfaces of the detector substrate and using them to apply an electric field through the bulk of the material. This electric field causes the charge carriers generated by a particle hit to drift towards one of the electrodes, with electrons and holes collected on opposite sides of the device.

Diamond tracking detectors are generally built using intrinsic material, as it is already highly resistive and has a very low leakage current in standard operating procedures. Silicon however usually has a significant leakage current, and as such silicon devices are made out of doped material, with implants with the opposite dopant type on the surfaces, thus creating p/n junctions. Applying a reverse bias creates a depletion region with no mobile carriers. Once a particle interacts with this device it releases some charge carriers which produce a current pulse that is detectable due to the lack of other carriers present.

A number of different detector geometries can be used for planar devices. One such geometry is a simple pad detector, a detector with a low segmentation with only one or a small number of readout channels with macroscopic dimensions. Devices like this are good for some applications such as beam monitoring, where the motion of individual particles is not important [44], or for applications with low position resolution requirements and a low event rate, such as Transient Current (TCT) measurements to study the electrical properties of a material [45].

Pad devices are not good for applications where the motion of large numbers of individual particles need to be known with high precision, and for this purpose the detectors need to be highly segmented to acquire useful information. To achieve this there are two possible approaches: strip devices which are highly segmented in only one direction and pixel devices which are highly segmented in two dimensions.

Some strip devices currently in use consist of strips with a length of several millimeters in one direction which are separated by < 100 µm in the other. One example of a system that functions like this is the ATLAS SCT. This section of the ATLAS inner detector is designed to provide 8 measurements along each track. This sub-detector is composed entirely of silicon strip devices, with dimensions of 6.36×6.4 cm^2, and consists of 780 strips of 80 µm pitch [46]. These strips are generally wirebonded to the readout electronics.

The highly segmented alternative to a strip geometry is a pixel geometry, where the device is highly segmented in two dimensions, generally with a pitch of ~ 100 µm in both directions, with each pixel individually bump-bonded to the readout electronics. This process will be described in more detail in section 3.5. There are many examples of this technology in operation in current experiments: the FE-I4 chip, with pixel dimensions of 50×250 µm^2 makes an important contribution to tracking in the ATLAS detector [47]. Likewise, the CMS ROC, consisting of 100×150 µm^2 pixels is a vital part of the CMS tracker [48].

There are a number of advantages and drawbacks to each of these approaches. Pixel devices are generally more expensive and require a more complex fabrication

process. Due to the fact that the electronics has to be placed directly under the sensor material, pixel devices are usually thicker than strip sensors in the active region. This is a problem for tracking detectors as ideally they should measure the position of the hit without affecting the motion of the particle and this is more likely to happen with thicker devices.

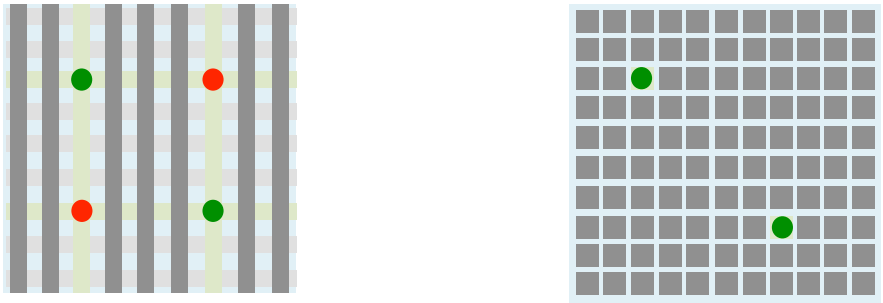

(a) (b)

Figure 2.1: The effect of two simultaneous hits on a pair of perpendicular strip detectors (a) and a pixel detector (b). The positions of the two hits are shown by the green circles and the ghost hits in the strip case are shown by red circles. In the strip case, without more information, it is not possible to determine which of the four possible hit positions are real and which are not.

Strip devices are generally thinner than pixel devices as the readout electronics are not required to be directly underneath the sensor. Thus for applications where material thickness is critical this presents an advantage. They are also more simple and cheaper to fabricate. The main disadvantage of these devices is that they only provide position information in one direction. This is usually overcome by placing two sensors back to back with the strips angled with respect to each other. By combining the information from the two sensors it is then possible to get a precise position measurement in both directions. This presents a problem in a high luminosity environment where there are a number of simultaneous hits, as it can create a number of ghost hits, as shown in Fig. 2.1. This problem becomes more prominent as the rate of particle traversing the detector increases. In particle physics experiments this means that, in general, detector layers closest to the interaction point, which are subject to the highest particle fluence, consist of pixel devices. Further from the interaction point the area that needs to be covered by detectors to cover the same pseudorapitidy range greatly increases, and the fluence of the particles

through the detectors decreases, this allows the use of strip devices as there is a reduced likelihood of ghost tracks, and it provides a great reduction in the required detector cost.

2.3 3D detectors

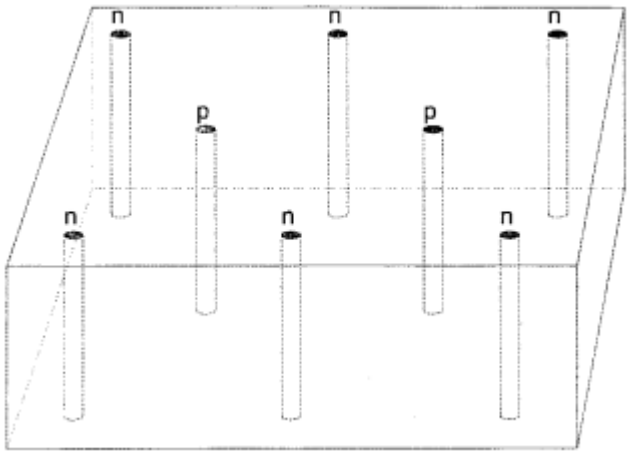

Figure 2.2: The structure of a 3D detector with electrodes inside the bulk of the detector material [49]

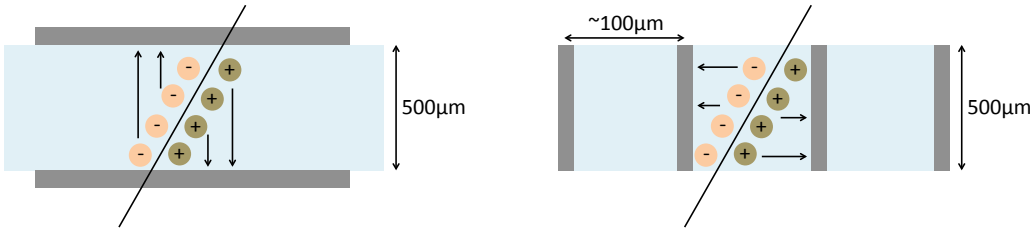

(a) (b)

Figure 2.3: A comparison between (a) 2D and (b) 3D device geometries. A 3D geometry allows the decoupling of the electrode separation and detector thickness, allowing charges produced in the semiconductor to travel a shorter distance to be collected without affecting the magnitude of the generated signal.

3D detector technology was first developed for silicon detectors [49] and has been used in Particle Physics experiments. It currently makes up 25% of the ATLAS

IBL [50]. 3D detectors are expected to play a greater part in future Particle Physics experiments as they have been proven to be a viable technology.

In 3D detectors, rather than placing the electrodes on the surface of the detector material, as is the case for planar detectors, the electrodes are fabricated within the bulk of the material as shown in Fig. 2.2. In silicon, Deep Reactive Ion Etching (DRIE) is used to remove material from the bulk creating columnar holes which are filled with polysilicon and then doped [49].

3D detectors present a great advantage because the inter-electrode spacing is not limited by the thickness of the wafer used. This means that electrodes can be placed closer to each other, decreasing the distance that electrons and holes have to travel before reaching an electrode, making them less likely to be trapped. A demonstration of these concepts is shown in Fig. 2.3. This results in a faster response time and an increased radiation hardness of the detectors as well as a reduction of the required bias voltage, while not compromising the size of the signal by reducing the detector thickness.

2.4 Properties of diamond

As large collider experiments such as the LHC continue to be developed they are required to reach higher energies and luminosities. These changes have the effect of increasing the particle fluence through the detectors meaning that they will have to remain in operation after higher radiation doses before they can be replaced. The desire for these detectors to remain in operation for longer is driving the development of new, increasingly radiation hard devices to be used in such experiments.

One way of increasing radiation hardness is to use a more radiation tolerant material. A good candidate for a new detector material is diamond as it has some interesting properties [37]:

1. it has a very high bond strength (43eV needed to displace an atom)
2. it has a large bandgap (5.5eV)
3. it has a very high thermal conductivity, allowing it to be cooled much more effectively

The combination of these properties leads diamond to have a very high breakdown field and also make it very radiation resistant.

Having a high band gap (5.5 eV), means that diamond has a very low intrinsic carrier concentration, and hence a very low leakage current. Diamond detectors can therefore be fabricated by using intrinsic material and only need simple surface

contacts, rather than requiring operation as a reverse bias diode. However this also means that significantly more energy is needed to create an electron-hole pair resulting in a lower signal. The large bandgap also means that the defect states, produced as the detector suffers radiation damage, will not be as easily excited as in silicon, so the negative effects of this type of radiation damage will be mitigated by pumping the device, as described in detail in Section 2.1.1.2.

Diamond (5.7) also has a lower dielectric constant than silicon (11.9), hence it has a lower capacitance, resulting in a much lower level of noise.

Advances in fabrication techniques have lead to the development of Chemical Vapour Deposition (CVD) produced diamond which allows the production of high quality polycrystalline (pCVD) diamond wafers, as well as large, high quality single crystal (scCVD) diamonds. This fabrication process will be described in more detail in Section 3.1.

Beam tests were carried out with pCVD diamond detectors and they were found to have good position resolution (comparable to silicon detectors), and a signal to noise ratio between 60:1 and 8:1 (depending on the shaping time of the electronics). The samples were also found to retain a good signal to noise ratio after irradiations of up to 1×10^{15} pcm^{-2} [32].

Tests carried out at BaBar using two pCVD diamonds have shown that diamond detectors can perform reliably over extended periods of time at high voltage, remaining stable with a very low leakage current (< 0.1 nA) without showing any signal degradation [32].

Diamond detectors have also been used for the ATLAS beam condition monitors (BCM) [51] as well as the DBM [52] due to their high radiation resistance. The BCM and DBM are used in the ATLAS experiment to detect any anomalous beam events that could cause background or damage to the inner parts of the detector.

The main requirements of these detectors are determined by the tough environment present at the LHC. They require very good radiation resistance, to withstand a fluence of 10^{15} cm^{-2} particles over their expected ten year lifetime, and timing requirements, due to bunch crossings in the LHC occurring every 25 ns; meaning that these detectors require ≈ 1 ns rise time, ≈ 3 ns narrow width and ≈ 10 ns baseline restoration [51].

Trapping centers lead to a significant negative impact on the charge collection distance in diamond. Due to the large bandgap of diamond however, the trap states will be relatively far from the conduction or valence bands, hence once a charge carrier is trapped in one of these trapping centers, it will not easily be released. Pumping the device in the appropriate environment (e.g. away from UV light) will

have the effect of passivating the traps, and these traps will remain passivated until they are exposed to enough energy to be released, for example using UV radiation and it can remain in that state for many months [31].

3. 3D diamond detector fabrication

3.1 Manufacture of diamond

Natural diamonds are expensive, are generally small in size and have inconsistent electrical properties; it is therefore preferable to use synthetic diamonds grown in the lab [37]. Diamonds were first synthesized in 1955 by high-pressure high-temperature (HPHT) deposition [53]. This method of diamond synthesis produces high purity single crystal diamonds, however it currently has its limitations, chiefly the limited size of diamonds that can be grown and the extremely high cost of the necessary apparatus [54]. Since then, another method of diamond synthesis has been developed: Chemical Vapour Deposition (CVD). With this method it is possible to grow amorphous carbon with sp^2 or sp^3 bonds, as well as single crystal and poly crystalline diamond [55]. The properties of the material grown depend on a large number of factors, including the growth speed, the amount and distribution of seed crystals and the gas mixture used.

The CVD process uses gas phase chemical reactions to synthesize diamonds. They are usually grown on substrates of molybdenum, silicon nitride, tungsten carbide [54] or iridium [56] from a gas mixture containing a hydrocarbon (usually CH_4) to provide the carbon, and a hydrogen plasma. Atomic hydrogen generated in the plasma breaks up the methane (as well as any long chain organic molecules that may form) into reactive CH_2 radicals which can then form the required bonds; it preferentially etches graphitic sp^2 carbon over the sp^3 carbon that makes up the diamond lattice, and it also terminates the dangling bonds on the diamond surface during growth, resisting the formation of sp^2 bonded surface reconstructions. The atomic hydrogen in the plasma also abstracts hydrogen bonded to the surface of the diamond, producing sites where the methyl components can adsorb onto the surface, allowing growth to continue [57].

CVD processes can be divided into two categories based on the type of excitation that is used: Heated Gas CVD and Ionization Plasma CVD, and each of these two categories can be split into a further two categories [58].

Heated Gas CVD:

1. Thermal Induced: the gas phase is activated using a hot filament or surface [54].
2. Chemical Induced: the energy is provided by the exothermic conversion of a process gas [54].

Ionization Plasma CVD:

1. Electromagnetic Excitation: the gas mixture is excited using electromagnetic waves, usually using either radio frequencies, microwave frequencies or a variety of laser types, such as excimer (3000 THz); Nd:YAG (281 THz); CO_2 (28.3 THz) [54].
2. Electrically Induced: Using DC plasma discharge between two electrodes; can be either glow discharge or arc discharge based on the applied voltage [54].

Electrical properties of CVD diamonds vary with thickness, the charge collection distance for example, which is often used as a measure of quality of the material, varies with the thickness of the substrate [37]. It has also been shown that for pCVD material the amount of grain boundaries varies with material thickness, with the quality of material improving as the thickness of the wafer increases [59]. A cross-section of polycrystalline material is shown in Fig. 3.1.

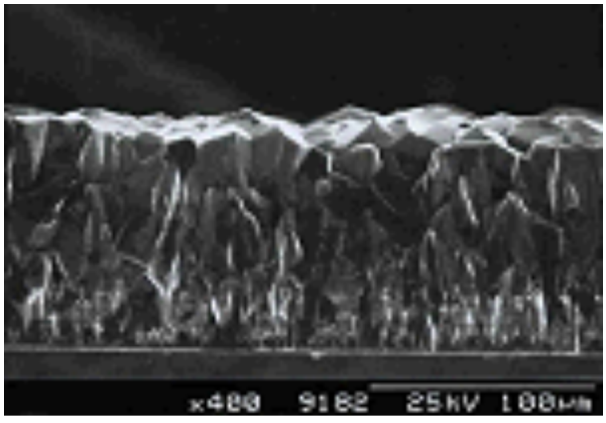

Figure 3.1: Cross-section of 100 µm thick pCVD diamond material [60].

Diamonds from three different manufacturers were used in this thesis: E6 [61], which produce both single crystal (scCVD) and polycrystalline (pCVD) material, II-VI [62], which produce pCVD material and IIa [63], which in the past produced scCVD diamond, but have now left the industry. Recently AuDiaTec has started diamond production and are a possible future source of diamonds for detector applications [64]. These are not the only organizations involved in the commercial

production of CVD diamonds, however the others are currently unable to produce enough diamonds of the desired quality in the required quantities.

Technological advancements to allow the production of electronic grade diamonds using an HPHT process are also being investigated, largely by New Diamond Technologies (NDT) [65]. Early results are promising, but the technology is not yet developed enough, and the diamonds produced are not yet of a high enough and consistent quality to be used as detectors [66].

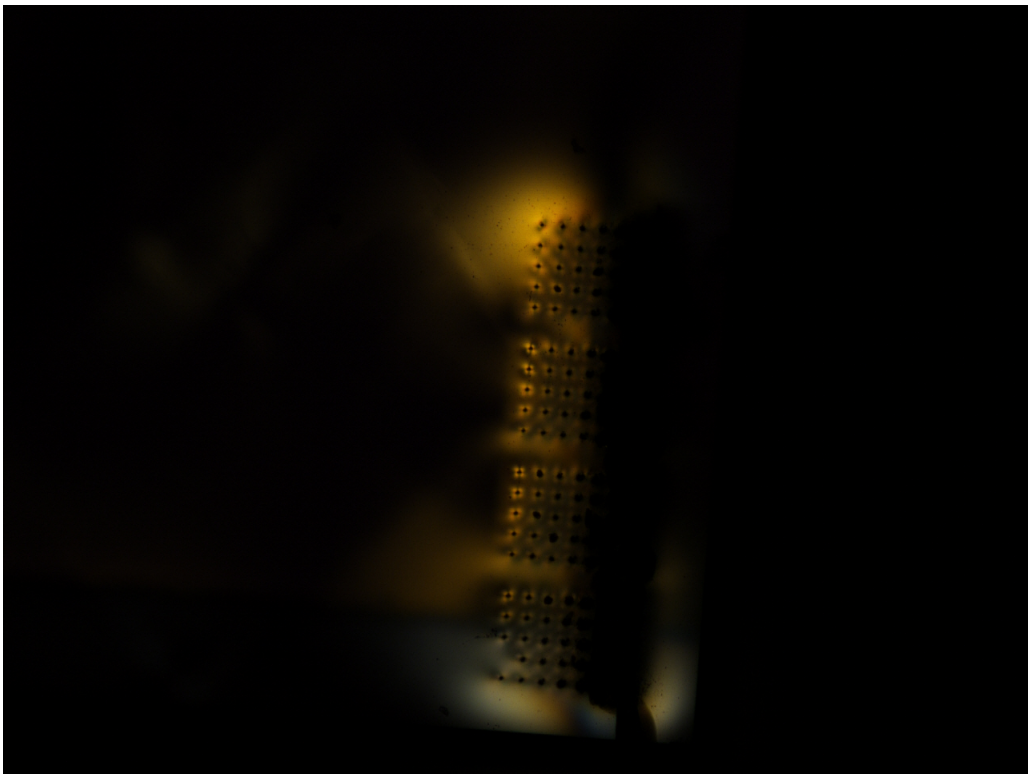

Figure 3.2: Photograph of graphitic arrays in a single crystal diamond sample taken through crossed polarizers.

In recent years, the capabilities have been developed to allow laser microstructuring of the diamond bulk [67, 68, 69]. This has raised the possibility of being able to apply the radiation resistant 3D geometry to a material that is more radiation resistant than silicon, hence creating detectors that have extreme radiation hardness characteristics. This eventually led to the development of the first 3D diamond detectors [70] [71].

In this case, electrodes are produced by using short, focused UV laser pulses to induce graphitization of the diamond, producing a column as the sample is moved with respect to the focal point of the laser, as shown in Fig. 3.3. One of the main issues with this fabrication procedure is that as graphite is less dense than diamond,

as soon as it is formed it expands, and hence it risks causing internal stress and cracks in the diamond. This effect is demonstrated in Fig 3.2 as the high stress region around a column changes the polarization of light passing through it, allowing it to be observed when the sample is placed between crossed polarizers. Since cracks can prevent some of the charge from reaching the collection electrode, this is undesirable.

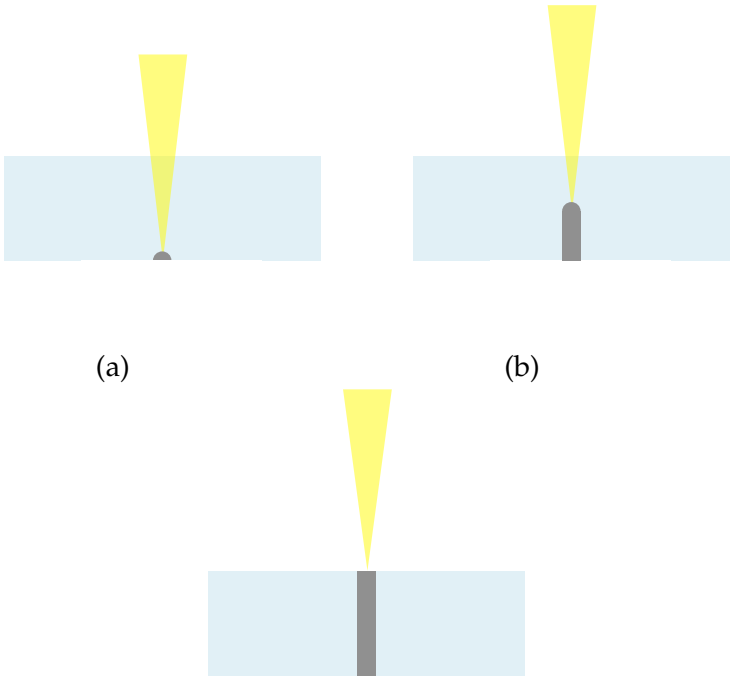

Figure 3.3: Diagrams showing the fabrication of a graphitic column.

Most detectors produced so far have had the readout columns read out in lines. One way to connect the lines of columns was to use a metalization layer on the surface of the diamond. This requires the sample to be extremely clean as otherwise the metalization may not adhere to the sample, hence making wire-bonding impossible. Cleaning should only be done before graphitization to reduce the risk of damaging the surface of the graphitic columns, which can affect the quality of the contacts. For future tracking detectors it will be necessary to read out cells individually; this will require the sample to be bump-bonded to a pixel chip, requiring the production good metallic contacts to the columns.

Alternatively, detectors have been produced where the lines of readout columns are connected using graphitic channels on the surface of the diamond [72] [73] [74].

This solution however is only viable in the long term for applications where position resolution is less important, such as dosimetry. With this approach it is not possible to read out columns individually and it is therefore not possible to reach a sufficient position resolution.

3.2 Diamond cleaning

There is a significant amount of literature describing processes for the cleaning of diamond. For diamond detectors to be viable, there needs to be a procedure for depositing mechanically and electrically stable metal contacts on the surface of the material. First of all the diamonds need to be cleaned. There are many different methods described in the literature [75, 76, 77, 78, 79]. The consensus is that the diamond should be cleaned of any non-diamond carbon and organic compounds using a solution of either CrO_3 + H_2 SO_4 [75] [77] [78] or H_2O_2 + H_2SO_4 [77]. Next it is necessary to remove any metal impurities from the surface of the diamond (which is especially necessary for the leftover Chromium if CrO_3 was used). This is achieved by using Aqua Regia (3HCl + HNO_3) [75] [78] .

As progress has been made in the production of CVD diamonds, the quality of the material and the surface finish received from the manufacturers have improved. Therefore, metalization success for newer diamonds is less reliant on the cleaning procedure used. It is still important however for old or recycled samples that have been used in experiments and which have not always been within a cleanroom environment and have residues such as glue or epoxy on the surface. The procedure used in Manchester is based on the procedure developed within the RD42 collaboration and is as follows:

1. The sample is kept for $\sim$ 5 minutes in a boiling 3:1 HCl($\approx 37\%$):HNO_3($\approx 70\%$) mixture (aqua regia). This has the main purpose of removing any metallic impurities on the surface of the sample.
2. The sample is kept for $\sim$ 5 minutes in a boiling 3:2 H_2SO_4($\approx 98\%$):HNO_3($\approx 70\%$) mixture. This mixture has the purpose of removing any non diamond carbon on the surface of the sample.
3. The sample is kept for $\sim$ 5 minutes in a boiling 1:1 H_2SO_4($\approx 98\%$):H_2O_2($\approx 30\%$) mixture (piranha etch). This is an oxygen rich mixture and has the purpose of ensuring the surface bonds on the diamond sample are oxygen terminated rather than hydrogen terminated, ensuring improved qualities of the contact, as well as further cleaning the sample of any organic residue on the

surface. It is possible to test the surface termination in the lab, as if the sample is hydrogen terminated it will be somewhat hydrophobic, whereas if it is oxygen terminated it will be hydrophilic.

4. The sample is thoroughly rinsed in de-ionized water between each of these steps to remove any excess solution from the previous step.

5. These steps are then repeated a further at least once, but can be repeated again if contaminants are found through optical inspection after the cleaning process.

Furthermore, if the sample is being recycled (i.e. if a previous metalization has to be removed in order to deposit a new one to produce a different device), before the cleaning steps using acids the metalization must be removed. It is preferable for this to be done chemically as this will avoid damaging the surface of the sample, and thus causing its electrical properties to deteriorate considerably. If this is not possible it can be mechanically removed, however this procedure can produce some subsurface damage, meaning that the surface layers of the sample (up to $10-15$ µm in depth) have to be removed using a plasma treatment to bring the sample back to optimal performance.

Table 3.1 lists a few different surface impurities and metalizations, and the combination of chemicals that has been used to remove them.

Surface contaminant	Removal technique	Treatment Details
Gold	I_2 and KI based gold etchant [80] or aqua regia	$\sim$ 5 min treatment, room temperature
Chromium	Cerium based chromium etchant [81]	$\sim$ 5 min treatment, room temperature
Titanium	CP4 solution ($\sim$ 1 : 1 HF:HNO_3 diluted in water)	$\sim$ 5 min treatment, room temperature
Ti-Tungsten (W-Ti) Alloy	CP4 solution ($\sim$ 1 : 1 HF:HNO_3 diluted in water)	$\sim$ 5 min treatment, room temperature
Hardman Double Bubble Epoxy [82]	Piranha Solution (3:1 H_2SO_4 : H_2O_2)	$\sim$ 20 min treatment, no additional heating

Table 3.1: Removal method of various diamond surface impurities and metalizations

3.3 Graphitization process

Laser induced graphitization of conductive channels in diamond has been developed over a number of years. Lasers can be used to produce graphitic structures in diamond [83] [84]. More recently, as this process has been further developed, the effects of varying the wavelength have been studied and it has been shown that for this purpose, short pulse lengths improve the quality of the graphitic structures by being better able to control the columns properties, making them more uniform and reducing damage to surrounding material, and that such graphitic structures are less dense than the surrounding carbon, leading to the formation of a surface bulge [67]. This is a problem for 3D devices as this bulge could affect the metalization of the device, and within the diamond bulk, the expansion of the the graphitic material could lead to the development of cracks and high stress regions in the bulk as shown in Fig. 3.2.

The potential to produce structures stretching further into the diamond bulk was quickly realized, and it was determined that to minimize damage to the surrounding material laser pulses of < 150 fs are required [68]. These structures were found to have a diameter of $\sim$ few µm and depths of several hundred µm [85]. There were still problems with the viability of this technique, chiefly a lack of homogeneity of the produced structures and lack of control over the structure shape, which limited how small the produced structures could become [69].

These structures will prove advantageous for the production of radiation detectors. This lead to the first 3D diamond detectors realized with the fabrication of electrodes within the bulk of the diamond, read out via a surface metalization [70] [71]. 3D diamond detectors made entirely of carbon have also been realized, with columnar electrodes connected together by graphitic channels along the surface of the diamond [72] [73], this is advantageous as carbon is non toxic and connecting columns using surface metalization has not always been successful and is dependent on having a perfectly clean surface. This could be a preferable approach for detectors for dosimetry, where the geometries required are similar to those used in prototype devices [74]. For high energy physics applications, where a pixel readout is necessary to achieve the desired position resolution, being able to produce a contact on the detector with a surface metalization is still a requirement and hence this avenue should not be neglected.

The quality of the produced electrodes in the first devices was not good, and the production not reliable enough for these devices to achieve widespread use. A number of studies were carried out to further develop this technique [86] [87] and

to better understand the structure of the columns [88].

Significant advancements have been made in the laser graphitization of diamond in recent years, chiefly by using a Spatial Light Modulator (SLM) to correct any aberrations in the laser beam. As well as to account for the deformation of the focal point at different depths within the diamond. This reduces the size of the focal point of the laser within diamond [89], allowing the production of smaller and less resistive columns. This new process allows for better control of the focal point of the laser allowing the production of arbitrarily shaped electrodes with smaller dimensions, as well as the possibility of fabricating multiple electrodes simultaneously. This method has already lead to an improved column fabrication success rate compared to previous devices [90].

Over the last few years a number of studies have been carried out to understand how the parameters used for column fabrication (such as laser power, energy, movement speed of the diamond through the focal point of the laser), affect the quality of the column produced, the composition of the column (the sp^2:sp^3 carbon ratio) and the physical and electrical properties of the columns [86] [87] [91]. Further studies of the properties of the electrodes produced using a graphitization process, particularly using the new SLM technology, are still ongoing and will be described in more detail in Section 9.5.

Some studies have also been performed to achieve a different approach to producing 3D diamond detectors, removing columns of material using a microprocessing technique, such as reactive ion etching or electron beam induced etching and producing contacts by electroplating the diamond with chromium [92]. These processes present an interesting prospect for the future of 3D diamond technology, by potentially greatly reducing the fabrication time of the columns and producing electrodes with a greatly lowered resistance. However this process is still in the early stages of development.

3.4 Surface contacts on diamond

3.4.1 Metal-semiconductor contacts

To produce a diamond detector (3D or otherwise) it is necessary to produce electrical contacts on the diamond, these will either consist of a metal or a graphite like material (a semi-metal [27]).

The contact produced can either behave like a Schottky diode [93]; providing

rectifying behavior, or it can behave as an ohmic contact. Generally an ohmic contact forms when the work function of the metal (energy needed to eject an electron from the surface of the material) is lower than that of the semiconductor [94].

For detector applications, as well as many other applications of CVD diamond, it is desired to produce well-characterized and stable ohmic contacts.

3.4.2 Production of surface contacts on diamond

There are two approaches that can be taken for producing surface contacts on diamond: by laser-writing a graphitic pattern on the surface in the same way as 3D electrodes are produced, or by the deposition of a surface metalization. Laser writing has some advantages, mainly that it can be done as part of the laser processing already required, it reduces the cleanliness requirement of the substrates (surface impurities, as long as they do not obscure the diamond have no effect on this processing), and it also allows detectors to be built entirely of carbon, which is advantageous for radiotherapy applications. However it also has drawbacks. It is irreversible, meaning that it can not be used to produce simple contacts to test the diamond quality before producing a device with the same sample. It is a process that damages the surface of the diamond by converting the top layers into graphitic material. It introduces some surface roughness to the sample, and it makes it more difficult to bond to the diamond, especially when producing highly segmented devices such as pixel detectors.

The alternative approach to surface graphitized contacts is to deposit a surface metalization on the diamond which solves all the previously stated problems of using graphitic surface contacts. There are a number of different ways to achieve this as described below.

Before any processing can commence the sample must be thoroughly cleaned, as any particles of dust or impurities on the surface will cause breaks in the metalization as shown in Fig. 3.4. The cleaning procedure to be used is already described in Section 3.2. Once a sample has been sufficiently cleaned, it is necessary to define an area on the sample to metalize, this can be done using either a shadow mask or a photolithographic process.

A shadow mask consists of having a layer of material between the source of the metal atoms (either a sputtering target or metals for evaporation, the advantages and drawbacks of each method will be discussed later) and the sample. This material has holes machined into it where the metal atoms will pass through and adhere to the surface of the device being processed. The advantages of this method are that it is cheap and quick, ideal for depositing pads on the surface of samples to test

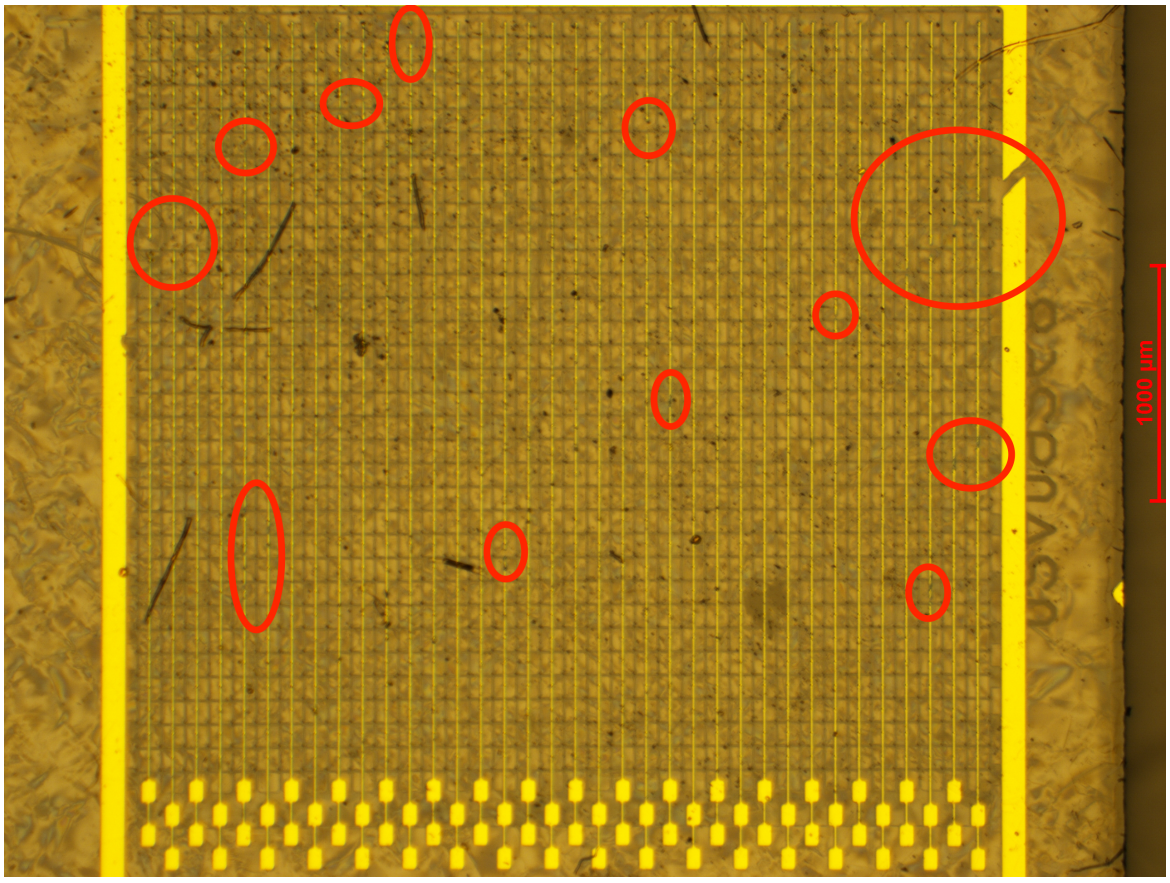

Figure 3.4: Photo showing breaks in the metalization caused by impurities on the surface of the diamond [95]

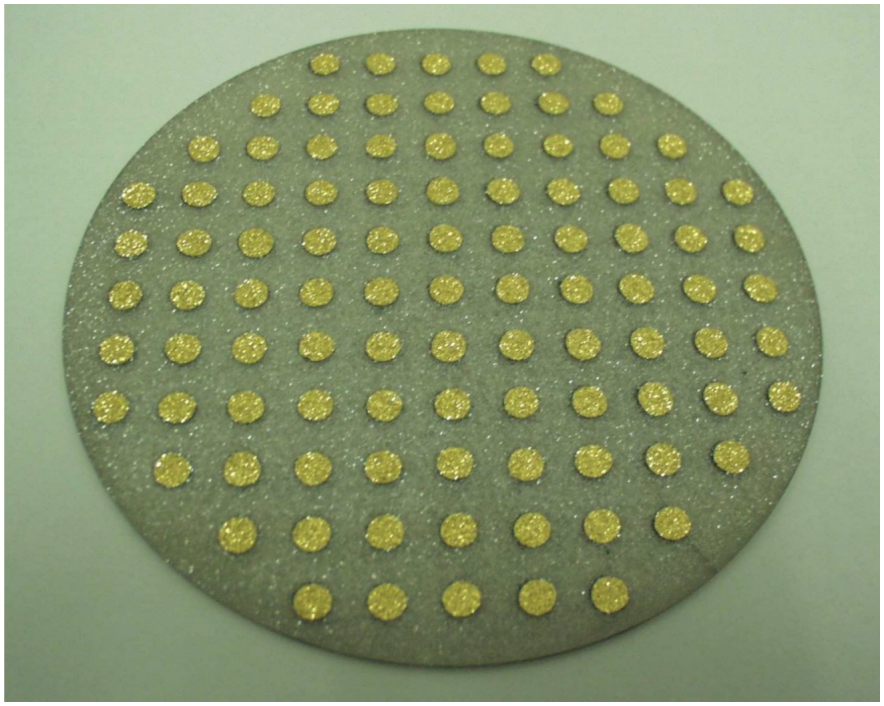

Figure 3.5: A 6 inch diamond wafer with circles deposited on the surface used to measure the quality of material produced [52]. The processing was done using a shadow mask.

the quality of the material as shown in Fig. 3.5. However this method has many drawbacks: the resolution of the masks is low and it is not possible to use it to produce highly segmented detectors. The mask is not stuck to the sample, meaning that it is possible for the sample to move during processing, introducing defects to the metalization and, due to the nature of the sputtering process, it means that if the sample is not perfectly in contact with the mask, some metal will spread underneath the mask, meaning that the contact will not be well defined.

The alternative to a shadow mask is to use a photolithographic process. Photolithography is a standard process in semiconductor device manufacture with many different applications. The process used for diamond electrodes is:

- once the sample is sufficiently clean a layer of photoresist (generally a long chain organic molecule or polymer dissolved in a solvent) is applied to the sample by a spin-coating process
- the sample is held by a vacuum chuck, and some drops of photoresist are placed on it
- the sample is then spun at $\approx 3000 - 5000$ rpm for $30 - 60$ seconds (with different processes and applications having different requirements), this allows the photoresist to spread evenly across the surface of the sample, with a thickness

dictated by the rotation speed while the excess material is drained away.

This process leaves a bead of photoresist along the edges of the sample which can be several times thicker than the rest of the photoresist. This can have a negative impact on the later stages of processing at these edges, and is particularly problematic in diamond, due to the small size of the samples, meaning that steps have to be taken to overcome this. This is overcome by placing the sample in a holder with such that the top surface of the sample is at the same height as the surrounding parts of the holder, meaning that the beads would not form on the sample, or ensuring that the sample moves more quickly, minimizing the size of the beads.

Once the sample has been spin-coated it is baked to allow the solvent in the photoresist to evaporate and the photoresist to harden. After this the sample is exposed to UV light through a photolithography mask. The masks used in Manchester consist of a glass substrate with a thin layer of Chrome on it, with clear regions where the metalization pattern appears. The mask is then brought in contact with the photoresist covered sample and UV light is shone through the mask on the regions of the device where metal is required. Depending on the machine used, it is also possible for the mask to be placed at a distance from the sample with optics being used to project a UV image of the mask onto the sample [96], however, this method was not used for any of the detectors described in this thesis. Exposure to UV light causes the molecules in the photoresist to undergo a chemical reaction making them soluble in a developing solution. The sample is then developed in developing solution, dissolving all the photoresist in the regions where metal will be deposited.

Again depending on the application required it is also possible to use a photoresist material that undergoes polymerization during exposure, leaving the unexposed areas more soluble to developing solution, however this was not suited for the applications discussed in this thesis.

Once the photoresist mask has been finished, the sample then undergoes a short (≈ 5 minutes) oxygen plasma treatment, which has the effect of further cleaning the diamond surface, as well as making the surface bonds oxygen terminated rather than hydrogen terminated. This improves the adhesion of the metal contacts. This step is also carried out if a shadow mask is used rather than photolithography.

After the plasma treatment, metal contacts are deposited on the surface of the diamond. Depending on what is required the composition of the metalization can be changed. The metalization is done through either evaporation or sputtering.

Evaporation is carried out by heating a piece of metal in a vacuum to the point where it slowly evaporates, the atoms that evaporate travel radially outwards and adhere to the surfaces they land on, including the sample. The evaporation setup

used in Manchester consists of a vacuum chamber which is served by a two stage pump system consisting of a mechanical roughing pump and a diffusion pump. The sample is placed in the vacuum chamber directly above a rotating stage allowing the deposition of multiple metals without breaking the vacuum. The metals are placed on this stage on a tungsten or molybdenum surface. Once the desired vacuum is reached ($\sim 10^{-6}$ mbar) a current is passed through this surface causing it to heat up past the melting point of the metal and eventually it becomes hot enough to allow the metal to evaporate. Once a metalization layer has been deposited the stage is rotated to allow the deposition of the next layer.

Sputtering consists of accelerating ions created as part of an RF plasma towards a metal target, releasing atoms from that target which then travel towards and are deposited on the sample. Sputtering is a much slower process that allows better control of the thickness of the metal films, as well as allowing the deposition of films thinner and more uniform than possible with evaporation. For the devices described in this thesis, this was not required but was sometimes used due to better availability of equipment.

The sputtering setup used consists of a vacuum chamber, with two slots allowing for metal targets to be placed at the top of the chamber, while the samples to be metalized are placed at the bottom of the chamber. The chamber is evacuated using a two stage pump system and once it has been sufficiently evacuated a small amount of argon gas is injected into the chamber (it is necessary for this to be a noble gas to stop it reacting with the metal atoms). A radio frequency electric field is applied to the chamber, separating electrons from their atoms creating a plasma as the electrons and ions are accelerated up and down the chamber. Energetic ions can then be accelerated and hit the metal targets causing individual atoms to be displaced. These travel towards, and eventually land on the samples below.

For the samples discussed in this thesis, a two layer combination was used, the first metal on the surface of the diamond determines the properties of the contact. Usually carbide forming metals (such as chromium and titanium which are both used in this thesis) produce low resistivity contacts [37] and have good adhesion. These are topped by a layer of gold to protect the contacts from the atmosphere, preventing degradation. Alternatively, if the sample is to be bump bonded, the highly segmented metalization consisting of a small pad for each pixel, known as the Under Bump Metalization (UBM) is usually a titanium-tungsten alloy [97].

Once the metal has been deposited, the sample undergoes a lift-off process, where the photoresist is dissolved by acetone, removing any metal on top of it, leaving metal only in the regions of the device where no photoresist was present [98].

Finally the samples undergo an annealing step, where they are heated in an inert atmosphere, this allows the atoms of the metal to diffuse a short distance into the diamond, as well as allowing atoms to diffuse between the two layers of metal. This improves the stability of the contact [99] [75], however it also makes the contacts more difficult to remove as removing the metal atoms that have diffused into the diamond is a non trivial endeavor. The temperature used is $\approx 450^{\circ}$C, higher temperatures can lead to the production of an alloy of the two metals used in the contact, which is not desirable. This can be overcome to some extent by introducing a third metal layer between the two already described as this will serve as a barrier to diffusion [75], however this is not necessary for most applications and can needlessly complicate the metalization process for negligible benefits. A series of diagrams detailing the required steps for diamond metalization are shown in Fig. 3.6.

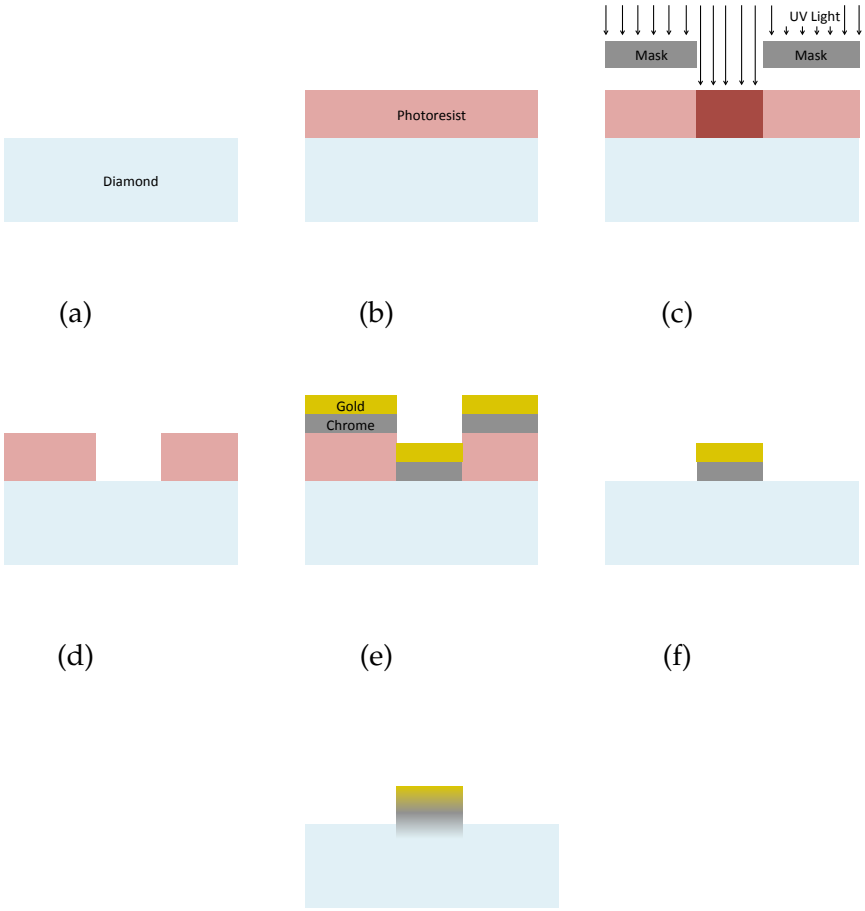

Figure 3.6: The various steps required to produces surface contacts on a diamond sample; the sample is thoroughly cleaned (a), it is then spin-coated in photo resist and baked (b). The sample is then exposed to UV causing a reaction in the exposed photoresist (c) which is then removed in a development step (d). A two layer Chrome-Gold metalization is deposited on the sample (e), after which any excess metal is lifted off the chip by removing the photoresist (f). Then finally the sample is annealed by heating it at $\sim 450°$C making the contacts more stable.

3.5 Detector readout

Once metal contacts have been placed on the surface of the sensor it is necessary to output the signal to a readout chip. This can be done using either wire-bonds or bump-bonds depending largely on the structure of the detector.

Bump-bonds are required when pixels are individually read out by the chip. There are many examples of pixel detectors which require the use of this technique:

the inner three tracking layers of the ATLAS detector at the start of operation consisted of Silicon devices with a pixel size of 50×250 µm^2 [12]; the upgraded LHCb Vertex Locator (VELO), will consist of 55×55 µm^2 pixels based on the TimePix family of chips [100] [101]; the ATLAS diamond beam monitor (DBM) [52] and the Insertable B-Layer [11] both have a pixel size of 50×250 µm^2 based on the FE-I4 chip [47].

Pixel sensors are metalized on both sides; the readout side having a highly segmented UBM, whereas the other side of the sensor generally only has one large pad covering the whole device. A layer of photoresist is then deposited on the readout chip and is exposed using a different mask. It is then developed, leaving gaps in the photoresist where the bumps will be placed. After this, a thick (~ 10 µm) layer of solder is deposited on the device. The photoresist is removed and the device heated in a reflow step to allow the solder bumps to take a spherical shape as shown in Fig. 3.7. This process is carried out on both the sensor and the chip, with the solder material used depending on the limitations of the device. Solder bumps can also optionally be placed on the UBM of the sensor. Finally the chip is aligned, placed on the sensor and heated to the melting point of the solder allowing the creation of electrical and mechanical contacts between the chip and the sensor material. This is known as a flip chip assembly process [102]. Diagrams detailing the bump bonding process are shown in Fig. 3.8.

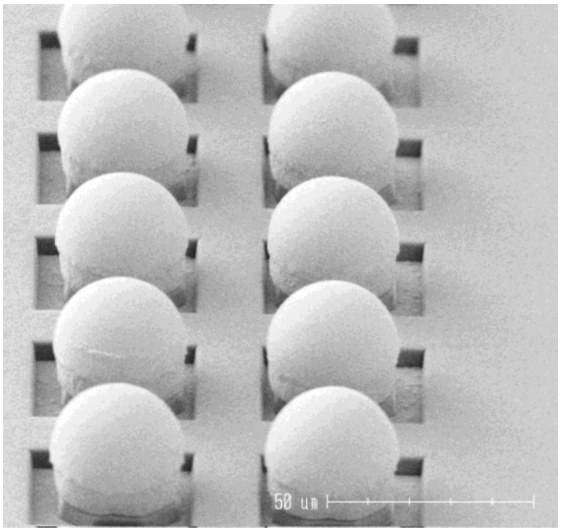

Figure 3.7: SEM image showing the solder bumps on a pixel chip [103]

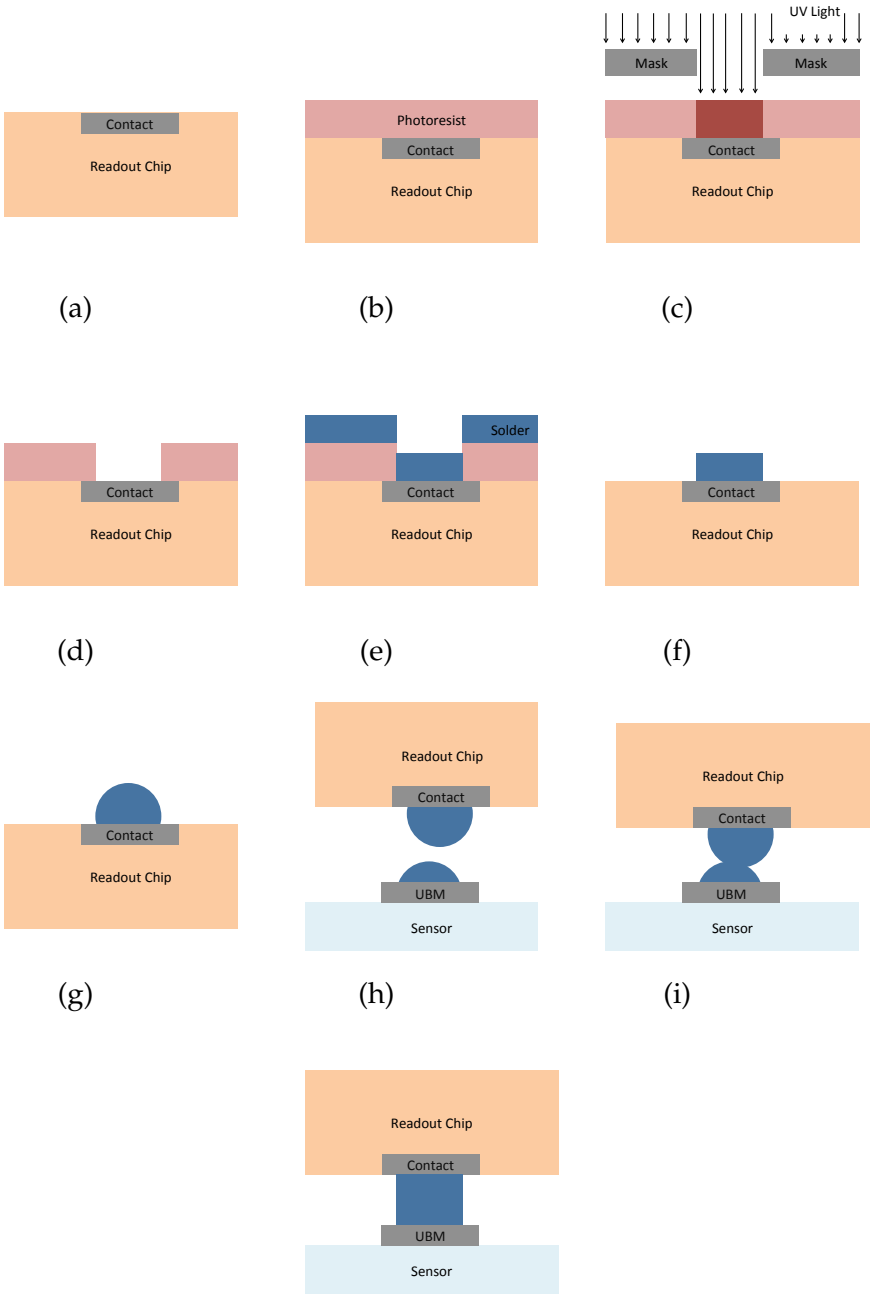

Figure 3.8: The various steps required to bump bond a sensor to a pixel chip. The chip is first cleaned and prepared (a), it is then spin-coated in photo resist and baked (b). The chip is then exposed to UV causing a reaction in the exposed photoresist (c) which is then removed in a development step (d). The solder metal is then deposited over the chip (e), after which any excess solder is lifted off the chip by removing the photoresist (f). The chip is heated in a reflow step allowing the remaining solder to form a bump (g). The chip is flipped and aligned with the sensor (h) and is brought into contact with the sensor (i). Finally the chip is heated in another reflow step (j) allowing the bump to connect to the sensor, the surface tension also brings the detector and the chip into better alignment.

When bump bonding is not necessary, it is generally easier and more convenient to use wirebonding. This is normally possible when pixels are unnecessary, for example with a smaller number of particles crossing the detector as a result of it either being further away from the interaction point, such as the ATLAS SCT [104], or simply having less interactions, such as the current LHCb VELO and tracker systems [105] [106].

Another example where the low rate of particles crossing the detector planes allows the use of simpler technology is the silicon telescope used to test the diamond devices described in the later chapters of the thesis [107].

The majority of diamond devices described in subsequent sections are operated as strip devices, with columns connected by metalization strips. The strips are then wirebonded to the readout system. Of the remaining devices, some have been operated as 3D pad detectors, in these cases accurate position resolution was not necessary as the samples were used to measure radiation doses or luminosities (Sections 6 and 9.1) while more recently some pixel devices have been produced (Section 9.4 and 9.6).

3.6 Readout systems used in experiments

A number of experiments and measurements have been performed during the course of this project, and a number of devices have been manufactured, each measurement setup having different readout chains.

3.6.1 IBIC readout chain

Two different sets of Ion Beam Induced Currant (IBIC) and Time Resolved Ion Beam Induced Current (TRIBIC) measurements were carried out using a proton beam at the RBI in Zagreb; the data was obtained using a self trigger on the signal, for the TRIBIC data, the current induced by the incident photon was amplified by a Cividec C2 2 GHz broadband current amplifier [108] and digitized with a Lecroy Wavemaster-8500 5 GHz sampling scope [109] [110]. In the case of the IBIC measurements, two adjacent channels were read out separately whereas for the TRIBIC measurements, only one channel was read out.

3.6.2 CERN test beam readout chain

A number of experiments were carried out using proton beams at CERN. The data for these experiments was recorded using the Strasbourg Telescope [107]. The telescope consists of 4 sets of Silicon strip detectors, each with 50 µm pitch, allowing for precise positions measurements in the both the x and y axes, with the z axis along the direction of the beam. Two 7×7 mm^2 scintillators provide an external trigger source [111].

The samples were read out using a VA2 read out chip [112], a low noise CMOS amplifier array, with a 2 µm s shaping time, consisting of 128 channels, analogue readout with DC coupling, with each of the readout strips connected to a different channel of the chip.

3.6.3 Pixel chips

For future applications it is desirable for each cell to be read out individually instead of reading out long lines of cells as a strip device. Therefore work was undertaken to produce 3D diamond pixel devices based on both the CMS readout chip and the ATLAS FE-I4 chip.

Each pixel cell generally has an analogue section consisting mainly of an amplifier and a discriminator, which then outputs the data to the digital section of the pixel (which can cover more than one pixel), which allows the data to be synchronized and transferred from the chip to be stored and analyzed.

3.7 Summary of devices discussed

The following is a list of samples which have been used in the body of work described in this thesis.

A detailed list and description of the photolithographic masks that have been produced is given in section A, whereas a detailed description of the properties of each sample is given in section B.

These devices can be divided into four groups:

1. Devices to study whether 3D diamond technology is viable.
2. Detectors produced for beam monitoring as part of CMS BCM
3. 3D diamond pixel detectors, proving that 3D diamond devices can function as pixel detectors.

4. 3D diamond devices that are being prepared for future measurements to test whether smaller cell sizes are feasible.

Devices to test the viability of 3D diamond technology

Sample Name	Mask Used	Purpose of sample
Batch 2 scCVD	Batch 2 Mask	Sample tested to prove viability of 3D geometry in single crystal diamond (Results described in section 5.2).
Batch 2 pCVD	Batch 2 Mask	Sample tested to prove viability of 3D geometry in polycrystalline diamond (Results described in section 5.3).
Manchester Sample	Manchester Mask	Sample used to study the effect of varying column fabrication parameters on the quality of the columns produced [86]. It was subsequently measured at test beams, the results of which are described in section 5.1.
Göttingen Sample	Manchester Mask	Sample produced to test column resistivity obtained using different column fabrication parameters, results from which are described in section 9.5 and elsewhere [87].
Florence device	Christie Mask	This sample was used to take some measurements at the Christie hospital in Manchester for dosimetry studies which are briefly described in section 6.
Irradiation Sample	Manchester Mask	This sample was produced to test the effect of heavy irradiation on 3D diamond detectors. The resistance of a subset of the columns produced was measured both before and after irradiation and the results are reported in section 8.
Multi-pattern scCVD device	3D Multi-pattern Strip Mask	Device used to compare the charge collection properties in single crystal diamond of different possible 3D detector geometries, chiefly square cells and hexagonal cells. The results obtained from this sample are detailed in section 5.1.

Multi-pattern pCVD device	3D Multi-pattern Strip Mask and 3D Multi-pattern Pad Mask	Device used to compare the charge collection properties in polycrystalline diamond of different possible 3D detector geometries, chiefly square cells and hexagonal cells. Measurements made with this sample are described in section 9.2. These measurements were carried out using a 3D Multi-Pattern Strip metalization, this was then removed and the sample was re-metalized with a 3D Multi-pattern pad metalization, to perform some high rate studies.
Large Area 3D Strip Device	Full 3D Strip Detector Mask	3D diamond device with a large active area, produced to prove whether the fabrication process could be extended to produce large area devices. Measurements made with this sample are described in section 9.3.

Table 3.2: List of the various 3D diamond devices produced to test the viability of this technology

Detectors for the CMS BCM

Sample Name	Mask Used	Purpose of sample
Manchester CMS device	Christie Mask	Sample laser processed and metalized in Manchester, was then inserted into the CMS BCM. This work is described in section 9.1.
Manchester-Oxford CMS device	Christie Mask	Sample laser processed in Oxford and metalized in Manchester, was then inserted into the CMS BCM. This work is described in section 9.1.

Table 3.3: List of the 3D diamond devices that have been fabricated for the CMS BCM

3D diamond pixel devices

Sample Name	Mask Used	Purpose of sample
CMS Pixel device	CMS Pixel Mask	This was the first successfully produced 3D diamond pixel device and was manufactured to prove that 3D diamond devices would function as pixel detectors with current pixel chips. Work carried out with this sample is discussed in section 9.4.
ATLAS FE-I4 Pixel device	Modified FE-I4 Pixel mask	This sample was produced to test whether 3D diamond technology would work when combined with currently available pixel chips. Due to defects in the diamond, the modified FE-I4 mask was produced to metalize this sample. Work carried out with this sample is discussed in section 9.4.

Table 3.4: List of the 3D diamond pixel devices that have been produced

3D diamond devices for future studies

Sample Name	Mask Used	Purpose of sample
50 µm Pitch CMS pixel device	50 µm Pitch CMS pixel mask	Sample produced to test whether large area 3D diamond pixel detectors with 50 µm cells are feasible and compatible with currently available pixel chips. This device is discussed in section 9.6.

Table 3.5: List of the 3D diamond devices with 50 µm pitch being produced and tested for future applications.

4. Simulation of diamond devices

To run a simulation using TCAD, a mesh modeling a subsection of the desired device (e.g. one pixel) as a set of discrete nodes is created. Hence by applying the governing equations of semiconductors to each node, it is possible to model the behavior of the device.

A mesh for the device to be simulated is created and the boundary conditions (e.g. electrode voltage) can be set, and the steady state properties such as the electric-field pattern can be studied. The current-voltage (and similar) characteristics can also be studied using a quasistationary simulation. In a quasistationary simulation the system is solved for a steady state, after which the boundary conditions are changed slightly and the system is solved again in a stationary state.

Time dependent (transient) simulations, such as a particle hitting the device, can also be performed. First of all the device is brought to the initial state using a quasistationary simulation. Then it is possible to simulate an initial distribution of charge carriers (e.g. that caused by a particle hit). The transient simulation then calculates the rate of change of carrier densities and potentials at each point in the mesh after each time step. This is repeated for a pre-determined set of time steps.

In the case of a 3D detector geometry, the electric field is not constant through the bulk material as is the case for planar detectors, but it varies as a function of distance from the electrodes. As a result of this the electric field will be extremely high near to the electrodes, therefore high field effects will need to be taken into account.

Drift velocity is linearly proportional to the applied field at low electric fields, [26] hence the time interval between collisions τ_c is independent of the applied field. This only holds if the drift velocity of the carriers is small compared to their thermal velocity. Therefore as drift velocity increases with increasing field, there is a departure from the linear relationship as the drift velocity approaches the thermal velocity. Eventually, at sufficiently high fields the drift velocity approaches a saturation velocity as shown in Fig. 4.1 [26].

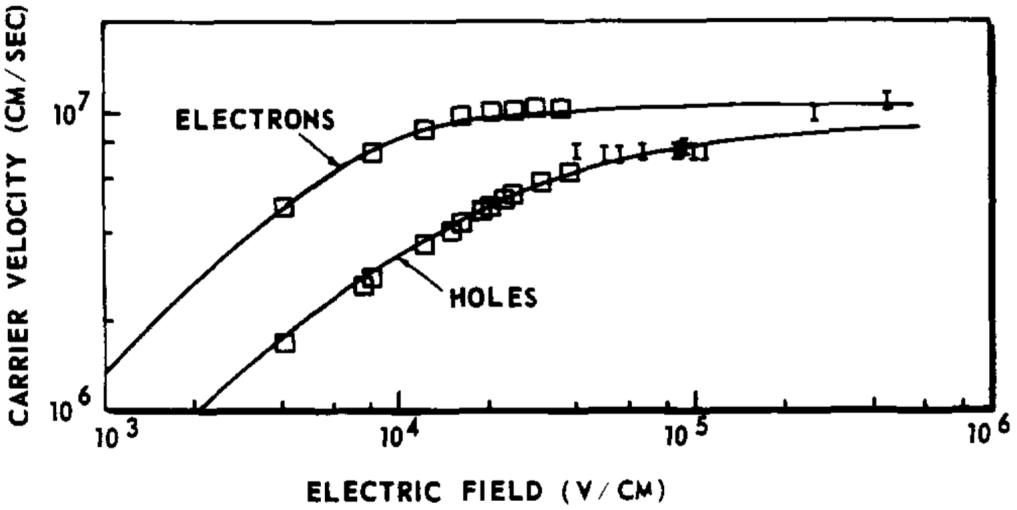

Figure 4.1: Relationship between the drift velocities of electrons and holes to the applied field in silicon [43].

4.1 Introduction of diamond model

As TCAD is a program primarily used by the semiconductor industry, which is dominated by silicon technology, TCAD itself is optimized for silicon devices. Parameters needed to simulate other materials are included, however as diamond is still not a widely used material in the semiconductor industry, there are no diamond models present in TCAD. Thus before any detector device simulations can be performed the parameters required to simulate diamond need to be added.

A new material is created in the parameter file used for the simulations, this contained various properties required for accurate simulations. First of all, the diamond bandgap energy of 5.5 eV and a dielectric constant of 5.7 were used in the initial simulation [113].

A field dependent mobility model is introduced into the simulation, following the Caughey-Thomas model [43], using an electron saturation velocity $v_{s,e} = 9.6 \times 10^6$ cms^{-1}; a hole saturation velocity $v_{s,h} = 14.1 \times 10^6$ cms^{-1}; low field electron mobility $\mu_{0,e} = 1714$ cm^{2}V^{-1}s^{-1}, and low field hole mobility $\mu_{0,h} = 2064$ cm^{2}V^{-1}s^{-1} as measured by Pernegger et al. [45].

To test the validity of this model, it is compared to experimental data, using the data from Pernegger et al. [45]. This paper describes some transient current (TCT) measurements performed on 470 µm thick diamond using α particles produced by a collimated ^{241}Am source, with an energy loss in the diamond of 5.38MeV. Alpha particles with this energy stop ~ 10 µm into the diamond, thus, by measuring the

current pulse induced on the electrode on the opposite surface once an electric field has been applied across the diamond, it is possible to measure the time taken for charge carriers to cross the diamond as a function of electric field, and thus deduce the mobility of the carriers as a function of the applied electric field. The properties of both types of carriers can be measured by simply changing the polarity of the field across the diamond, as one carrier type travels only a short distance to reach the electrode by which it is collected. Such TCT measurements are ideal for testing these parameters in simulations as the required geometry is simple, the electric field is uniform and each carrier type can be studied individually. This experiment is duplicated in the simulation. First of all a 3D mesh was created representing a block of diamond with an electrode on each surface.

A mesh is a network of nodes that replicates the structure of the device, it is defined by inputing the basic device structure, chiefly the dimensions and material composition of the device to be simulated, as well as mesh spacing required for the device, defining the separation of the nodes.

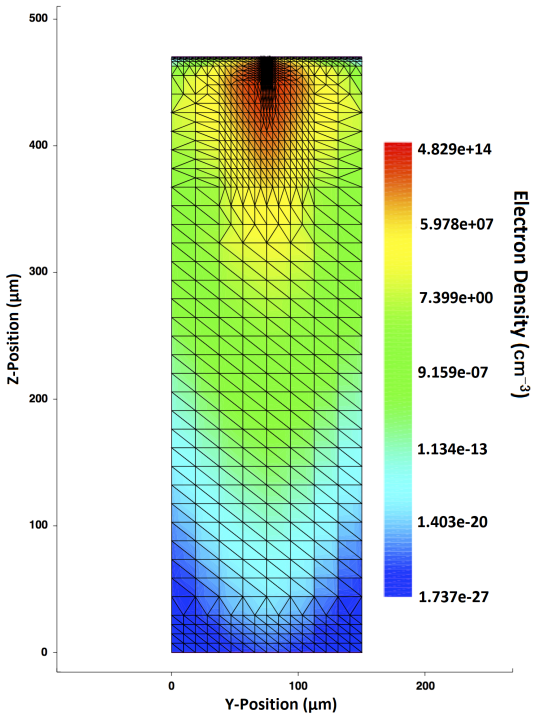

Figure 4.2: The mesh used for the TCT simulations, the electron density after an alpha particle hit is also shown. The picture shows that for most of the device the mesh spacing is quite large, however is gets progressively smaller close to the point of the alpha particle hit.

The simulations assume that the "quasi-Fermi" potentials (quantities proportional to the natural logs of electron and hole concentrations) vary linearly between each node, as this is an approximation it is therefore desirable for the mesh spacing to be small. Reducing the mesh spacing however greatly increases the computation time. A good compromise for this is to use different mesh spacings in different regions of the device, so that only areas with a high charge concentration or electric field have small mesh spacings whereas other areas have much larger spacings, thus reducing the required simulation time [39]. Fig. 4.2 shows the mesh used for the TCT simulations.

After the mesh is built and a quasistationary simulation is performed to bring the device to the expected starting state, a charge density is introduced below one of the electrodes to simulate an α particle hit as part of a transient simulation. A large spike is observed in the current at the start of the simulation after the charge is injected. This is due to the carriers that are traveling towards the nearest electrode. Due to the limited response time of the electronics, and the processing performed on the pulses to reduce noise, this spike does not appear in the experimental data.

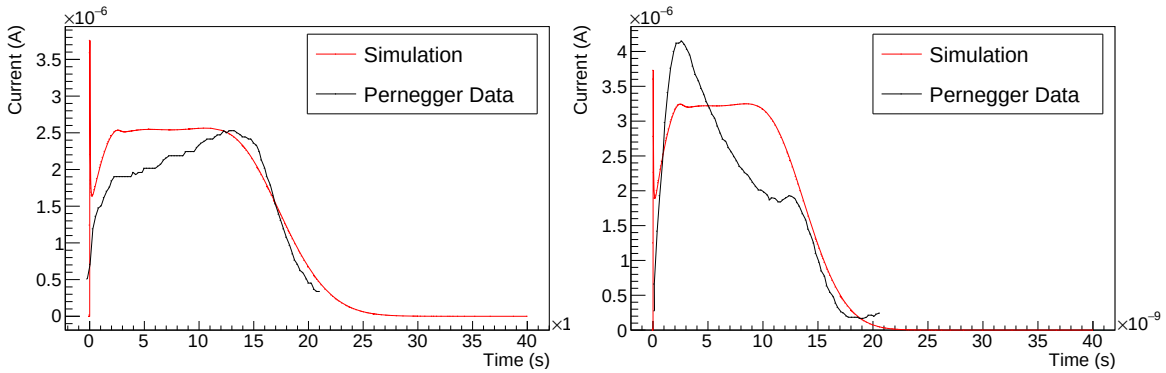

(a) (b)

Figure 4.3: Comparison of the curves obtained using TCT measurements [45] and the curves obtained using TCAD simulation. (a) is the current due to electron drift, and (b) is the current due to hole drift.

Figure 4.3 shows that simulated pulse duration was in good agreement with the experimental data. The tested sample appears to have a significant concentration of space charge, causing the deviation from a flat top normally expected in TCT measurements. In this case there is a negative space charge, this means that at the start of the measurement there is a large amount of negative charge between the electrons and the collection electrode, which causes the electrons to slow down and hence produce a lower instantaneous current. As the electrons travel through the

material, they reach the point where there is an equal amount of space charge on either side, which cancels its effect. After this the electrons see a space charge from the opposite direction, which pushes them towards the collection electrode, increasing their drift velocity and hence the instantaneous current observed, with the opposite effect observed for holes. As the space charge is spread uniformly throughout the material, these two effects cancel out and the pulse duration is unaffected by the presence of the space charge. The experimental data was obtained on a single crystal diamond sample fabricated when the procedure to produce such devices was relatively new, meaning that the material quality was not optimal, and a number of defects are present leading to the space charge. In the last decade however the production process of scCVD diamond detectors has improved to the point where the impurity concentration for electrical grade scCVD diamonds is < 5 ppb [114] with a negligible amount of structural defects. It is therefore possible to neglect the effect of space-charge observed in these measurements as it is not observed in modern samples.

5. Measurements and simulation of 3D diamond detectors

The first 3D devices tested were made using scCVD diamond [70], this was because scCVD material can achieve better charge collection, with fewer impurities ($\sim 10\%$ of pCVD material [114]) and also does not have the complex crystal structure observed in pCVD material, which has significant impact on the charge collection within the diamond, with some regions providing better charge collection than others, dependent on a number of factors including depth within the diamond [59].

Simulations of scCVD devices are also a useful stepping stone to full pCVD simulations. State of the art, unirradiated detector grade scCVD material currently has a low amount of impurities, to the point where their effects are almost negligible in the situations where the material is being studied.

Test beams campaigns were carried out on a number scCVD detectors: in 2011 an scCVD 3D diamond detector was measured at CERN using 120 GeV protons, which can be treated as MIPs [111]. Other test beams were carried out with different scCVD 3D diamond detectors, in 2013 and 2016 further test beams were carried out at the Ruđer Bošković Institute (RBI) in Zagreb using 4 and 4.5 MeV protons respectively. Measurements were also carried out on a pCVD device using 120 GeV protons at CERN to test the viability of pCVD material for the production of 3D diamond devices.

5.1 IBIC, TRIBIC and photon measurements

Time Resolved Ion Beam Induced Current (TRIBIC) measurements are a powerful technique to understand the signal generated by a device by hitting the device with a particle beam and recording the current pulse generated by individual hits [115]. This differs from TCT measurements because ion beams can achieve a good position resolution, in this case, the micro-beam used at the RBI can achieve a position resolution of ~ 1 µm [116], thus making this a very powerful technique for studying

charge carrier properties of devices that do not have a uniform electric field, as is the case for 3D devices.

A selection of 3D diamond devices have been studied using this technique, most notably in 2013 [110] and 2016 [117] testbeam campaigns. These measurements were carried out to study the effects of varying fabrication parameters (such as cell geometry and the effect of column diameter) in 3D diamond as well as to understand charge collection in these devices.

The two measured devices discussed in this thesis are:

- An scCVD Manchester device (described in section B.1.3), used to study the effects of different column fabrication parameters was measured using 15keV photons at Diamond Light Source (DLS) and 4MeV at RBI
- An scCVD Multi-pattern device (described in section B.1.7), used to measure the effect of varying cell geometry on the performance of the detector. This was measured with 4.5MeV protons at RBI

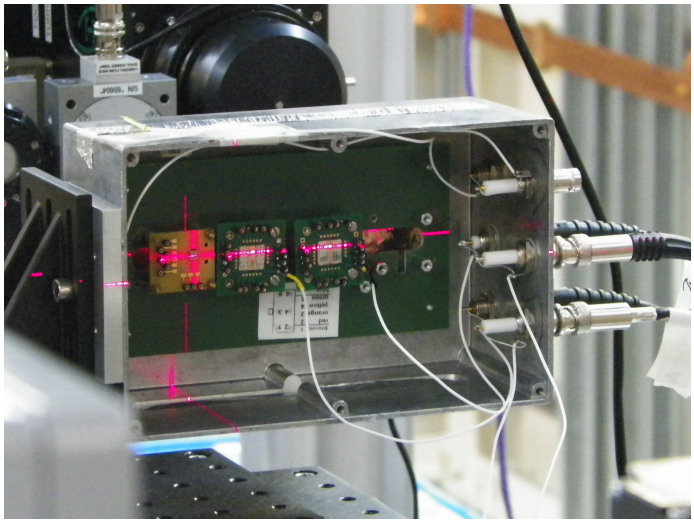

Figure 5.1: Experimental setup of the diamond light source measurements. The left most sample in the box is the 3D diamond sample that was measured. The laser light indicates the approximate position where the photon beam would hit the device. During measurement the box is sealed to prevent ambient light from entering and disturbing the measurement. The stage upon which the box is mounted then moves in the plane perpendicular to the beam to allow the beam to hit the sample at different positions

The data obtained at RBI was recorded by triggering on the signal itself using the readout chain described in section 3.6.1. A significant amount of ringing noise was present in the current pulses measured as part of the first dataset as a result of the system not being optimized for transient current measurements [110]. To address

this problem the sample measured in 2016 was mounted on a new PCB designed for high frequency response [117], this successfully removed the ringing noise.

The Manchester sample was also tested at the B16 beamline at the Diamond Light Source (DLS) [118] using a beam of 15 keV photons with a FWHM of 5 µm, and a flux of 10^6 photonss^{-1}, making this effectively a DC measurement. The sample was measured at 6 different voltages, however it was only possible to measure two of the arrays due to time restrictions. During the measurements the samples were placed in an sealed aluminium box. In order to allow the beam to enter the box, slots were cut in the sides and the top of the box, and to prevent ambient light entering the box and disrupting the measurements the sample, these slots were covered in aluminium foil. A photograph of this setup is shown in Fig. 5.1.

When the beam was turned on, a voltage was applied to the HV electrodes using a CAEN power supply [119], while the current in the readout channels was read out and recorded by Keithley [120].

5.1.1 Studies performed on the Manchester device

Device production

The Manchester device consists of a $4.7 \times 4.7 \times 0.5$ mm^3 diamond obtained from E6 [61] containing four different arrays of columns manufactured using a range of different beam fluences between $\approx$ 2 Jcm^{-2} and $\approx$ 5 Jcm^{-2}, resulting in column diameters ranging from ≈ 5 µm to ≈ 10 µm [86].

Each of the arrays consisted of area of 5x5 square cells with a pitch of 120 µm, for a total of 244 columns each extending the entire length of the diamond. In each array the signal columns are connected in 5 strips of 5 cells by a surface metalization, making this a 3D strip device. In the arrays shown in Fig. 5.2 the signal columns are the ones located in either horizontal or vertical lines of 5 columns. Similarly, all the remaining columns on each array are connected together and are used to bias the sample and are referred to as bias columns. Metalizations for both bias and signal columns were placed on the same side of the device, and a series of dots was placed on the reverse side of the device contacting each column individually. This was done in order to more easily probe the resistivity of the columns.

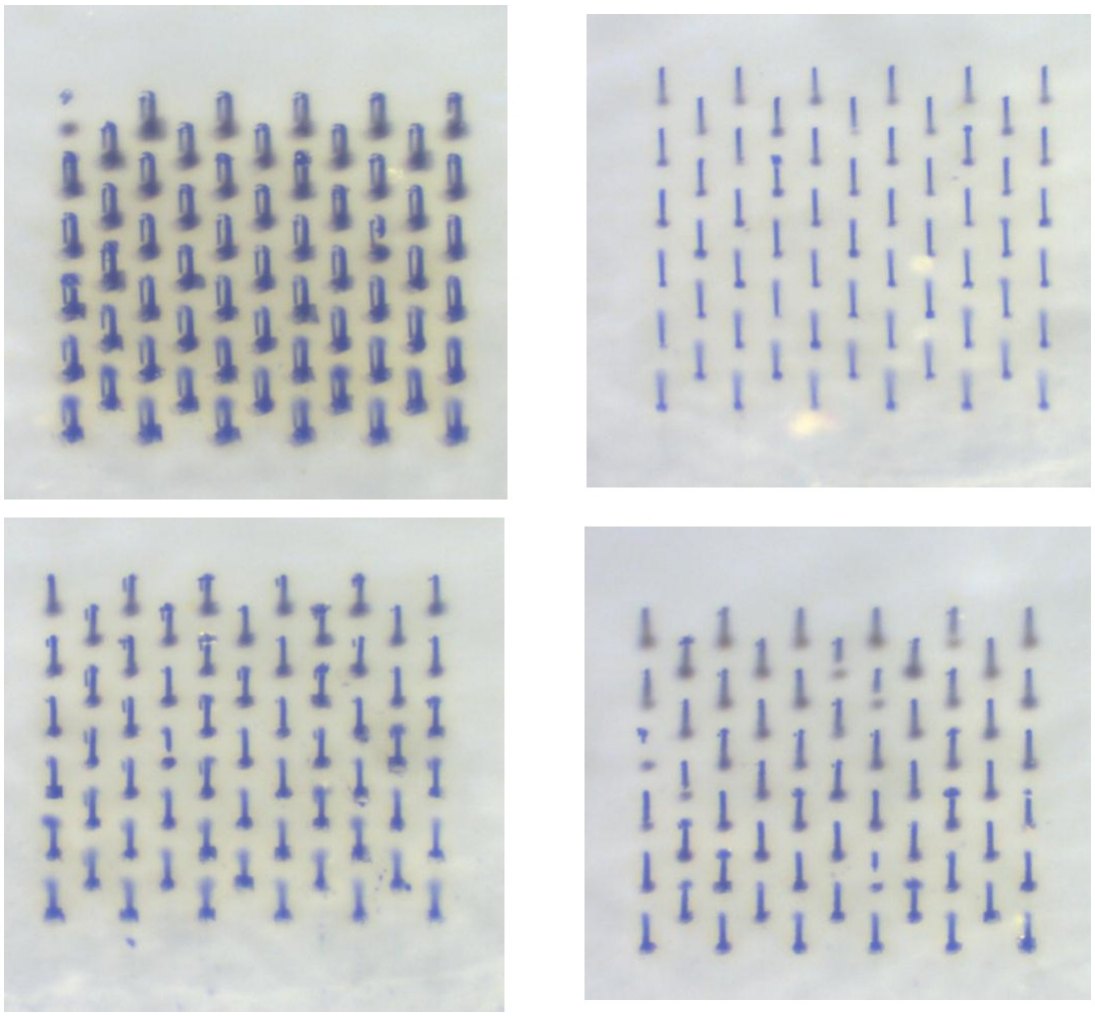

Figure 5.2: The four arrays of graphitic electrodes on the Manchester sample, the energy densities are, clockwise from top left: 5 Jcm^{-2}, 2 Jcm^{-2}, 3.5 Jcm^{-2}, 3 Jcm^{-2}

After laser processing the sample was metalized using a standard photolithographic process (as described in Section 3.4). A titanium (≈ 35 nm) and gold (≈ 60 nm) metalization was sputtered onto the sample, which was annealed for 5 minutes in a nitrogen atmosphere at $250°$C.

Using the front side metalization, the sample was then wirebonded to a PCB. Due to limitations of space and number of available readout channels, only two readout channels were connected for each array. The aim of this was to obtain measurements of charge sharing between two neighboring channels, as well as studying the charge collection of the individual lines. The sample is shown in Fig. B.3.

Photon measurements

The signal observed in each cell was consistent to $\approx 10\%$ for each applied bias voltage. At higher voltages, signal collection was more uniform throughout the cell, and significantly more charge was collected (up to 50%). This analysis is described in more detail elsewhere [91].

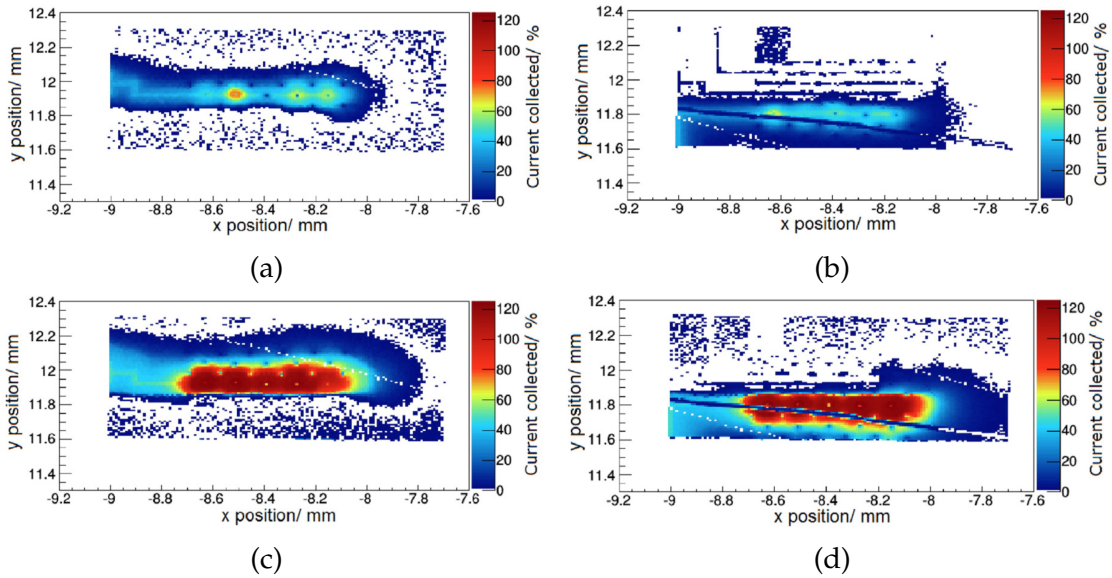

Figure 5.3: The photon data. Two adjacent channels were read out separately at different voltages, (a) data from channel 1 at -5 V, (b) data from channel 2 at -5 V, (c) data from channel 1 at -40 V, (d) data from channel 2 at -40 V. A bond wire located above the sample is also visible in the data for channel 2 as long thin region with a low signal

IBIC and TRIBIC measurements

The sample was tested at the Ruđer Bošković Institute (RBI) using a beam of 4 MeV protons, with a FWHM of ≈ 1 µm. A set of measurements was taken with this setup with a combination of IBIC (Ion Beam Induced Current) measuring only the total charge collected by each hit, and TRIBIC (Time Resolved Ion Beam Induced Current), recording a current pulse for each hit position. Due to time constraints it was only possible to measure one array, the array fabricated with an energy density of 2 Jcm^{-2} was chosen as this was one of the arrays which was measured with the photon data.

Again, two adjacent strips were connected in order to study the charge sharing as well as the charge collected by individual cells. In this case a voltage was applied to the signal columns which were then also read out, while the HV columns were grounded. A photograph of the sample ready to be measured is shown in Fig. 5.4.

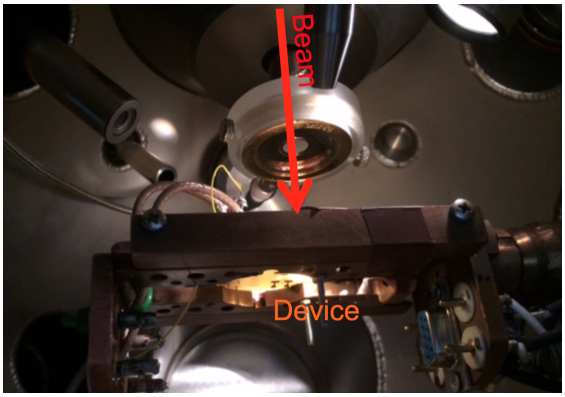

Figure 5.4: The 3D diamond Manchester device in the RBI setup ready to be tested. The beam enters from the top of the picture.

Charge collection in this case was greatly improved upon from the photon data, with close to 100% charge collection efficiency at ± 5 V and up to $120 \pm 20\%$ at ± 40 V, with uniformly high charge collection throughout the whole cell, consistent with full charge collection, as seen in Fig. 5.5. This was likely due to the different ionization profiles of photons and proton microbeams. Similarly to the photon data, a small amount of charge sharing was observed in the transition between the two strips being studied.

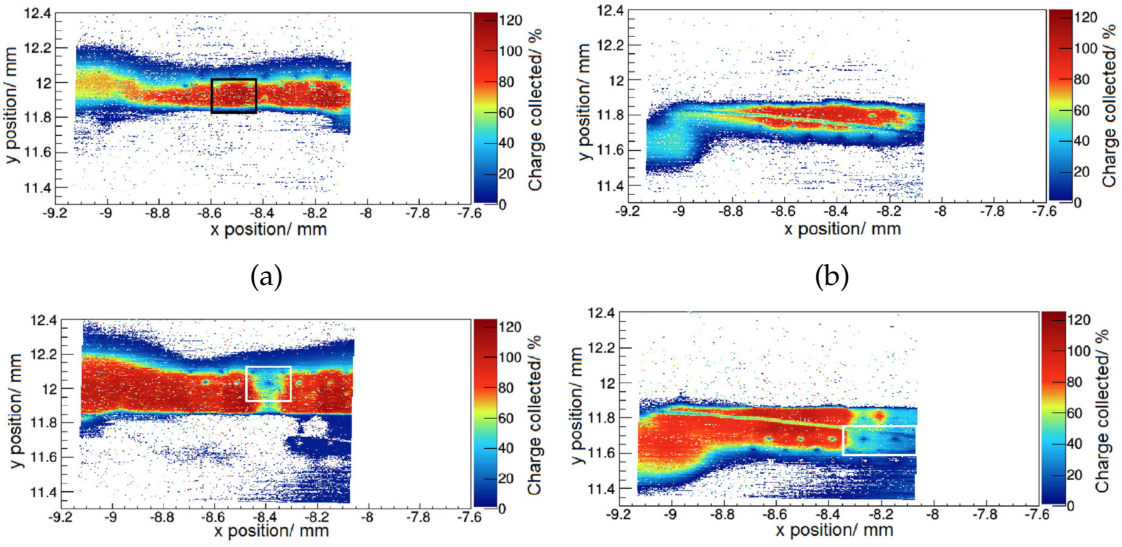

Figure 5.5: Data obtained from the IBIC experiment. Two adjacent channels were read out separately at different voltages, (a) data from channel 1 at -5 V, (b) data from channel 2 at -5 V, (c) data from channel 1 at -40 V, (d) data from channel 2 at -40 V. Some regions are highlighted in these plots. The highlighted region in (a) is a working cell thats was chosen for further study, while the highlighted regions in (c) and (d) show regions of low charge collection.

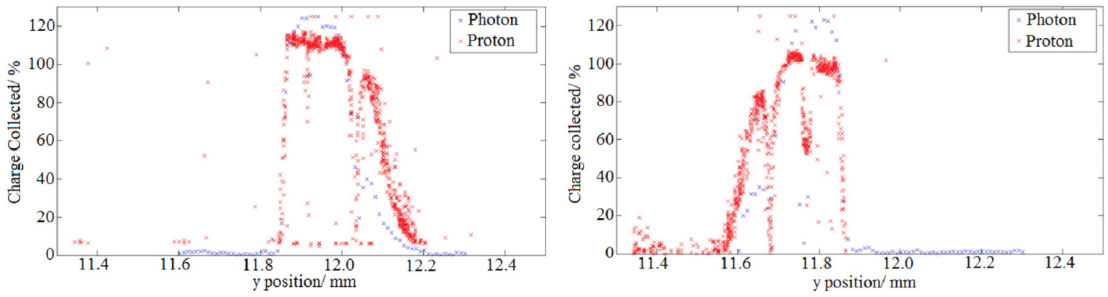

(a) (b)

Figure 5.6: Percentage of charge collected in channel 1 (a) and channel 2 (b) as a function of position at a bias of -40 V for both photon and IBIC data. There is a small region where significant charge sharing occurs between the two strips being measured

TRIBIC data was also taken with this sample, recording a transient current pulse for each hit in a set of positions throughout the cell. The current pulse was amplified using a Cividec C2 2 GHz broadband current amplifier and digitized with a Lecroy Wavemaster-8500 5 GHz sampling scope.

Due to the setup not being optimized for these measurements a ringing noise was observed in a significant portion of the pulses as shown in Fig. 5.9. It was however possible to remove this by carrying out a Fourier transform and eliminating the relevant frequency. The total collected charge was then plotted as a function of position as shown in Fig. 5.10.

TRIBIC simulations

TCAD simulations were then performed using the same parameters described in Section 4.1. Three dimensional simulations were carried out on an area of the device equivalent to a quarter cell, this was limited due to time constraints as 3D simulations take significant computing resources and time, and getting the required amount of points on a larger mesh would take too long. Due to the incident particles being 4 MeV protons, having a Bragg peak at ~ 80 µm depth as shown in Fig. 5.7, the charge concentration generated is not uniform through the thickness of the detector, for this reason it was decided that the use of a 3D geometry was necessary for these simulations. An image of the mesh used is shown in Fig. 5.8.

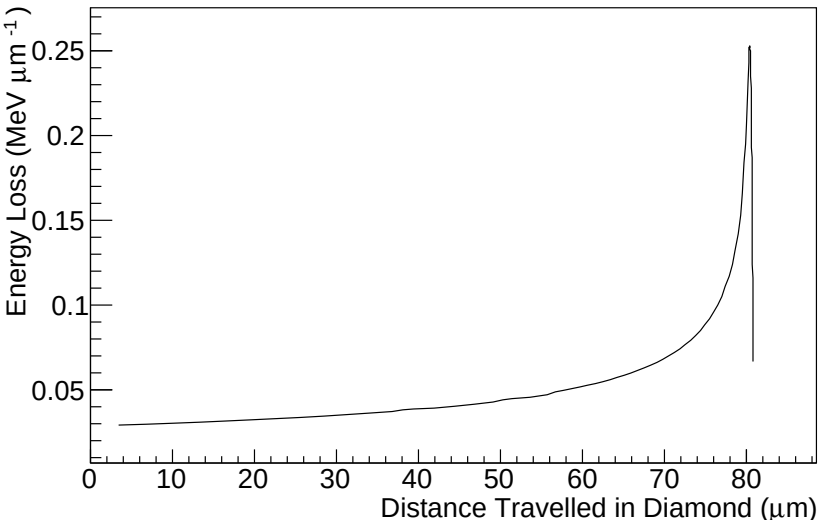

Figure 5.7: Energy deposited as a function of depth for a 4MeV proton in diamond calculated using the data from the National Institute of Standards and Technology [121]

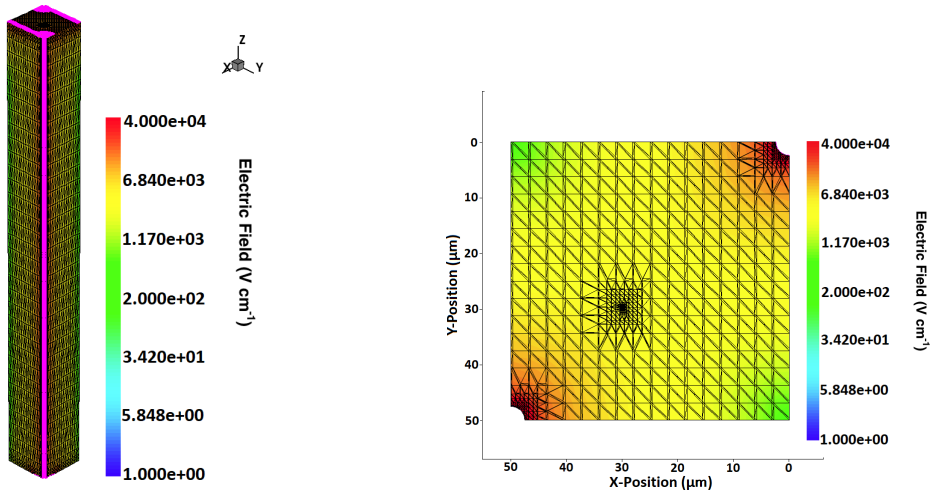

(a) (b)

Figure 5.8: Mesh used for the TRIBIC simulations, (a) shows the full 3D mesh, whereas (b) shows a 2D cut of the mesh at a depth of 80 µm, the absolute value of the electric field is shown by the color scale. The finer meshing around the point X=30, Y=30 is due to the simulated hit for this example occurring at that position.

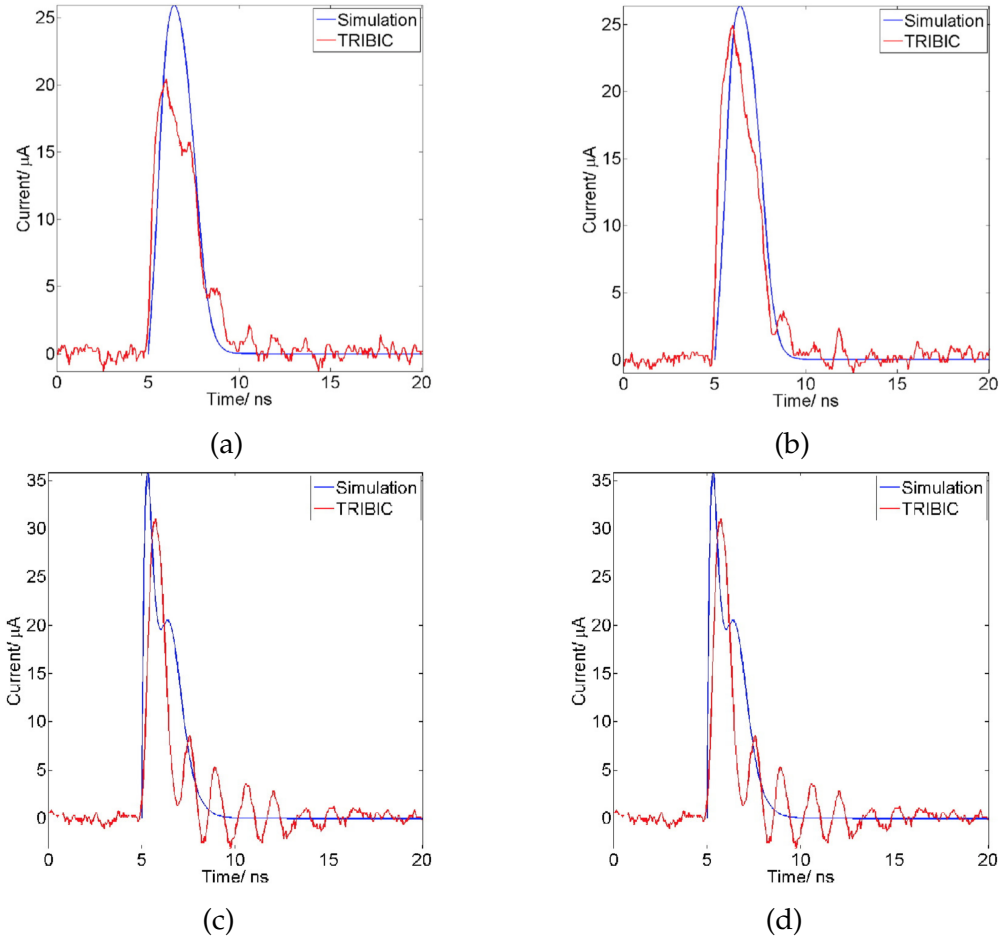

Figure 5.9: Comparison of the pulses obtained from the experimental data and the simulation. The data shown in (a) and (b) are taken from the midpoint of the diagonal connecting the bias and signal electrodes, whereas (c) and (d) are measurements from a position close to the bias electrode. (a) and (c) are measurements with a bias voltage of 60 V whereas (b) and (d) were taken using a bias voltage of -60 V

Once the mesh was built, a quasistationary simulation was used to ramp the voltage up to the required operating voltage, achieving the required starting conditions, after which a charge is injected during a transient simulation. In this scenario, in order to approximate a Bragg peak, the particle induced charge region was split into two, with a low charge density track between the surface of the device and the position of the Bragg peak and a high charge density track at the peak position. The low charge density track had a charge density of 5.882×10^{-5} pCµm^{-1}, an average value of the charge deposited in the track leading to the charge peak and extended from the surface of the device to a depth of 80 µm, while the high charge segment was located between 75 µm and 85 µm below the detector surface and had a charge density of 4.235×10^{-3} pCµm^{-1}, the combination of the charge deposited in these two track was tuned to produce the same number of carriers as those produced due

to a real particle hit. The quarter cell area was split into a grid of small squares, and the previously described charge density was simulated at the centre of each of these squares and compared to similar positions within the experimental data. Due to the electronics used not being designed for this type of measurement, a significant ringing noise was observed in the experimental data, nevertheless the pulses in the simulation and experimental data were compared and are shown in Fig. 5.9.

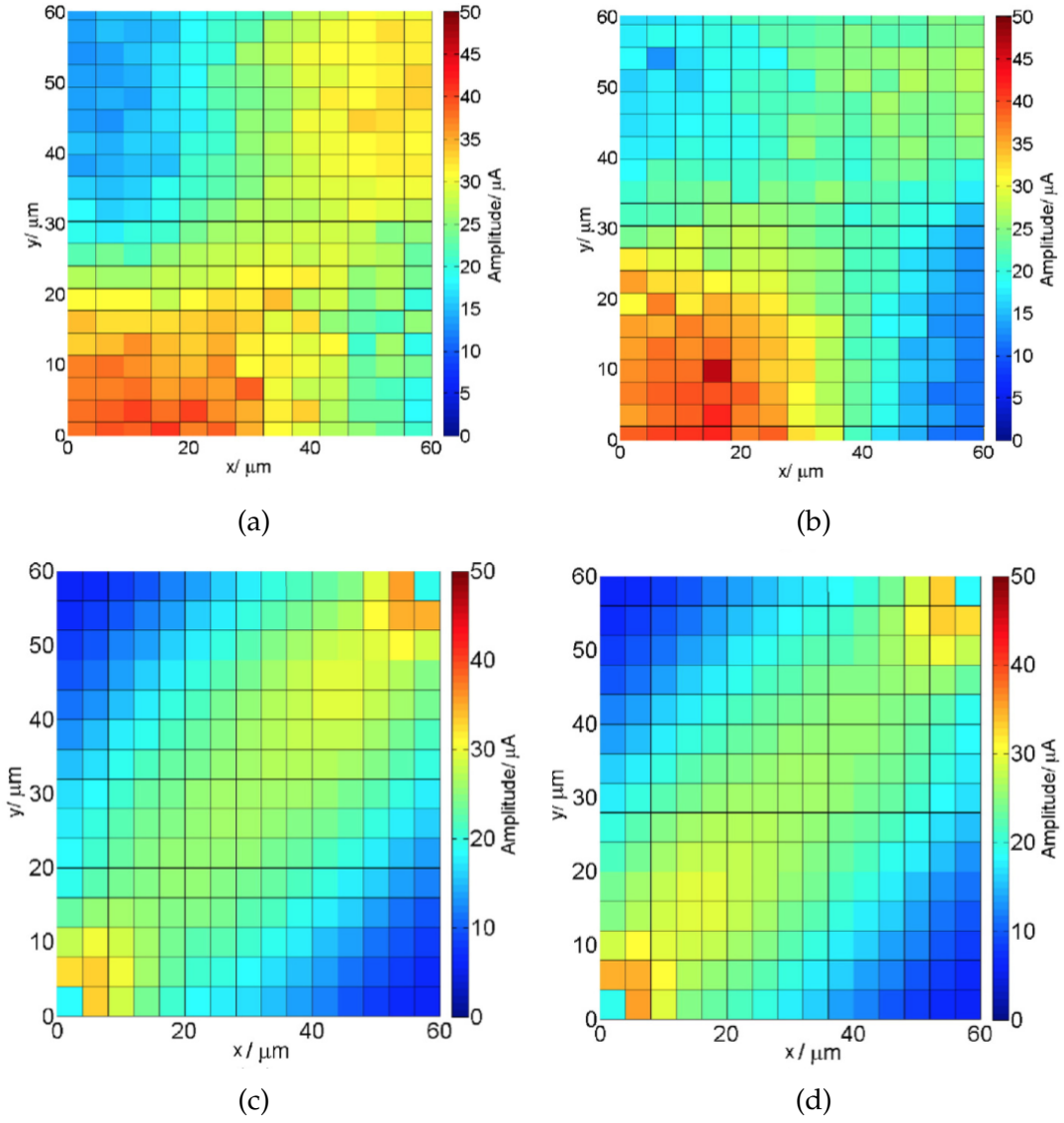

Figure 5.10: Amplitude of the current pulse due to a 4 MeV proton hit obtained experimentally as a function of position at +60V (a) and -60V (b), as well as the simulated the amplitude of the current pulse as a function of position at +60V (c) and -60V (d). The plots represent an area of a quarter cell, where a readout column is located at (0,0) and a bias column is located at (60,60)

To compare charge collection through the quarter cell, the peak pulse height

(after the ringing effect was removed using a Fourier transform) was plotted as a function of position as shown in Fig. 5.10. In both cases the peak pulse height is asymmetrical, due to the different drift velocities between electrons and holes. In the experimental data however, this asymmetry is significantly greater. This can be explained by considering the effects of neighboring cells. These are not present in the simulation and thus all the weighting field lines originating in the signal electrode finish on the bias electrode, whereas in a real device a number of them would finish on electrodes in neighboring cells. A more complete study of the weighting field and its effects is presented in Sections 5.2.3 and 5.3.2. Apart from the asymmetry the agreement between data and experiment is good and it gives a clear visual representation of the effects on charge collection of having a non uniform electric field in a 3D geometry.

5.1.2 Single crystal 3D multi-pattern

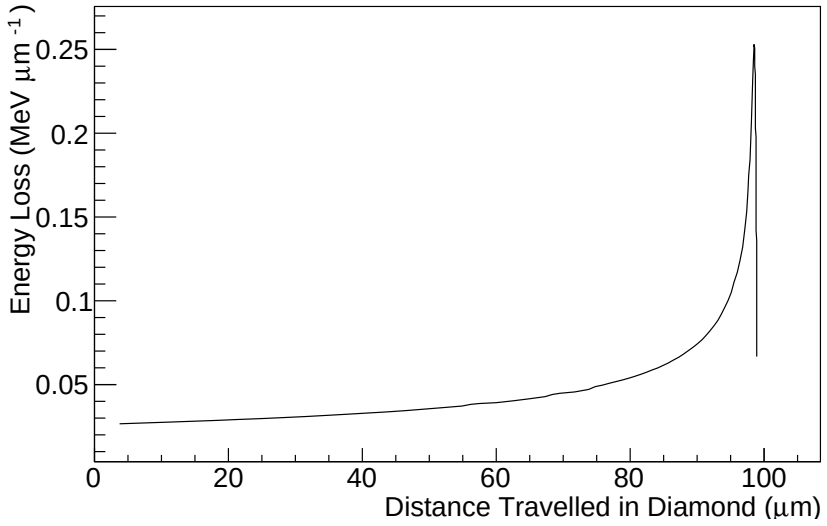

Figure 5.11: Energy deposited as a function of depth for a 4.5MeV proton in diamond calculated using the data from the National Institute of Standards and Technology [121]

The purpose of the sample was to test the viability of this new fabrication technique as well as producing a comparison between different possible 3D geometries. The device was manufactured from a diamond obtained from IIa [63]. The sample is a single crystal, electronic grade diamond with dimensions of $4 \times 4 \times 0.4$ mm^3. The graphitic electrodes were manufactured using the new SLM technique [89] [90] and

were measured to have a thickness of ≈ 2 µm. Standard photolithographic techniques were used to apply a patterned metalization on the sample as described in section 3.4. The masks were designed such that the sample would have the bias metalization on one side and the readout on the other. On the signal side, the metalization applied was 51.1 nm chromium and 73.9 nm gold, while on the bias side the metalization applied was 52.4 nm chromium and 75.7 nm gold. The metalization was deposited by evaporation and after metalization the sample was annealed for 4 minutes at 400°C. The photolithographic mask used for this sample is described in Appendix A.1.4 and a photograph of the sample is shown in Fig. B.6. This mask was designed to have the capability of comparing a 3D strip device to a 3D phantom (a device with the same metalization geometry as the 3D device, but no columns) and a planar strip device, however only the 3D device was used for these measurements.

The areas of the 3D strip and 3D phantom detectors were split into three parts, one with square cells with 100×100 µm^2 dimensions, one with rectangular cells with 100×200 µm^2 dimensions and one with hexagonal cells with dimensions of 100×116 µm^2. An image of the sample ready for measurement is shown in Fig. B.6.

The sample was measured at RBI, using the setup described in previous sections, with an increased proton energy of 4.5 MeV, the board on which the sample was mounted was also replaced with a new high frequency board to reduce the ringing effects observed previously. Protons of this energy deposit most of their energy in a Bragg peak as shown in Fig. 5.11. IBIC and TRIBIC measurements of the sample were taken, particularly studying the square and hexagonal geometries, the electronics were optimized for high frequency response to reduce the ringing effect that had been observed in the previous set of measurements.

Firstly the IBIC technique was used to measure the Charge Collection Efficiency (CCE). The CCE as a function of positions for different voltages in different geometries is shown in Fig. 5.12. The charge collection efficiency as a function of voltage is shown in Fig. 5.13.

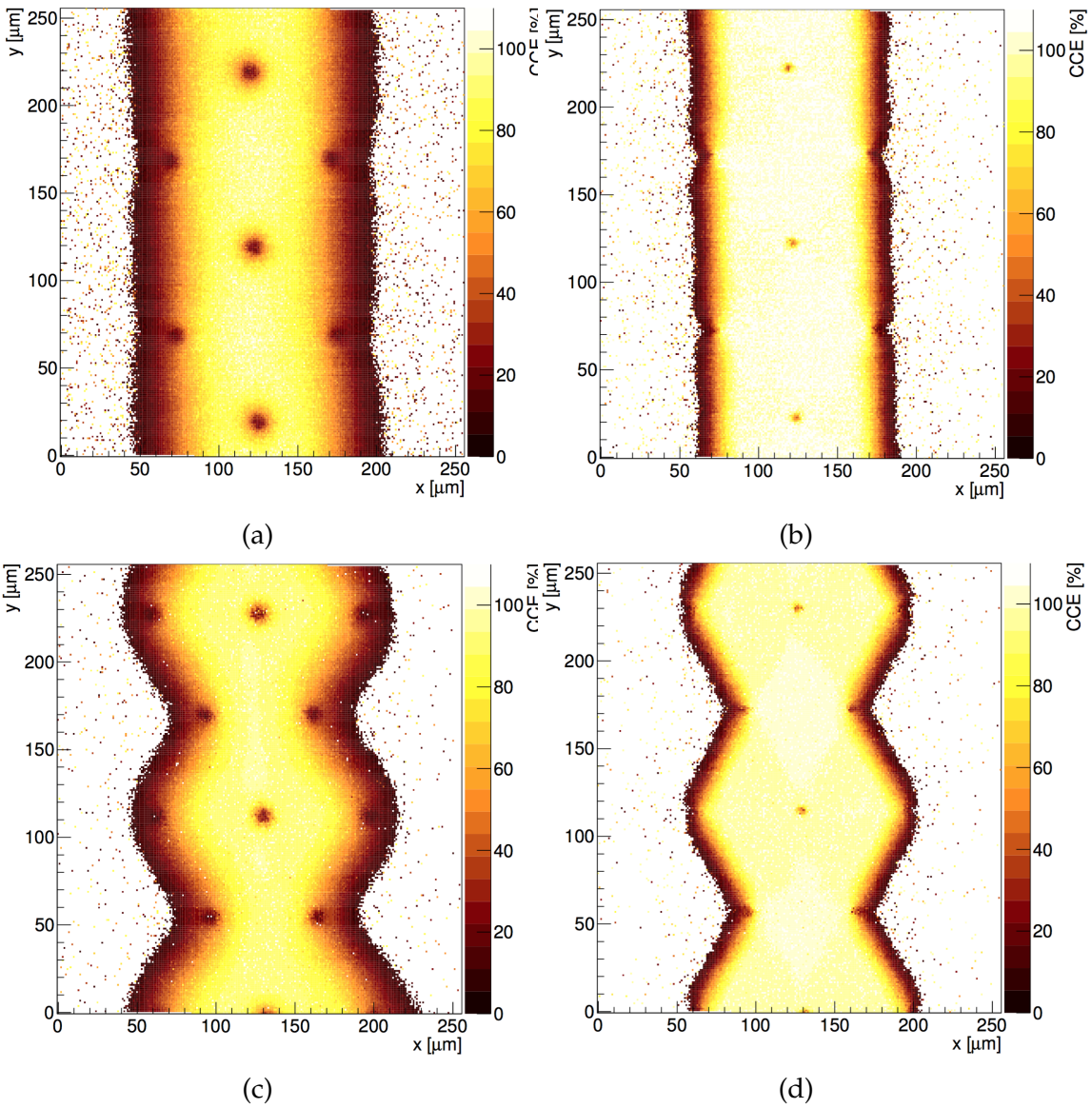

Figure 5.12: Charge collection efficiency of the measured cells as a function of hit position for (a) square cells and -2 V, (b) square cells and -20 V, (c) hexagonal cells and -2 V, (d) hexagonal cells and -20 V.

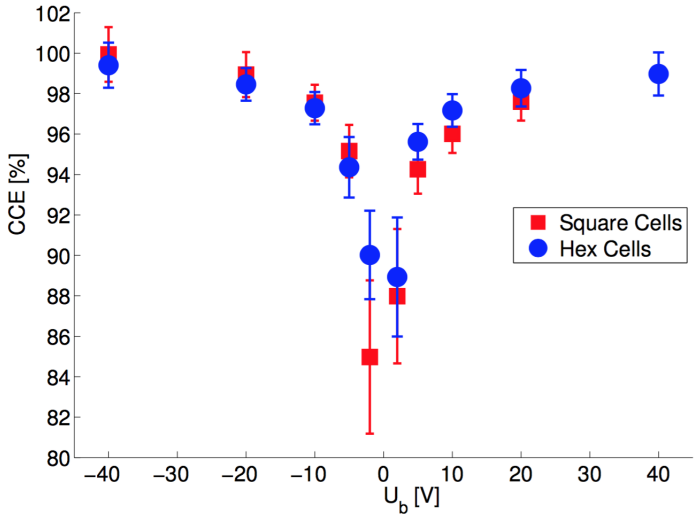

Figure 5.13: Charge collection efficiency for this device as a function of voltage for different cell geometries.

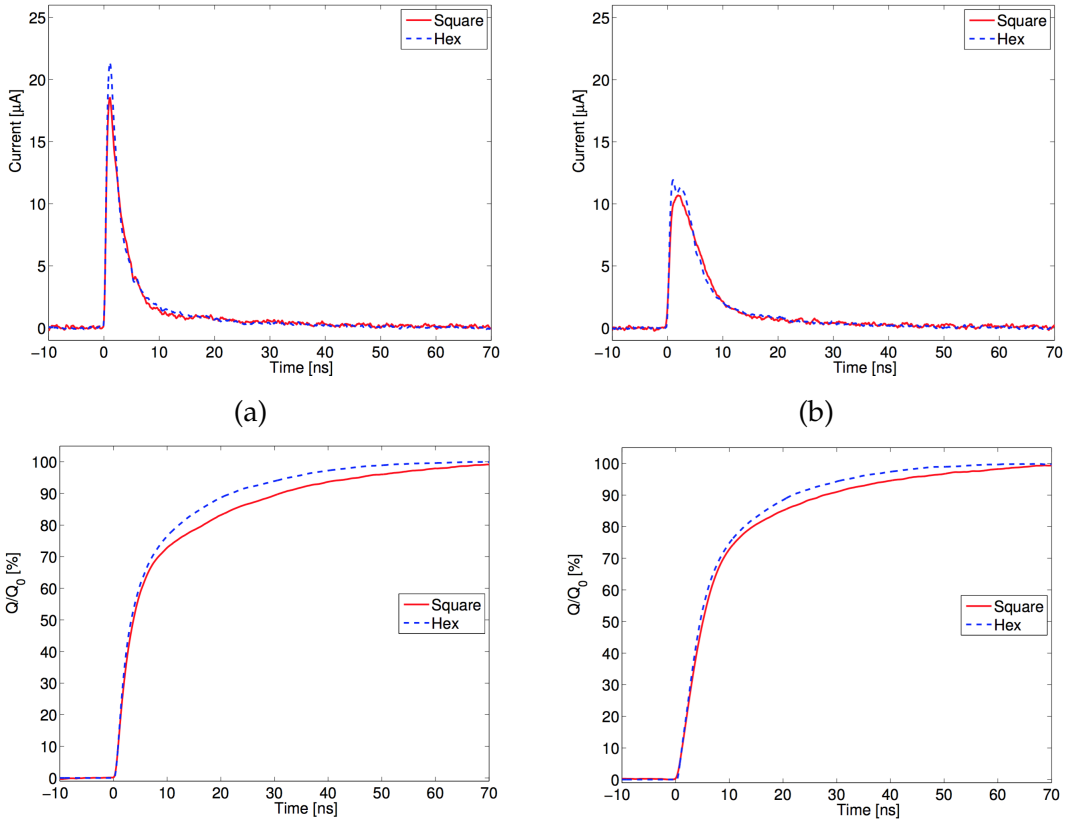

Figure 5.14: (a) Current pulse in the high field region, (b) current pulse in the low field region, (c) current integral in the high field region, (d) current integral in the low field region

TRIBIC measurements were then performed as described in section 5.1.1, to explore the electric field distribution of the device at 20 V with the proton beam incident of the readout side of the electrode.

The current pulses measured with this technique in both high and low field regions of the cell were compared for square and hexagonal cells as shown in Fig. 5.14. While not conclusive, this does point to hexagonal cells providing somewhat better charge collection than square cells.

3D multi-pattern device simulation

In order to simulate more points in the device and to simulate a larger area to allow the study of charge sharing effects, it was necessary to reduce the time required for the simulations. These simulations were performed in two dimensions, which required the verification that this would give accurate results.

For planar devices two dimensional simulation can be performed by taking a cut of the device through its thickness as the electric field does not have a complex structure in the plane of the detector. This is not achievable with 3D devices, therefore the simulation plane has to be a plane parallel to the surface of the device. As a result of this, it is not possible to replicate the Bragg peak structure in 2D simulations making this the equivalent of simulating a MIP traveling through the device. It is therefore necessary to test what the difference would be between these situations.

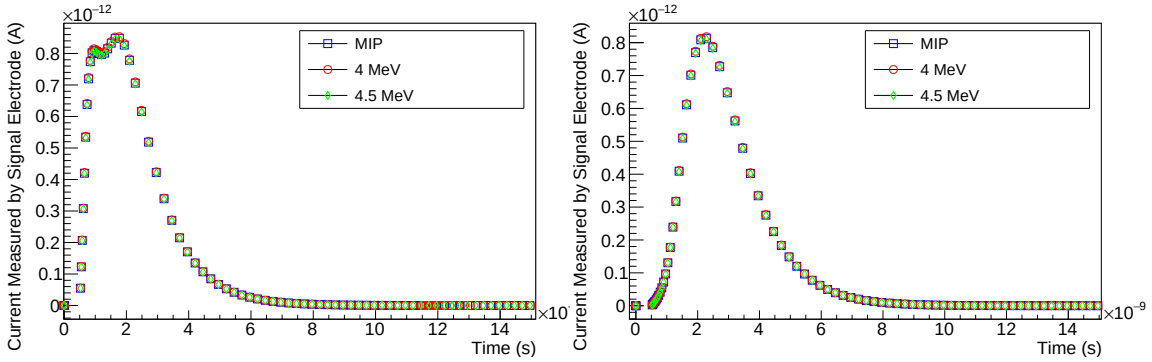

(a) (b)

Figure 5.15: Comparison of the pulses obtained by simulating a MIP and two different Bragg peak energies in (a) a high field region and (b) a low field region of the the simulated device

Simulations were performed in a 3D mesh with no surface metalization comparing a MIP simulation with Bragg peaks due to 4MeV and 4.5MeV protons. The

results of this simulation after normalization are shown in Fig. 5.15. The negligible differences between these simulations confirms that this is a viable approach.

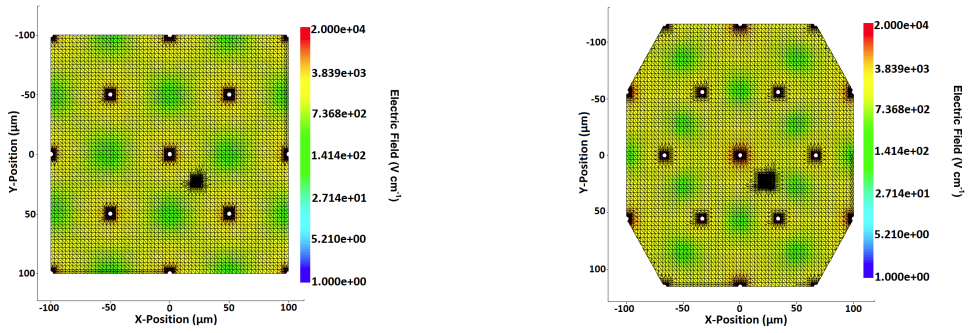

(a) (b)

Figure 5.16: The square (a) and hexagonal (b) cell meshes used for simulations of the multi-pattern design. Both meshes are for particle hits at X=22.5 µm, Y=22.5 µm. In each case the applied bias voltage is 20V.

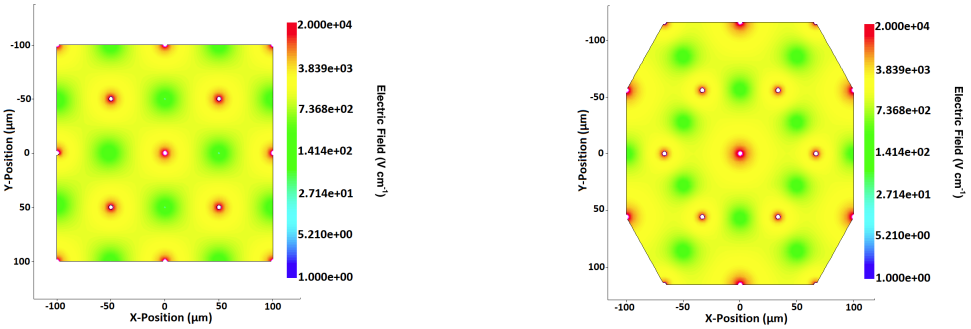

(a) (b)

Figure 5.17: The electric field of the device at 20 V for (a) square cells and (b) hexagonal cells

Simulations are carried out to recreate the behavior of this device. The simulations are limited to two dimensions to limit the required amount of processing time. A two dimensional mesh is created representing a 2×2 array of square cells, in order to include the effects of the neighboring cells. A resistance of 175 kΩ is applied to each of the electrodes and the simulated charge density of the hit is set to that of a MIP (6.4×10^{-6} pC), with the other parameters set to the same values as described in the previous sections. The simulations are also carried out for hexagonal cells, where a mesh is created simulating an approximate area of a 2×2 array of cells. These meshes are shown in 5.16. To simulate the effect of the amplifier chain on the signal pulse, the simulated output current is passed through a frequency filter of 2 GHz.

These meshes are then used to simulate the experimental data. Firstly, as previously stated a quasistationary simulation was used to raise the voltage to the operating voltage of the device. The electric field within the device at 20V is shown in Fig. 5.17.

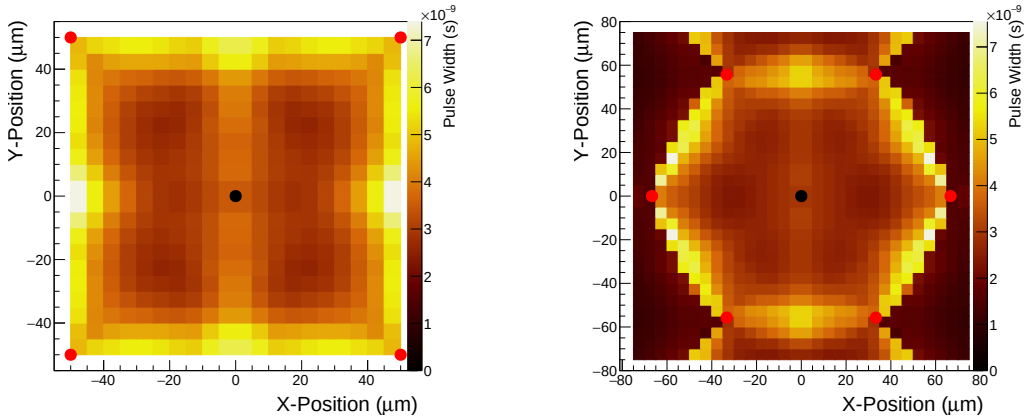

(a) (b)

Figure 5.18: Width of the simulated pulses as a function of position for a voltage of 20 V for (a) square cells and (b) hexagonal cells. The width is defined as the time for which the pulse is above 50% of its peak amplitude

The simulated device is brought to the required starting conditions, hits incident on the device are simulated. The device is split into a number of squares with dimensions of 5×5 µm^2 with a simulated hit at the centre of each square, in order to build a picture of how charge is collected over the whole cell. The simulated hits are limited to the area of a quarter cell to reduce the required computation time, while gathering enough information to reconstruct the measured current pulses for hits throughout the whole cell. Fig. 5.18 shows the width of the pulses produced in the simulation as a function of positions within the cell. Fig 5.19 shows a comparison between pulses in square cells and hexagonal cells in both high and low field regions within the cell. The simulations are in reasonable agreement with the experimental data, considering the simplifications that have been carried out. The structure of the pulses has been recreated well, including the two peak structure observed in the experimental data though it is somewhat less pronounced in the simulation. The two peak structure is due to the different travel times of the different types of charge carriers, this effect is only noticeable in the low field regions as in higher field regions the two peaks are too close together and it is not possible to resolve them with the electronics.

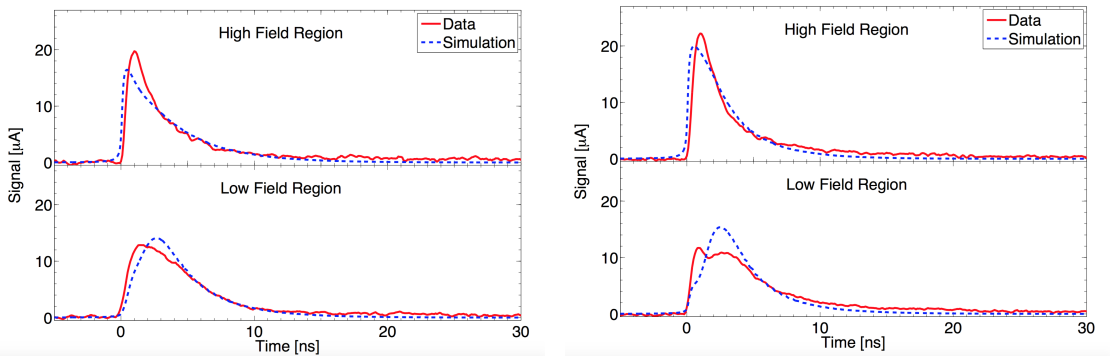

(a) (b)

Figure 5.19: Comparison between simulated and measured pulses for both low and high field regions for (a) a square cell geometry and (b) a hexagonal cell geometry.

5.2 Test beam measurements and simulations of scCVD devices using 120 GeV protons

5.2.1 Experimental setup and device fabrication

Two detectors, a 440 µm thick scCVD device (described in section B.1.1) and a ≈ 500 µm thick pCVD device (described in section B.1.2), material for which was obtained from Element Six [61], were measured at the CERN H6 beamline [3] using 120 GeV protons between 2011 and 2015 [111].

The Strasbourg telescope [107] was used to make these measurements. This telescope consists of 4 x and 4 y silicon strip detector planes with a pitch of 50 µm for track reconstruction and two scintillators for triggering.

During the testbeams, the protons arrived at the sample in spills lasting ≈ 10 s, during each spill the telescope scintillators produced between 10000 and 50000 coincidence triggers, up to 3600 of which were saved. A relatively low rate of incident protons was required for these experiments to avoid producing multiple tracks in the silicon telescope as, since the silicon planes were strip devices, his could produce ghosts hits, and having single tracks would remove this ambiguity.

These devices used the batch 2 geometry consisting of 3 different arrays (a description of the mask used for these devices is given in section A.1.1):

- A planar strip device with 50 µm pitch; this is a device geometry that has been extensively used for past planar diamond devices [122] and is very well understood and is used as a control sample which the performance of the other detectors can be compared to.

- There was also a 3D strip detector consisting of square 150 µm cells, each with a graphitic signal electrode in the center and a bias electrode at each corner of the cell. The bias electrodes were all connected along the surface of the diamond whereas the signal electrodes were connected in strips to be read out separately. The performance of this device could be compared directly to the planar strip device as they are made of the same material.
- Finally there was a 3D phantom strip detector. This is a device that has the same metalization pattern as the 3D device, however no columns have been produced in this detector. This device was designed to be compared to the 3D detector directly in order to understand how much charge is collected by the surface metalization and how much by the graphitic electrodes.

After various column fabrication tests, the optimum laser processing parameters with the highest column drilling success rate for the 3D devices were found to be a focal point energy density of 2 Jcm^{-2} and a translation speed of 20 µms^{-1} [86].

A full description of the graphitization process has been given in Section 3.3. After the graphitization process, it was determined by optical inspection that the column graphitization process efficiency (percentage of columns that contained a conductive graphitic channel through the entire thickness of the diamond) for these devices reached $\approx 92\%$, with the successfully processed columns having a measured diameter of (6 ± 1) µm. Another array was produced on both samples with a similar geometry, but with a 100 µm pitch. This device however was not measured. The detectors had a Cr-Au surface metalization produced using a photolithographic process as described in section 3.4, through which they were read out [111].

5.2.2 Test beam measurement of scCVD device

The diamond strip device was biased at 500 V throughout, with a leakage current of < 2 nA, while the 3D and 3D phantom devices were biased at 25 V, with a leakage current of < 1 nA.

The performance of the 3D diamond device was then analyzed using both a clustered (starting from the diamond channel with the hit position as predicted by the track reconstructed from the Silicon planes, to which are added adjacent channels with a signal greater than 3σ, where σ is the common mode subtracted noise) and transparent (sum of the 3 strips closest to the predicted hit position) analysis and compared to the strip and phantom device. The full details of the analyses are already described elsewhere [123]. The charge collected in the device as a function

of the position is shown in Fig. 5.20. In this image there are areas in the 3D device with a low charge collection, which are due to broken, unconnected or missing electrodes. Fig. 5.21 shows a comparison for the charge spectra for each of the 3 detectors.

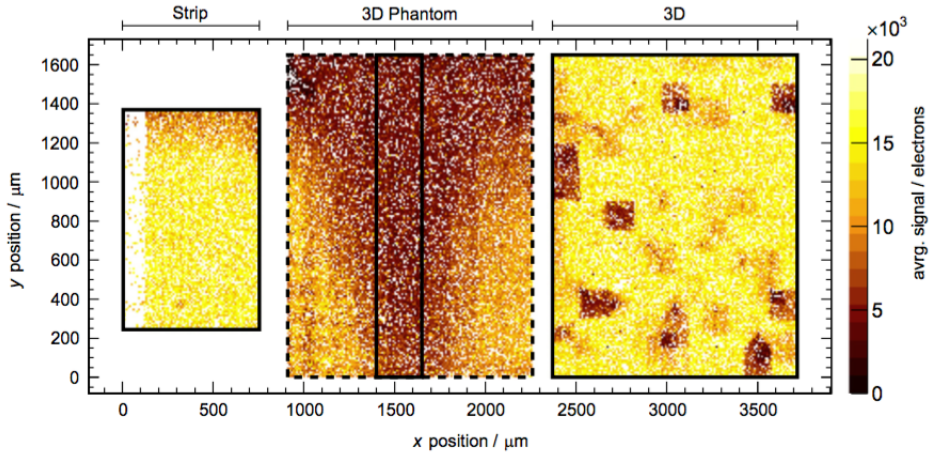

Figure 5.20: Charge collected as a function of position in the 3 regions of batch 2 scCVD device. The strip detector extends beyond the acceptance region of the trigger scintillators. The charge collection of the 3D phantom device was distorted due to the electric field of the 3D and planar strip devices leaking into this region, thus only events in the highlighted central region of the 3D phantom device were used for further calculations.

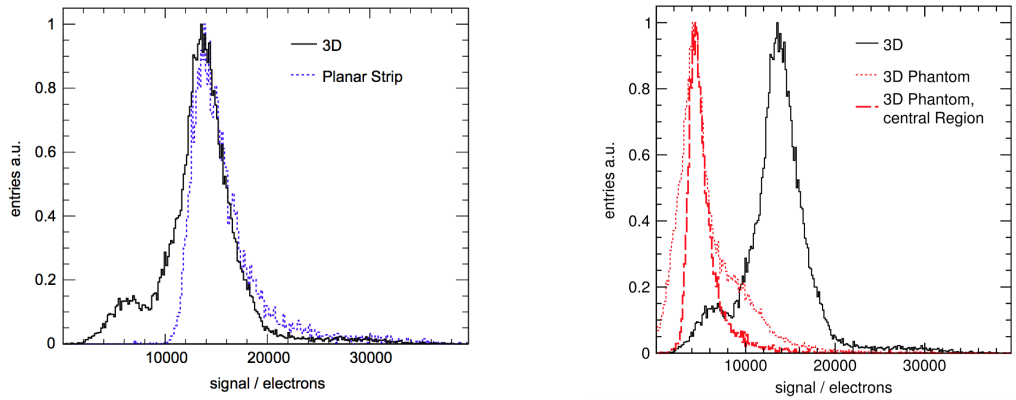

(a) (b)

Figure 5.21: Cluster charge spectra of each of the three devices, (a) is a comparison between the planar strip device (blue) and the 3D device (black) while (b) is a comparison between different regions of the 3D phantom device (red) and the 3D device (black).

The charge spectrum of the 3D device shows some substructure due to the presence of two peaks, one in good agreement with the strip device spectrum and the

smaller peak with a similar position to the 3D phantom peak, leading to the conclusion that the smaller peak is largely due to hits in the 3D device where the charge is collected only by the surface metalization due to missing columns. Another phenomenon is the presence of regions where negative signals are observed. These negative signals are well above the noise level, especially in the second closest strip to the predicted hit position and were clustered around the positions of a limited selection of bias electrodes in the 3D device, as shown in Fig. 5.22, leading to the conclusion that these negative events are the result of defective bias columns.

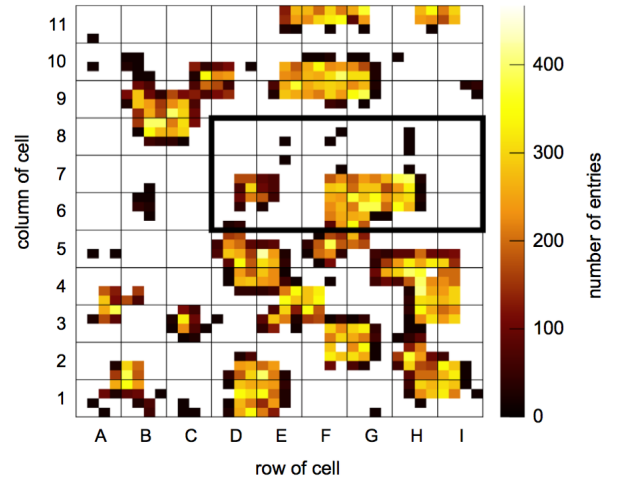

Figure 5.22: Negative charge collected by the 3D device, as a function of position.

A fiducial region of the 3D device, highlighted in Fig. 5.22, is used for further analysis to mitigate the effect of defects of the fabrication process on the analysis. This section was used as it is a large continuous region with no broken signal electrodes. During the analysis events with a negative signal greater than 700e were excluded. The analysis was then repeated using the events within the fiducial region that passed these criteria. The charge collection spectrum was again compared to the collection spectrum of the strip device as shown in Fig. 5.23.

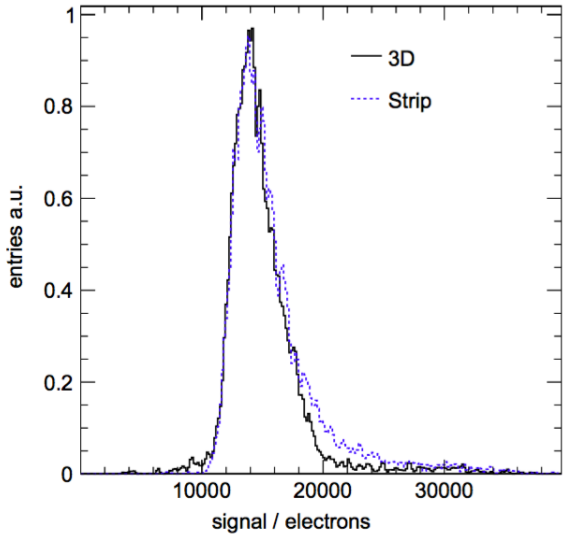

Figure 5.23: Comparison of the charge spectrum of hits in the fiducial region of the 3D device and the charge spectrum of hits in the planar strip device.

These two spectra are in excellent agreement with each other, leading to the conclusion that at least for a single crystal device a 3D device can achieve a similar performance to a planar strip device at an order of magnitude lower operating voltage, proving that as long as the column fabrication issues can be solved 3D detectors can provide a viable alternative to planar devices.

5.2.3 scCVD device simulation

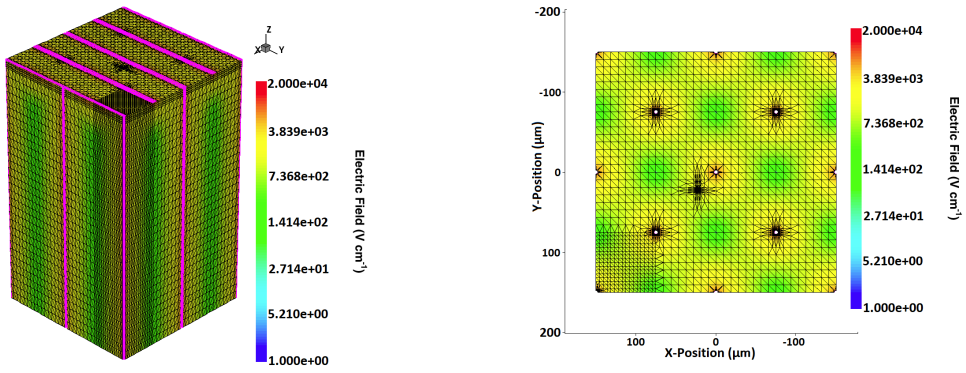

(a) (b)

Figure 5.24: (a) the 3D mesh used for simulations of this device and (b) a 2D cut of the mesh at a depth of 250 µm in the device. The columns are connected along the surface in the Y-direction to replicate the effect of the surface metalization in the detector. The field shown in these plots is that of an applied bias of 25V

TCAD simulations were used to understand what caused negative charge events to be clustered in such a way. A 3D mesh was produced containing a 2x2 array of 150 µm square cells to match the geometry used in the measured device as shown in Fig. 5.24. To limit the amount of time required for these simulations traps were excluded for the time being.

The device was raised to a voltage of 25 V using a quasistationary simulation, using the same material parameters defined in Section 4.1, after which the passage of a MIP was simulated at a selection of 25 regularly spaced positions within a quarter cell of the mesh.

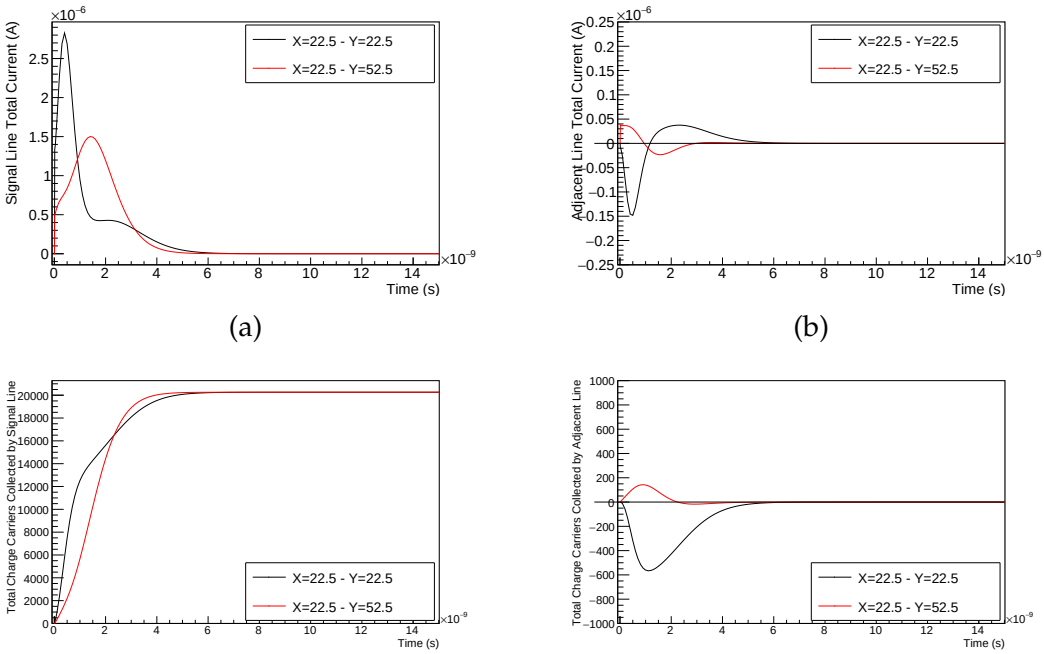

Figure 5.25: Simulated instantaneous current observed by (a) the closest strip to the hit and (b) the second closest strip to the hit, as well as the simulated integral of the current for the closest strip (c) and the second closest strip (d), for two different positions in the cell.

When no traps are present, full charge collection occurs and most of the charge is collected by the nearest electrode, with a negligible amount collected by the 2nd or 3rd closest electrodes, however even if the charge collected by these electrodes is ≈ 0 the instantaneous current at the electrode due to the movement of the generated charge carriers is not negligible, but rather it produces a signal with both a positive and negative component as shown in Fig. 5.25. The combined integral of the positive and negative parts must be zero as no charge is collected by these electrodes. The order in which these two components appear is dependent on the

position of the hit.

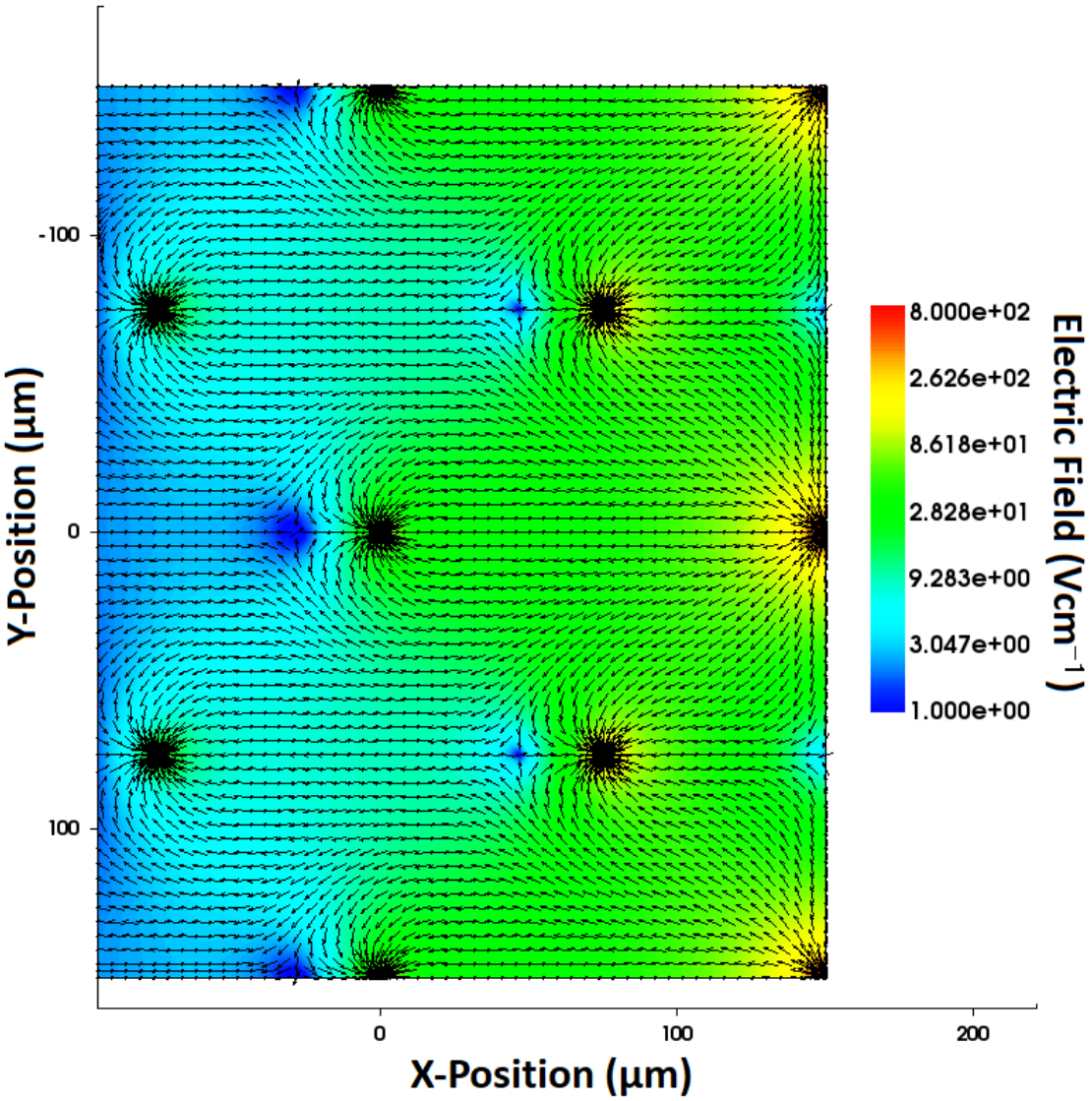

Figure 5.26: Weighting field due to a 3D electrode, the color scale represents the strength of the weighting field, whereas the arrows show the direction of the field lines. The weighting field spreads out radially from the electrode within the cell, however at the edges of the cell the field curls round the electrodes. As a result of this an electron-hole pair produced in the neighboring cell will have to travel through regions of the device where the weighting field changes direction, hence producing the bi-polar signals.

This phenomenon can be explained using Ramo's theorem described in Section 2.1.3. The instantaneous current measured by an electrode is dependent on the weighting field due to that electrode. The weighting field due to a 3D signal electrode is shown in Fig. 5.26. For an electron-hole pair produced in the neighboring

cell, at least one of the carriers will traverse a region of space where the component of the weighting field parallel to its direction of motion will change sign, thus changing the sign of the instantaneous current induced by that carrier, hence explaining the bi-polar signals.

Once this effect was understood, a similar mesh (shown in Fig. 5.27) was produced, with a missing HV electrode to replicate the effect of having a missing or otherwise unconnected HV electrode and a similar set of simulations was carried out using this mesh.

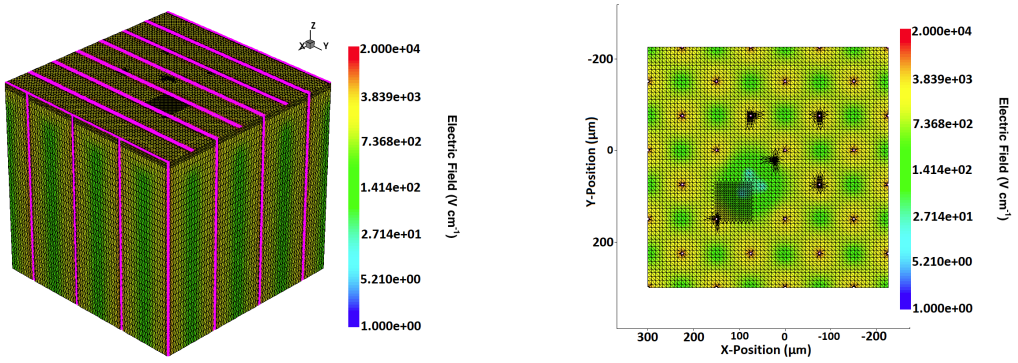

(a) (b)

Figure 5.27: (a) the 3D mesh and (b) a 2D cut of the mesh at a depth of 250 µm into the device with a missing HV electrode used for simulations of this device.

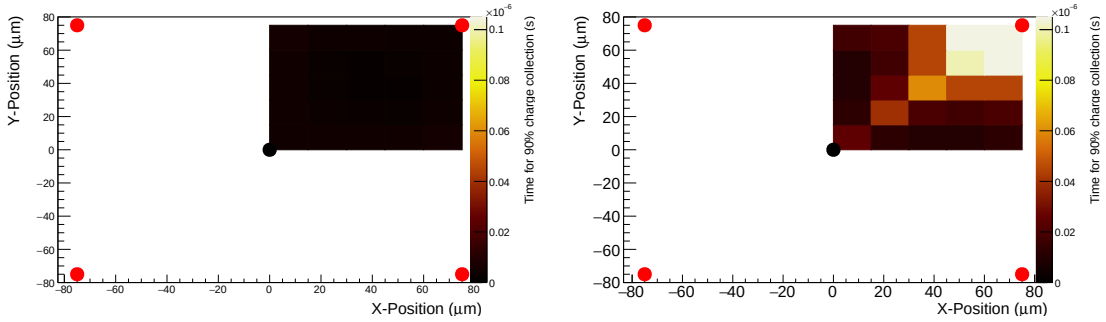

(a) (b)

Figure 5.28: Time required for 90% charge collection for both an intact cell (a) and a device with a missing HV column (b)

The time required for the collection of 90% of the charge as a function of position was compared for the two sets of simulations and is shown in Fig. 5.28. While for the intact cell charge collection occurs quickly with 90% of the charge collected within 10 ns independent of the position, for the cell with a missing bias column,

charge collection takes significantly longer, with certain regions requiring in excess of 100 ns seconds to achieve 90% charge collection.

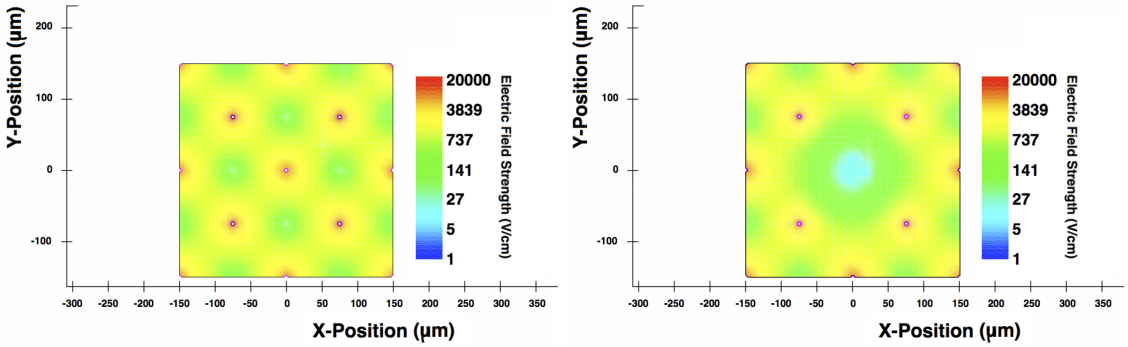

(a) (b)

Figure 5.29: Comparison of the electric field of an intact device to the electric field of a device with a missing HV electrode.

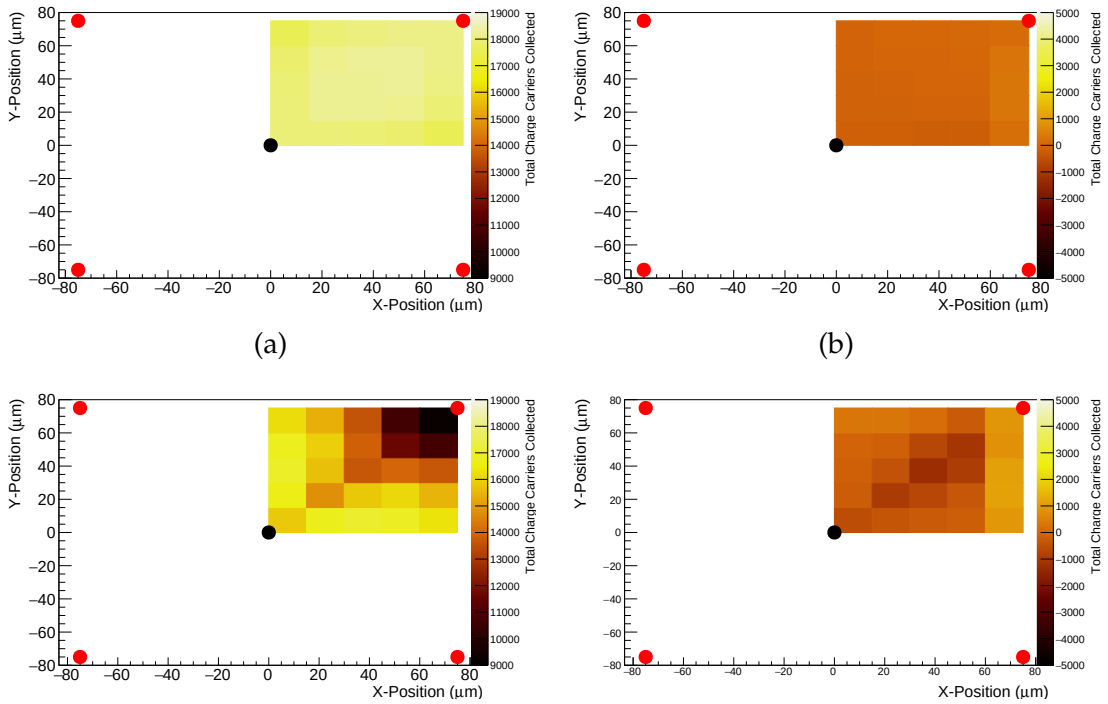

(a) (b)

(c) (d)

Figure 5.30: The simulated charge collection with a charge carrier lifetime of 70ns for an intact device (a) and (b) and for a device with a missing HV column (c) and (d). (a) and (c) show the charge collected by the nearest strip, while (b) and (d) show the charge collected by an adjacent strip.

By comparing the simulated electric field of both situations (Fig. 5.29), it can be concluded that in both cases the 3D geometry means that the field is not uniform

throughout the cell and in both cases in some regions the electric field is very low, but if an electrode is missing, the low field region is significantly larger.

The simulations so far were carried out with the expectation of full charge collection and no recombination or charge trapping, however, due to the time needed for full charge collection in the device with a missing column, it is expected that not all the charge will be collected, so a limited charge lifetime was added to the simulation results by multiplying the instantaneous current plot by an exponential decay function to get an approximation for the effects of a finite charge lifetime. The results are shown in Fig. 5.30. With a charge lifetime of 70 ns the differences in the simulation with a fully intact cell were small (below detection limits of the experiment), however in the simulation with the missing electrode there was a significant difference in the total charge collection, with about half the total charge collected and a large negative signal observed by the second closest electrode. This is a reasonable quantitative agreement with Fig. 5.20 with $\sim 50\%$ of the charge collected around broken bias electrodes, with the negative charge regions in good agreement with Fig. 5.22.

5.2.4 Conclusions from scCVD device studies

The results of this test beam successfully proved that 3D diamond is a viable technology, the charge collected by the 3D device was comparable to that collected by the strip device, even though the applied bias voltage was only 25V on the 3D device compared to the 500V on the strip device.

These experiments also showed that issues still remained to be fixed with the laser processing, as a number of columns were found to be broken, missing or unconnected. From the simulations it was possible to understand what effect these column connection failures would have on the performance of the device.

5.3 Polycrystalline 3D device measurement and simulation

5.3.1 pCVD device measurement

A pCVD diamond sample was measured using the experimental setup at CERN. Due to concerns with the effectiveness of surface metal contacts, for this sample the same metalization pattern shown in Appendix A.1 was deposited on both sides of the sample to add redundancy. In this case the strip device was biased at 500

V throughout, with a leakage current of < 2 nA, while the 3D and 3D phantom devices were biased at 70 V, with a leakage current of < 5 nA.

As described previously, the performance of the 3D device was analyzed using both a clustered and transparent analysis and was then compared to the performance of the planar device on the same sample. Full details of the analysis are described elsewhere [123]. The charge collected in the device as a function of the position is shown in Fig. 5.31. Unlike the scCVD device described earlier, where the collected charge was more or less uniform within the planar and 3D regions, excluding broken cells, in this case the collected charge varies greatly as a function of position. The size of these features is ~ 100 µm, which is consistent with the grain size in polycrystalline electronic grade material [124]. Beyond the non uniform features, there are also a few regions with a rectangular shape with a low collected charge, which are suspected to be cells with broken signal columns as before.

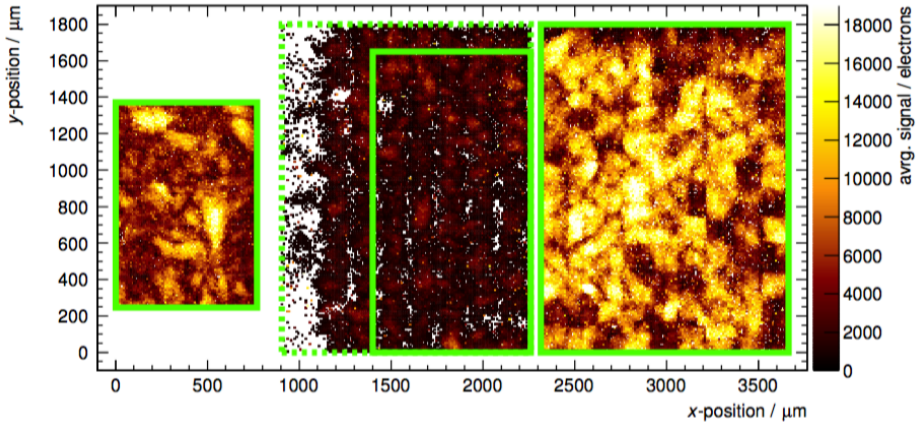

Figure 5.31: Charge collected as a function of position in the 3 regions of batch 2 pCVD device. The region on the left is the planar device, the region on the right is the 3D device, while the middle region is the 3D phantom. From this plot it is already noticeable how the working regions of the 3D device are performing better than the planar device.

Again, the charge spectrum for each of the three regions was plotted as shown in Fig. 5.32; like in the single crystal device it shows that the 3D phantom performs significantly worse than the other two detectors, and that there is some structure in the spectrum for the 3D device. In this case however, the 3D spectrum shows a significant improvement compared to the planar device.

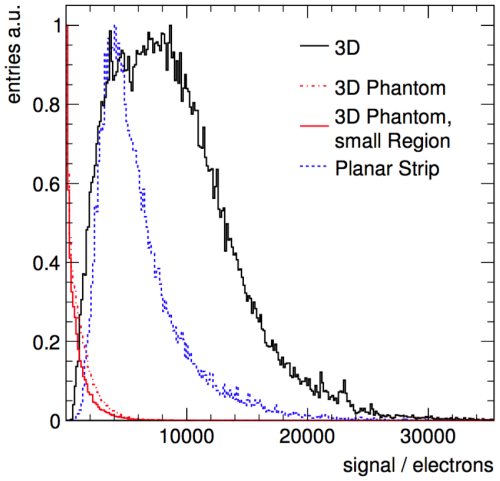

Figure 5.32: Charge spectra of the pCVD device. The 3D device is performing significantly better than the planar device. There is some structure in the spectrum of the 3D device; as in the previous case this is likely due to the effect of some cells with missing or otherwise unconnected electrodes.

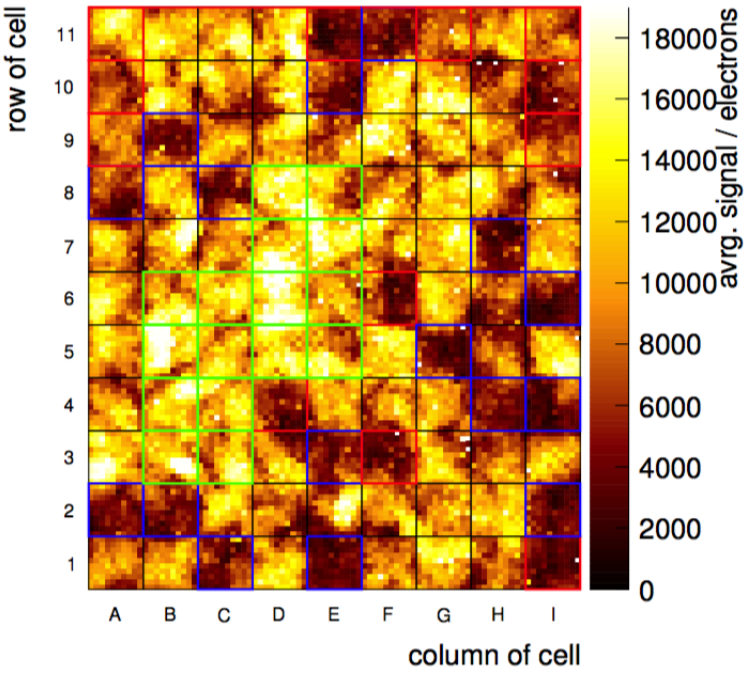

Figure 5.33: Cluster charge as a function of position in the area of the 3D device. The cells highlighted in blue and red are cells with suspected issues with the readout electrode, with the blue cells used for alignment. The cells highlighted in green are the cells used for the full analysis, and the mean signal response of each cell, with a threshold chosen to distinguish between suspected broken cells and intact cells.

Similarly to the single crystal device, it was necessary to limit the fiducial region

of the 3D detector to a region of fully working cells, however due to the polycrystalline structure, it was necessary to have a more robust method to find broken cells. Therefore the average charge collected by each cell was calculated using the transparent cluster method as the sum of the two highest signals in a three channel cluster, and a cut of 7300 electrons was used to identify cells with broken readout electrodes; the results of this are shown in Fig. 5.33.

As for the single crystal device, events with negative charge signals were observed, unlike for the single crystal device however, where the events with a significant negative charge appeared only around a small selection of bias electrodes, these events are present throughout the whole detector area and generally appear clustered around readout electrodes. This is shown in Fig. 5.34. The positions of the hits producing negative charges within a cell and the average total measured charge as a function of position are shown in Fig. 5.35.

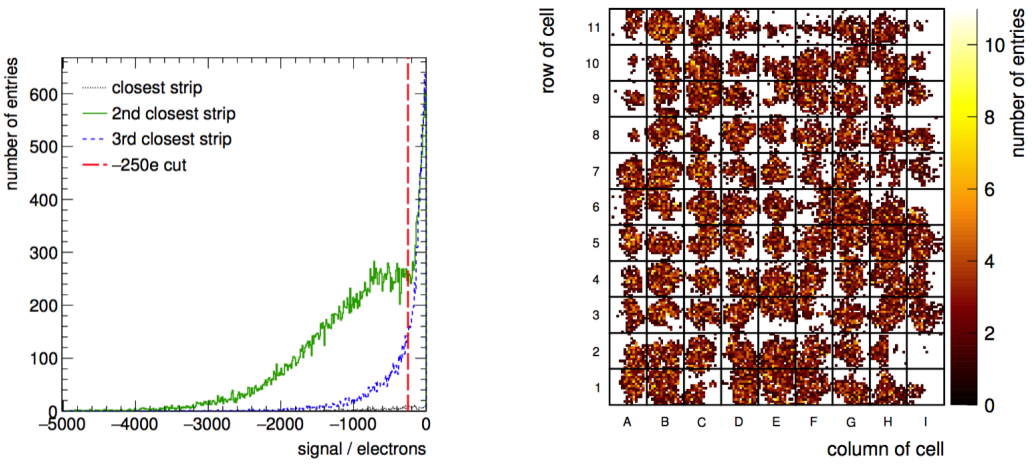

(a) (b)

Figure 5.34: (a) the spectrum of the measured negative charges, separated according to which strip they were measured by relative to the hit and (b) the negative charge events as a function of position within the detector.

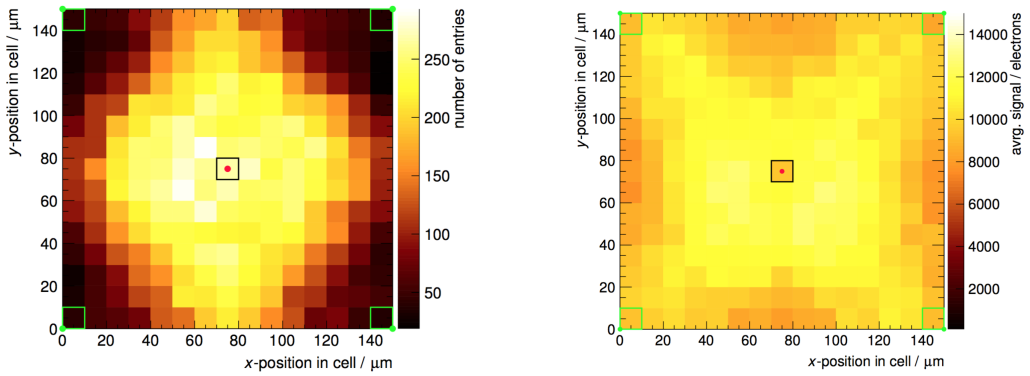

(a) (b)

Figure 5.35: (a) the positions of the negative charge events superposed in one cell. and (b) the average measured cluster charge as a function of position within the cell in the region used for the analysis.

Finally, the charge spectrum for events in the fiducial region of the 3D device at 70 V was compared to the charge spectrum for the planar device at 500 V (Fig. 5.36).

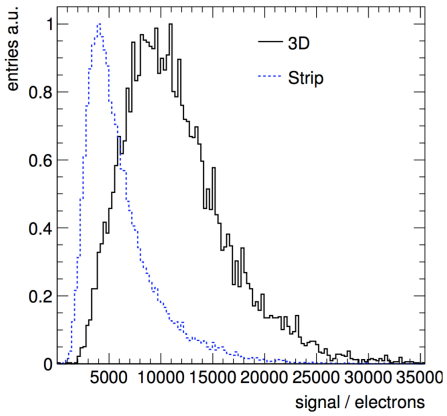

Figure 5.36: Comparison of the charge spectrum of hits in the fiducial region of the 3D device at 70 V and the charge spectrum of hits in the planar strip device at 500 V.

The charge spectrum of the 3D device shows a significant improvement compared to the planar device, achieved at a significantly lower voltage. Normally it is expected to achieve only partial charge collection in pCVD material; in this case however the 3D device performed significantly better than the planar device, achieving $\sim 60\%$ charge collection.

5.3.2 pCVD device simulation

To understand the occurrence of events with a negative collected charge, simulations were performed to replicate the observed behavior. As was previously shown in section 5.1.2 while simulating a MIP, the difference between a 2D and 3D simulation is small enough to be neglected. To improve the understanding of the processes involved, it was necessary to increase the number of simulated hits throughout the cell. To achieve this in a realistic time frame, it was necessary to limit the simulations to two dimensions. A mesh was then created to perform these simulations, this is shown in Fig. 5.37.

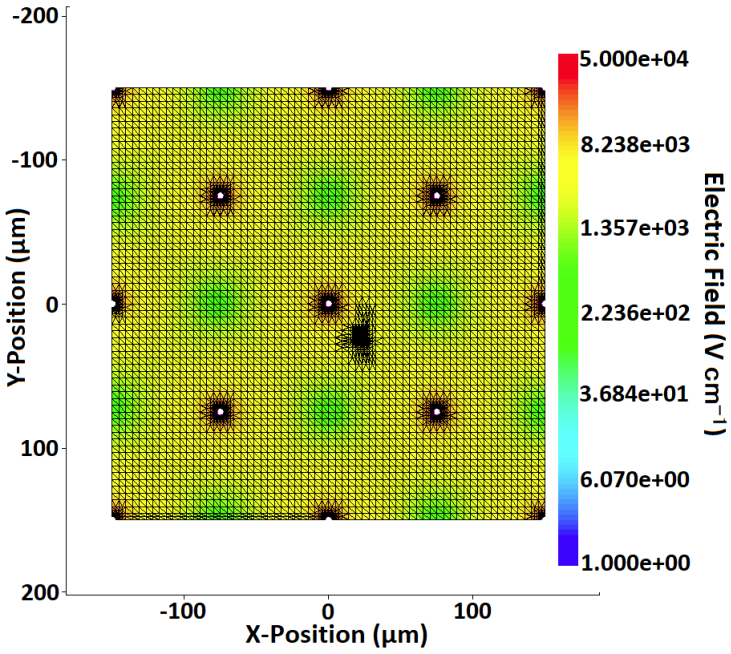

Figure 5.37: Mesh used to simulate pCVD device, showing the field due to an applied bias of 75V.

Full charge collection is currently not achievable in pCVD devices due to the short charge collection distance of the material [59] [125] [126]. However, there is still some controversy when considering where the charge is trapped. Fig. 5.31 shows that the material is not uniform. Two different approaches were therefore tried to understand how charge is trapped in pCVD material, either trapping at a grain boundary, or uniformly throughout the material.

Simulations were run to simulate the effect of charge trapping occurring at grain boundaries only, a large concentration of traps was added to a 5 µm layer of material in the mesh, as shown in Fig. 5.38. This layer was subsequently modified to study how the position and shape of the boundary region affected the collected charge.

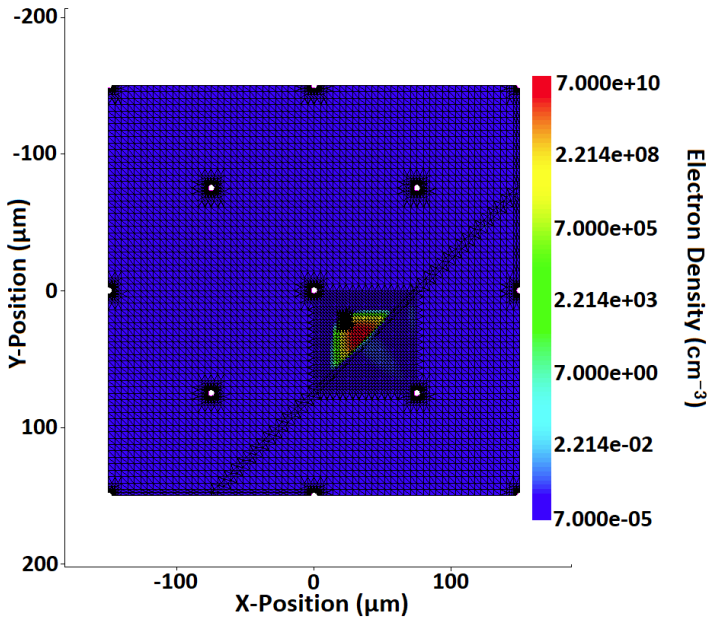

Figure 5.38: Mesh used to simulate pCVD device, with a thin layer of material used to simulate a grain boundary in the extreme case that the boundary traps all the charge passing through it.

To simulate the effect of charge trapping occurring uniformly through the bulk of the material, the current pulse measured by the signal electrode is multiplied by an exponential decay function. This is the same process as described for the sc-CVD material but with a significantly shorter charge lifetime. Even if this approach is not useful for describing the effect in individual cells, it is expected to provide a good approximation for the average effect throughout the whole detector (Fig. 5.35). Figs. 5.39-5.42 show the results of these simulations displaying both the total charge collected as well as the negative signals observed by adjacent cells. These results were then compared to the experimental data as shown in Figs. 5.43 and 5.44.

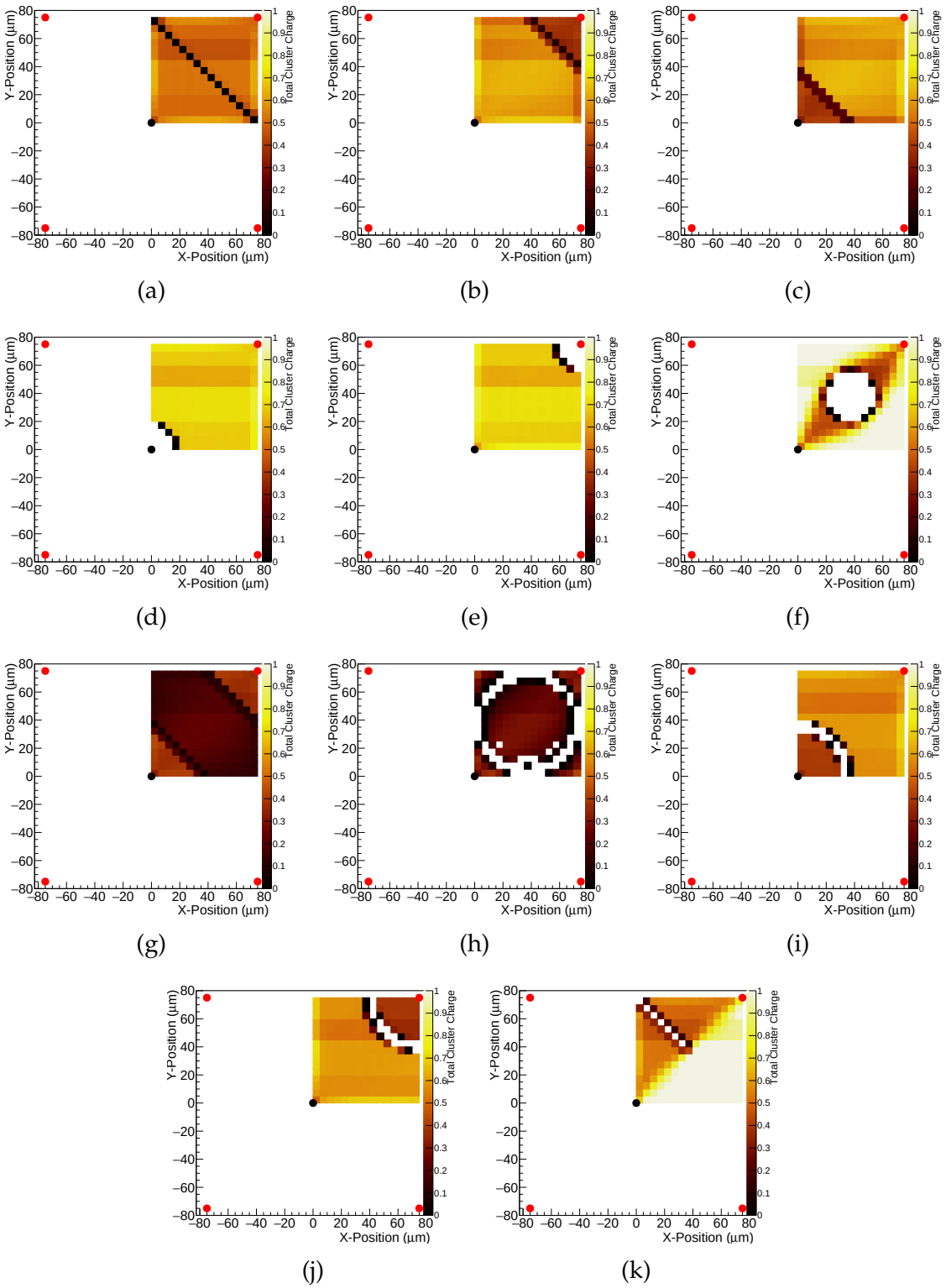

Figure 5.39: Simulated charge collected as a function of position for the simulations where charge is trapped at a grain boundary, with each plot having a grain boundary in a different position.

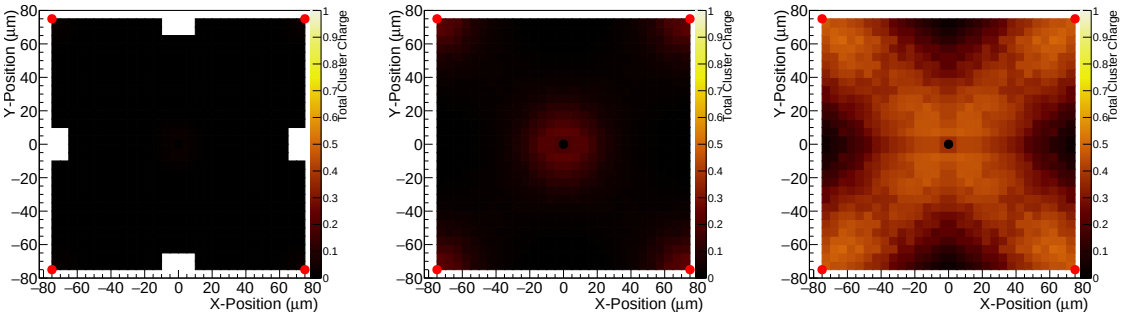

(a) $\tau = 0.01$ ns (b) $\tau = 0.1$ ns (c) $\tau = 1$ ns

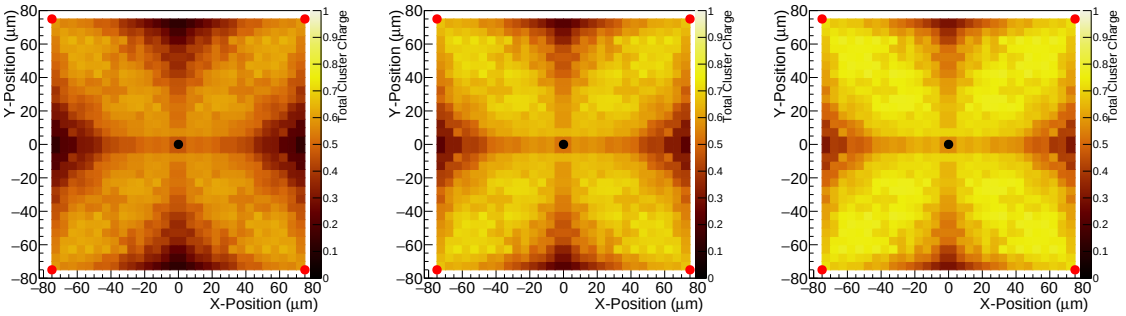

(d) $\tau = 2$ ns (e) $\tau = 3$ ns (f) $\tau = 4$ ns

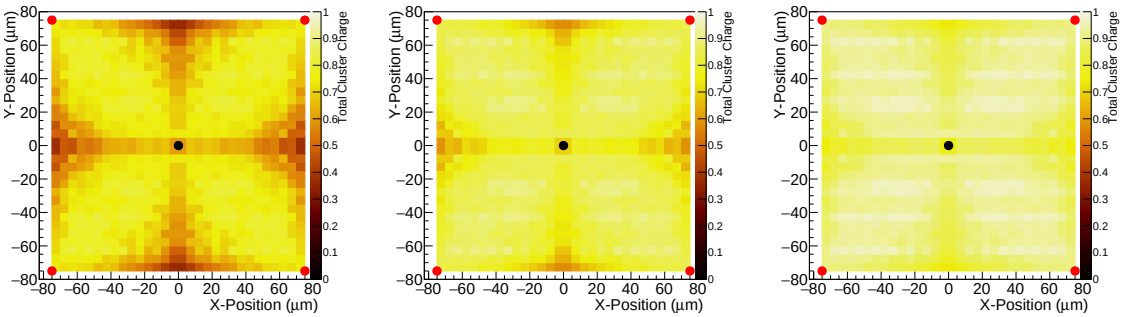

(g) $\tau = 5$ ns (h) $\tau = 10$ ns (i) $\tau = 20$ ns

Figure 5.40: Simulated charge collected as a function of position for simulations where the charge is uniformly trapped through the bulk of the material. Different plots are produced for different charge lifetimes.

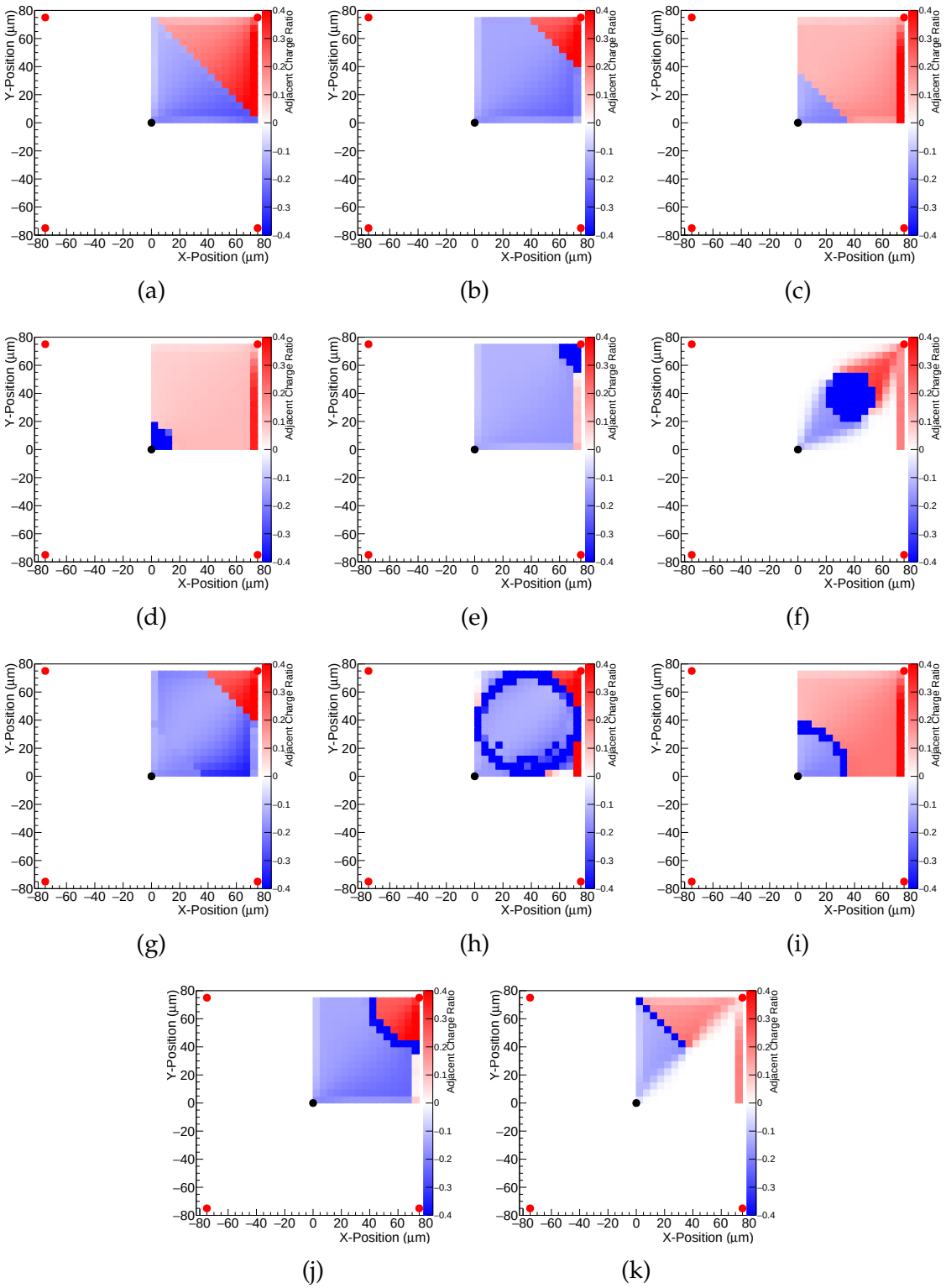

Figure 5.41: Simulated negative charge collected by the next nearest cell as a function of position for the simulations where charge is trapped at a grain boundary, with each plot having a grain boundary in a different position.

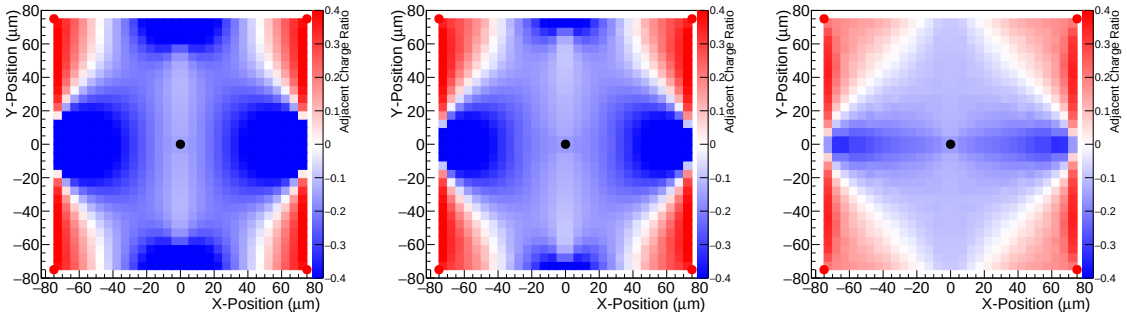

(a) $\tau = 0.01$ ns (b) $\tau = 0.1$ ns (c) $\tau = 1$ ns

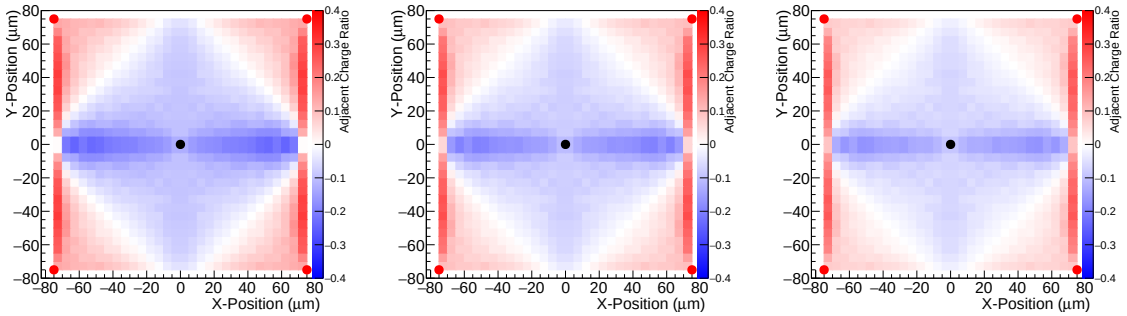

(d) $\tau = 2$ ns (e) $\tau = 3$ ns (f) $\tau = 4$ ns

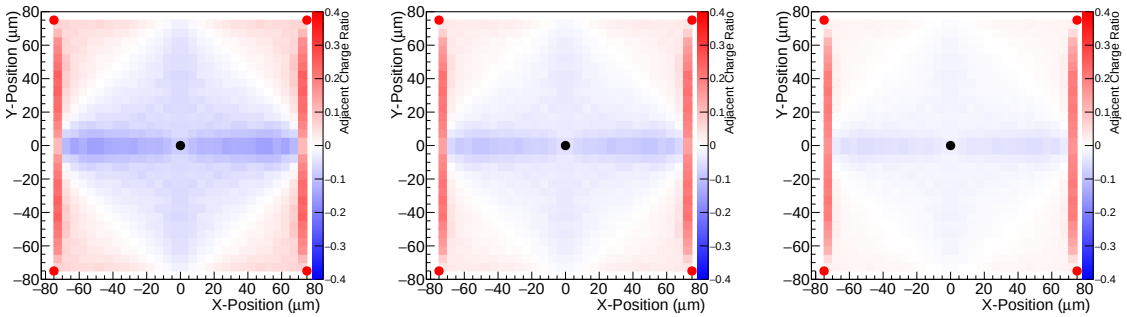

(g) $\tau = 5$ ns (h) $\tau = 10$ ns (i) $\tau = 20$ ns

Figure 5.42: Simulated negative charge collected by the next nearest cell as a function of position for simulations where the charge is uniformly trapped through the bulk of the material. Different plots are produced for different charge lifetimes.

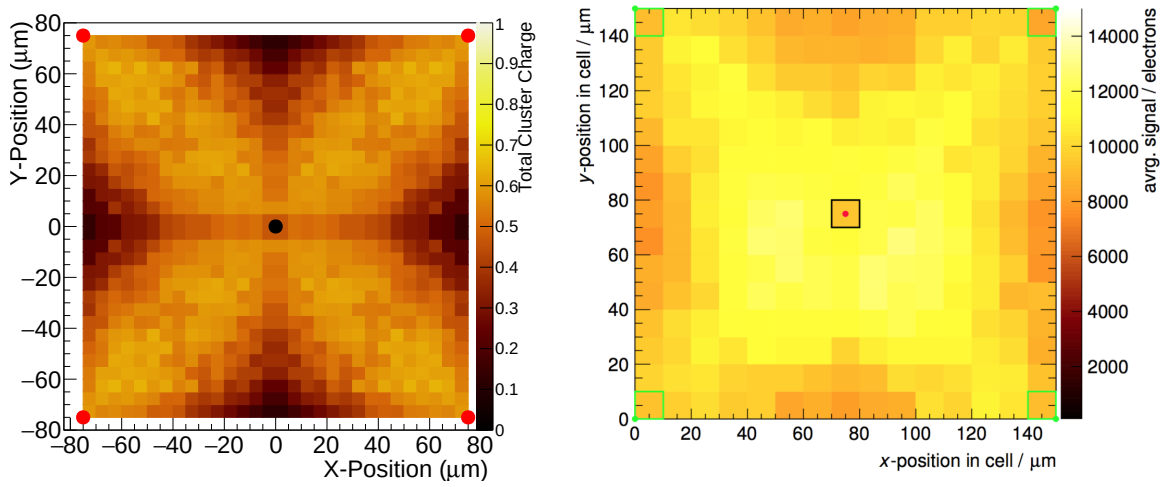

(a) (b)

Figure 5.43: Comparison between the average charge collected as a function of position within a cell from simulated charge collection (a) and the experimental data [123] (b) (for simulations with only bulk trapping and a charge lifetime of 2 ns)

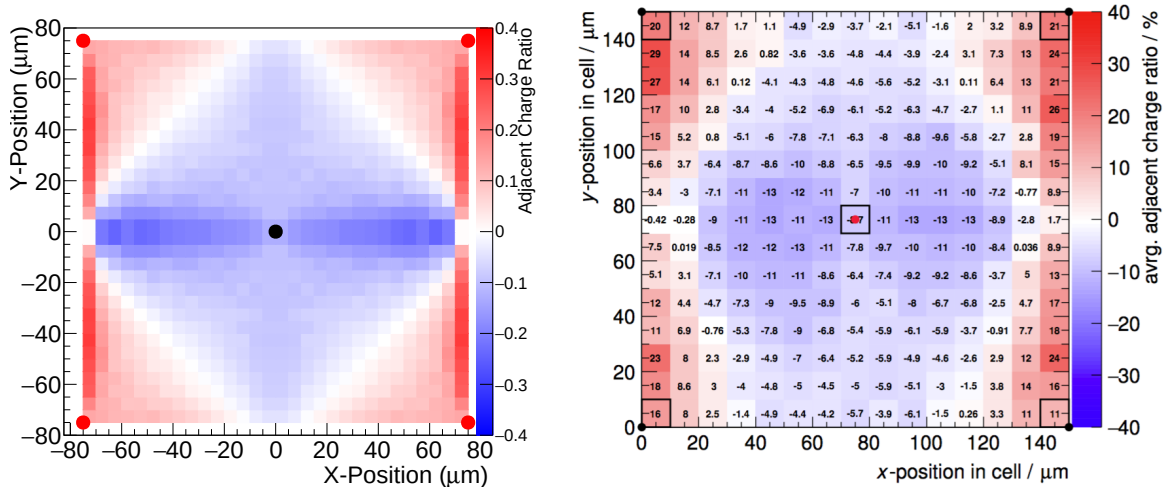

(a) (b)

Figure 5.44: Comparison of the average charge collected as a function of position by the next nearest strip in simulations (a) (for simulations with only bulk trapping and a charge lifetime of 2ns) and experimental data [123] (b)

Remarkable agreement is observed between the simulations obtained assuming that trapping only occurs in the bulk of the material, with a charge lifetime of ≈ 2 ns. It is thus possible to conclude that the average behavior 3D pCVD devices can be approximated by assuming that trapping only occurs in the bulk of the material. While this does not explain all of the features observed in the experimental

data, the agreement between the two is very good, and as the negative charge areas are visible in individual cells, it is possible to deduce that bulk charge trapping is a dominant effect. There are limitations with the simulations as they are in two dimensions so do not include the surface metalization, they assume that the lifetime of electrons and holes are equal, and they do not include the resistance of the columns; this last point in particular means that the ≈ 2 ns charge lifetime obtained from the simulations is a lower bound on the real value, which is likely significantly greater as a higher column resistance results in a higher collection time.

The simulations where charge is only trapped at grain boundaries are not in good agreement with the experimental data, although they do successfully replicate the presence of some long thin regions with a low observed charge. While the dark lines in Fig. 5.33 do have the appearance of grain boundaries, the simulations indicate that while some trapping undoubtedly occurs in these region it does not explain the observed behavior. One possible explanation for these lines is that less charge is released by a hit in those regions due to the nature of the material.

5.3.3 pCVD device conclusions

A pCVD device has been successfully manufactured and achieved a charge collection of 63.6 % if the entire signal is included or 67.2 % if only the channels with positive signals are included in the full signal definition. This is a significantly greater collected charge than was achieved with the planar device on the same substrate (35 %). Similarly to the single crystal device there were problems with the success rate of column production, but the experiments showed that if this problem can be resolved pCVD 3D diamond detectors are a good prospect for future tracking detectors.

The simulations produced to replicate the behavior of this device have been in very good agreement with the observed measurements, and from them it is possible to conclude that the main performance barrier for 3D devices is the quality of the bulk material rather than the presence of grain boundaries.

6. 3D diamond dosimetry

Several 3D diamond devices have been tested at the Christie hospital with the prospect of making 3D diamond detectors with medical physics applications in radio therapy to provide real time monitoring during cancer treatments.

6.1 Dosimetry results

One such device is a 3D pad detector with an active area of $\sim 1.5 \times 1.5$ mm^2 and columns connected by surface graphitization was produce by the Florence group. This device (shown in Fig. 6.1) was measured using the setup shown in Fig. 1.5. Full details of this measurement are given elsewhere [74].

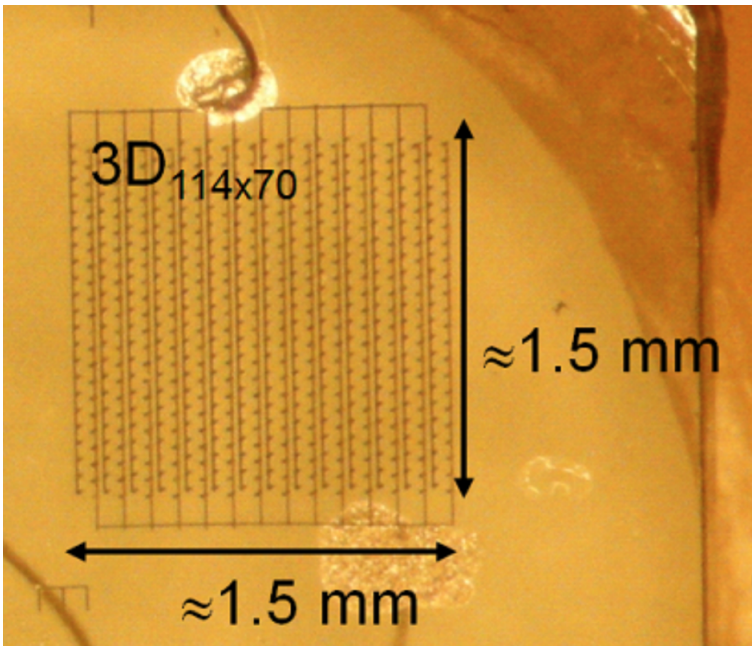

Figure 6.1: The detector used for this dosimetry measurement. This detector is made entirely of carbon, with graphitic 3D electrodes as well as graphitic channels connecting the columns in strips along the surface. All the signal columns are connected to each other in this way effectively producing a 3D pad detector.

The sample was tested with different dose rates and beam energies and the performance was compared for different bias voltages. Fig. 6.3 shows the current induced at different applied bias voltages by an irradiation with a dose rate of 585 MUmin^{-1}, where a Monitor Unit MU≈ 0.694 cGy. Fig. 6.4 shows the linear relationship obtained between the observed current signal and the applied bias voltage.

A 6 MV photon beam was used for all of these measurements; MV is the voltage used to accelerate the electrons to produce the radiation field, the energy spectrum of the photons produced by such a beam is shown in Fig. 6.2.

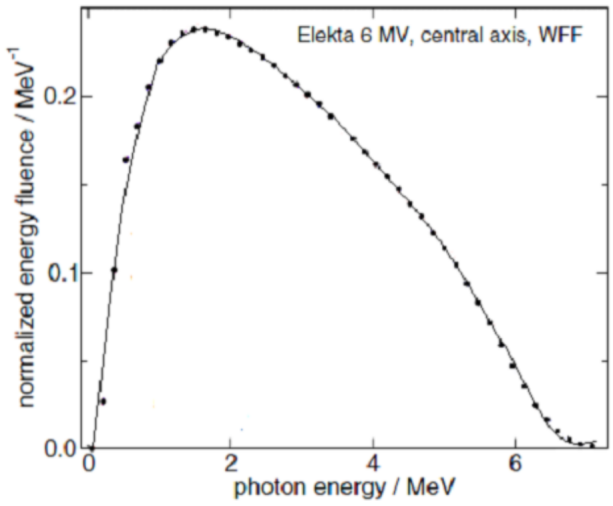

Figure 6.2: The energy spectrum of photons produced by a 6 MV beam

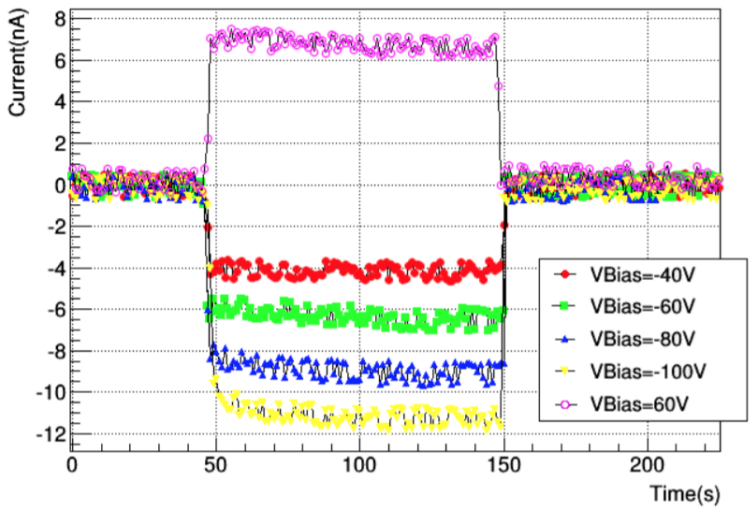

Figure 6.3: The signal induced in a 3D diamond detector at different bias voltages for a dose of 1000 MU with a dose rate of 585 MUmin^{-1} and an energy of 6 MV.

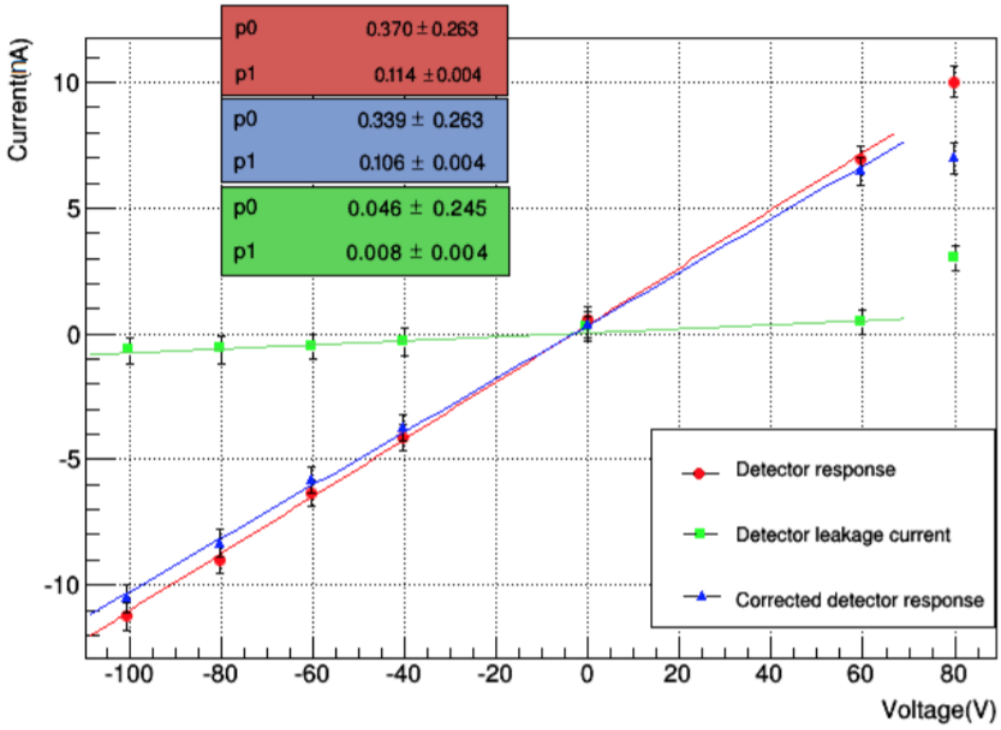

Figure 6.4: The average current induced in a 3D diamond detector at different bias voltages for a dose rate of 585 MUmin^{-1} and an energy of 6 MV. The green line represents the leakage current at different voltages, the red line is the average current observed in the device for each measurement, and the blue curve is the corrected detector response, obtained by subtracting the leakage current from the detector response.

For subsequent measurements it was chosen to operate the device at -80 V as this is a high voltage that is well within the voltage range where the voltage is proportional to the current induced. The relationship between dose and induced signal at this voltage. These plots are shown in Fig. 6.5.

Finally, an experiment was carried out to test whether the shape of the beam can be reconstructed using data obtained with a 3D diamond detector.

For this measurement a 10×10 cm^2 beam was used. The sample was placed at the centre of the beam and as before the sample was irradiated with a dose rate of 585 MUmin $^{-1}$ with a 6 MV beam at -80 V. The same measurement was then repeated a number of times after translating the sample in one direction with respect to the beam. This was then compared to the beam shape obtained with a GafChromic film [127], a film which undergoes a color change as it is exposed to radiation, allowing the measurement of the total dosage absorbed by the film. The results of these measurements are shown in Fig. 6.6-6.7.

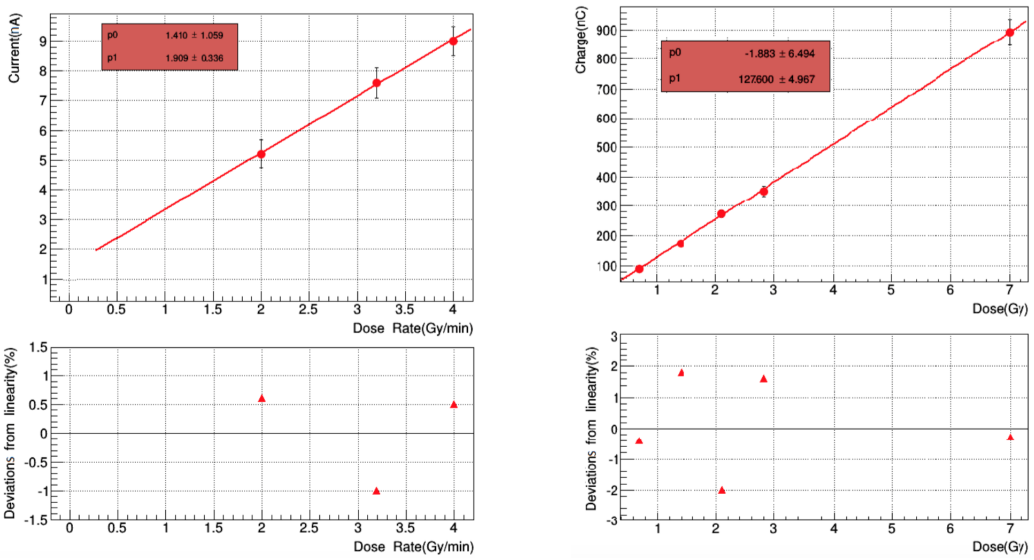

(a) (b)

Figure 6.5: The relationship between the observed signal and the dose received by the sample. The top plot in (a) shows that, as expected, there is a linear relationship between the dose rate and the current induced in the device, with the bottom plot showing the deviation of each data point from the fit line. The top plot in (b) shows that the cumulative charge collected during one of these measurements is proportional to the total dose delivered, with the bottom plot showing the residuals of these data points.

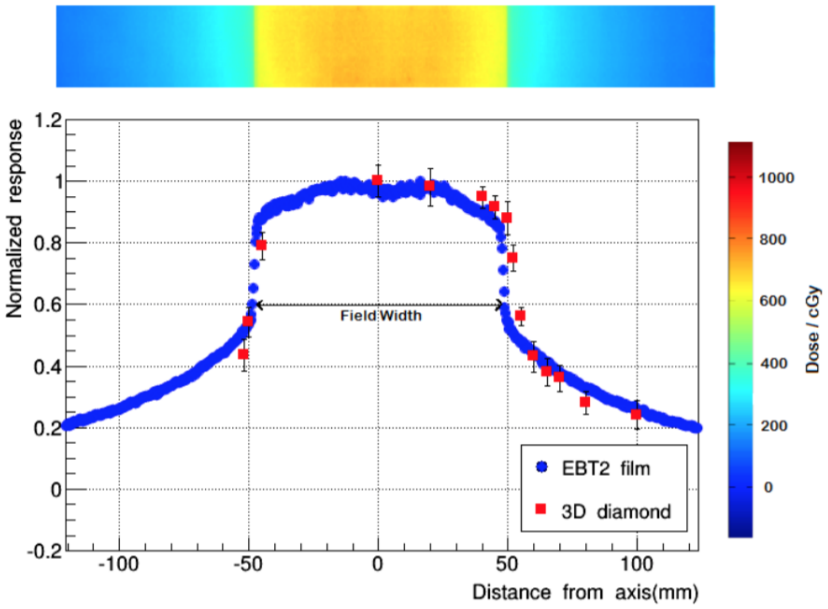

Figure 6.6: Beam profile measured by the film along with the normalized response of the detector.

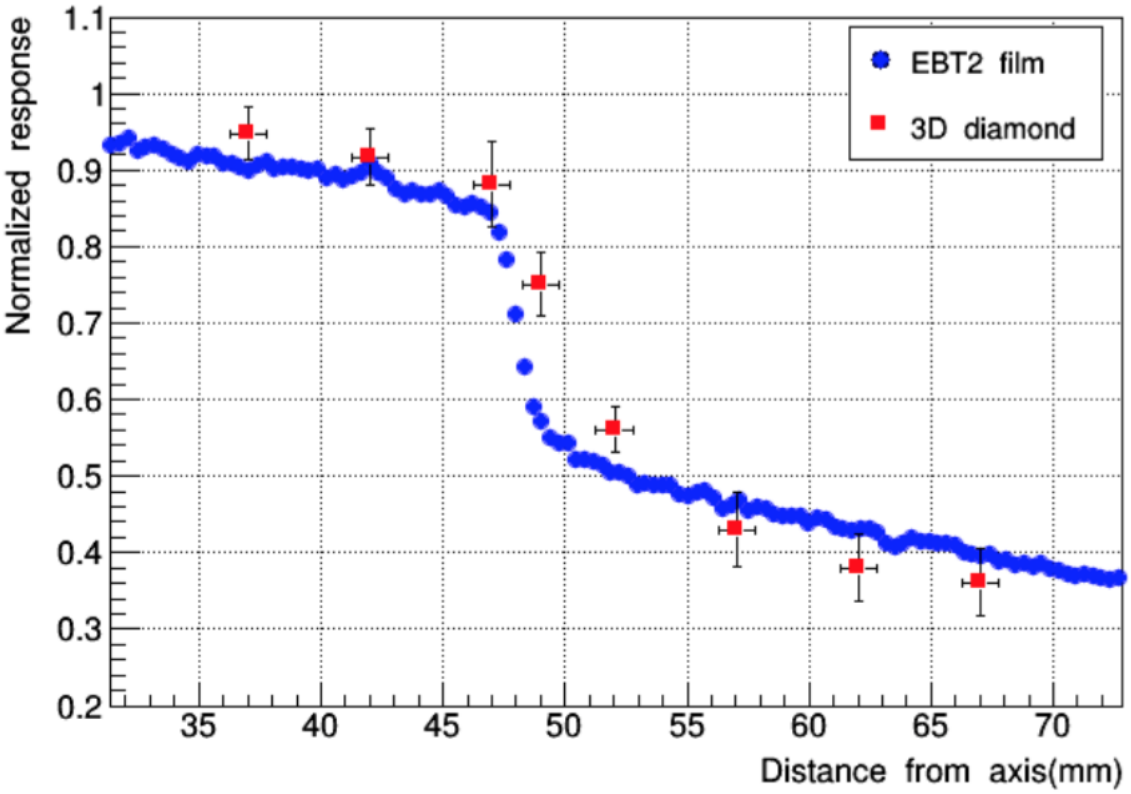

Figure 6.7: Beam profile measured by the film along with the normalized response of the detector in the penumbra region of the beam.

As can be seen from these plots the agreement between the two measurements is mostly good, however in the penumbra region (the transition region between the flat top of the radiation field, and the background) in Fig. 6.7, there is some divergence between the two measurements.

There are a number of possible explanations for this observations. One source of inaccuracy is the extent of the device. A bigger source of inaccuracy however is thought to be that the active area of this detector is not well insulated from the surrounding material, allowing it to collect charge produced at a significant distance from the graphitic array.

6.2 Dosimetry progress

To counteract both of these issues a new device was fabricated. This device (known as the Florence device, described in section B.1.5), aims to reduce the effect of both of these issues. This device consists of two graphitic arrays, in each of these arrays all the HV columns are connected as usual, however on the signal side each array

is split into three pads, with each pad surrounded by at least one ring of columns which are read out separately. The aim of this geometry is to provide a well defined active area for each pad, as the outer ring of columns would collect any charge created outside of it. The small size of each pad also helps reduce the inaccuracies introduced by the dimensions of the device. The columns were connected with a surface metalization. A photograph of this device is shown in Fig. 6.8.

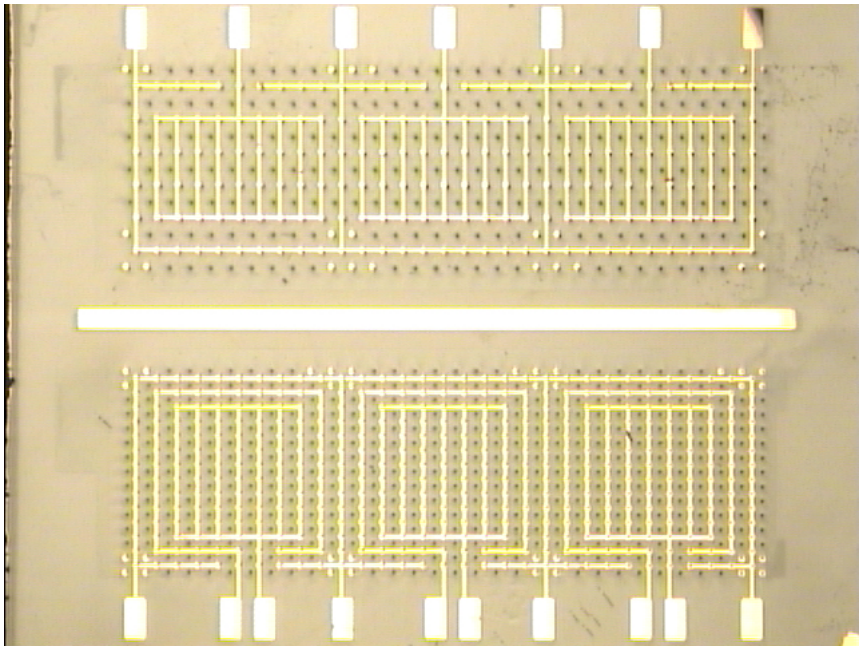

Figure 6.8: The front side metalization of the Florence sample.

As described in Appendix B.1.5, there were difficulties in the fabrication of this device, resulting in an imperfect metalization at the first attempt. The sample was measured at the Christie with this metalization with the aim of replicating and improving upon measurements made with the previous sample. Analysis of these measurements is still in progress. Since then the sample has been re-metalized and the metalization now is expected to be more stable, these measurements are to be repeated in the future with the new metalization.

7. Systematic simulation studies of varying device fabrication parameters

Before 3D diamond detectors can be seriously considered for future experimental applications, different fabrication parameters need to be tested to find the best combinations. Simulations are ideal for this task as once a good model is produced, it is faster and cheaper to tweak a selection of parameters within the model than it is to produce a large number of devices with all the different parameters and measure them using sources or test beams.

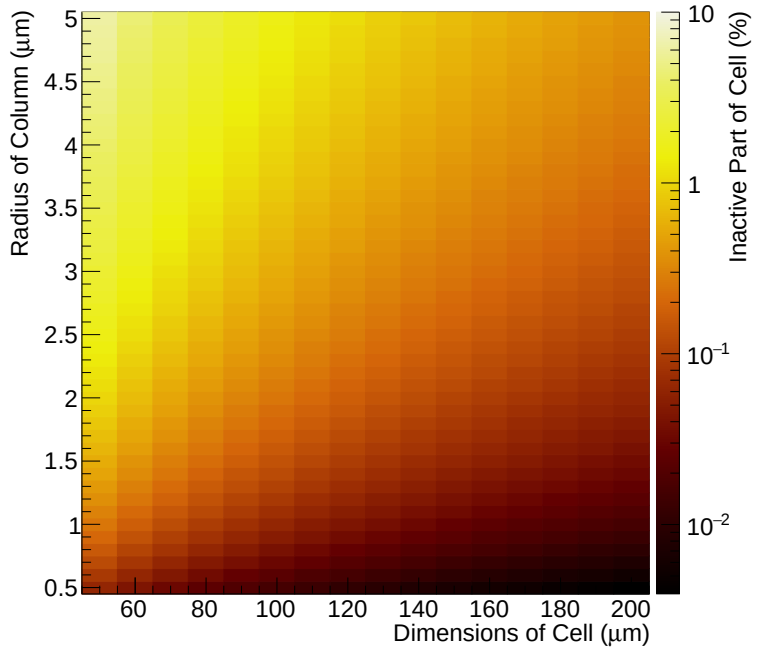

Figure 7.1: The percentage of the detector area that is inactive for different column radii and cell dimensions, assuming square cells.

Variation of the cell geometry has already been described in some detail in section 5.1.2. Further simulations were carried out to study the effect of varying the

column radius of the devices as well as the cell size. It can be expected that the ideal geometry would be small cell size, as, for equal applied electrode voltage, this would create a significantly higher electric field within the cell, as well as resulting in a smaller distance for the charge carriers to travel to reach an electrode. This would be combined with a small electrode radius: as the electrodes are not part of the active area of the device, decreasing their radius would increase the active area of the device and thus the efficiency of recorded hits, as is clearly seen in Fig. 7.1. Simulations need to be performed to understand how the variation of these parameters affects the charge collection properties of 3D diamond devices.

7.1 Varying column radius

One of the parameters that was varied in these simulations was the column radius. The model used for these simulations is the same model used for the pCVD simulations (section 5.3.2), with only bulk trapping as these simulations were deemed to provide good agreement with the experimental data. A range of five different electrode radii, ranging from 1 µm to 10 µm, were tested in these simulations using a mesh for 150×150 µm^2 cells.

The electric field produced for each electrode radius is shown in Fig. 7.2. This shows that if the electrode size is too small the radial dependence of the field causes a rapid drop off close to the electrode, resulting in a greatly reduced electric field in the low field regions of the device. As the column radius is increased, the electric field through the whole device increases, while resulting in a decrease in the active area of the device. This can be seen in Figs. C.4 and C.5 as in these cases the simulated particle hits the electrode and thus no signal is generated.

Figs. C.1-C.5 show the charge collected as a function of hit positions for different column radii; with an improvement for increased column radius due to the increased electric field within the device, however this shows that increasing column radius leads to a reduction in the device active area. As a result of this, the time taken for 90% of the deposited charge to be collected was used as a metric to determine the quality of the device. The variation in the time required to collect 90% of the deposited charge with different column radii is shown in Fig. 7.3.

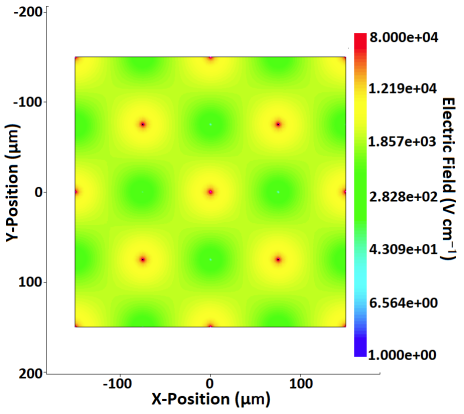

(a) $d = 1$ µm

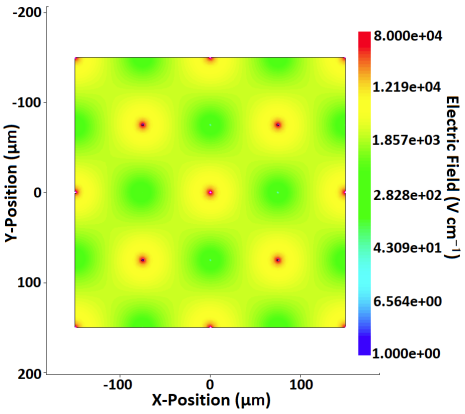

(b) $d = 2$ µm

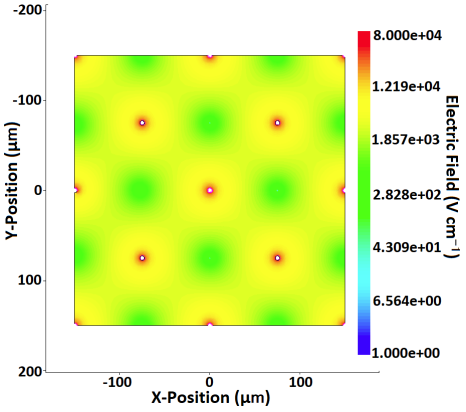

(c) $d = 5$ µm

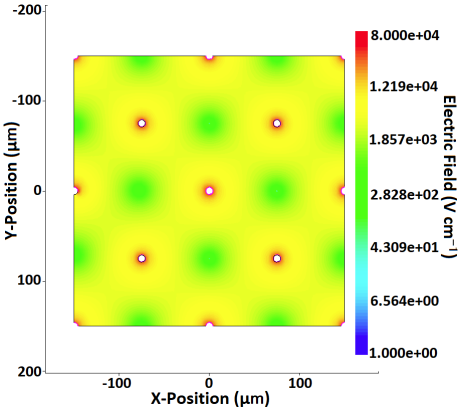

(d) $d = 8$ µm

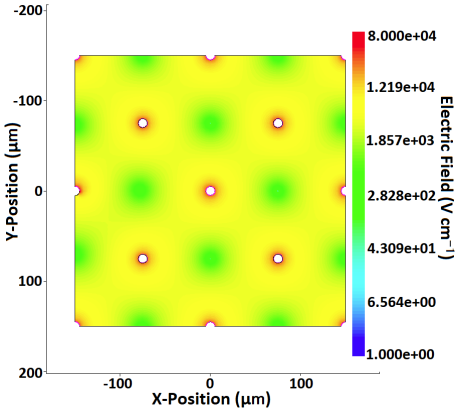

(e) $d = 10$ µm

Figure 7.2: The simulated electric field for different electrode radii at 75 V and a cell size of 150×150 µm^2.

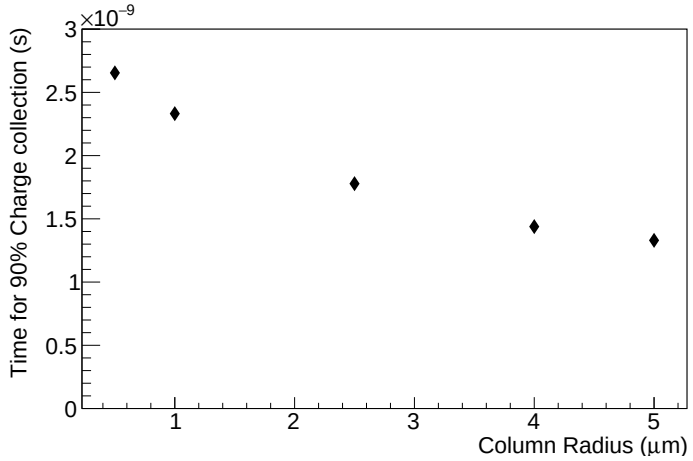

Figure 7.3: Relationship between the average time taken to collect 90% of the deposited charge throughout the cell and the column radius, for 150 µm cells at 75V.

Fig. 7.3 shows that the time taken for 90% charge collection starts to increase as the column radius is reduced due to the lower electric field in the device. In real devices this difference would be further increased due to the columns having a finite resistance. A high electrode resistance has the effect of increasing the time required for charge collection, thus columns with a lower cross section area, resulting in a higher resistance, would result in even slower charge collection. It was not possible to include the effects of column resistance in these simulations.

A column radius of ~ 2.5µm was a good compromise between minimizing the inactive area and minimizing the charge collection time. This column radius was used for the following set of simulations studying varying cell dimensions.

7.2 Varying cell size

Simulations were carried out to determine the effect of varying cell size on the collected cluster charge. The column radius used for these simulations was 2.5 µm with three different cell dimensions: 50×50 µm^2, 100×100µm^2 and 150×150 µm^2 with varying voltage. The results of the simulations for 150×150 µm^2 cells at 75 V have already been shown in Fig. C.3.

Fig. 7.4 shows the electric field of the 150×150 µm^2 cells with a 2.5 µm column radius and 75 V as well as similar plots for devices with cell dimensions of 100×100 µm^2 and 50×50 µm^2 and voltages of 25 V, 50 V, and 75 V.

Figs. C.6 - C.11 show the total measured cluster charge for different voltages, charge lifetimes and cell dimensions, and with a constant column radius of 2.5 µm, while Fig. 7.5 show the time to reach 90% charge collection as a function of voltage

for different cell dimensions.

These plots show that by reducing the dimensions of the cell, the average electric field in the cell will greatly increase while the electrode separation is decreased, allowing for charge carriers to be collected significantly faster even with lower bias voltages. Fig. 7.5 shows that using 50 µm cells results in a reduction of almost an order of magnitude in the time required for 90% charge collection when comparing 50 µm cells to 150 µm cells, even if the voltage is reduced from 75V to 25V. Thus if detectors with 50 µm can be successfully produced and operated, the performance will improve significantly.

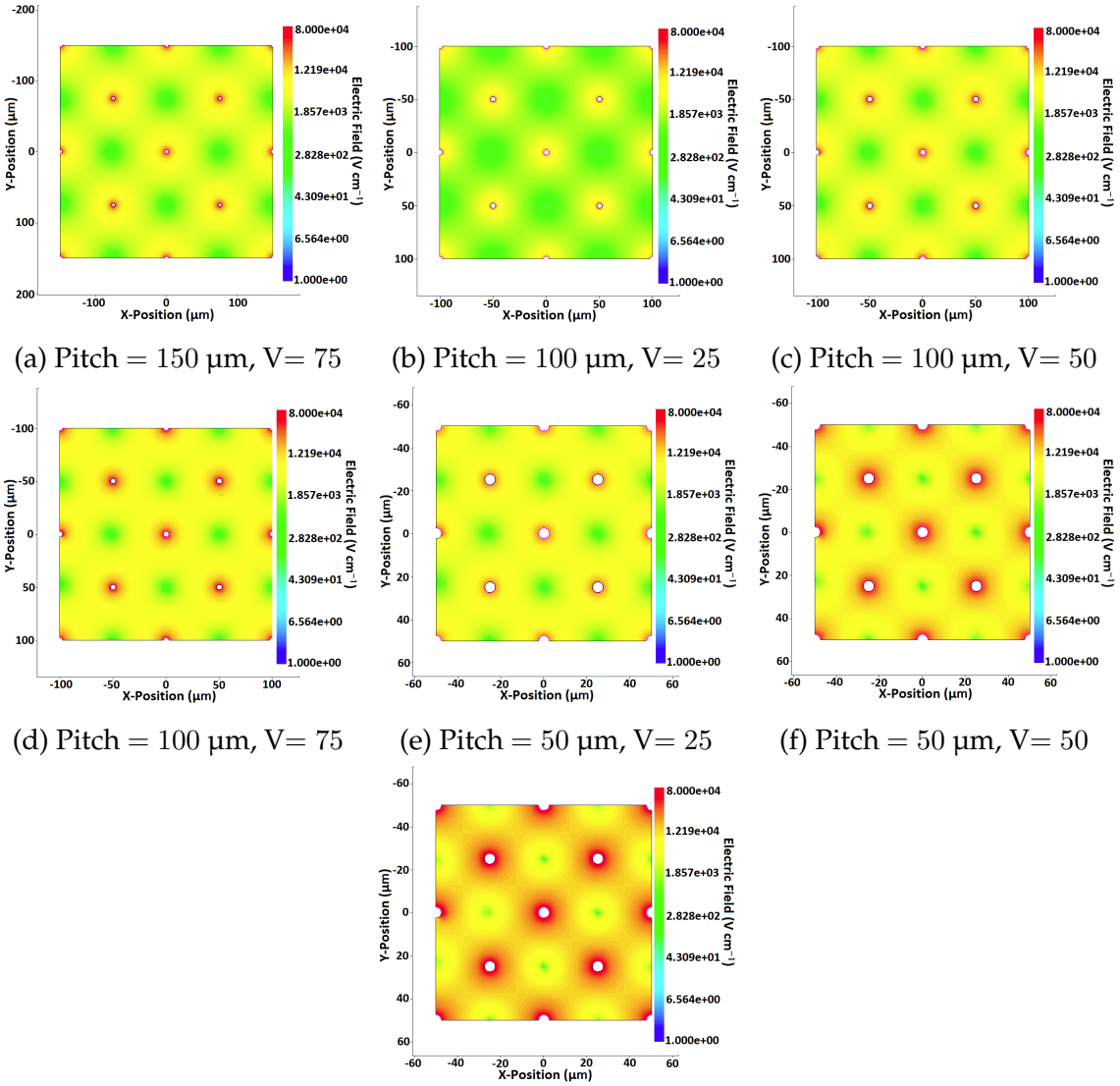

(a) Pitch $=$ 150 µm, V$=$ 75 (b) Pitch $=$ 100 µm, V$=$ 25 (c) Pitch $=$ 100 µm, V$=$ 50

(d) Pitch $=$ 100 µm, V$=$ 75 (e) Pitch $=$ 50 µm, V$=$ 25 (f) Pitch $=$ 50 µm, V$=$ 50

(g) Pitch $=$ 50 µm, V$=$ 75

Figure 7.4: Electric field of the simulated devices with a column radius of 2.5 µm

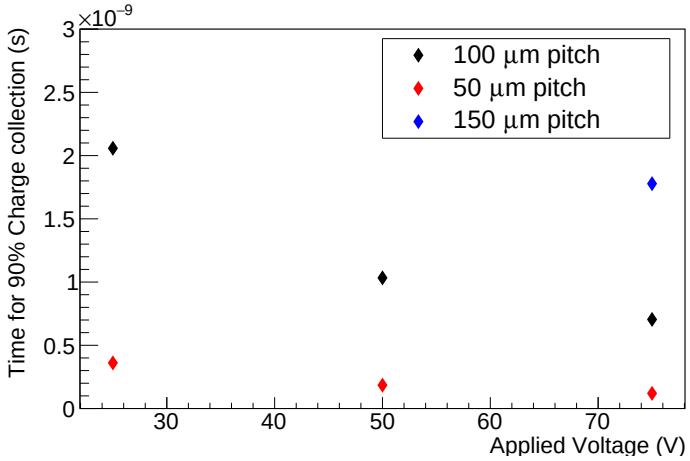

Figure 7.5: The relationship between the applied bias voltage and the time to achieve 90% charge collection for a column radius of 2.5 µm and 3 different cell dimensions

8. Irradiation studies

For 3D diamond detectors to be used in High Energy Physics experiments, it is necessary to prove that they are more radiation tolerant than the alternatives. In theory, 3D diamond combines the radiation hardness of a 3D geometry, which has been successfully used to increase radiation resistance in silicon, with the use of diamond as a detector material, which is inherently more radiation resistant. There are however some issues which are as yet unknown with this technology: chiefly, what are the effects of irradiation on the columnar electrodes in the bulk of the material.

8.1 Measurements of the irradiated sample

To investigate the effects of irradiation on the resistance of the columns a new device was manufactured in Oxford using a 400 µm thick, scCVD, optical grade diamond obtained from IIa [63], with 4 arrays of columns, with 2 different column radii of 1.1 µm and 1.4 µm.

The I-V curves of a subset of the columns were measured, after which the device was irradiated with 4×10^{15} protons cm^{-2} at the CERN Proton Synchrotron, after which the resistance of the same columns was measured again. The columns were manufactured through the entire ≈ 500 µm thickness of the diamond with a small 12×12 µm^2 pad on each surface reaching a depth of < 5 µm as this sample was not going to be used as a detector, and the extra area would make the measurement significantly simpler. A diagram of the device is shown in Fig. 8.1 while a photograph of the device is shown in Fig. 8.2. There were attempts to deposit a metalization on the device, however the process failed, leaving only a partial metalization, and due to time constraints on the availability of beam time it was not possible to repeat the process before the irradiation.

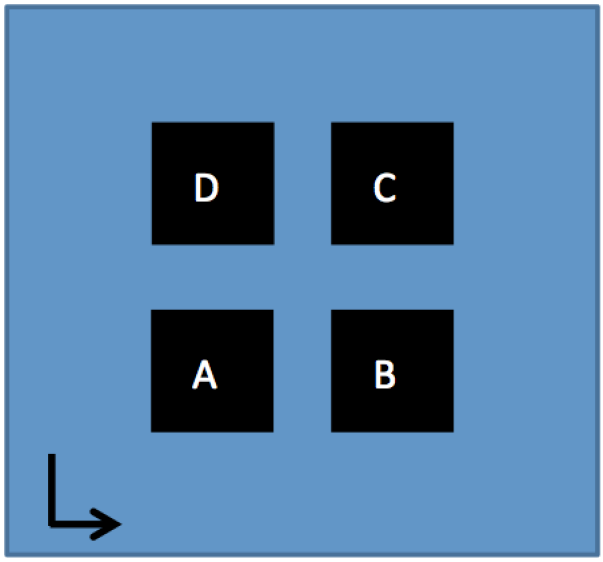

Figure 8.1: The relative position of the 4 arrays on the device, arrays A and B had a column radius of 1.1 µm while arrays C and D had a column radius of 1.4 µm. The arrow in the lower left structure is a graphitic structure fabricated within the diamond as a reference point and to allow to easily distinguish the sides of the diamond as well as the arrays.

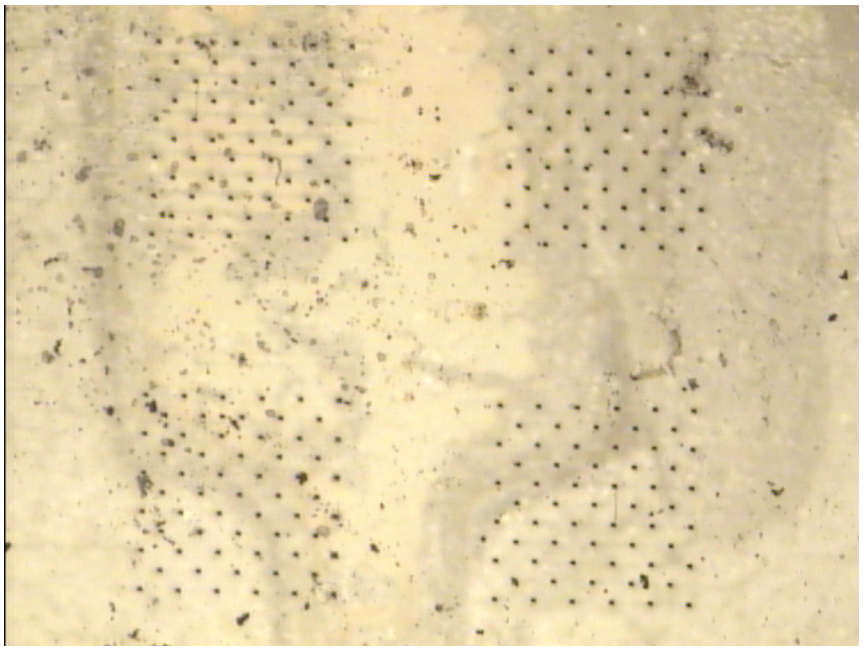

Figure 8.2: Sample used for these measurements, the arrays shown are, clockwise from top left: C, D, A, B.

To measure the resistance of the columns the sample was attached to a PCB using a conductive glue to contact one side of the columns. The resistance of the columns was then measured by probing individual columns and measuring their

I-V curves. For most columns the relationship was not linear (as shown in Fig. 8.3), this implied that a certain turn on potential needed to be overcome for the current to pass through the columns. This problem is described in more detail in Section 9.5. This phenomenon was not well understood before irradiation, and as a result of this it was not possible to extract accurate values for the pre-irradiation resistance of the columns as the I-V measurements did not overcome this potential.

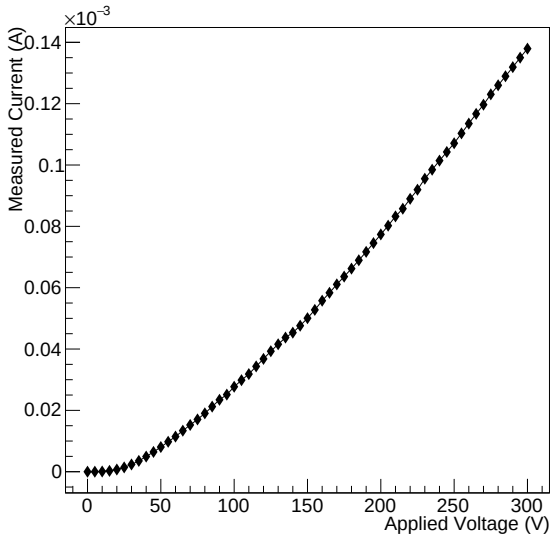

Figure 8.3: Typical IV curve of columns after irradiation. The non-ohmic section of the curve is due to a barrier potential. A discussion of this phenomenon is presented in section 9.5.

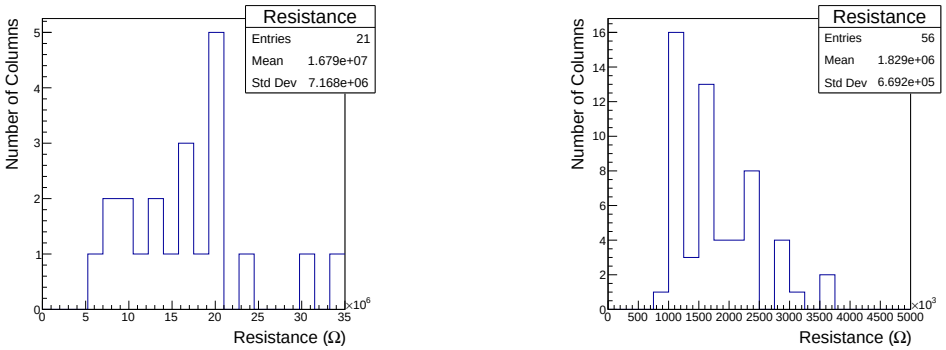

(a) Column Radius $= 1.1$ µm (b) Column Radius $= 1.4$ µm

Figure 8.4: Post irradiation resistance of the columns with the two different radii.

Fig. 8.4 shows the resistance of the measured columns. For the columns with a radius of 1.1 µm the post irradiation resistance is (16.7 ± 7.2) MΩ, and for the

columns with a radius of 1.4 µm the measured post irradiation resistance is (1.83 ± 0.67) MΩ.

These results are very promising as they show that the resistance of the columns remains low even after irradiation, suggesting that this is not a limiting factor with regards to detector performance. It is impossible to make quantitative conclusions at this stage however as it is not possible to get a good comparison to the pre-irradiation data. This would be required to see whether the columns do degrade over time.

9. Outlook

Further measurements are currently under way to drive forward the development of 3D diamond detectors; there are a number of different avenues currently under investigation:

- The column fabrication process needs some further refinement to find the optimum fabrication parameters and to make the process easily reproducible with different setups.
- Work is still being carried out to understand which geometry provides a better performance.
- To make the production of large area devices feasible in the future, the speed of the laser process must be significantly increased.
- 3D diamond devices must be tested in real experiments to understand if they can survive in these hostile environments while still providing useful data.
- If 3D diamond devices are to be used as pixel detectors it must be proven that they work after being bump bonded to a pixel chip.
- If 3D diamond detectors are to be used in future, they must be compatible with the hardware that will be used in future upgrades.

Work is currently ongoing in each of these areas to address all these issues.

9.1 3D devices tested in experiments

Before 3D diamond devices can be used as tracking detectors in HEP experiments, it is important that they are tested in such an environment to see if they work well, behave in a stable manner and can survive the required radiation dose.

Two devices were produced using ≈ 500 µm thick, electronic grade scCVD obtained from E6 [61], with the purpose of proving that 3D diamond is a viable technology by being used as part of the CMS BCM. One goal of these devices was also to compare the column fabrication processes performed in Manchester and Oxford.

As such, one sample was graphitized in Manchester, the other in Oxford, both were subsequently metalized in Manchester and then inserted into CMS.

These devices are described in more detail in Appendix B.2.1 and B.2.2; Fig. 9.1 shows an image of one of these samples.

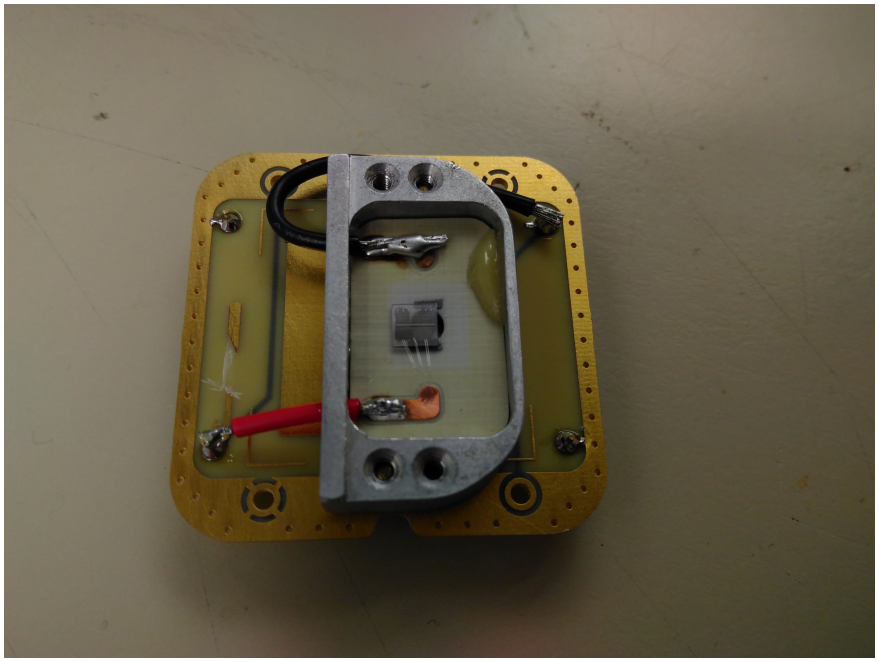

Figure 9.1: One of the samples before being placed in the CMS experiment.

Each sample has a selection of six 3D pads, with two different pitches. Due to hardware limitations it was possible to only connect one pad from each diamond. For the Oxford diamond one of the pads with the small pitch was connected, whereas for the Manchester diamond one of the pads with the larger pitch was connected.

The diamonds have been installed in the CMS experiment at the start of 2017, and have been running at 45V, preliminary results are promising with the diamonds operating stably over long periods of time and producing a current signal dependent on the luminosity, however the stability of these devices needs to be tested for longer periods of time, and their performance still needs to be calibrated.

9.2 Geometry studies of pCVD devices

Section 5.1 already describes some geometry studies that were performed on scCVD material. This indicated that a hexagonal geometry performs better than a square geometry; however more work is still needed, particularly to study what effect the

different geometry has in pCVD material.

For this purpose the 3D pCVD device was manufactured (described in section B.1.8). This device consists of a graphitic array with three different sections, containing square, rectangular and hexagonal cells. Adjacent to the 3D array there are also a 3D phantom device and a planar strip device as described previously to provide control measurements for the performance of a planar device made of the same material, and the effect of the surface metalization.

The sample was measured during a test beam in 2016 and analysis of the data obtained is still ongoing [128] and will not be discussed in detail in this thesis, however preliminary results agree with the results from the scCVD device suggesting that the hexagonal geometry provides the best performance.

9.3 Production of large area detectors

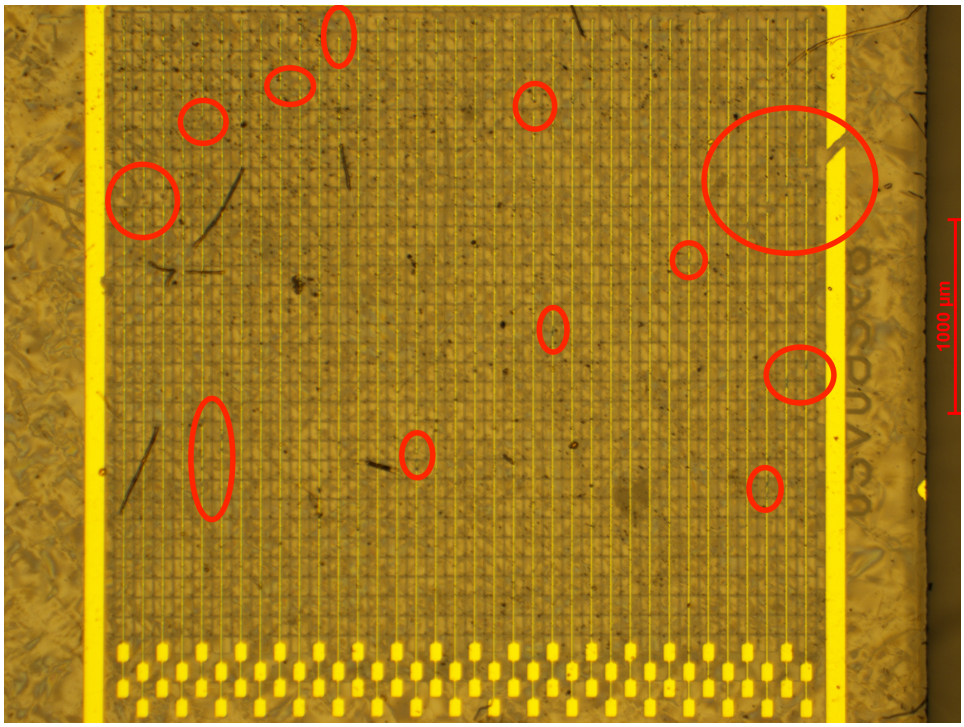

Figure 9.2: The front side metalization of the large area 3D strip detector. The regions with suspected breaks in the metalization have been highlighted.

Most semiconductor tracking detector applications in HEP require detectors that can be manufactured on a scale such that they can cover a large area, while the detectors discussed so far have a small active area with a relatively low number of columns.

A new device was built with the aim of producing and testing a sample an order of magnitude larger and with an order of magnitude more columns than previous devices. This device, described in Appendix B.1.9, consisted of a polycrystalline diamond with a thickness of ≈ 455 µm active area of 3.6×3.2 mm^2, which is almost an order of magnitude greater than previous samples. Each cell had a 100 µm pitch leading to a total of 1152 cells for the device.

The device was laser processed in Oxford and subsequently metalized in Ohio. Due to some suspected surface impurities a number of breaks were present in the metalization. The metalization on the surface of this sample is shown in Fig. 9.2.

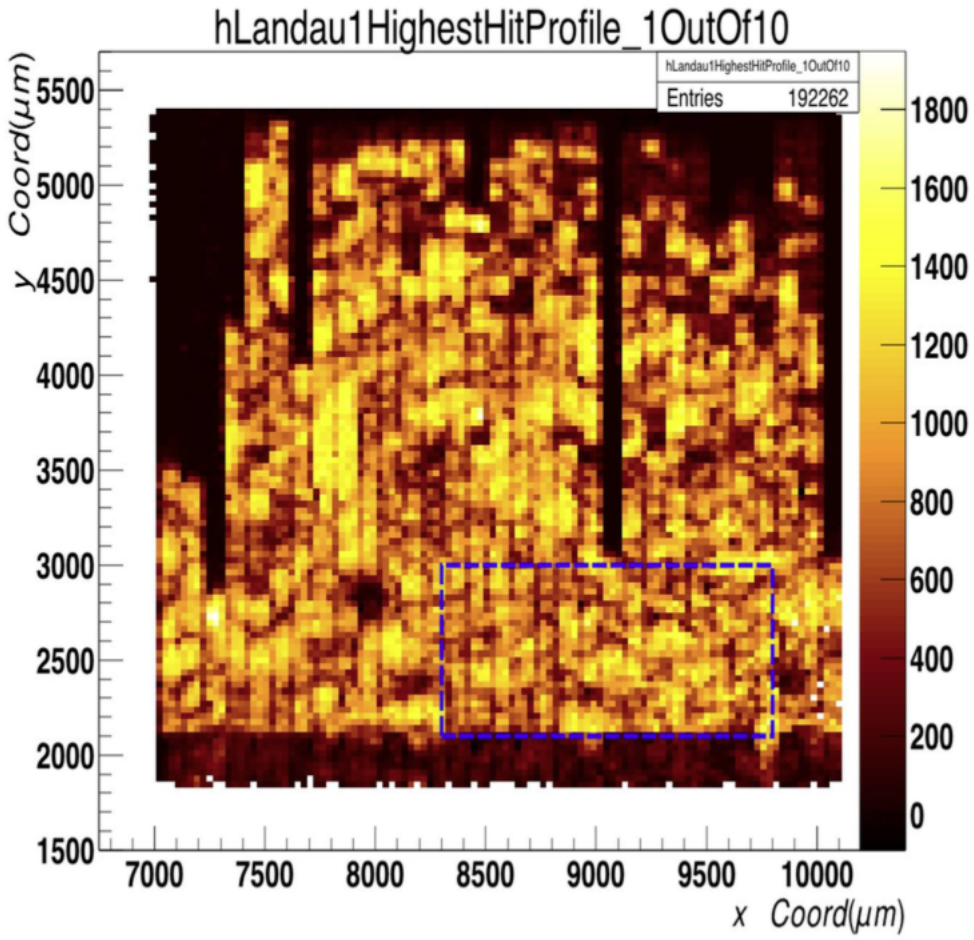

Figure 9.3: The charge collected as a function of hit position in the large 3D strip device [95].

The sample was subsequently measured at a test beam at CERN and the charge collected as a function of hit position was plotted as shown in Fig. 9.3. While non-uniformities due to the crystal structure remain, there is no evidence of significant problems with column connectivity, with the dead areas being explained either with breaks in the metalization or suspected cracks in the diamond (shown in Section

B.1.9). The breaks in the metalization appear to be due to surface impurities introduced due to mishandling of the sample. Since the production of this sample steps have been taken to reduce the occurrence of these errors.

A subsection of the device with no obvious defects was then chosen for further analysis. This section is highlighted in blue in Fig. 9.3. This section consisted of an area of 135 cells; analysis of the data from this region is still ongoing and will not be discussed in this thesis, but preliminary results indicate that within this region $\sim 85\%$ of the generated charge was collected, which is the highest ever such measurement for pCVD material of this thickness. The high charge collection was due to a number of factors, chiefly the reduced cell size compared to previous devices and the higher applied bias voltage that this device was able to take due to improvements made in the device fabrication process.

9.4 3D diamond pixel device production

Once the large area detector was build, the next step was to produce the first 3D diamond pixel detectors. For this purpose, two 3D sensors were prepared; one compatible with the CMS ROC, the other with the ATLAS FE-I4 chip.

9.4.1 CMS pixel device

The 3D diamond CMS pixel device (described in Appendix B.3.1) was the first device to be produced. To be compatible with the readout chip, the columns were fabricated to produce 100×150 µm^2 cells, with an active area of 3.1×3.0 mm^2, resulting in 620 pixels. The sample was measured in a test beam at the Paul Scherrer Institut. A continuous area of the device covering an area of 270 pixels was chosen for further analysis; only four of the pixel in this region were dead, which is a vast improvement on the success rate of the previous devices, this is also helped by the fact that if there is a break in a strip device the whole strip can break, whereas in a pixel device it would only affect one pixel.

It was then possible to calculate the hit detection efficiency of this device, with a preliminary result (including the dead cells) of $\approx 96\%$ efficiency, as shown in Fig. 9.4. However these are still preliminary measurements, since then the sample has been attached to a different chip with more optimized settings and further test beam campaigns and analysis are still ongoing.

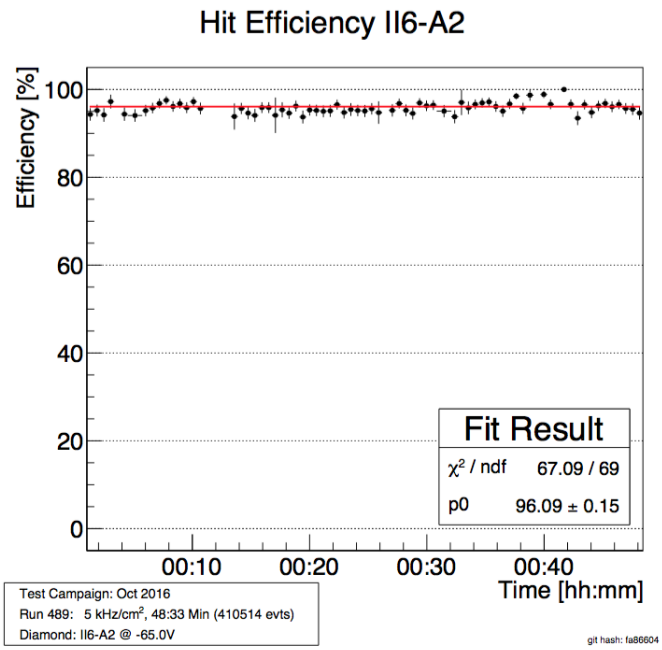

Figure 9.4: The tracking efficiency of the 3D diamond device [95].

9.4.2 ATLAS FE-I4 pixel device

A sensor compatible with the ATLAS FE-I4 chip was also prepared, this one also with the intention of testing two different cell geometries (square and hexagonal). A detailed description of this sample is given in Appendix B.3.2. After the column fabrication, a number of cracks and other defects were discovered in the sensor, this required the production of a new photolithographic mask designed to avoid these damaged area of the sensor (described in section A.2.3). This caused a delay in the production of the device, however it is currently in the process of being bump bonded, and will be available for test beam measurements in the future.

9.5 Improving the column fabrication process

For 3D diamond devices to be used in physics experiments it is necessary to further understand and improve the fabrication procedures. A number of studies have been performed, including studying the composition of columns fabricated using different parameters using the Göttingen sample [87] described in Appendix B.1.4 and studies aiming to improve the column fabrication success rate performed on the Manchester sample described in Appendix B.1.3 [86].

More recently the column quality has been improved significantly using a spacial light modulator (SLM) [89], allowing the production of columns with several

orders of magnitude lower resistance and with tunable dimensions to below 1 µm.

The SLM is a liquid crystal pixel device that alters the properties of a beam incident on it, in a way that can be tuned to produce the desired beam. One problem that occurs when shining a laser into diamond is that, due to the high refractive index of diamond and the different angle of incidence of the laser light into the diamond, the focal point is smeared in the direction parallel to the beam by differing amounts dependent on the depth of the focal point within the diamond, as shown in Fig. 9.5. This means that the the property of the material in the columns can vary as a result of the depth of the diamond, as the energy density at the point where the transition occurs in not uniform. The SLM can account for this by using the appropriate pattern to alter the properties of the beam as the focal point traverses the diamond, allowing a more reliable production of columns with consistent properties for their whole length. This is achieved by ensuring that the focus of the laser remains uniform for the entire length of the column by continuously altering the pattern as the sample moves through the focus.

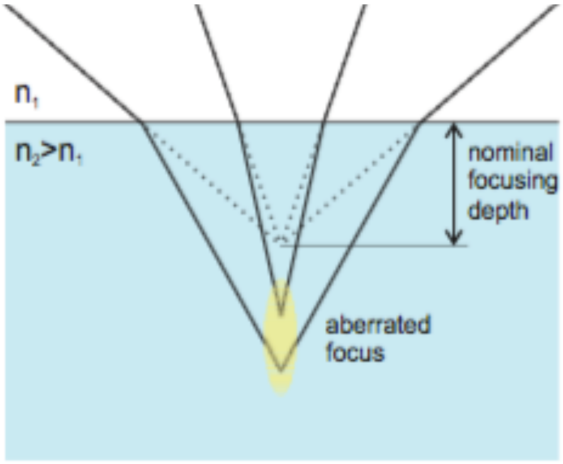

Figure 9.5: The effect on the focal point of the laser to the refractive index of diamond [90].

It was observed that columns produced using this technique are not always ohmic at low applied voltages. A possible explanation for this effect is that, due to smaller dimensions of the focal point in this case and the time between laser pulses, the column is not a continuous structure, but rather a line of graphitic dots separated by layers of diamond that act as a barrier. Early work on understanding this is in agreement with this explanation, however more comprehensive studies need to be carried out.

One of the major problems facing 3D diamond devices is the time taken for manufacture, with columns produced individually, each taking $\sim 10 - 30$ s to produce.

As a result of this, devices with 50×50 µm^2 cells and $\sim 3 \times 3$ mm^2 active area as described in Section 9.6, which contain ~ 7000 electrodes will take several days. If it is desired to produce tracking detectors covering a large area in future the problems with this manufacturing procedure become apparent. Future work will therefore focus on trying to increase the speed of the process as well as improving the reliability. One way to achieve this is to split the beam in order to produce a large number of columns in parallel rather than individually, however work has not yet begun on the development of this procedure.

Alternative approaches are also being considered to overcome this problem by moving away from laser processing. One way to do this would be through reactive ion etching, producing a hole in the diamond and then filling it with a conductive material. The advantage of this process is that all the columns will be produced simultaneously, and with the right material the electrodes will have significantly lower resistance values, however the electrodes produced with this technique will have a significantly larger diameter which would greatly reduce the percentage of active volume of the devices, particularly with small cell dimensions [129].

9.6 Future device production

As the LHC experiments will move towards higher luminosities, especially with the HL-LHC, it is desirable for the precision of the trackers to improve. As such, the possibility of 50 µm^2 pixels is being investigated for future upgrades [130]. It was therefore decided that the next step in the development of this technology should be to reduce the cell dimensions to 50 µm. To this end a number of masks have been designed to fabricate detectors with 50 µm cell dimensions (described in Appendix A.3). Masks have been designed for both 3D strip and 3D pixel devices. The pixel devices are designed to fit the current CMS ROC and ATLAS FE-I4 chips which do not have 50 µm pitch and therefore have the signal electrodes of several cells connected together to form micro-strips for the ATLAS chip design (Appendix A.3.2) and micro-pads for the CMS chip design (Appendix A.3.3). Manufacture of these devices has begun, with a 50 µm pitch pixel device based on the CMS ROC having been built and currently being studied. It is too early however to understand its performance.

10. Conclusion

In the last few years, great progress has been made on the development of 3D diamond detectors. A large number of 3D diamond devices have been manufactured and tested at a large number of different test beams contributing to an array of positive results.

A number of single crystal 3D diamond devices were tested in different environments to prove the viability of this technology. The Manchester device, is a simple 3D diamond device, was measured at both Diamond Light Source (DLS) and Ruđer Bošković Institute (RBI), achieving a charge collection of $\sim 100\%$ at 5 V. The data from these measurements was used to test a diamond model produced for TCAD, and good agreement between model and data was found. Another single crystal device was measured at RBI with both square and hexagonal cells. The results from this indicate that charge is collected more rapidly in hexagonal cells than square cells, however the results from this are not yet conclusive. More recent preliminary results on a polycrystalline device with the same geometry also support this conclusion.

Another single crystal device was tested at CERN. This device had three different detectors on it: a planar device, a 3D device, and a 3D phantom device, allowing a comparison of the three devices. TCAD simulations were used to study the charge collection in this device. They were able to successfully reproduce and explain the phenomena observed, including anomalies due to broken columns originating from problems in the fabrication process. The performance of the 3D device and the planar device were compared and the performance of the 3D device was found to match the performance of the planar device with an applied bias voltage an order of magnitude lower.

A device with the same geometry was manufactured using polycrystalline diamond to test the viability of using this material for 3D devices due to its lower cost and the larger substrate area available. In this sample the 3D device was found to collect $\approx 60\%$ of the charge, which is significantly higher than for the planar device. Simulations were also carried out to try and reproduce polycrystalline material and

the simulations were found to be in good agreement with the experimental data.

Once the TCAD model was verified using experimental data, it was possible to simulate devices with different fabrication parameters to find the optimal set of parameters for future devices. These simulations found that reducing the cell dimensions increases the charge collection due to the higher field within the cell. It was also found that columns with smaller radius reduce the collected charge. Hence, in future devices, with cell dimensions of ≈ 50 µm to ≈ 150 µm, the optimum column radius is ≈ 2.5 µm.

The development of these devices has also allowed us to carry out the first tests of 3D diamond as a technology for medical dosimetry with positive results. A 3D device was tested using a radiotherapy machine at the Christie hospital and a linear relationship between the dose rate and the current induced in the device was found. The device was also used to successfully measure the beam profile. New devices are under development with a geometry purposely designed for this application.

Tests have also started to determine the radiation tolerance of 3D diamond devices. One such test is reported in the thesis. After irradiation, the resistance of the electrodes of a 3D diamond device was found to be low enough that it would not affect the operation of such a device.

These results have allowed the development of these devices to move forward and a number of new devices are currently being produced or tested. Two 3D diamond devices have been produced and are being tested as beam monitors in the CMS experiment, verifying whether these devices can operate in the high radiation environment of particle physics experiments. Pixel devices have also been produced, with preliminary measurements indicating that they are working well, with a very high efficiency $\approx 96\%$ with a very small fraction of broken cells. This has been made possible by the recent advances in the fabrication techniques of 3D diamond devices, greatly reducing the number of missing columns in in the most recently produced samples.

A. Mask design

Section 3.4 describes the metalization process required to produce contacts on diamond devices. To produce the finely structured metalization required to operate these devices, masks suitable for photolithography have to be produced. The masks generally consist of a glass slab with a thin layer of chrome on one side, the chrome has gaps on it to allow the UV light to pass through. The masks used for the work described in this thesis were produced industrially by JD-Photodata [131] after a CAD design of the required metalization pattern was designed. A number of masks for 3D devices were produced as part of the work detailed in this thesis for different applications; these are described in the following sections.

A.1 Mask designs for generic devices

A number of generic masks were designed to test the viability of 3D diamond detectors. The purpose of detectors manufactured using these masks range from testing different column fabrication parameters, testing different device geometries and the viability of 3D diamond devices for different applications.

A.1.1 Batch 2 mask

The Batch 2 mask (shown in Fig. A.1) is a mask used to produce some of the early 3D diamond devices. The purpose of these devices was to provide a proof of principle of the 3D diamond technology by building three detectors on the same diamond, a 3D detector, a strip detector and a 3D phantom detector. The 3D and the 3D phantom were kept at the same voltage as each other by connecting together their bias metalization, allowing the strip device to operate at a different voltage. This allows for the direct comparison of both planar and 3D devices at operating voltages, while also studying the effects of metalization only with the phantom device.

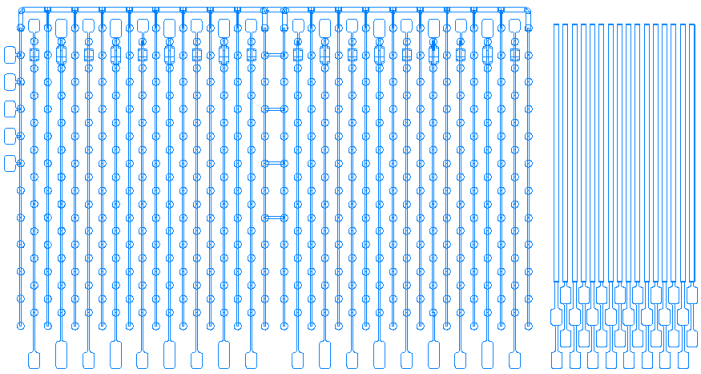

Figure A.1: The Batch 2 mask. This masks contains three separate detectors; a strip detector on the right, a 3D detector on the left and a 3D phantom detector (metalization with no columns) in the middle

A.1.2 Manchester mask

The Manchester mask shown in Fig. A.2 was primarily designed to be used in devices fabricated with different column parameters to study how the performance is affected by the columns, and to measure the resistivity of the columns. This masks consists of four 5×5 arrays of 120 µm square cells with the signal columns connected by strips of metal on the surface resulting in a 3D strip detector. Each array consists of a total of 61 columns, with the back side metalization allowing for the measurement of the resistance of individual columns. In later iterations of this mask, a large cross is present on this back side of the mask, this was added to ease alignment during processing.

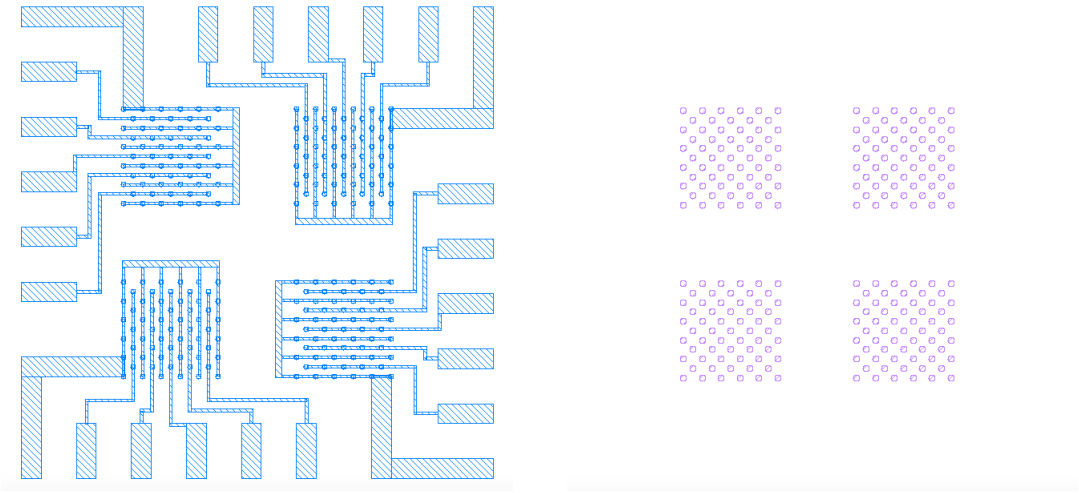

(a) (b)

Figure A.2: (a) the front side and (b) the back side of the Manchester mask.

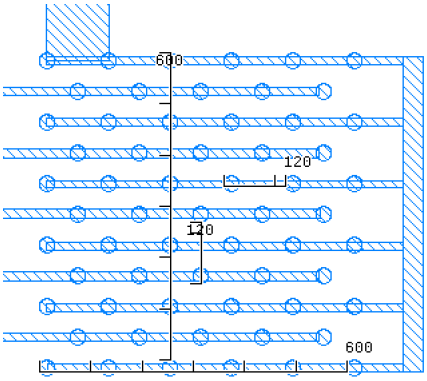

Figure A.3: A subsection of the mask, with measurements showing the cell dimensions and the array dimensions of the Manchester mask measured in microns

A.1.3 Christie mask

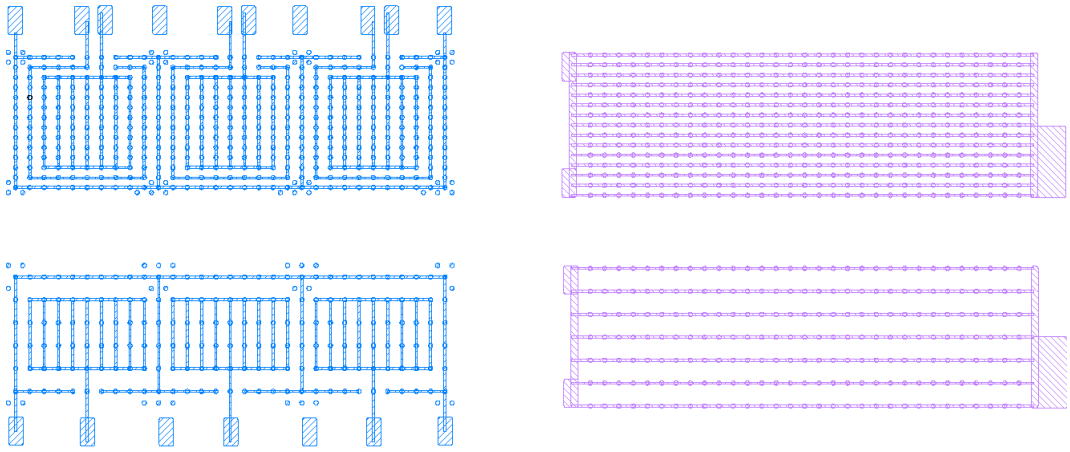

(a) (b)

Figure A.4: Image showing (a) the front side and (b) the back side of the Christie mask.

The Christie mask (shown in Fig. A.4)is a mask that was designed with the intention of making the first tests of 3D diamond technology for medical applications, although it was use for other applications as well. It consists of two different graphitic arrays with different column spacings (the smallest with cell dimensions of 70×100 μm^2 and the largest with cell dimensions of 160×100 μm^2). All the bias columns for each array are connected together by the backside metalization, whereas the readout columns are connected in a series of three pads for each array, each surrounded by guard ring structures. The motivation for this was for the pads to provide very

well defined regions from which charge is collected, and hence use this to measure the current produced by a radiation beam through the device. This application means that precise position resolution is not necessary, and it also means that this mask is a viable design for beam monitoring applications. The mask was later updated to add some features to improve alignment and increase redundancy.

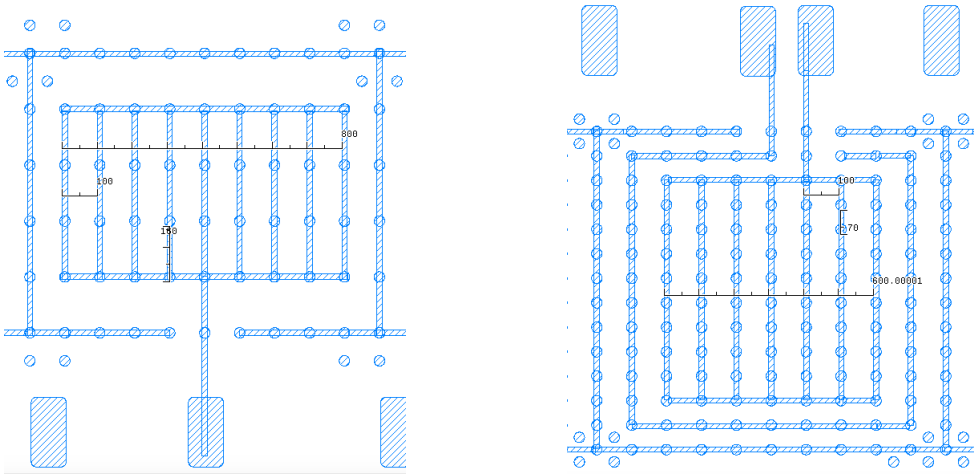

(a) (b)

Figure A.5: A subsection of the readout side metalization of (a) the large cell array and (b) the small cell array, highlighting the dimensions of the mask in microns

A.1.4 3D multi-pattern strip detector mask

The 3D Multi-pattern strip mask (shown in Fig. A.6) was designed to test and compare three different possible 3D geometries: 100×100 µm^2 square cells, 100×200 µm^2 rectangular cells, and 100 µm pitch regular hexagonal shaped cells. As well as a 3D array, this mask also has a 3D "phantom" array to allow a direct comparison between the charge collection due to the surface metalization and the collection due to the graphitic columns. The device also has a planar strip array to allow a direct comparison between a planar geometry and a 3D geometry. The bias metalization for this device is on the back side of the detector, with all the bias columns connected together, while the signal columns are connected by metal strips of the front side of the device. Placing signal and bias metalization on different sides allows for the reduction of the risk of shorting signal and bias columns due to problems during photolithography, and reduces the problems caused by surface effects as the pitch is planned be reduced in future devices. Being able to deposit metalization and connect columns on both sides is also a pre-requisite step to the production of pixel devices, as such it was also important to test this procedure.

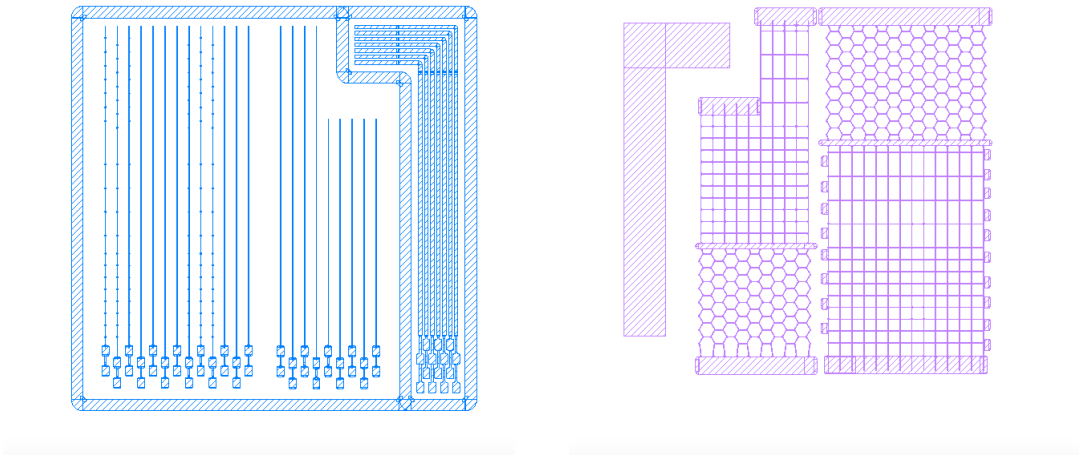

(a) (b)

Figure A.6: (a) the front side (the different structures are from left to right: the readout metalization of the 3D, 3D phantom and planar strip detectors) and (b) the back side metalization mask (with the different structures being from right to left the bias metalization of the 3D, 3D phantom and planar strip detectors) of the 3D Multi-pattern strip device.

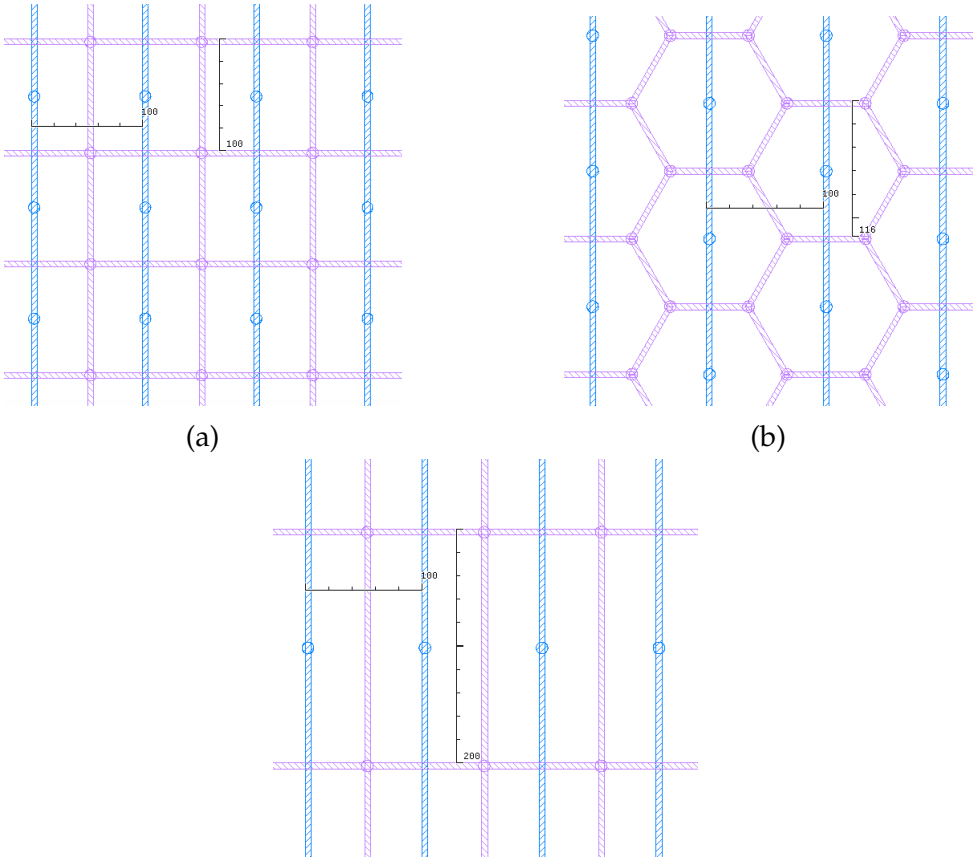

Figure A.7: Sections of the Multi-pattern strip detector mask with measurements showing the cell dimensions in microns. (a) shows the square cell section, (b) shows the hexagonal cell section, (c) shows the rectangular cell section

A.1.5 3D multi-pattern pad detector mask

The 3D Multi-pattern pad design (shown in Fig. A.8) was designed to work on the same array of graphitic electrodes as the Multi-pattern strip device (Fig. A.6). It also consists of the same array of graphitic electrodes with a combination of 100×200 μm^2 rectangular cells, and 100 µm pitch regular hexagonal cells; however in this case, rather than being a strip device, the cells are connected in differently sized pads. The purpose of this device geometry was to undergo rates studies, looking at how the signal is affected by the rate of particles passing through the device. The phantom and planar detectors present in the strip device were instead replaced by a single phantom device, exactly matching the layout of the main graphitic array.

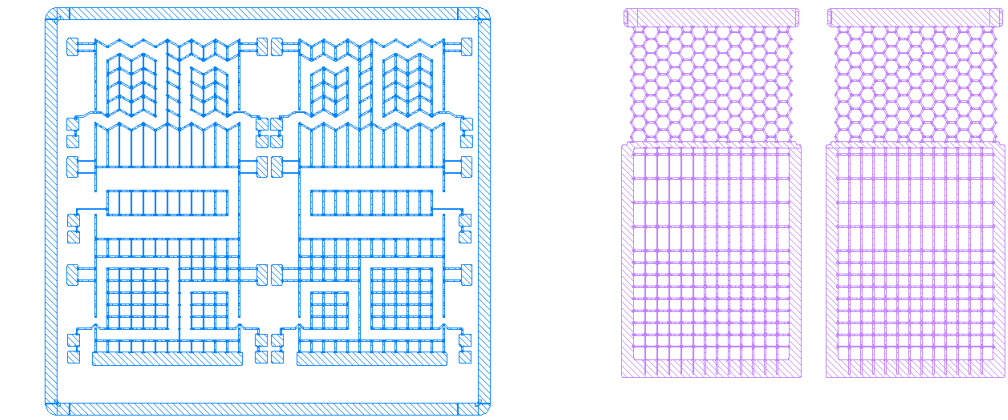

(a) (b)

Figure A.8: (a) the front side (with the 3D structure on the left and the phantom structure on the right) and (b) the back side (with the 3D structure on the right and the phantom structure on the left) metalization mask of the 3D Multi-pattern pad device.

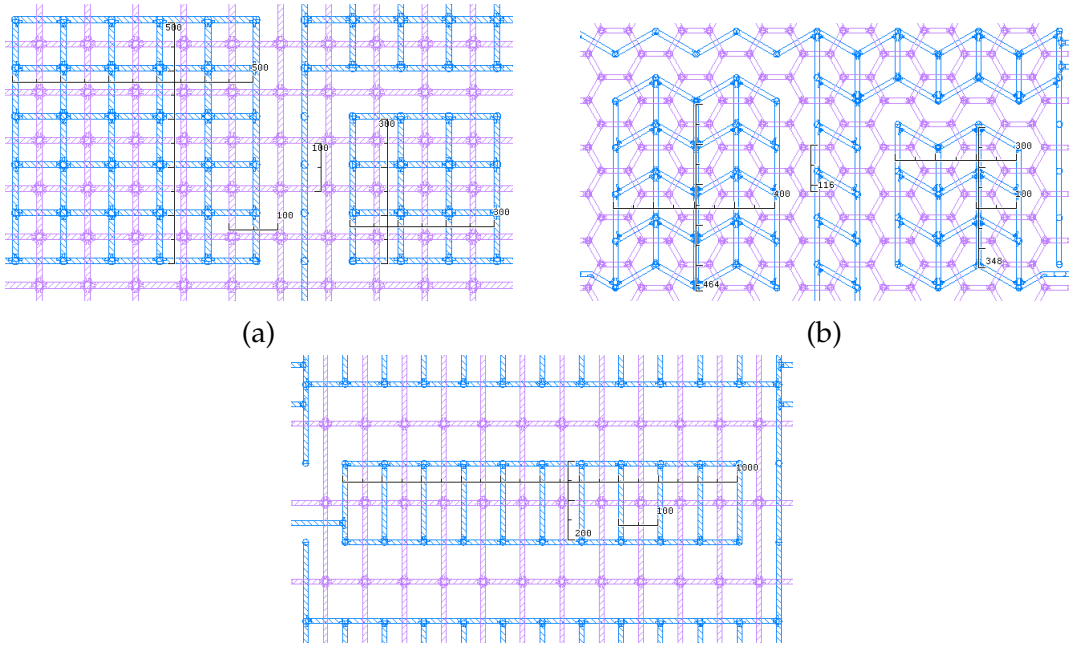

(a) (b)

(c)

Figure A.9: Sections of the Multi-pattern pad detector mask with measurements showing the cell and pad dimensions in microns. (a) shows the square cell section, (b) shows the hexagonal cell section, (c) shows the rectangular cell section

A.1.6 Full 3D strip detector mask

The "Full 3D" strip device, shown in Fig. A.10, was designed to be a large area 3D diamond devices. All the 3D diamond detectors previously produced have had a relatively small active area. To make 3D diamond an attractive alternative for tracking detectors it must be proven that the production process can be extended to produce larger area devices. The 3D Multi-pattern detectors have an active area of $\sim 1.3 \times 2.6$ mm^2, this device is designed to have an active area of 3.6×3.2 mm^2, more than double the previous record, though still not as large it is hoped to achieve, building this device is nonetheless a significant step forward towards building large area 3D devices.

This is a strip device consisting of 36 strips, each connecting 32 signal electrodes for a total of 1152 100×100 µm^2 cells.

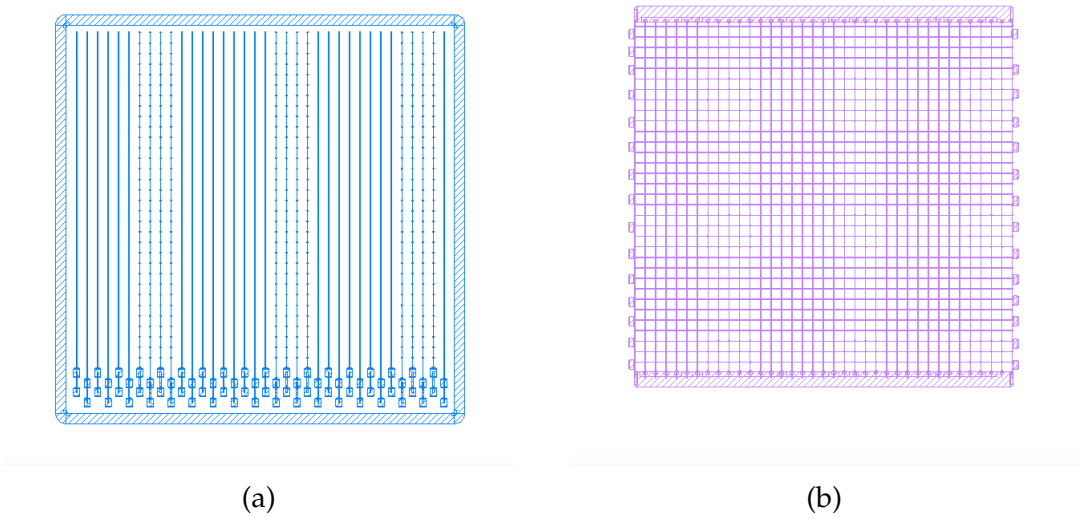

(a) (b)

Figure A.10: (a) the front (readout) side and (b) the back (bias) side metalization mask of the Full 3D strip device.

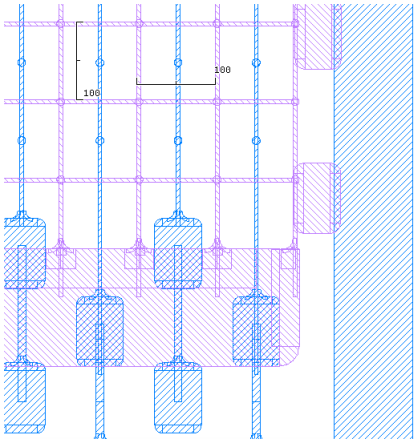

Figure A.11: A section of the Full 3D strip detector mask with measurements showing the cell dimensions in microns.

A.2 Mask designs suitable for current readout chips

Once the viability of 3D diamond devices for high energy physics applications was proven, a number of masks were designed with patterns that would allow the production of 3D diamond sensors to be used in conjunction with chips that are currently in use by the LHC experiments, chiefly the CMS pixel readout chip [48] and the ATLAS FE-I4 chip.

A.2.1 CMS pixel mask

Fig. A.12 shows the CMS ROC compatible 3D diamond pixel mask. The chip was designed for 150×100 µm^2 rectangular pixels, and as such it was decided to maintain these pixel dimensions for these devices. The active area for this device was 3.1×3.0 mm^2, for a total of 620 pixels.

In future it is hoped that to minimize potentials shorts and other problems with 3D devices the columns can be manufactured starting from one of the diamond surfaces and stopping ~ 15 µm below the other surface, with readout and bias electrodes starting on opposite sides. As such a mask was produced to allow the bias side of the diamond to have a simple pad metalization, as well as a grid metalization, as this is easier to manufacture and minimized the potential for unconnected columns.

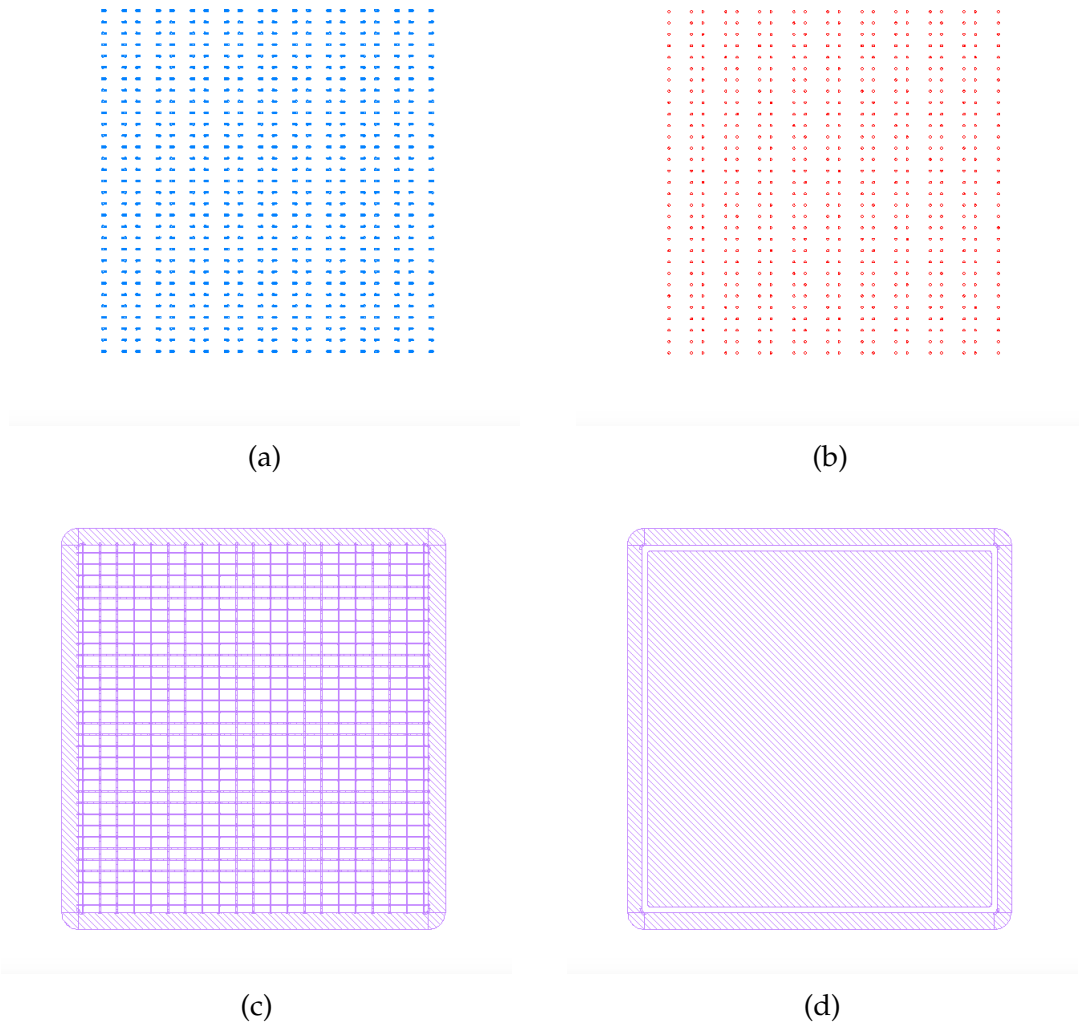

Figure A.12: The mask to produce a sensor compatible with the current CMS readout chip, with (a) the under bump metal, (b) the bumps, (c) the bias grid metalization and (d) the bias pad metalization

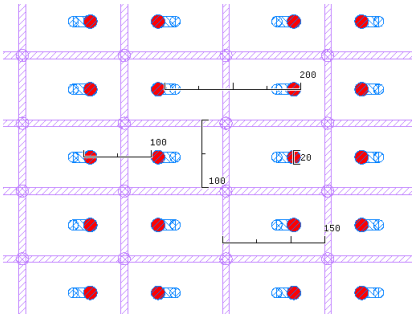

Figure A.13: A subsection of the CMS pixel mask, with the different layers superposed showing the various dimensions of the mask in microns.

A.2.2 FE-I4 pixel mask

A mask was also designed to make a sensor compatible with the current ATLAS FE-I4 chip. This mask (shown in Fig. A.14) was designed to have pixel dimensions of 250×50 µm^2 pixels. This is not an ideal layout for 3D detectors. It was decided to also test a hexagonal cell geometry.

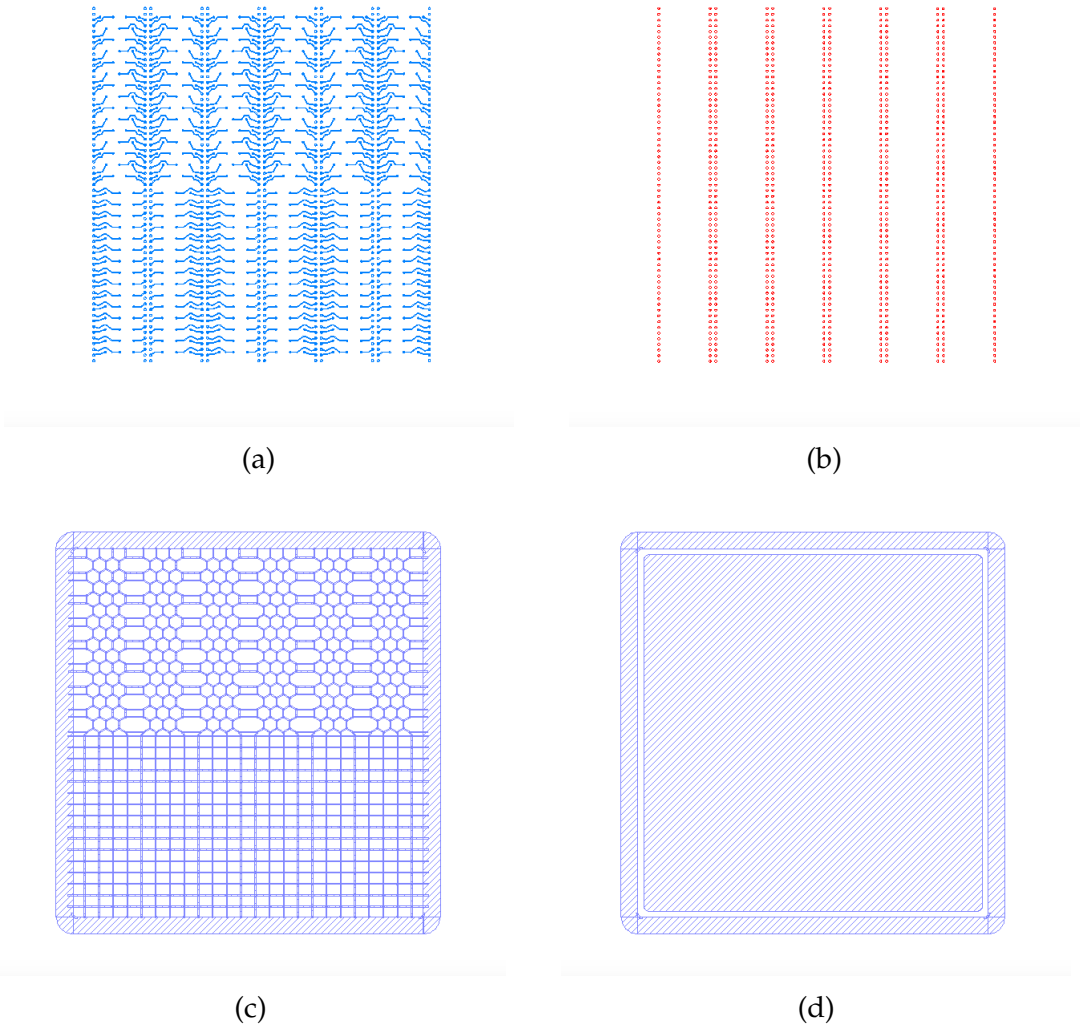

Figure A.14: The mask to produce a sensor compatible with the current ATLAS FE-I4 readout chip, with (a) the under bump metal, (b) the bumps, (c) the bias grid metalization and (d) the bias pad metalization

The sensor area was split into two separate areas, one with rectangular 125×100 µm^2 cells, the other with 100 µm pitch regular hexagonal cells. A metalization pattern was then designed to connect each pixel to a bump. Due to the location of the bumps it was decided that the areas of the device where the bumps are to be

located would not be active.

The idea of using regular hexagonal cells was scrapped for future experiments as differences in pitch in the X and Y directions would make it incompatible with the available pixel electronics, as a result masks designed for future devices are expected to have flattened hexagons allowing the pitch to be the same in both directions.

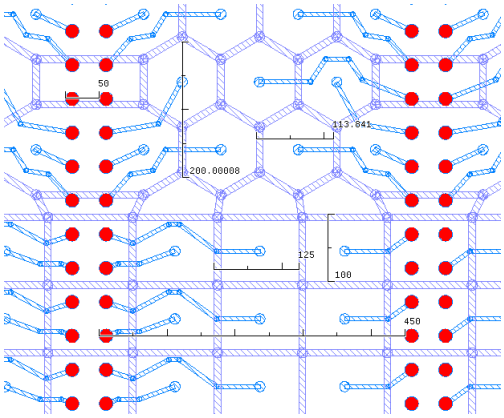

Figure A.15: A subsection of the FE-I4 pixel mask, with the different layers superposed showing the various dimensions of the mask in microns.

A.2.3 Modified FE-I4 pixel mask

A modified version of the ATLAS FE-I4 was later also produced (shown in Fig. A.16). After the columns were fabricated the sensor for this device it was discovered that a small number of mistakes were made during the fabrication process. Some defects (potential cracks) were also observed within the diamond and it was speculated that these may cause a short or other failure of this device should they be connected. As such it was decided that the mask should be modified to avoid using the areas of the sensors where these issues were present.

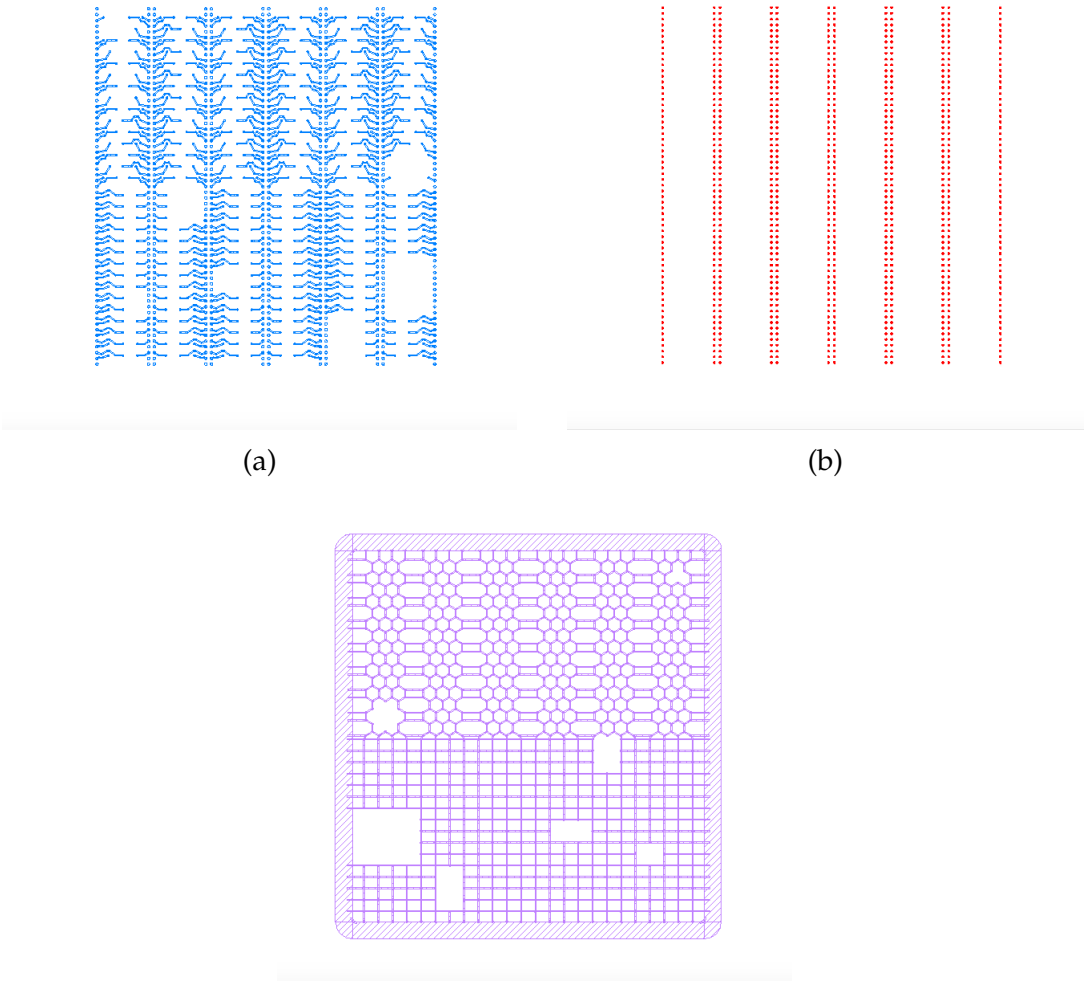

(a) (b)

(c)

Figure A.16: The mask to produce a sensor compatible with the current ATLAS FE-I4 readout chip, with (a) the under bump metal, (b) the bumps, (c) the bias grid metalization and (d) the bias pad metalization. This mask was modified to account for errors made when producing the columns as well as to avoid areas where imperfections were present in the diamond.

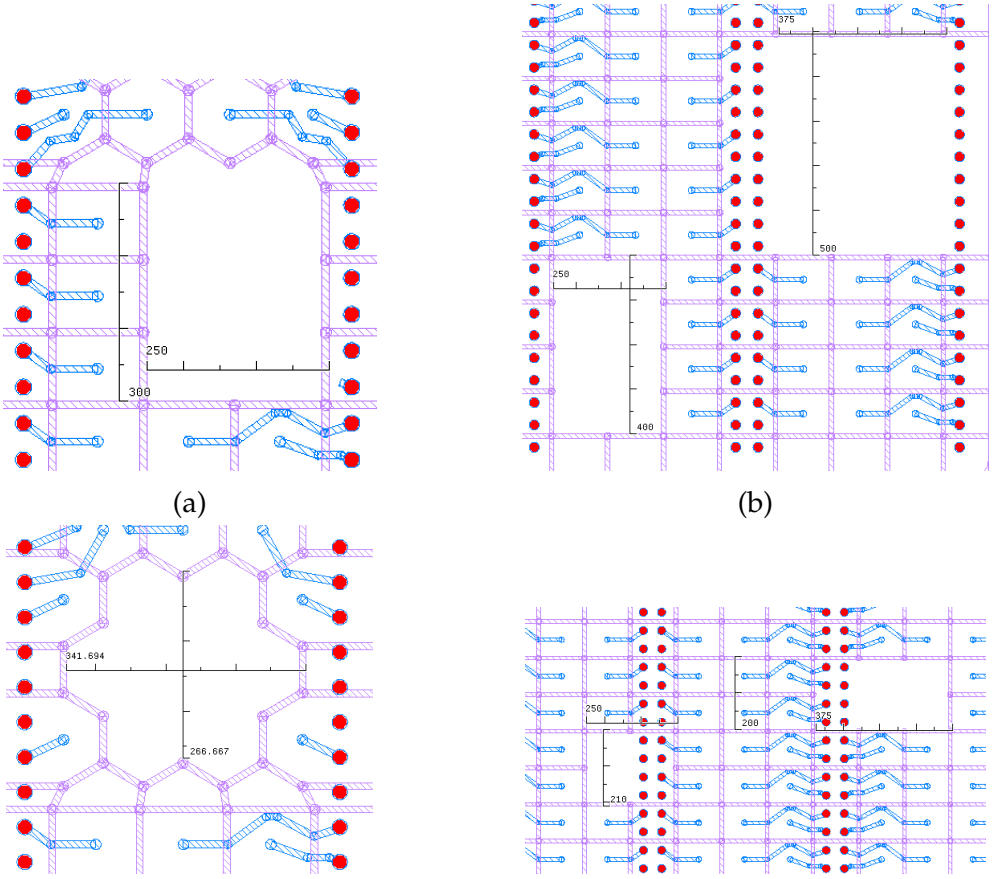

Figure A.17: Subsections of the modified FE-I4 pixel mask, with the different layers superposed showing the dimensions of some of the changed areas in microns.

A.3 Mask designs to test geometries for future applications

As described in section 2.3, the radiation hardness and charge collection efficiency (especially in pCVD) of 3D detectors can be improved by reducing the inter-electrode separation. To investigate the viability of producing such detectors (as well as making 3D diamond technology compatible with future readout chips [130]), a number of masks have been produced, these masks were designed to both test the different possible cell geometries in strip devices, as well as producing masks to make sensors compatible with the current generation of readout chips.

A.3.1 50 µm pitch strip devices

A 3D strip device consisting of 50 µm square cells was designed. This device (shown in Fig. A.18) has an active area of 3.35×2.65 mm^2, for a total of 3551 cells. As future readout chips are envisioned having 50×50 µm^2 pixels, it was important to test the viability of fabricating and operating large area devices with these cell dimensions. Devices with similar dimensions were also fabricated to test the viability of using hexagonal cells; Fig. A.19 shows a similar 3D strip device mask with slightly flattened hexagonal cells with a pitch of 50 µm in both directions, while Fig. A.20 shows another similar design with a combination of square and hexagonal cells.

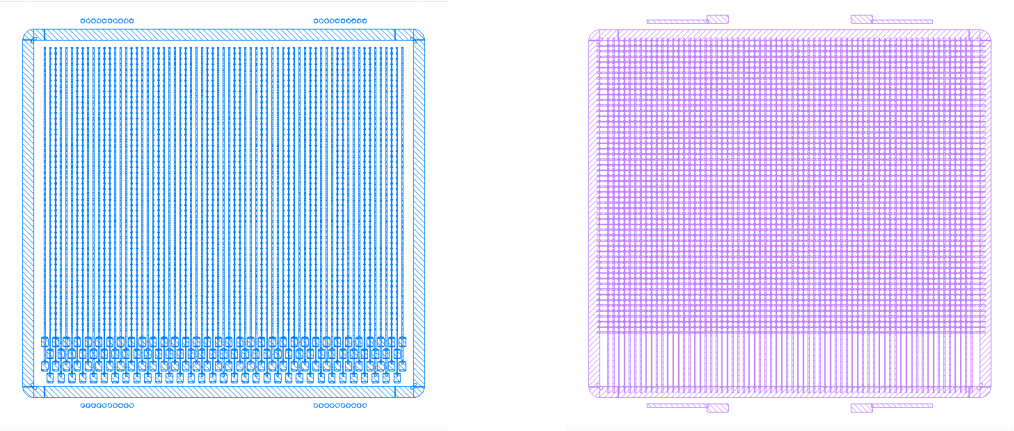

(a) (b)

Figure A.18: The mask design for (a) the readout side and (b) the bias side of a 50 µm pitch 3D strip diamond detector with square cells

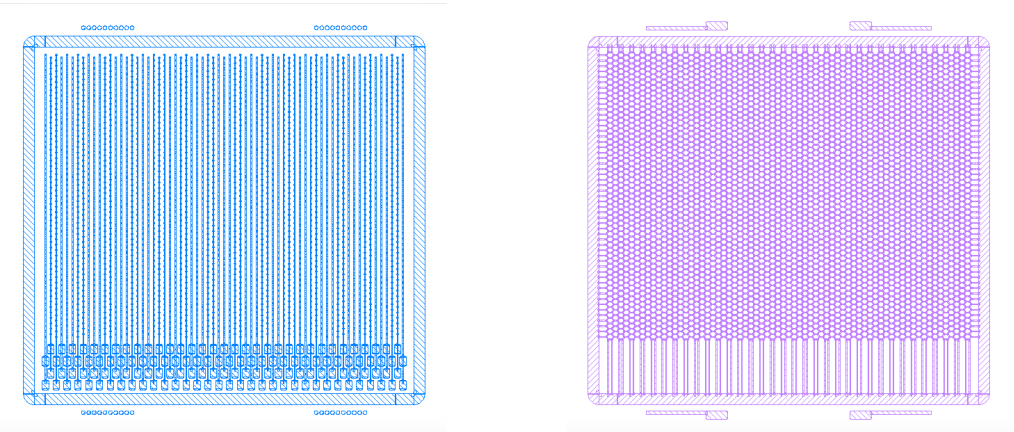

(a) (b)

Figure A.19: The mask design for (a) the readout side and (b) the bias side of a 50 µm pitch 3D strip diamond detector with hexagonal cells

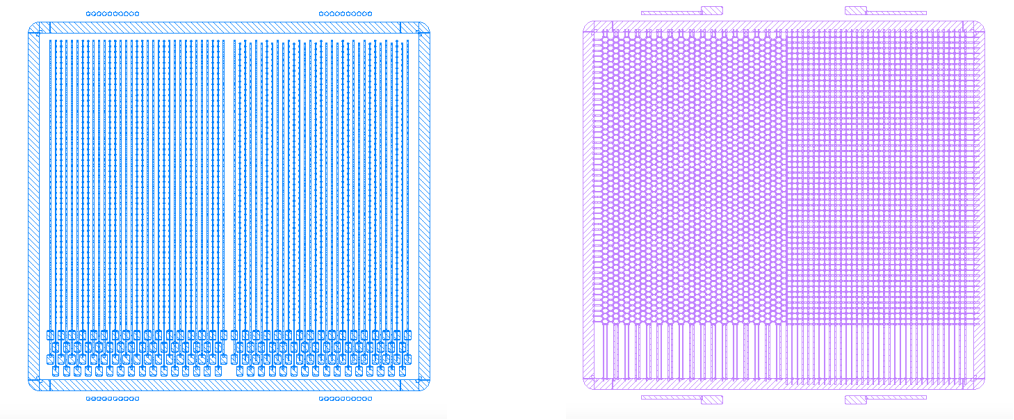

(a) (b)

Figure A.20: The mask design for (a) the readout side and (b) the bias side of a 50 µm pitch 3D strip diamond detector with a combination of square and hexagonal cells

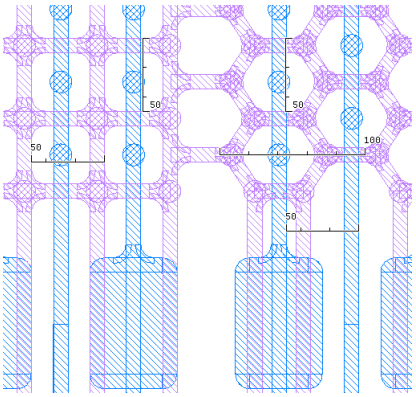

Figure A.21: A subsection of the 50 µm pitch combined strip mask, with the different layers superposed showing the various dimensions of the mask in microns.

A.3.2 50 µm pitch, FE-I4 compatible pixel devices

It was envisioned to also produce 50 µm pitch pixel devices. Masks were made to produce sensors compatible with the FE-I4 pixel chip. The masks were designed for the same electrode arrays as those described in the previous section to allow the possibility to test a diamond first as a 3D strip device and then as a 3D pixel device. Fig. A.22 shows the square cell pixel mask, Fig. A.23 shows the hexagonal cell pixel mask and Fig. A.24 shows the combined square and hexagonal pixel mask.

As the FE-I4 chip was designed for 250×50 µm^2 pixels, sets of 5 cells were connected together using metal micro-strips along the surface of the sensor. As before, both a grid and a pad metalization masks were prepared for the bias side.

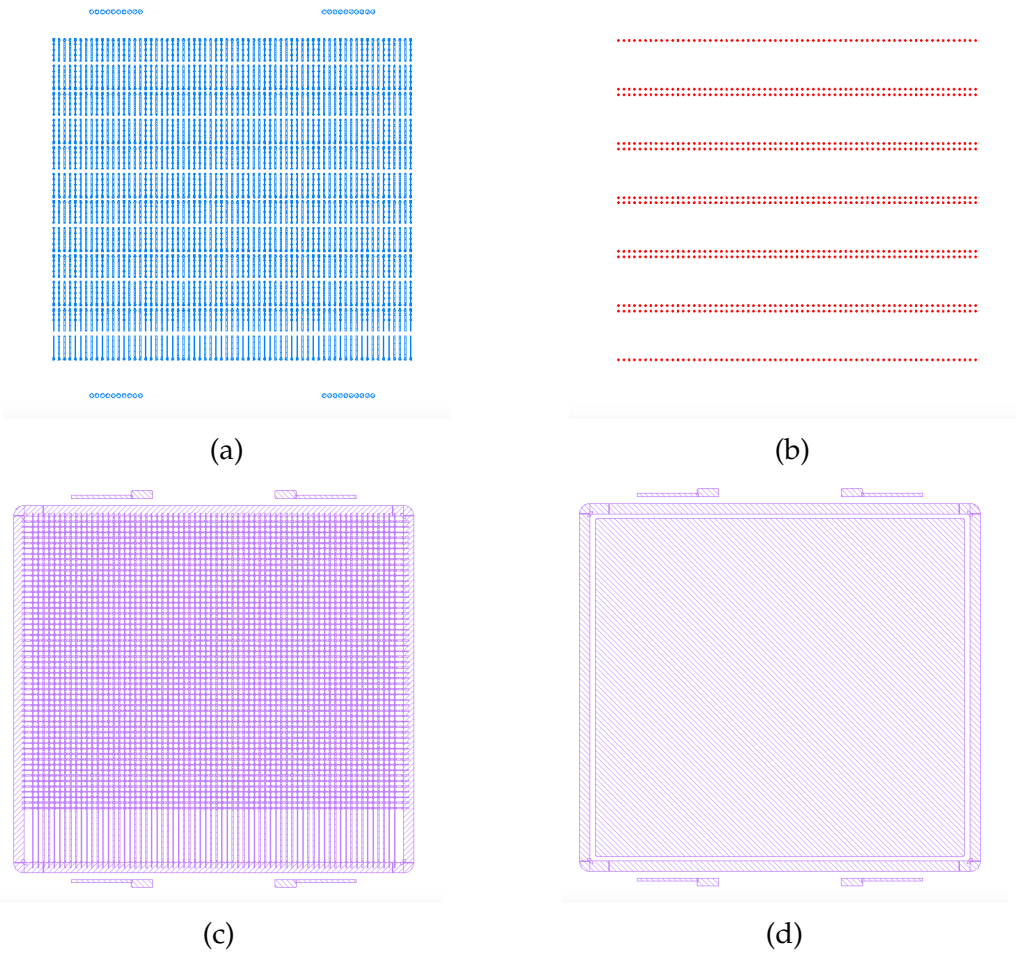

Figure A.22: The mask design for (a) the under bump metal, (b) the bumps, (c) a bias grid metalization and (d) a bias pad metalization of an FE-I4 compatible 50 µm pitch 3D pixel diamond detector with square cells

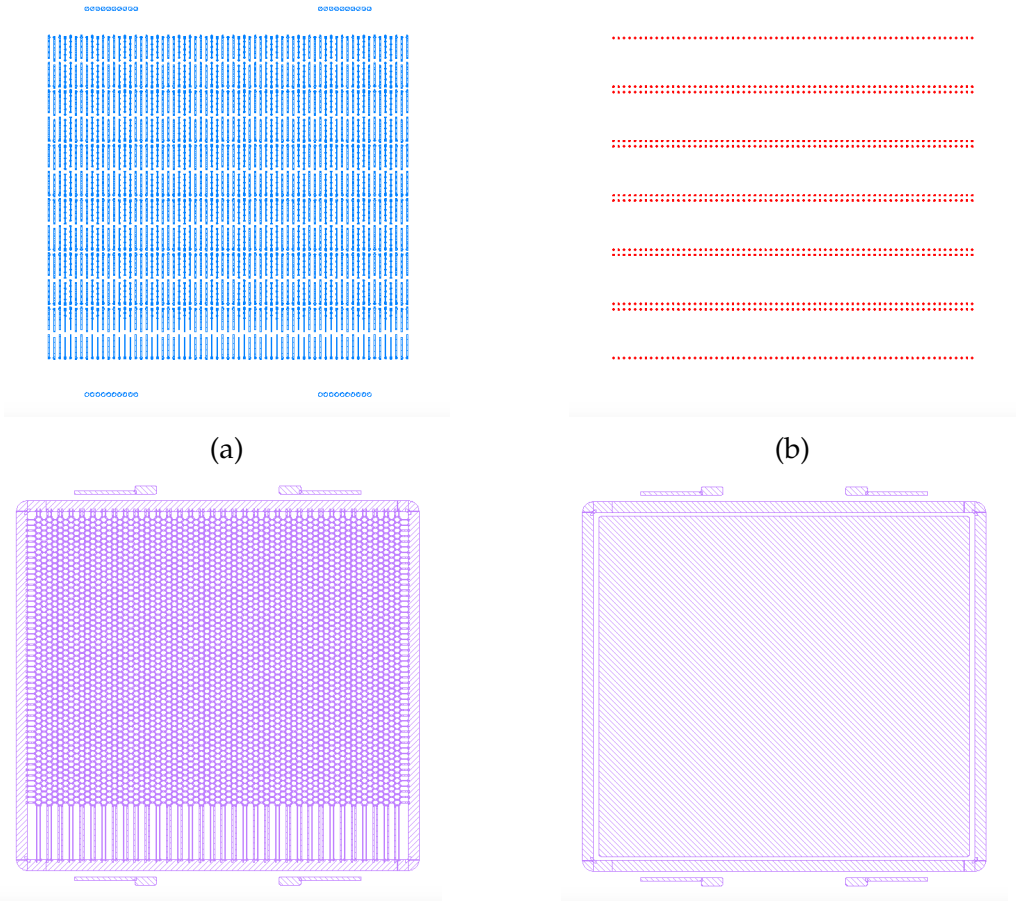

(a) (b) (c) (d)

Figure A.23: The mask design for (a) the under bump metal, (b) the bumps, (c) a bias grid metalization and (d) a bias pad metalization of an FE-I4 compatible 50 µm pitch 3D pixel diamond detector with hexagonal cells

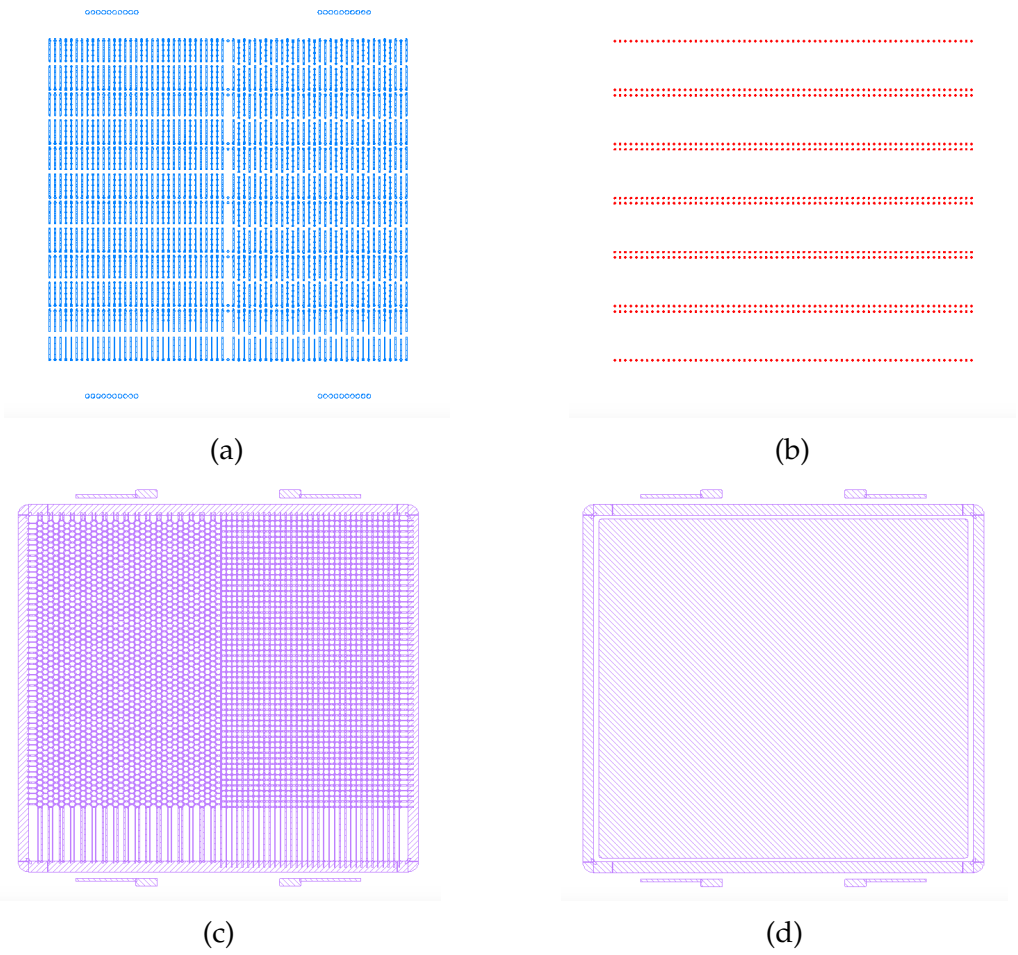

Figure A.24: The mask design for (a) the under bump metal, (b) the bumps, (c) a bias grid metalization and (d) a bias pad metalization of an FE-I4 compatible 50 µm pitch 3D pixel diamond detector with a combination of square and hexagonal cells

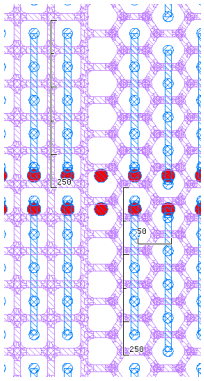

Figure A.25: A subsection of the 50 µm pitch combined FE-I4 pixel mask, with the different layers superposed showing the various dimensions of the mask in microns.

A.3.3 50 µm pitch, CMS compatible pixel device

A mask was also designed to produce detectors with square 50×50 µm^2 cells compatible with the current CMS ROC. As previously stated, the current chip is designed for 150×100 µm^2 rectangular pixels. Therefore to make the sensor compatible with the chip, groups of 6 cells were connected together using a surface metalization. Images of the mask are shown in Fig. A.26.

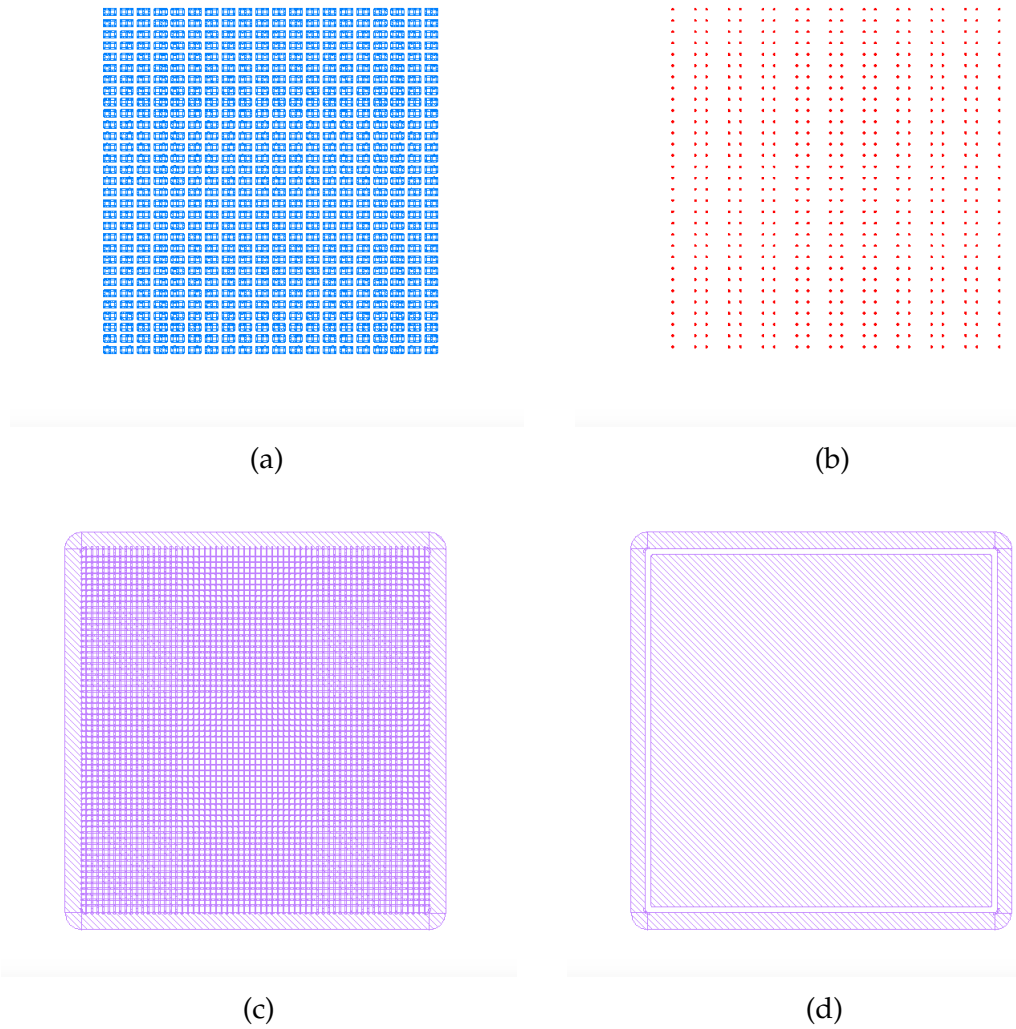

Figure A.26: The mask design for (a) the under bump metal, (b) the bumps, (c) a bias grid metalization and (d) a bias pad metalization of a CMS ROC compatible 50 µm pitch 3D pixel diamond detector with square cells

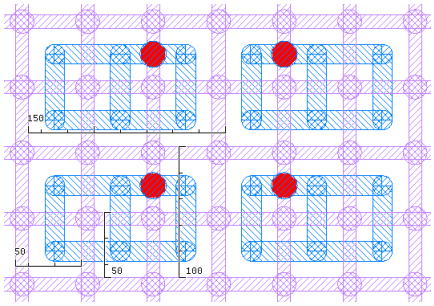

Figure A.27: A subsection of the 50 µm pitch CMS ROC pixel mask, with the different layers superposed showing the various dimensions of the mask in microns.

B. Description of devices

A number of different devices were produced or tested as part of the work reported in this thesis. A brief description of these devices is given in this section:

B.1 Devices to test the viability of 3D diamond dechnology

Firstly, a number of devices were built to prove the feasibility of 3D diamond technology as well as to test different properties of this technology, such as the charge collection efficiency, the effects of irradiation and searching for the optimal fabrication parameters.

B.1.1 Batch 2 scCVD

The Batch 2 scCVD (show in Fig. B.1) was an early 3D diamond device manufactured from a 440 µm thick, electronic grade E6 [61] diamond designed to prove that 3D devices could achieve comparable if not better performance than planar devices in single crystal material, this was achieved by having three different sensor areas, one with a planar geometry, one with a 3D geometry and one with a 3D "phantom" geometry (same metalization pattern as the 3D detector but with no graphitic electrodes), the metalization mask used for this device is decribed in section A.1.1; this was done to assure that the comparison was made using material of the same quality that had undergone identical processing for all three detectors. The column fabrication was performed at the University of Manchester, after which the sample was metalized with a chrome-gold metalization at the Ohio State University. The sample was measured at CERN and the results obtained during those test beams have been published [111]. This work is described in more detail in section 5.2. After these measurements were successfully carried out, the sample was stripped of its metalization and underwent an irradiation campaign. After irradiation attempts were made to re-metalize and remeasure the sample, however these attempts were

unsuccessful and it appeared that the metalization did not achieve a good contact with the columns. It was not possible to determine if the problems were due to the radiation damage or to some of the other processes carried out on the device. To test whether irradiation would affect the properties of the columns a new sample was produced to undergo irradiation studies, this sample is described in section B.1.6.

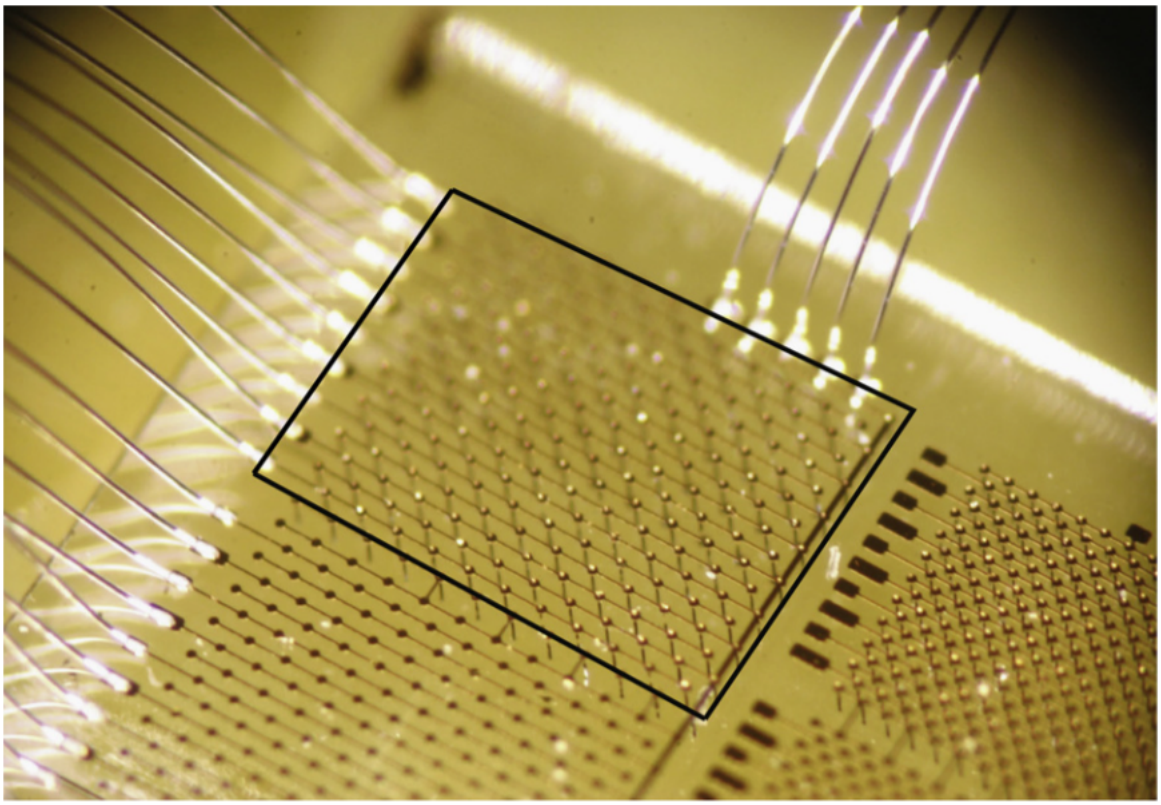

Figure B.1: The batch 2 scCVD device showing the 3D detector highlighted by the black square, alongside the 3D phantom detector. The other detector visible to the right of the image was not used for any measurements

B.1.2 Batch 2 pCVD

The Batch 2 pCVD (show in Fig. B.2) was produced to the same specifications as the similar single crystal device, however it was made from ≈ 500 µm thick polycrystalline, electronic grade material obtained from E6 [61]. As for the single crystal device, this was created to prove that a 3D detector could achieve similar, if not better performance than a planar device in polycrystalline material. Again, the column fabrication was performed at the University of Manchester, after which the sample was metalized with a chrome-gold metalization at the Ohio State University. This device was measured at CERN and details of these measurements are presented in section 5.3 and are also described in greater detail elsewhere [123]. To avoid issues

with metalization the sample was metalized with the same pattern on both sides.

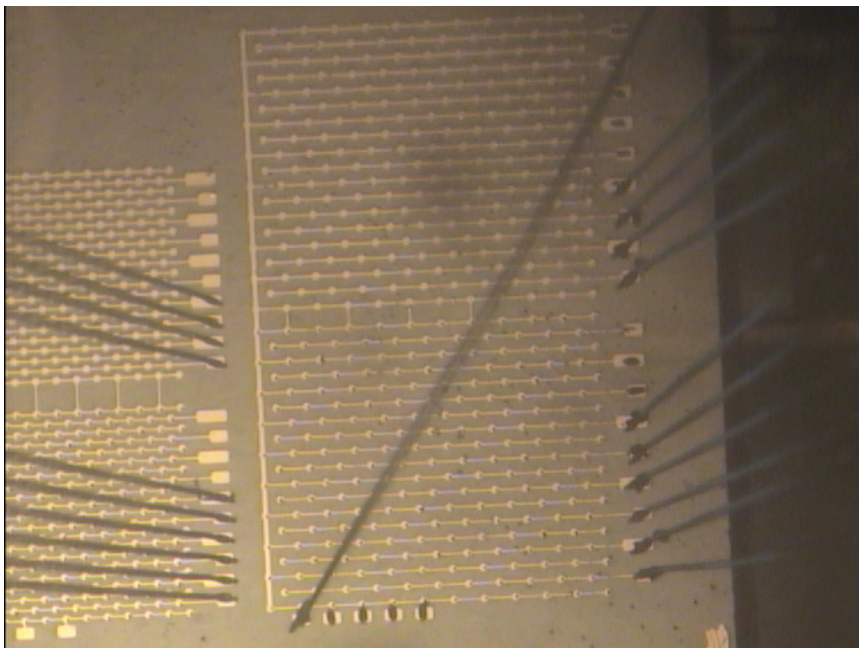

Figure B.2: Photograph of the batch 2 pCVD device showing the 3D and 3D phantom detectors, the bias electrodes of the two devices are connected together to be certain that both of them are held at the same bias to allow a fair comparison of the two detectors

B.1.3 Manchester sample

The Manchester sample was manufactured from a ≈ 500 µm thick, single crystal, E6 [61] diamond to study the effect of varying fabrication parameters on the quality of the columns produced, as such four graphitic arrays were produced matching the Manchester mask (described in section A.1.2). Details of these studies are presented elsewhere [86] [91]. The columns were fabricated at the University of Manchester, after which a titanium-gold metalization was deposited on the sample, also at the University of Manchester. This sample was then tested at both the Diamond Light Source and the Ruđer Bošković Institute (RBI), details of these measurements are provided in section 5.1.1.

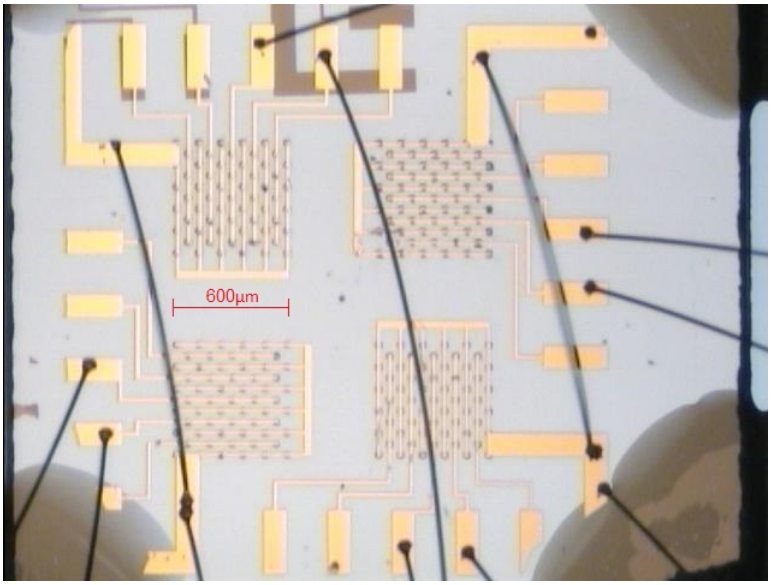

Figure B.3: Photograph of the Manchester detector, showing the four arrays, and the wirebonds connecting them to the PCB. Due to space issues, only two readout strips were connected for each array

B.1.4 Göttingen sample

The Göttingen Sample, shown in Fig. B.4, manufactured from polycrystalline optical grade E6 [61] diamond, was used to study the effects of varying fabrication parameters of graphitic electrodes in 3D diamond. This device was made using the same design as the Manchester sample. The column fabrication was performed in the Georg-August-Universität, Göttingen and a chromium-gold metalization was deposited at the University of Manchester. The details of the column fabrication and the results of these experiments are detailed elsewhere [87].

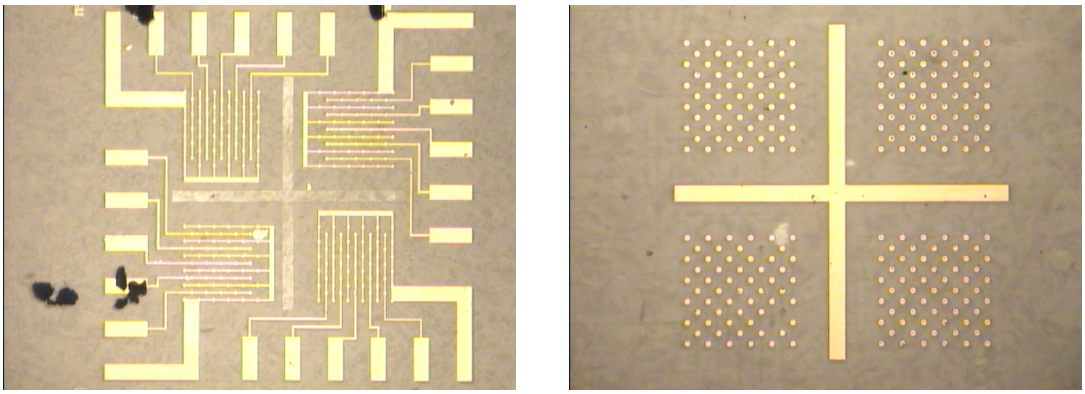

(a) (b)

Figure B.4: Images showing (a) the front side and (b) the back side of the Göttingen sample after metalization

B.1.5 Florence device

The Florence sample was a 400 µm thick, electronic grade, single crystal diamond, obtained from IIa [63], fabricated at the Universitá degli studi di Firenze, with arrays designed to fit the Christie mask (section A.1.3) and subsequently metalized at the University of Manchester. Initially the metalization was two layer chrome-gold on the readout side and only one layer chrome on the bias side due to issues occurring during the metalization process. The sample was used in this configuration for some measurements, but eventually the metalization degraded, as such the sample was cleaned and re-metalized with chrome-gold on both sides, sample post re-metalization is shown in Fig. B.5.

This sample was used to take some measurements at the Christie hospital in Manchester for dosimetry studies which are briefly described in section 6.

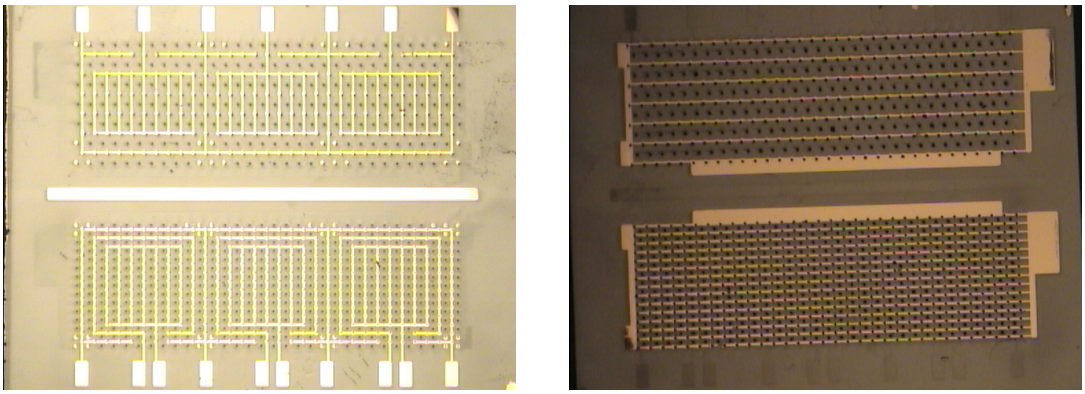

(a) (b)

Figure B.5: Images showing (a) the front side and (b) the back side of the Florence sample after the second metalization was deposited

B.1.6 Irradiation sample

A 3D diamond sample was produced to study the effect of irradiation on the resistance of the columns. This consisted of a single crystal 400 µm thick, optical grade diamond, obtained from IIa [63] and was laser processed at the University of Oxford using the SLM technique. The sample was designed to be compatible with the Manchester mask (described in section A.1.2), and therefore consists of four arrays of columns. The columns were produced with two different diameters.

Metalization on this sample mostly failed, however as the sample was produced with small graphitic pads at the surface of each column, it was still possible to measure the resistance of the columns. The resistance of the columns was measured before and after irradiation, and the results are described in section 8.

B.1.7 Multi-pattern scCVD

The single crystal Multi-pattern sample was produced using a 400 µm thick, electronic grade single crystal diamond produced by IIa [63]. An array of columns was produced with a mixture of cells with three different shapes to match the Multi-pattern mask (described in section A.1.4). The sample was measured using a proton microbeam at (RBI) in Zagreb, with the intention of studying the effects of varying cell geometry, and at the Christie hospital. Details of the measurements carried out at RBI are described in section 5.1 and also presented in more detail elsewhere [117]. A photograph of this sample is shown in Fig. B.6.

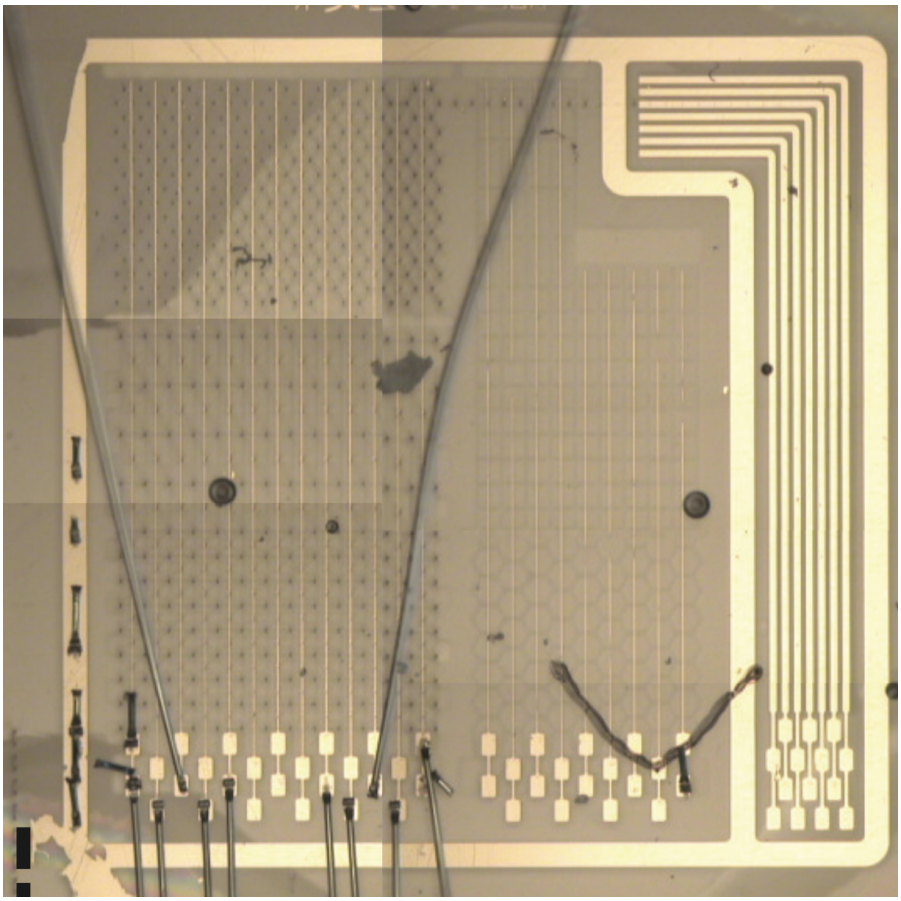

Figure B.6: The Multi-pattern sample, only the 3D detector area was used. To study the charge collected by individual cells, five of the strips were read out: a central strip with 2 adjacent strips in either direction to isolate it, allowing the accurate study of the charge collected by the central strip of cells

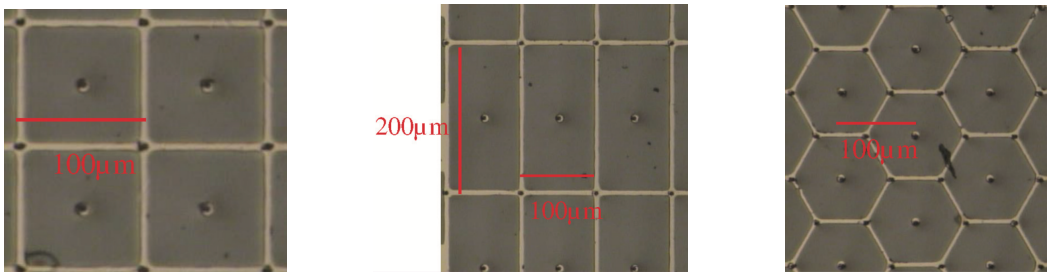

(a) (b) (c)

Figure B.7: Sections of the bias side metalization for the sub-array with (a) square cells, (b) rectangular cells, (c) hexagonal cells

B.1.8 Multi-pattern pCVD

The polycrystalline Multi-pattern sample was produced using an electronic grade polycrystalline diamond produced by II-VI [62]. It was laser processed at the University of Oxford with the same geometry as the single crystal Multi-pattern device, and was subsequently metalized using a chrome-gold metalization at the Ohio State University. Measurements with this device were primarily aimed at comparing charge collection of square and hexagonal cells. This sample was used in measurements at CERN. The analysis of this data is still in the early stages, some details of the measurements are described in section 9.2.

After these measurements the metalization was stripped from this sample and was replaced with the Multi-pattern Pad metalization described in section A.1.5, to carry out some high rate measurements with this sample. Some tests have already been carried out on this device, however more work is needed to analyze the results.

B.1.9 Large area 3D strip device

The large area 3D strip device was and electronic grade polycrystalline sample, produced to test how the production process of 3D diamond detectors could be extended to large area devices. A graphitic array was produced at the University of Oxford to be compatible to the full 3D mask (described in section A.1.6). The sample was subsequently metalized at the Ohio State University and underwent a series of measurements at CERN, which are described in section 9.3. Due to some suspected surface impurities, the metalization in the sample was not perfect and there were a number of breaks, an image of the signal side metalization, along with the suspect positions of the breaks is shown in Fig. 3.4. While testing this sample, a large leakage current was present, and although there were no issues with the data obtained from the sample, it was decided that this should be avoided in future. One

possible explanation for the high leakage current is the cracks visible in Fig. B.8, so for the ATLAS FE-I4 sample described in section B.3.2 it was decided to exclude similar regions from the active area.

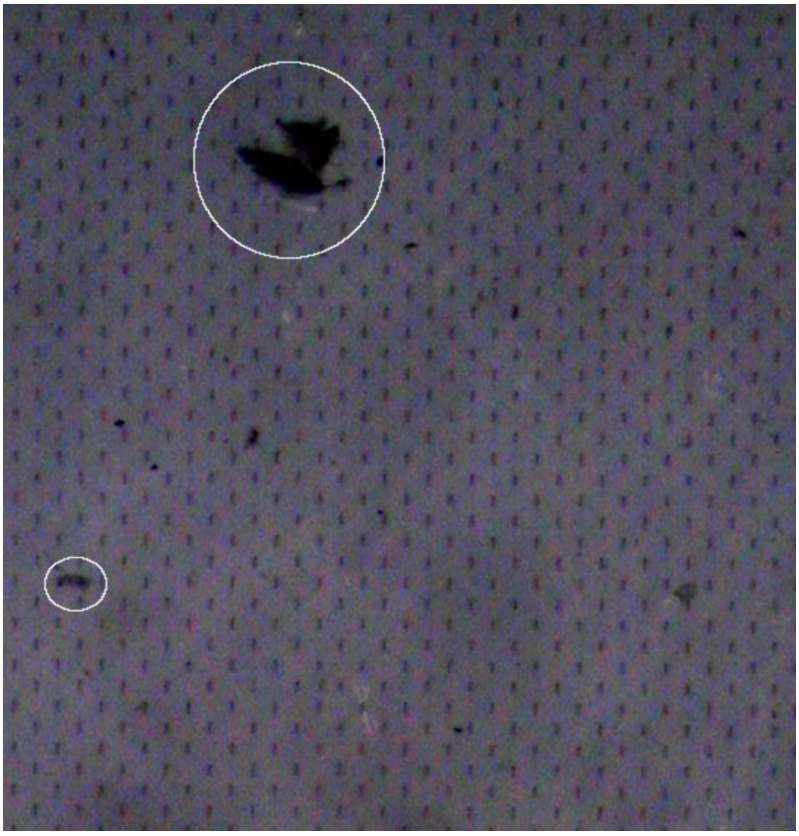

Figure B.8: A section of the large area 3D strip device after column fabrication but before metalization, this picture highlights some of the suspected cracks in the material [132]

B.2 Detectors for the CMS BCM

Two 3D diamond devices were produced and have been installed in the CMS BCM in order to test how the technology would perform as a beam monitor in a HEP experiment before detectors are made to rely on these devices. Both of these devices were designed with two arrays of graphitic electrodes with the intention of using the Christie metalization mask (seen in section A.1.3). These devices were manufactured at the University of Manchester and at the University of Oxford in order to have a direct comparison between the columns obtained with each setup. Of the six readout channels available for each device, only one was used. More details of these devices are given in section 9.1.

B.2.1 Manchester CMS device

The Manchester CMS detector was produced from 500 µm thick, single crystal, electronic grade E6 [61] diamond. The graphitic columns in this device were produced at the University of Manchester using the SLM technique. The sample was also subsequently metalized at the University of Manchester, before being installed in the CMS experiment.

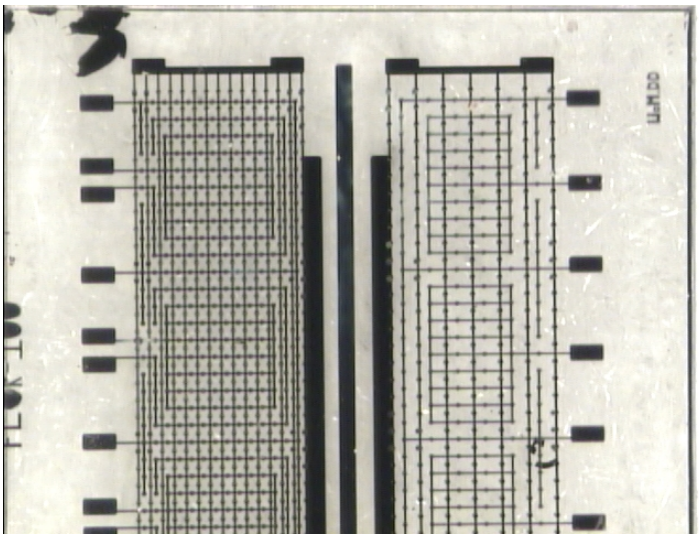

Figure B.9: Image showing the bias side of the sample laser processed in Manchester, the signal side metalization can be seen through the diamond

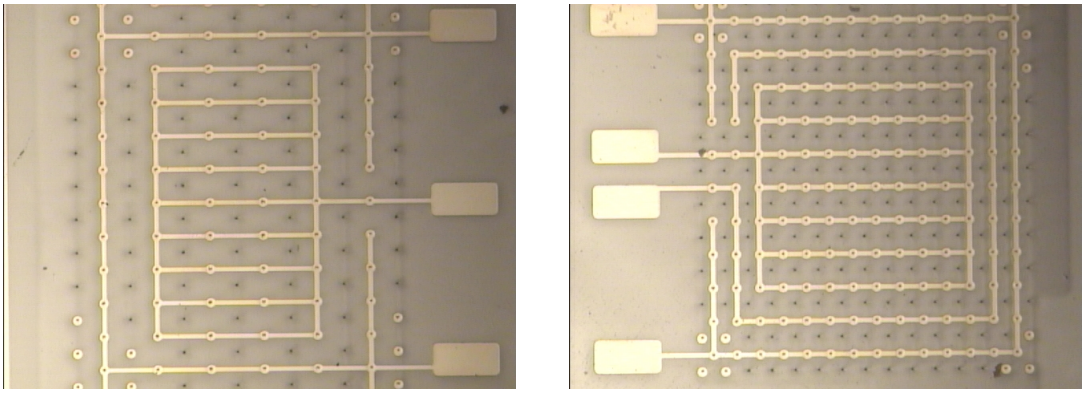

(a) (b)

Figure B.10: Segments of the front side metalization of the Manchester CMS sample; (a) shows one channel of the large cell array and (b) shows one channel of the small cell array

B.2.2 Manchester-Oxford CMS device

The Manchester-Oxford CMS detector was produced from 500 µm thick, single crystal, electronic grade E6 [61] diamond. The graphitic columns were produced at the University of Oxford using the SLM technique. The sample was then metalized at the University of Manchester, before being installed in the CMS experiment.

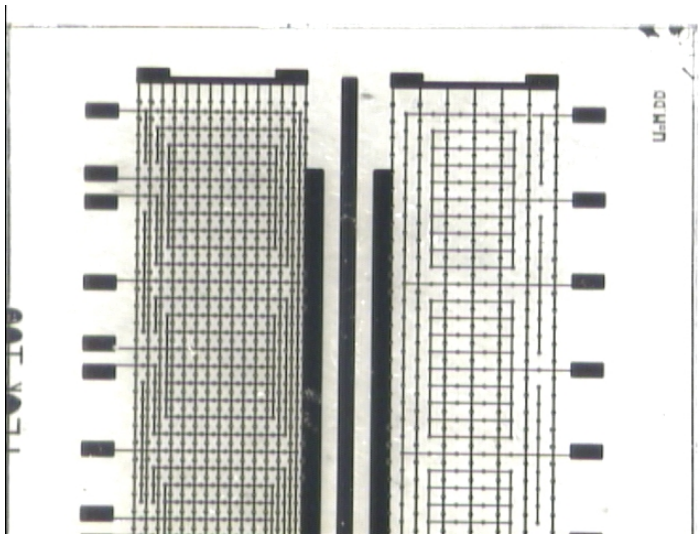

Figure B.11: Image showing the bias side of the sample laser processed in Oxford, the signal side metalization can be seen through the diamond

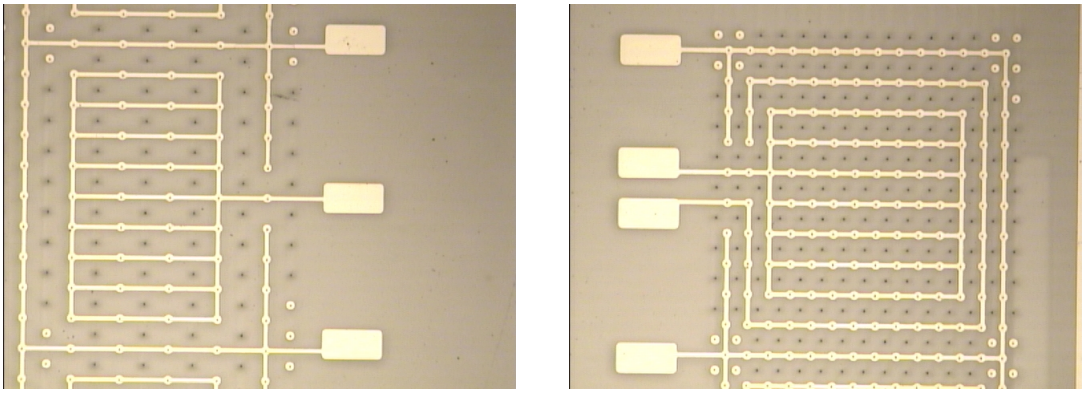

(a) (b)

Figure B.12: Image showing segments of the front side metalization of the Manchester-Oxford CMS sample; (a) shows one channel of the large cell array and (b) shows one channel of the small cell array

B.3 3D diamond pixel devices

It was eventually possible to produce 3D diamond pixel devices, a 3D diamond sensor was produced to be compatible with the current pixel readout chips employed by both the ATLAS and CMS experiments.

B.3.1 CMS pixel device

The CMS pixel device (shown in Figs. B.13 -B.14) was the first successfully produced and tested 3D pixel device. An array of columns was produced at the University of Oxford, and the sample was subsequently metalized and bump-bonded to a readout chip at Princeton University. The mask used to produce contacts on this sample is described in section A.2.1. The sample was measured at the PSI in Zürich. More details of these measurements are given in section 9.4.

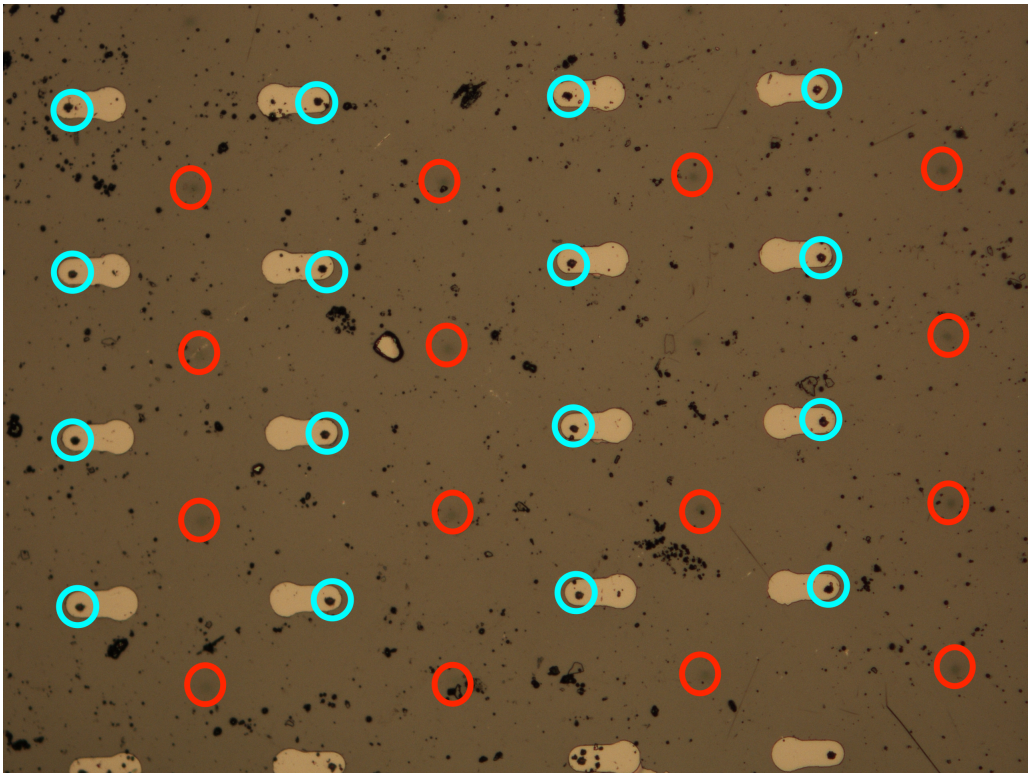

Figure B.13: Image showing the under bump metal for the CMS pixel device, the metalization for each pixel is a small strip, with a larger circle on one side where the bump will be connected and the electrode on the other. The signal columns are indicated by the blue circles, whereas the red circles show the position of the bias columns, these appear as lighter, more diffuse dots as they do not penetrate through the entire diamond

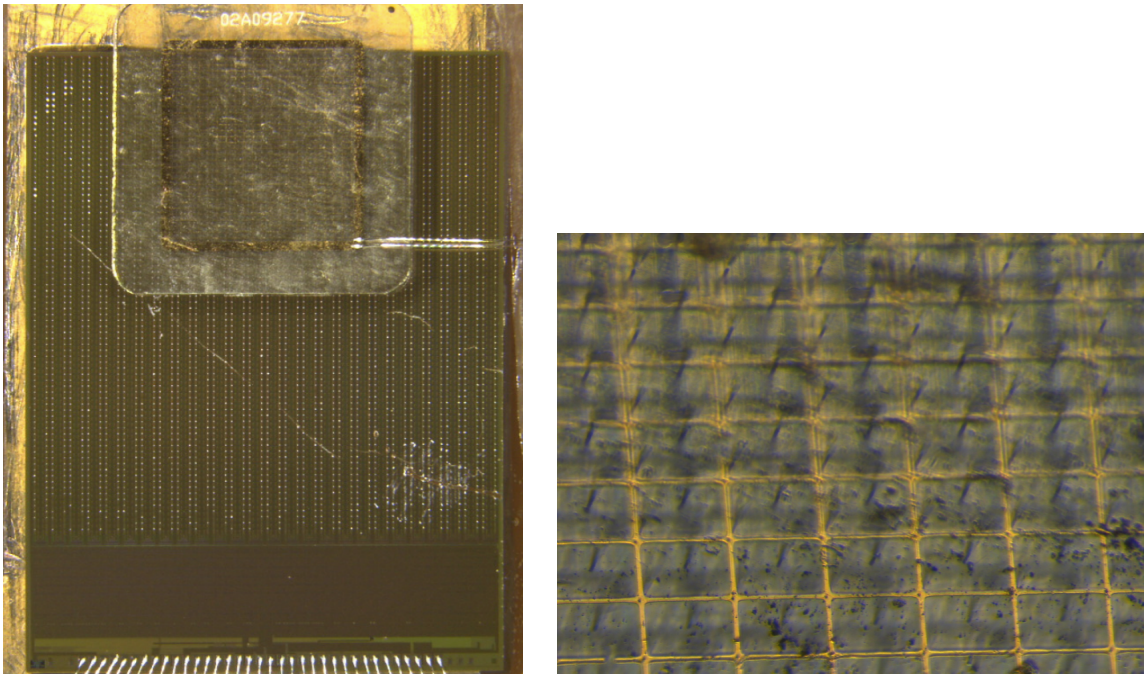

(a) (b)

Figure B.14: Images showing (a) the 3D diamond sensor bump bonded to the CMS ROC and (b) the bias side metalization showing the graphitic electrodes penetrating into the diamond.

B.3.2 ATLAS FE-I4 pixel device

The ATLAS FE-I4 pixel device is an electronic grade, polycrystalline diamond, obtained from II-VI [62]. It was laser processed at the University of Oxford to fit the FE-I4 mask (described in section A.2.2) and after laser processing some structures were observed within the diamond, chiefly suspected cracks that would have potentially caused a short between bias and readout channels. As such the mask was modified as shown in section A.2.3, to avoid using any region of the device that could give rise to any of these issues. The sample was metalized at the Ohio State University and subsequent processing was carried out at IZM [133].

More details of the plans for this sample are given in section 9.4.

B.4 3D diamond devices for future studies

B.4.1 50 µm pitch CMS pixel device

The 50 µm Pitch CMS pixel device is a pCVD 3D diamond sensor designed to be compatible with the current CMS ROC to verify that 3D sensors with 50 µm cells

can function as pixel devices, and to compare their performance to previous 3D devices with larger cell dimension. The current CMS ROC consists of pixels with dimensions of 100×150 µm^2. To make the sensor compatible with the current ROC it was therefore necessary for sets of six pixels to be read out together as micro-pads. The photolithography mask used for this device is described in section A.3.3.

C. Systematic simulation studies of varying device fabrication parameters

C.1 Cluster charge as a function of hit position for different column diameters

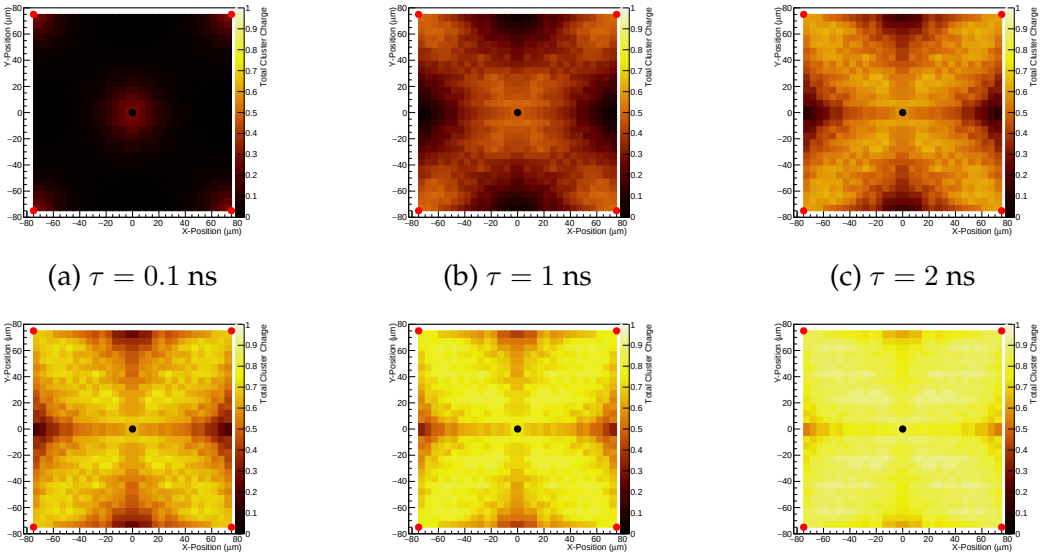

(a) $\tau = 0.1$ ns (b) $\tau = 1$ ns (c) $\tau = 2$ ns

(d) $\tau = 3$ ns (e) $\tau = 5$ ns (f) $\tau = 10$ ns

Figure C.1: Total cluster charge collected as a function of hit position within the cell for different charge lifetimes at 75 V for 150×150 µm^2 cells with an electrode diameter of 1 µm

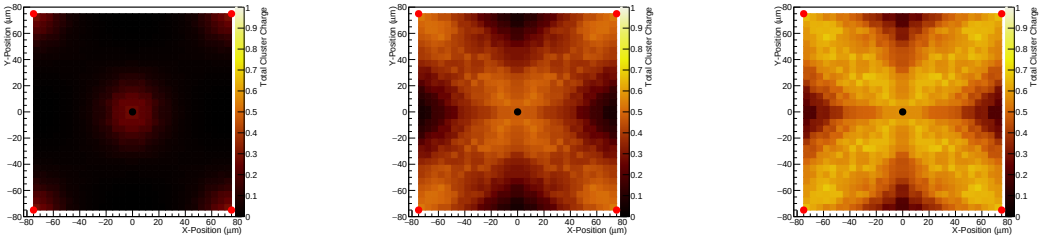

(a) $\tau = 0.1$ ns (b) $\tau = 1$ ns (c) $\tau = 2$ ns

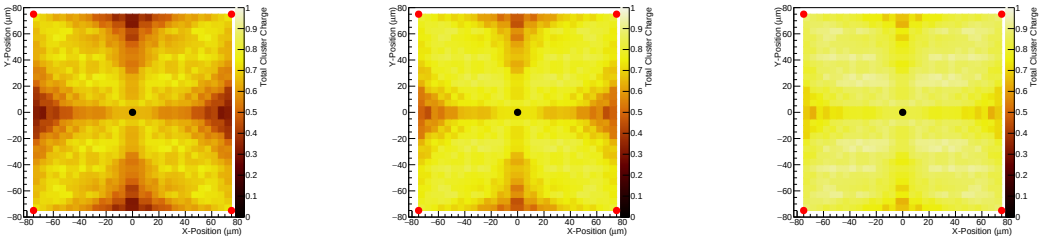

(d) $\tau = 3$ ns (e) $\tau = 5$ ns (f) $\tau = 10$ ns

Figure C.2: Total cluster charge collected as a function of hit position within the cell for different charge lifetimes at 75 V for 150×150 µm^2 cells with an electrode diameter of 2 µm

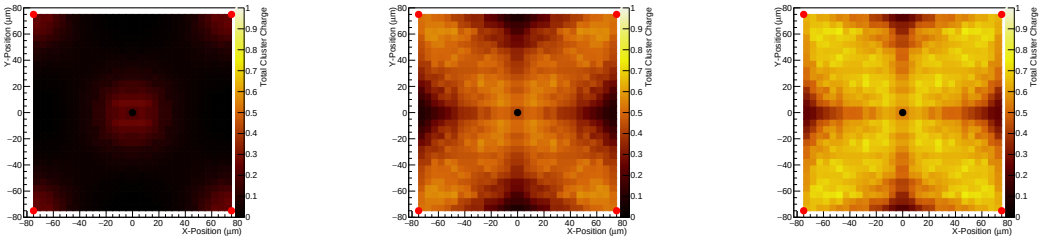

(a) $\tau = 0.1$ ns (b) $\tau = 1$ ns (c) $\tau = 2$ ns

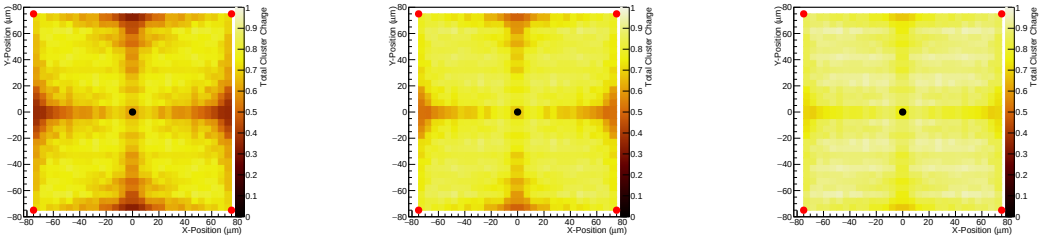

(d) $\tau = 3$ ns (e) $\tau = 5$ ns (f) $\tau = 10$ ns

Figure C.3: Total cluster charge collected as a function of hit position within the cell for different charge lifetimes at 75 V for 150×150 µm^2 cells with an electrode diameter of 5 µm

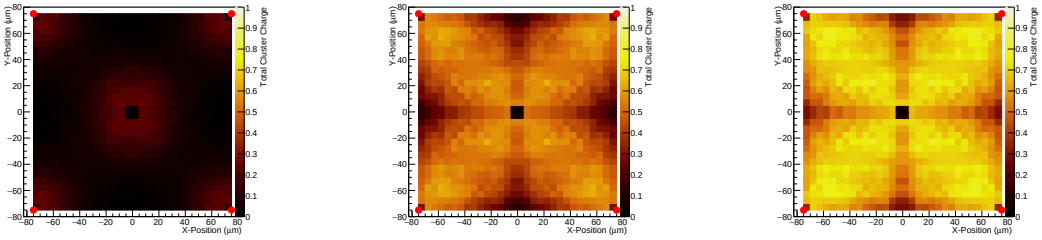

(a) $\tau = 0.1$ ns (b) $\tau = 1$ ns (c) $\tau = 2$ ns

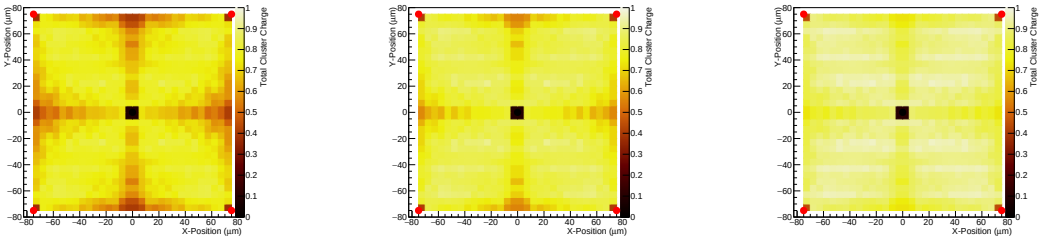

(d) $\tau = 3$ ns (e) $\tau = 5$ ns (f) $\tau = 10$ ns

Figure C.4: Total cluster charge collected as a function of hit position within the cell for different charge lifetimes at 75 V for 150×150 µm^2 cells with an electrode diameter of 8 µm

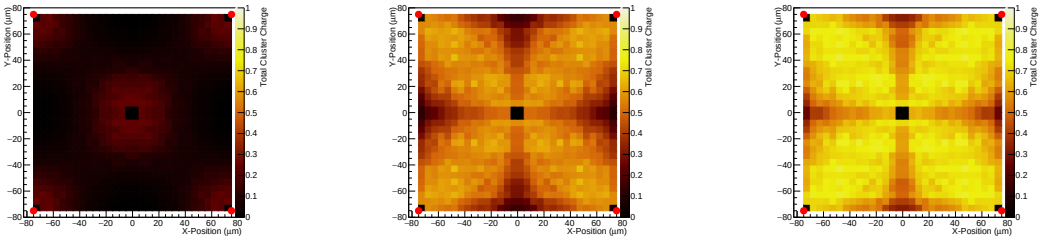

(a) $\tau = 0.1$ ns (b) $\tau = 1$ ns (c) $\tau = 2$ ns

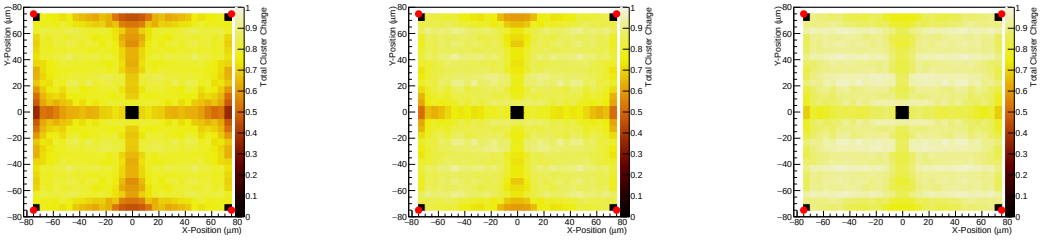

(d) $\tau = 3$ ns (e) $\tau = 5$ ns (f) $\tau = 10$ ns

Figure C.5: Total cluster charge collected as a function of hit position within the cell for different charge lifetimes at 75 V for 150×150 µm^2 cells with an electrode diameter of 10 µm

C.2 Cluster charge as a function of hit position for different cell dimensions

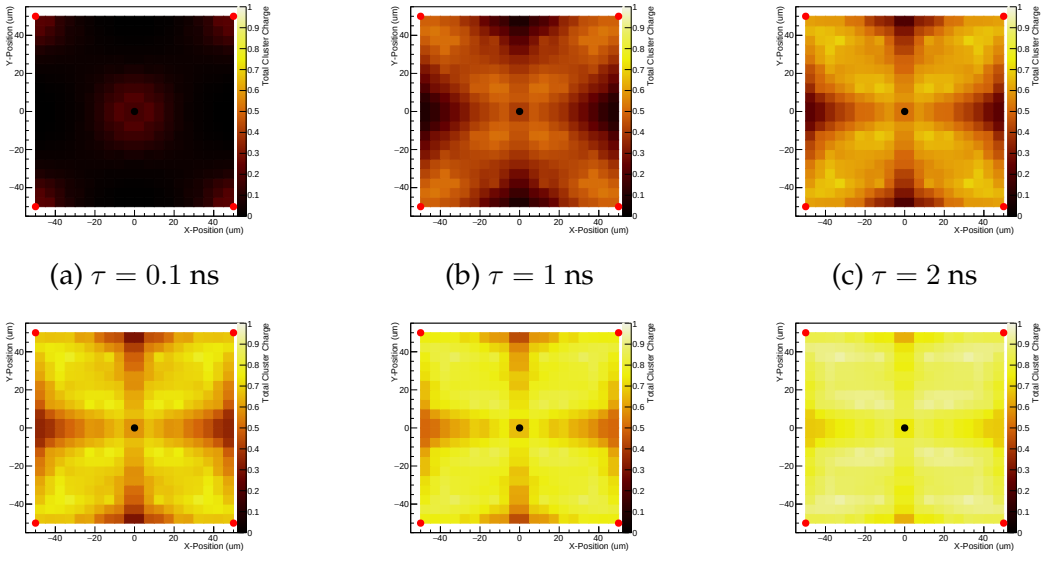

(a) $\tau = 0.1$ ns (b) $\tau = 1$ ns (c) $\tau = 2$ ns

(d) $\tau = 3$ ns (e) $\tau = 5$ ns (f) $\tau = 10$ ns

Figure C.6: Total cluster charge collected as a function of hit position within the cell for different charge lifetimes at 25 V for 100×100 µm^2 cells with an electrode diameter of 5 µm

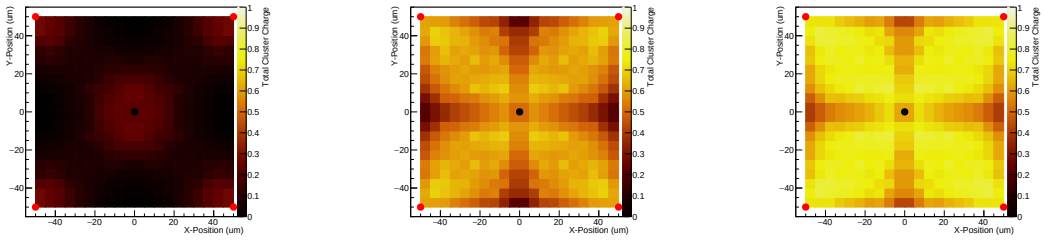

(a) $\tau = 0.1$ ns (b) $\tau = 1$ ns (c) $\tau = 2$ ns

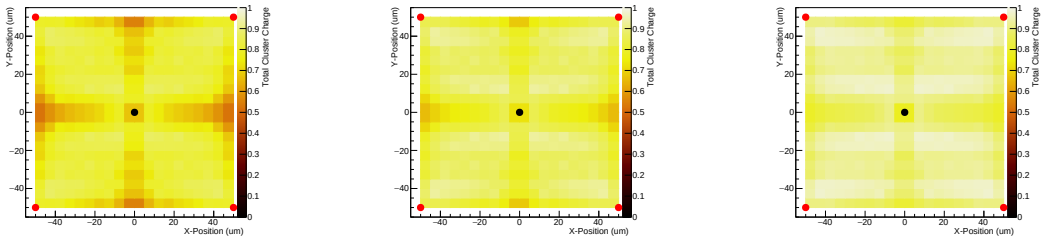

(d) $\tau = 3$ ns (e) $\tau = 5$ ns (f) $\tau = 10$ ns

Figure C.7: Total cluster charge collected as a function of hit position within the cell for different charge lifetimes at 50 V for 100×100 µm^2 cells with an electrode diameter of 5 µm

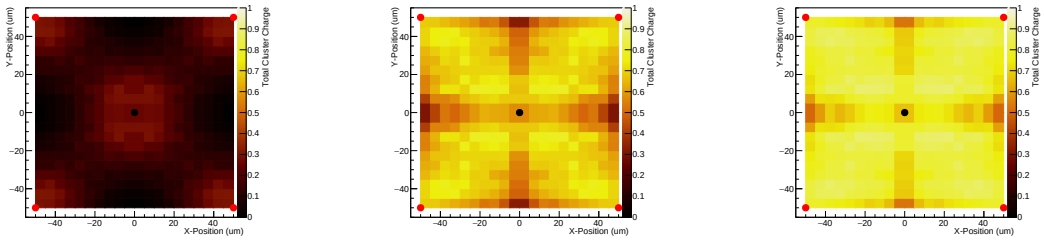

(a) $\tau = 0.1$ ns (b) $\tau = 1$ ns (c) $\tau = 2$ ns

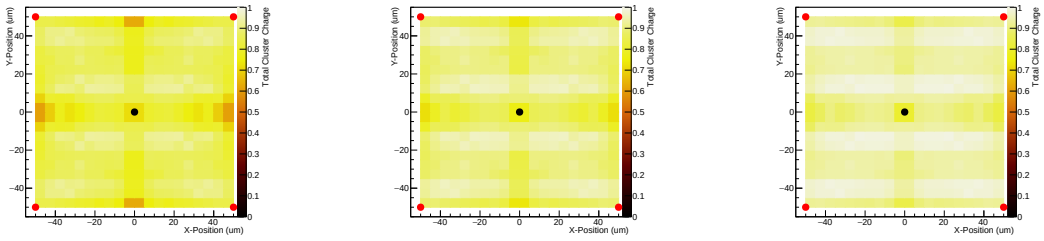

(d) $\tau = 3$ ns (e) $\tau = 5$ ns (f) $\tau = 10$ ns

Figure C.8: Total cluster charge collected as a function of hit position within the cell for different charge lifetimes at 75 V for 100×100 µm^2 cells with an electrode diameter of 5 µm

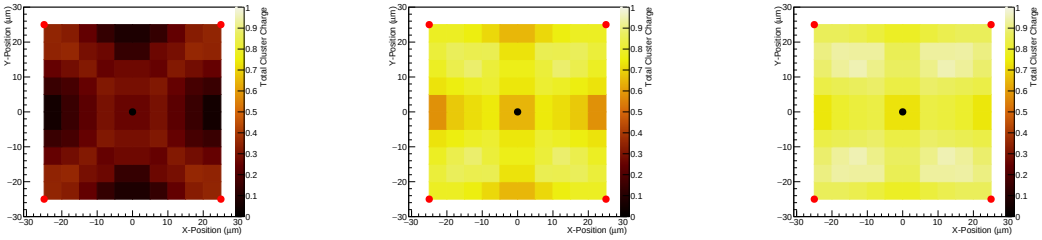

(a) $\tau = 0.1$ ns (b) $\tau = 1$ ns (c) $\tau = 2$ ns

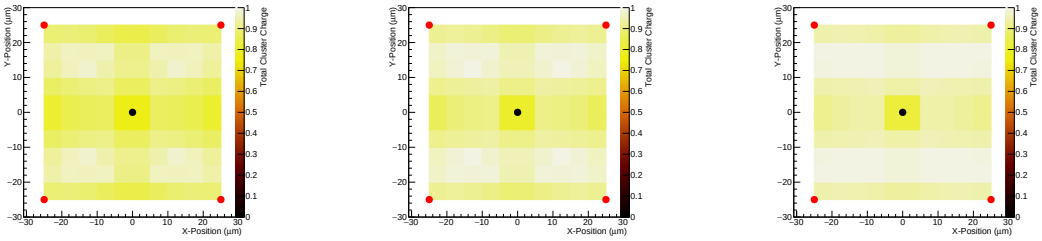

(d) $\tau = 3$ ns (e) $\tau = 5$ ns (f) $\tau = 10$ ns

Figure C.9: Total cluster charge collected as a function of hit position within the cell for different charge lifetimes at 25 V for 50×50 µm^2 cells with an electrode diameter of 5 µm

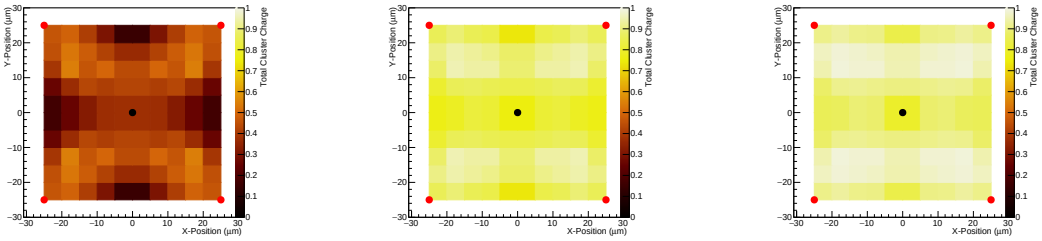

(a) $\tau = 0.1$ ns (b) $\tau = 1$ ns (c) $\tau = 2$ ns

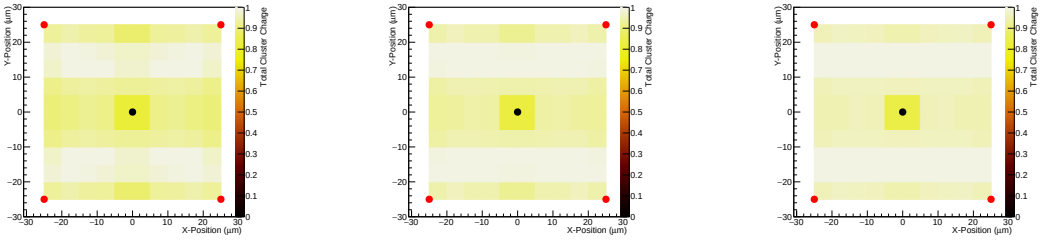

(d) $\tau = 3$ ns (e) $\tau = 5$ ns (f) $\tau = 10$ ns

Figure C.10: Total cluster charge collected as a function of hit position within the cell for different charge lifetimes at 50 V for 50×50 µm^2 cells with an electrode diameter of 5 µm

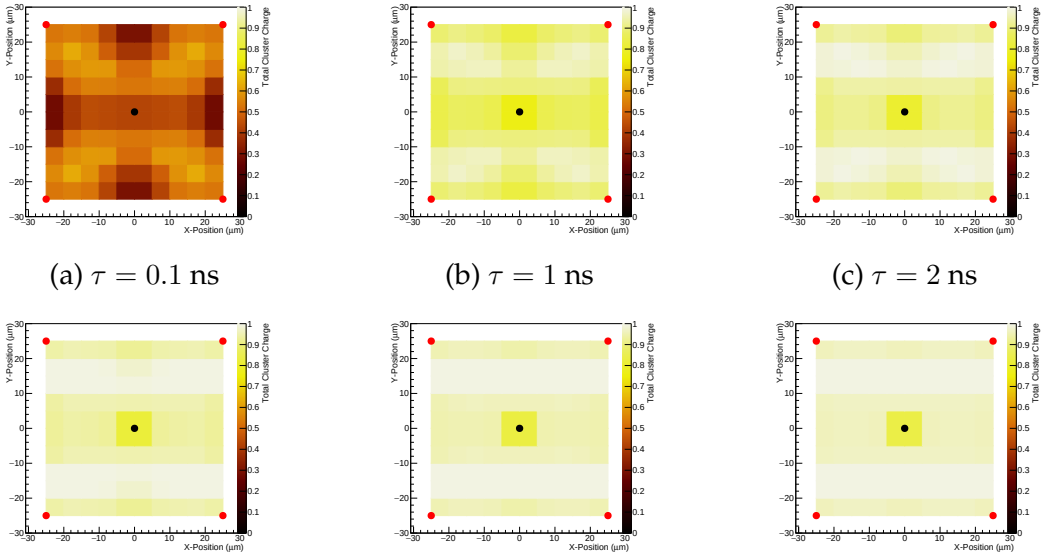

(a) $\tau = 0.1$ ns (b) $\tau = 1$ ns (c) $\tau = 2$ ns

(d) $\tau = 3$ ns (e) $\tau = 5$ ns (f) $\tau = 10$ ns

Figure C.11: Total cluster charge collected as a function of hit position within the cell for different charge lifetimes at 75 V for 50×50 µm^2 cells with an electrode diameter of 5 µm

References

[1] The History of CERN, online, 2018 http://timeline.web.cern.ch/timelines/the-history-of-cern.

[2] CERN, The accelerator complex, online, 2018 http://home.cern/about/accelerators.

[3] CERN H6 beam line, online, 2018 http://sba.web.cern.ch/sba/BeamsAndAreas/resultbeam.asp?beamline=H6.

[4] C. Lefèvre. The CERN accelerator complex. Complexe des accélérateurs du CERN. Dec 2008.

[5] ATLAS Collaboration. *ATLAS Detector and Physics Performance, Technical Design Report Volume 2*. CERN/LHCC 99-15, 1999.

[6] ATLAS Collaboration. Observation of a new particle in the search for the Standard Model Higgs boson with the ATLAS detector at the LHC. *Physics Letters B*, 716(1):1 – 29, 2012.

[7] CMS Collaboration. Observation of a new boson at a mass of 125 GeV with the CMS experiment at the LHC. *Physics Letters B*, 716(1):30 – 61, 2012.

[8] CERN, Computer generated image of the whole ALTAS detector, online, 2018 http://cds.cern.ch/record/1095924.

[9] CERN, Computer generated image of the ALTAS inner detector, online, 2018 http://cds.cern.ch/record/1095926.

[10] G. Aad et al. Atlas pixel detector electronics and sensors. *Journal of Instrumentation*, 3(07):P07007, 2008.

[11] M. Capeans et al. ATLAS Insertable B-Layer Technical Design Report. Technical Report CERN-LHCC-2010-013. ATLAS-TDR-19, CERN, Geneva, Sep 2010.

[12] ATLAS Collaboration. *ATLAS Detector and Physics Performance, Technical Design Report Volume 1*. CERN/LHCC 99-14, 1999.

[13] A. Vogel. ATLAS Transition Radiation Tracker (TRT): Straw Tube Gaseous Detectors at High Rates. Technical Report ATL-INDET-PROC-2013-005, CERN, Geneva, Apr 2013.

[14] Letter of Intent for the Phase-I Upgrade of the ATLAS Experiment. Technical Report CERN-LHCC-2011-012. LHCC-I-020, CERN, Geneva, Nov 2011.

[15] M Shochet, L Tompkins, V Cavaliere, P Giannetti, A Annovi, and G Volpi. Fast TracKer (FTK) Technical Design Report. Technical Report CERN-LHCC-2013-007. ATLAS-TDR-021, Jun 2013. ATLAS Fast Tracker Technical Design Report.

[16] C. Buttar. ATLAS Upgrade Programme. *ATLAS UK 2016*, 1 2016.

[17] T. Kawamoto, S. Vlachos, L. Pontecorvo, J. Dubbert, G. Mikenberg, P. Iengo, C. Dallapiccola, C. Amelung, L. Levinson, R. Richter, and D. Lellouch. New Small Wheel Technical Design Report. Technical Report CERN-LHCC-2013-006. ATLAS-TDR-020, Jun 2013. ATLAS New Small Wheel Technical Design Report.

[18] Collaboration ATLAS. Letter of Intent for the Phase-II Upgrade of the ATLAS Experiment. Technical Report CERN-LHCC-2012-022. LHCC-I-023, CERN, Geneva, Dec 2012.

[19] S. Terzo. The Phase-II ATLAS ITk Pixel Upgrade. Technical Report ATL-ITK-PROC-2017-002, CERN, Geneva, May 2017.

[20] C. Buttar and D. della Volpe. Letter of Intent for the Phase-II Upgrade of the ATLAS Experiment. Technical Report ATL-COM-UPGRADE-2012-040, CERN, Geneva, Oct 2012.

[21] T. Todorov. Alternative very forward layout, (talk given at ATLAS upgrade week, April 2014).

[22] F. Marsolat, D. Tromson, N. Tranchant, M. Pomorski, M. Le Roy, M. Donois, F. Moignau, A. Ostrowsky, L. De Carlan, C. Bassinet, C. Huet, S. Derreumaux, M. Chea, K. Cristina, G. Boisserie, and P. Bergonzo. A new single crystal diamond dosimeter for small beam: comparison with different commercial active detectors. *Physics in Medicine and Biology*, 58(21):7647, 2013.

[23] C. Leroy and P. Rancoita. *Principles of Radiation Interaction In Matter and Detection (3rd Edition)*. World Scientific, 2012.

[24] W.-M. Yao et al. Review of Particle Physics. *Journal of Physics G*, 33, 2006.

[25] ALICE collaboration. First results of the ALICE detector performance at 13 TeV. Aug 2015. ALICE-PUBLIC-2015-004.

[26] S.M. Sze. *Semiconductor Devices Physics and Technology*. Wiley, 1985.

[27] C. Kittel. *Introduction to Solid State Physics*. Wiley, 2005.

[28] J.P. Goss, P.R. Briddon, R. Jones, and S. Sque. Donor and acceptor states in diamond. *Diamond and Related Materials*, 13:684 – 690, 2004. 14th European Conference on Diamond, Diamond-Like Materials, Carbon Nanotubes, Nitrides and Silicon Carbide.

[29] M. Moll. Radiation damage in Silicon particle detectors: Microscopic defects and macroscopic properties. 1999. DESY-THESIS-1999-040.

[30] P. Van Zant. *Microchip fabrication: a practical guide to semiconductor processing*. McGraw-Hill, 1997.

[31] W. Adam et al. The development of diamond tracking detectors for the LHC. *Nuclear Instruments and Methods in Physics Research Section A: Accelerators, Spectrometers, Detectors and Associated Equipment*, 514:79 – 86, 2003. Proceedings of the 4th International Conference on Radiation Effects on Semiconductor Materials, Detectors and Devices.

[32] H. Kagan. Recent advances in diamond detector development. *Nuclear Instruments and Methods in Physics Research Section A: Accelerators, Spectrometers, Detectors and Associated Equipment*, 541:221 – 227, 2005. Development and Application of Semiconductor Tracking Detectors Proceedings of the 5th International Symposium on Development and Application of Semiconductor Tracking Detectors (STD 5) Development and Application of Semiconductor Tracking Detectors.

[33] W. Adam et al. Performance of irradiated CVD diamond micro-strip sensors. *Nuclear Instruments and Methods in Physics Research Section A: Accelerators, Spectrometers, Detectors and Associated Equipment*, 476(3):706 – 712, 2002. Proceedings of the 3rd International Conference on Radiation Effects on Semiconductor Materials, Detectors and Devices.

[34] V. G. Palmieri, K. Borer, S. Janos, C. Da Viá, and L. Casagrande. Evidence for charge collection efficiency recovery in heavily irradiated Silicon detectors operated at cryogenic temperatures. *Nuclear Instruments and Methods in Physics Research Section A: Accelerators, Spectrometers, Detectors and Associated Equipment*, 413(2):475 – 478, 1998.

[35] J. T. Buchan, M. Robinson, H. J. Christie, D. L. Roach, D. K. Ross, and N. A. Marks. Molecular dynamics simulation of radiation damage cascades in diamond. *Journal of Applied Physics*, 117(24), 2015.

[36] M.J. Caturla, T. Diaz de la Rubia, and George H. Gilmer. Disordering and defect production in silicon by keV ion irradiation studied by molecular dynamics. *Nuclear Instruments and Methods in Physics Research Section B: Beam Interactions with Materials and Atoms*, 106(1):1 – 8, 1995.

[37] C. Bauer et al. Recent results from the RD42 Diamond Detector Collaboration. *Nuclear Instruments and Methods in Physics Research Section A: Accelerators, Spectrometers, Detectors and Associated Equipment*, 383(1):64 – 74, 1996. Development and Application of Semiconductor Tracking Detectors.

[38] M. Pomorski, E. Berdermann, W. de Boer, A. Furgeri, C. Sander, and J. Morse. Charge transport properties of single crystal cvd-diamond particle detectors. *Diamond and Related Materials*, 16:1066 – 1069, 2007. Proceedings of Diamond 2006, the 17th European Conference on Diamond, Diamond-Like Materials, Carbon Nanotubes, Nitrides and Silicon Carbide Diamond 2006.

[39] D. Pennicard. 3D detectors for Synchrotron Applications. *University of Glasgow PhD theses repository*, pages 151–153, 2009.

[40] W. Shockley. Currents to conductors induced by a moving point charge. *Journal of Applied Physics*, 9(10), 1938.

[41] S. Ramo. Currents induced by electron motion. *Proceedings of the IRE*, 27(9):584–585, 1939.

[42] P. De Visschere. The validity of Ramo's theorem. *Solid-State Electronics*, 33(4):455 – 459, 1990.

[43] D.M. Caughey and R.E. Thomas. Carrier mobilities in silicon empirically related to doping and field. *Proceedings of the IEEE*, 55(12):2192–2193, Dec 1967.

[44] E. Griesmayer, C. Bloomer, P. Kavrigin, and Ch. Weiss. The Use of Single-crystal CVD Diamond as a Position Sensitive X-ray Detector. In *Proc. of International Beam Instrumentation Conference (IBIC'16), Barcelona, Spain, Sept. 13-18, 2016*, number 5 in International Beam Instrumentation Conference, pages 71–74, Geneva, Switzerland, Feb. 2017. JACoW. doi:10.18429/JACoW-IBIC2016-MOPG14.

[45] H. Pernegger, S. Roe, P. Weilhammer, V. Eremin, H. Frais-Kölbl, E. Griesmayer, H. Kagan, S. Schnetzer, R. Stone, W. Trischuk, D. Twitchen, and A. Whitehead. Charge-carrier properties in synthetic single-crystal diamond measured with the transient-current technique. *Journal of Applied Physics*, 97(7), 2005.

[46] ATLAS Experiment, Semiconductor Tracker (SCT), online, 2018 http://atlasexperiment.org/sct.html.

[47] M. Barbero. The FE-I4 Pixel Readout Chip and the IBL Module. Technical Report ATL-UPGRADE-PROC-2012-001, CERN, Geneva, Jan 2012.

[48] M. Barbero, W. Bertl, G. Dietrich, A. Dorokhov, W. Erdmann, K. Gabathuler, St. Heising, Ch. Hörmann, R. Horisberger, H.Chr. Kästli, D. Kotlinski, B. Meier, and R. Weber. Design and test of the cms pixel readout chip. *Nuclear Instruments and Methods in Physics Research Section A: Accelerators, Spectrometers, Detectors and Associated Equipment*, 517(1):349 – 359, 2004.

[49] C. Kenney, S. Parker, J. Segal, and C. Storment. Silicon detectors with 3-D electrode arrays: fabrication and initial test results. *Nuclear Science, IEEE Transactions on*, 46(4):1224–1236, Aug 1999.

[50] C. Nellist. *Characterisation and Beam Test Data Analysis of 3D Silicon Pixel Detectors for the ATLAS Upgrade*. PhD thesis, University of Manchester, Manchester, 2013.

[51] A. Gorišek, V. Cindro, I. Dolenc, H. Frais-Kölbl, E. Griesmayer, H. Kagan, S. Korpar, G. Kramberger, I. Mandić, M. Meyer, M. Mikuž, H. Pernegger, S. Smith, W. Trischuk, P. Weilhammer, and M. Zavrtanik. ATLAS diamond beam condition monitor. *Nuclear Instruments and Methods in Physics Research Section A: Accelerators, Spectrometers, Detectors and Associated Equipment*, 572(1):67 – 69, 2007. Frontier Detectors for Frontier Physics Proceedings of the 10th Pisa Meeting on Advanced Detectors.

[52] M. Cerv. The ATLAS Diamond Beam Monitor. Technical Report ATL-INDET-PROC-2013-021, CERN, Geneva, Nov 2013.

[53] F.P. Bundy, H.T. Hall, H.M. Strong, and R.H. Wentorf. Man-made diamonds. *Nature*, 176:51 – 55, 1955.

[54] M. Schwander and K. Partes. A review of diamond synthesis by CVD processes. *Diamond and Related Materials*, 20(9):1287 – 1301, 2011.

[55] Y. Ando, S. Tobe, T. Saito, J. Sakurai, H. Tahara, and T. Yoshikawa. Enlargement of the diamond deposition area in combustion flame method by traversing substrate. *Thin Solid Films*, 457(1):217 – 223, 2004. The 16th Symposium on Plasma Science for Materials (SPSM-16).

[56] M. Mayr, O. Klein, M. Fischer, S. Gsell, and M. Schreck. Recent progress in the growth of heteroepitaxial diamond for detector applications. 4th ADAMAS Workshop, GSI, Darmstadt, 2015.

[57] R. J. Nemanich, J. A. Carlisle, A. Hirata, and K. Haenen. CVD diamond-Research, applications, and challenges. *MRS Bulletin*, 39(6):490–494, 2014.

[58] B. V. Spitsyn, L. L. Bouilov, and A. E. Alexenko. Origin, State of the Art and Some Prospects of the Diamond CVD. *Brazilian Journal of Physics*, 30(3):14–19, 2000.

[59] A. Oh, T. Wengler, M. Ahmed, C. Da Viá, and S. Watts. A study of the charge collection properties of polycrystalline CVD diamond with synchrotron radiation. *Diamond and Related Materials*, 20(3):398 – 402, 2011.

[60] University of Bristol, Diamond films on Planar (Flat) Substrates, online, 2018 `http://www.chm.bris.ac.uk/pt/diamond/semflat.htm`.

[61] Element6, online, 2018 `http://www.e6.com/`.

[62] II-VI Incorporated, online, 2018 `http://www.ii-vi.com`.

[63] IIa Technologies, online, 2018 `http://2atechnologies.com`.

[64] Augsburg Diamond Technology GmbH, online, 2018 `http://www.audiatec.de`.

[65] New Diamond Technology, online, 2018 `http://ndtcompany.com`.

[66] M. Pomorski. Electronic properties of IIa HPHT diamond samples from New Diamond Technology. 5th ADAMAS Workshop, GSI, Darmstadt, 2016.

[67] T.V. Kononenko et al. Effects of pulse duration in laser processing of diamond-like carbon films . *Diamond and Related Materials*, 14(8):1368 – 1376, 2005.

[68] T.V. Kononenko, M. Meier, M.S. Komlenok, S.M. Pimenov, V. Romano, V.P. Pashinin, and V.I. Konov. Microstructuring of diamond bulk by IR femtosecond laser pulses. *Applied Physics A*, 90(4):645–651, 2008.

[69] T.V. Kononenko, V.I. Konov, S.M. Pimenov, N.M. Rossukanyi, A.I. Rukovishnikov, and V. Romano. Three-dimensional laser writing in diamond bulk. *Diamond and Related Materials*, 20(2):264 – 268, 2011.

[70] A. Oh, B. Caylar, M. Pomorski, and T. Wengler. A novel detector with graphitic electrodes in CVD diamond. *Diamond and Related Materials*, 38(0):9 – 13, 2013.

[71] B. Caylar, M. Pomorski, and P. Bergonzo. Laser-processed three dimensional graphitic electrodes for diamond radiation detectors. *Applied Physics Letters*, 103(4):–, 2013.

[72] T. Kononenko et al. All-carbon detector with buried graphite pillars in CVD diamond. *Applied Physics A*, 114(2):297–300, 2014.

[73] S. Lagomarsino et al. Three-dimensional diamond detectors: Charge collection efficiency of graphitic electrodes. *Applied Physics Letters*, 103(23), 2013.

[74] K. Kanxheri, L. Servoli, A. Oh, F. Munoz Sanchez, G.T. Forcolin, S.A. Murphy, A. Aitkenhead, C.J. Moore, A. Morozzi, D. Passeri, M. Bellini, C. Corsi, S. Lagomarsino, and S. Sciortino. Evaluation of a 3D diamond detector for medical radiation dosimetry. *Journal of Instrumentation*, 12(01):P01003, 2017.

[75] H.A. Hoff, G.L. Waytena, C.L. Vold, J.S. Suehle, I.P. Isaacson, M.L. Rebbert, D.I. Ma, and K. Harris. Ohmic contacts to semiconducting diamond using a Ti/Pt/Au trilayer metallization scheme. *Diamond and Related Materials*, 5(12):1450 – 1456, 1996.

[76] J. Wang, H. Chen, Y. Bai, X. Lu, and Z. Jin. Pattern metallization on diamond thick film substrate. *Diamond and Related Materials*, 9:1632 – 1635, 2000.

[77] C.M. Zhen, Y.Y. Wang, Q.F. Guo, M. Zhao, Z.W. He, and Y.P. Guo. Ohmic contacts on diamond by B ion implantation and Ta/Au metallization. *Diamond and Related Materials*, 11(9):1709 – 1712, 2002.

[78] J.A. von Windheim, V. Venkatesan, D.M. Malta, and K. Das. Comparison of the electric properties of single-crystal and polycrystalline diamond by hall effect and capacitance-voltage measurements. *Diamond and Related Materials*, 2:841 – 846, 1993. Diamond 1992.

[79] R.E. Harper, C. Johnston, P.R. Chalker, D. Totterdell, I.M. Buckley-Golder, M. Werner, E. Obermeier, and M. Van Rossum. Contacts to doped and undoped polycrystalline diamond films. *Diamond and Related Materials*, 1:692 – 696, 1992. Proceedings of the Second European Conference on Diamond, Diamond-like and Related Coatings.

[80] Sigma-Aldrich, Gold etchant, online, 2018 `http://www.sigmaaldrich.com/catalog/product/aldrich/651818`.

[81] Sigma-Aldrich, Chromium etchant, online, 2018 `http://www.sigmaaldrich.com/catalog/product/aldrich/651826`.

[82] Royal Adhesives, online, 2018 `http://www.royaladhesives.com/`.

[83] S. Deshmukh, L. M. Hitchcock, E. W. Rothe, and G. P. Reck. Graphitization of synthetic diamond by 193 nm laser light: Comparison of 12C-enriched diamonds with those of natural isotopic composition. *Diamond and Related Materials*, 3(3):195 – 197, 1994.

[84] S. Gloor, W. Lüthy, and H.P. Weber. Submicron laser writing on diamond. *Diamond and Related Materials*, 8(10):1853 – 1856, 1999.

[85] T.V. Kononenko, M.S. Komlenok, V.P. Pashinin, S.M. Pimenov, V.I. Konov, M. Neff, V. Romano, and W. Lüthy. Femtosecond laser microstructuring in the bulk of diamond. *Diamond and Related Materials*, 18:196 – 199, 2009. NDNC 2008 Proceedings of the International Conference on New Diamond and Nano Carbons 2008.

[86] I. Haughton. *3D detectors for the High Luminosity LHC, with a feasibility study into the observation of ZZ production in the Z -> ee/uu Z -> TT channel with the ATLAS detector*. PhD thesis, University of Manchester, Manchester, 2015.

[87] L. Graber. *Radiation Hard 3D Diamond Sensors for Vertex Detectors at HL-LHC*. PhD thesis, Georg-August-Universität Göttingen, Göttingen, 2015.

[88] K.K. Ashikkalieva, T.V. Kononenko, E.A. Obraztsova, E.V. Zavedeev, A.A. Khomich, E.E. Ashkinazi, and V.I. Konov. Direct observation of graphenic nanostructures inside femtosecond-laser modified diamond. *Carbon*, 102(Supplement C):383 – 389, 2016.

[89] B. Sun, P. S. Salter, and M. J. Booth. High conductivity micro-wires in diamond following arbitrary paths. *Applied Physics Letters*, 105(23):231105, 2014.

[90] I. Haughton. 3D diamond detectors for tracking and dosimetry. *12th Trento Workshop on Advanced Silicon Radiation Detectors*, 2 2017.

[91] S. A. Murphy. *An Investigation of Processing Techniques and Characterisation Methods for 3D Diamond Detectors*. PhD thesis, University of Manchester, Manchester, 2017.

[92] E. Lukosi, T. Wulz, S. Spanier, and G. Riley. Diamond Efforts at the University of Tennessee. *RD42 Collaboration Meeting*, 2 2015.

[93] W. Schottky. Halbleitertheorie der Sperrschicht. *Naturwissenschaften*, 26(52):843–843, 1938.

[94] K.F. Brennan. *The Physics of Semiconductors*. Cambridge University Press, 1999.

[95] G. Forcolin for the RD42 collaboration. Recent beam test results of 3D detectors constructed with poly-crystalline CVD diamond. *12th Trento Workshop on Advanced Silicon Radiation Detectors*, 2 2017.

[96] Semiconductor Fabrication: Photolithography, online, 2018 `http://britneyspears.ac/physics/fabrication/photolithography.htm`.

[97] W. Adam et al. The first bump-bonded pixel detectors on CVD diamond. *Nuclear Instruments and Methods in Physics Research Section A: Accelerators, Spectrometers, Detectors and Associated Equipment*, 436(3):326 – 335, 1999.

[98] J. Singh. *Semiconductor Optoelectronics, Physics and Technology*. McGraw-Hill, 1995.

[99] C.A. Hewett and J.R. Zeidler. Ohmic contacts to epitaxial and natural diamond. *Diamond and Related Materials*, 2(10):1319 – 1321, 1993.

[100] The LHCb Collaboration. LHCb VELO Upgrade Technical Design Report. Technical Report CERN-LHCC-2013-021. LHCB-TDR-013, CERN, Geneva, Nov 2013.

[101] X. Llopart et al. Timepix, a 65k programmable pixel readout chip for arrival time, energy and/or photon counting measurements. *Nuclear Instruments and Methods in Physics Research Section A: Accelerators, Spectrometers, Detectors and Associated Equipment*, 581:485 – 494, 2007. Proceedings of the 11th International Vienna Conference on Instrumentation.

[102] T. Fritzsch, K. Zoschke, M. Woehrmann, M. Rothermund, F. Huegging, O. Ehrmann, H. Oppermann, and K. D. Lang. Flip chip assembly of thinned chips for hybrid pixel detector applications. *Journal of Instrumentation*, 9(05):C05039, 2014.

[103] R. Bates, C. Buttar, T. McMullen, L. Cunningham, G. Pares, L. Vignoud, F. Munoz, and S. Vahanen. Thin hybrid pixel assembly fabrication development with backside compensation layer. *14th Vienna Conference On Instrumentation*, 2 2016.

[104] *ATLAS inner detector: Technical Design Report, 1*. Technical Design Report ATLAS. CERN, Geneva, 1997.

[105] The LHCb Collaboration. *LHCb VELO (VErtex LOcator): Technical Design Report*. Technical Design Report LHCb. CERN, Geneva, 2001.

[106] The LHCb Collaboration. *LHCb inner tracker: Technical Design Report*. Technical Design Report LHCb. CERN, Geneva, 2002. revised version number 1 submitted on 2002-11-13 14:14:34.

[107] C. Colledani, W. Dulinski, R. Turchetta, F. Djama, A. Rudge, and P. Weilhammer. A submicron precision Silicon telescope for beam test purposes. *Nuclear Instruments and Methods in Physics Research Section A: Accelerators, Spectrometers, Detectors and Associated Equipment*, 372(3):379 – 384, 1996.

[108] CIVIDEC Instrumentation, online, 2018 `https://cividec.at`.

[109] Teledyne Lecroy, online, 2018 http://teledynelecroy.com.

[110] G.T. Forcolin, V. Grilj, B. Hamilton, L. Li, M. McGowan, S.A. Murphy, A. Oh, N. Skukan, D. Whitehead, and A. Zadoroshnyj. Study of a 3D diamond detector with photon and proton micro-beams. *Diamond and Related Materials*, 65:75 – 82, 2016. Special Issue 26th International Conference on Diamond and Carbon Materials DCM 2015.

[111] F. Bachmair, L. Bäni, P. Bergonzo, B. Caylar, G. Forcolin, I. Haughton, D. Hits, H. Kagan, R. Kass, L. Li, A. Oh, S. Phan, M. Pomorski, D.S. Smith, V. Tyzhnevyi, R. Wallny, and D. Whitehead. A 3D diamond detector for particle tracking. *Nuclear Instruments and Methods in Physics Research Section A: Accelerators, Spectrometers, Detectors and Associated Equipment*, 786:97 – 104, 2015.

[112] Integrated Detectors and Electronics AS, Data Sheet VA2 Readout Chip, Oslo, Norway. 2014.

[113] L. S. Pan, S. Han, and D. R. Kania. *Diamond: Electronic Properties and Applications*. Kluwer Academic, Dordrecht, 1995.

[114] S. Mathias and J. Dodson. Diamond material for radiation detectors. 1st ADAMAS Workshop, GSI, Darmstadt, 2012.

[115] H. Schone, D. S. Walsh, F. W. Sexton, B. L. Doyle, P. E. Dodd, J. F. Aurand, R. S. Flores, and N. Wing. Time-resolved ion beam induced charge collection (TRIBICC) in micro-electronics. *IEEE Transactions on Nuclear Science*, 45(6):2544–2549, Dec 1998.

[116] M. Jakšić, L. Kukec, and V. Valković. The Zagreb nuclear microprobe facility. *Nuclear Instruments and Methods in Physics Research Section B: Beam Interactions with Materials and Atoms*, 77(1):49 – 51, 1993.

[117] M.J. Booth, G.T. Forcolin, V. Grilj, B. Hamilton, I. Haughton, M. McGowan, S.A. Murphy, A. Oh, P.S. Salter, I. Sudić, and N. Skukan. Study of cubic and hexagonal cell geometries of a 3D diamond detector with a proton microbeam. *Diamond and Related Materials*, 2017.

[118] K. J. S. Sawhney, I. P. Dolbnya, M. K. Tiwari, L. Alianelli, S. M. Scott, G. M. Preece, U. K. Pedersen, and R. D. Walton. A test beamline on diamond light source. *AIP Conference Proceedings*, 1234(1):387–390, 2010.

[119] CAEN, online, 2018 http://www.caen.it.

[120] Tektronix, Keithley Instruments and Products, online, 2018 https://www.tek.com/keithley.

[121] National Institute of Standards and Technology, Stopping-power and Range Tables for Electrons, Protons, and Helium Ions, online, 2018 https://www.nist.gov/pml/.

[122] D. Meier. *CVD Diamond Sensors for Particle Detection and Tracking*. PhD thesis, Heidelberg U., 1999.

[123] F. C. Bachmair. *CVD Diamond Sensors In Detectors For High Energy Physics*. PhD thesis, Zürich, ETH, Zürich, 2016. Presented 19 Oct 2016.

[124] The Element Six CVD Diamond Handbook. 2015.

[125] J. Isberg, J. Hammersberg, H. Bernhoff, D.J. Twitchen, and A.J. Whitehead. Charge collection distance measurements in single and polycrystalline CVD diamond. *Diamond and Related Materials*, 13:872 – 875, 2004. 14th European Conference on Diamond, Diamond-Like Materials, Carbon Nanotubes, Nitrides and Silicon Carbide.

[126] M. Marinelli, E. Milani, A. Paoletti, A. Tucciarone, G. Verona Rinati, M. Angelone, and M. Pillon. Trapping-detrapping behavior in CVD diamond particle detectors. *Diamond and Related Materials*, 10(3-7):645 – 649, 2001. 11th European Conference on Diamond, Diamond-like Materials, Carbon Nanotubes, Nitrides and Silicon Carbide.

[127] GafChromic dosimetry films, online, 2018 http://www.gafchromic.com.

[128] D. A. Sanz Becerra. *TBA*. PhD thesis, Zürich, ETH, Zürich, 2019 (expected).

[129] T. Wulz, B. K. Canfield, L. M. Davis, S. Spanier, and E. Lukosi. Pulsed femtosecond-laser machining and deep reactive ion etching of diamond. *Diamond and Related Materials*, 74:108 – 113, 2017.

[130] T. Flick. The phase II ATLAS Pixel upgrade: the Inner Tracker (ITk). *Journal of Instrumentation*, 12(01):C01098, 2017.

[131] JD Photo Data, online, 2018 http://www.jd-photodata.co.uk.

[132] D. Sanz. 3D detector results from 2016 CERN test beams. *RD42 Collaboration Meeting*, 5 2016.

[133] Fraunhofer IZM, online, 2018 https://www.izm.fraunhofer.de/en.html.